Model-Based Impact Analysis of Vehicle-Integrated Photovoltaics and Vehicle-to-Grid on Electric Vehicle Battery Life

Antonios Kouzelis

TU Delft

Model-Based Impact Analysis of Vehicle-Integrated Photovoltaics and Vehicle-to-Grid on Electric Vehicle Battery Life

by

Antonios Kouzelis

to obtain the degree of Master of Science at Delft University of Technology,
to be defended publicly on November 30th, 2022.

Degree:	MSc Sustainable Energy Technology	
Track:	Autonomous Systems	
Faculty:	Electrical Engineering, Mathematics & Computer Science	
Section:	DC Systems, Energy Conversion & Storage	
Student number:	4484630	
Project duration:	February 14, 2022 – November 30, 2022	
Thesis committee:	Prof.dr.ir. P. Bauer,	TU Delft, committee chairman
	Dr.ir. R. Santbergen,	TU Delft, committee member
	Dr.ir. G.R. Chandra Mouli,	TU Delft, thesis supervisor
	Dr.ir. S. Bandyopadhyay,	Lightyear, external expert

November 19, 2022

TU Delft Delft University of Technology Lightyear

Preface

This thesis is the result of seven years of education, research and activities at Delft University of Technology, and is the final step in obtaining the Master's degree in Sustainable Energy Technology. Along the way, I have had the pleasure to be surrounded by many talented and kind people, some of whom I would like to thank.

Firstly, I would like to thank my supervisors from TU Delft and Lightyear, Gautham Ram and Soumya Bandyopadhyay. Gautham, it were both Lightyear employees and professors at TU Delft who highly recommended you as a supervisor, but I could not have not foreseen such a pleasant supervision throughout my thesis. I have been incredibly fortunate to benefit from your knowledge, motivation and feedback, which have further expanded my passion for sustainable mobility. Experiencing you light up the room during your presentation at the Battery on Wheels Conference is a testament that I am among many others inspired by your passion and knowledge. Soumya, on my fourth day at Lightyear back in September 2021, you inspired me to dive deeper into V2G, which essentially led me to conduct scientific research on the topic over the past 10 months. Your level-headed guidance and expertise helped me complete my thesis almost stress-free, for which I am grateful.

Secondly, I would like to thank the people at Lightyear for facilitating this research and for making working feel like leisure. A special thank you to Tom Selten for being a mentor since day one, and to Mayk Thewessen for taking the time to provide modelling support and engineering insights. Moreover, I would like to thank Bogdan Rosca, Simone Regondi, Tom van Beurden and everyone within the BDPA and Strategy teams for their support and encouragements throughout this project.

Last but certainly not least, a heartfelt thank you to my parents, Dimitris and Gelly, big brother, Konstantinos, and girlfriend, Tess, for inspiring me in all aspects of life. Both your love and your lessons have been invaluable. Together with my close friends, you have made me grow both personally and academically to become who I am today. Thank you for always being there and for supporting me throughout this journey.

I am excited to continue working on the publication of an article with my supervisors and hopefully present my work at the PVinMotion 2023 Conference. For now, I hope that the cool EV technologies described in my work will excite you as much as they excite me.

Antonios Kouzelis
Amsterdam, November 2022

Abstract

Electric vehicles (EVs) equipped with vehicle-integrated photovoltaics (VIPV) and EVs with vehicle-to-grid (V2G) technology can support in overcoming power grid challenges emerging from the energy transition. Despite the widespread benefits that VIPV and V2G have to offer, their potential impact on battery life governs their economic viability. Current studies on the impact of VIPV and V2G on battery life are often simplistic, use unrealistic battery data, and rarely investigate methods to reduce battery ageing. To fill this research gap, this study combines validated models to determine the impact of VIPV and V2G on EV battery life and investigates methods to reduce battery ageing.

First, an EV battery data generation model was developed to simulate EV load profiles with and without VIPV and V2G. Afterwards, a one-year mobility and charging profile was constructed based on EV driving data in the Netherlands and Germany. Subsequently, driving cycles were simulated using Lightyear's Vehicle Performance Model (VPM) to generate realistic per-second EV battery data. Following this, VIPV power generation profiles for the Netherlands and Spain were modelled using Lightyear's SolarSimulator tool. Thereafter, two load profiles of V2G services in the Netherlands were modelled, namely day-ahead electricity trading and automatic frequency restoration reserve (aFRR), both with a battery capacity retention limit during V2G of 50% state of charge (SoC) and 20% SoC. The VIPV and V2G load profiles were merged with EV battery data to generate eight EV battery datasets. Finally, the EV battery datasets were implemented in a semi-empirical NMC-based ageing model (NMC-AM) and a semi-empirical LFP-based ageing model (LFP-AM) to determine the impact of VIPV and V2G on battery life.

Results from the EV battery data generation model show that gradual VIPV charging can reduce the annual grid charging frequency by 23% in the Netherlands and 44% in Spain. Reduced grid charging frequency due to VIPV caused the battery to range at lower SoC, which is beneficial for battery calendar life. Consequently, NMC-AM suggests that VIPV could extend battery life by 6 months, while LFP-AM suggests a battery life extension of 2 months. However, additional irregularity in the load profile due to gradual VIPV charging is likely to have caused the ageing models to overestimate cycling ageing. Furthermore, the ageing models suggest that additional cycling due to V2G, with the aim of maximising profits for the EV owner, could shorten battery life by 7.8 to 12.5 years for NMC and by 1.2 to 3.9 years for LFP. The results of the ageing models indicate that LFP batteries are more resistant to additional cycling than NMC, which is in line with literature.

Additionally, simulated scenarios in which the SoC was kept at 50% or 100% for one month per year, showed that SoC regulation could extend battery life by up to 2 years, allowing for 38,000 km of additional driving range before the battery reaches its end of life (EoL). Furthermore, results suggest that VIPV could lower battery temperature by 10 °C within one sun hour and can keep the battery cool when parked in the sun, by 23 °C in the Netherlands and 35 °C in Spain. Ageing simulations in which VIPV was used to cool the average annual battery temperature by 5°C, suggest that VIPV can extend battery life by up to 4.6 years, allowing for 88,000 km of additional driving range before the battery reaches its EoL. SoC regulation can be performed by delayed VIPV charging, delayed grid charging, or V2G. Battery temperature regulation can be performed using VIPV or grid power. Taking electricity cost into account, grid-powered battery temperature regulation could prove to be a cost-effective method to extend battery life, especially for EVs experiencing extreme temperatures.

Furthermore, as semi-empirical ageing models often lack clarity regarding their implementation, are usually not based on ageing tests with irregular load profiles, do not consider path dependency, are based on accelerated ageing tests under limited operating conditions and on a particular battery cell chemistry and size, applying these ageing models on irregular load profiles or other cells may lead to ageing estimation errors. Consequently, to determine how VIPV impacts battery cycle life, it is recommended to conduct battery ageing tests under identical operating conditions, with and without VIPV. Further research on the impact of VIPV on battery life would help develop strategies that optimally balance VIPV power used for battery charging and for battery temperature regulation.

Concluding, this research shows promising initial findings on methods to reduce battery ageing using VIPV and V2G, which could further improve their business case, accelerating the transition to sustainable mobility.

Acronyms

aFRR automatic Frequency Restoration Reserve

ASM Alliance for Solar Mobility

BoH beginning of health

BSP balancing service provider

CBS Centraal Bureau voor de Statistiek

CC constant current

COP coefficient of performance

c-Si crystalline silicon

CEI cathode electrolyte interface

CL contact loss

C-rate current rate

CV constant voltage

DoD depth of discharge

DSO Distribution System Operator

e-mobility electric mobility

EoL end of life

EU European Union

EV electric vehicle

FAT full activation time

FCR Frequency Containment Reserve

GHG greenhouse gas

HV high voltage

HVAC HV air conditioning

ICE internal combustion engine

ISP imbalance settlement price

kWh kilowatt-hour

LAM loss of active material

LCO lithium cobalt oxide

LFP lithium iron phosphate

LFP-AM LFP-based semi-empirical ageing model

LLI loss of lithium inventory

LMO lithium manganese oxide

LTO lithium titanate oxide

LV low voltage

mFRR manual Frequency Restoration Reserve

MiG Mobility in Germany

MILP mixed integer linear program

NCA lithium nickel cobalt aluminium oxide

NiMH nickel-metal hydride

NMC lithium nickel manganese cobalt oxide

NMC-AMII second NMC-based semi-empirical ageing model

NMC-AM NMC-based semi-empirical ageing model

OBC onboard charger

OEM original equipment manufacturer

PMR power-to-mass

R&D research and development

RMSE root mean square error

SEI solid electrolyte interface

SEV solar electric vehicle

SoC state of charge

SoH state of health

SSB solid-state batteries

STC standard test conditions

TMY typical meteorological year

TSO Transmission System Operator

V2G vehicle-to-grid

V2X vehicle-to-everything

VIPV vehicle-integrated photovoltaics

WLTC Worldwide harmonized Light vehicles Test Cycle

WLTP Worldwide harmonised Light vehicles Test Procedures

Contents

List of Figures

List of Tables

1

Introduction

In both 2020 and 2021, the transportation sector was the most significant contributor to the European Union's (EU) greenhouse gas (GHG) emissions [20, 86]. With the intention of reducing GHG emissions from transportation, the EU recently announced measures that no longer allow cars or vans with an internal combustion engine (ICE) to enter the market from 2035 onwards [24]. Compared to ICE vehicles, electric vehicles (EVs) are responsible for a considerably smaller amount of GHG emissions [22, 100]. In Europe in 2021, the full life-cycle GHG emissions of an average EV were 66% lower than comparable ICE vehicles [27]. The introduction of EVs can thus plays a crucial role in decarbonising the transportation sector. Fortunately, global EV market penetration is estimated to reach 56% by 2035, as shown in the left graph of Figure 1.1 [58]. Although EVs can help reduce GHG emissions from the transportation sector, the increasing market penetration of EVs can cause grid congestion and electricity shortage risks for Transmission System Operators (TSOs) and Distribution System Operators (DSOs). Vehicle-to-grid (V2G), which enables EVs to discharge electricity into the power grid, and vehicle-integrated photovoltaics (VIPV) which enables EVs to charge using solar energy, can support grid operators in overcoming these power grid challenges.

EVs with V2G can enable a more reliable electricity grid by offering electricity trading and grid balancing services to TSOs. By charging from the grid when electricity demand is low and discharging into the grid when electricity demand is high, EVs can collectively act as a virtual power plant to even out energy imbalances for TSOs. EV owners can thereby benefit from low charging costs during low electricity demand and are financially compensated for offering balancing services during high electricity demand.

EVs with VIPV, or solar electric vehicles (SEVs), partially charge from the sun and are designed to be energy efficient. SEVs thereby naturally demand less electricity from the power grid compared to typical EVs, which helps DSOs reduce grid congestion [106]. Research suggests that a 20% market penetration of SEVs in the Netherlands could reduce investments in the Dutch power grid by €2.2 bn in the 2022-2040 period [71].

However, to realise the widespread implementation of VIPV and V2G, the technologies must be cost-effective [41]. By discharging and charging the battery, VIPV and V2G impact battery life. While the cost of batteries is expected to reduce significantly, batteries are expected to remain the most expensive subsystem of an EV, as shown in the right graph of Figure 1.1 [18, 46, 50]. The impact of VIPV and V2G on battery life thereby governs their economic viability [41, 89].

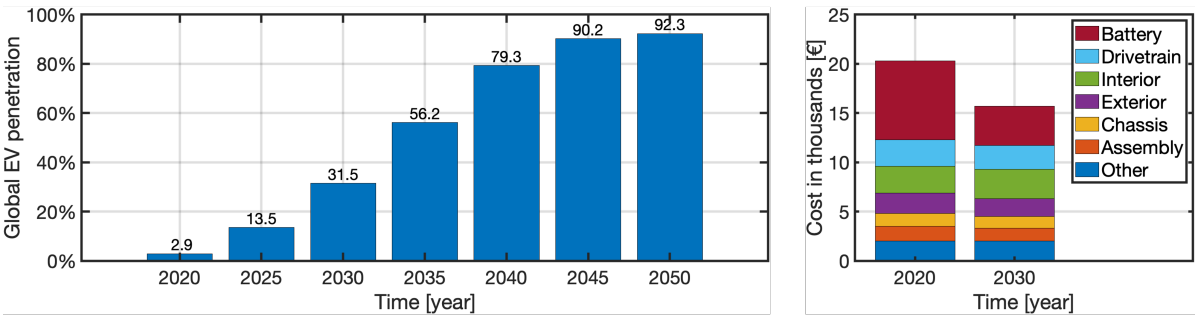

Figure 1.1: The left graph shows the estimated global EV market penetration forecast from 2020 to 2050 [58]. The right graph shows the estimated cost of manufacturing different EV subsystems for 2020 and 2030 [46].

Researchers agree that additional cycling for V2G services is harmful to Li-ion battery life [18, 59, 96, 106, 114]. One study found that when batteries are additionally cycled for V2G services with the aim of maximising profit for the EV owner, V2G services can result in a 75% increase in capacity loss [18]. Another study found that with an optimised V2G strategy, V2G can extend battery life [98]. Although researchers agree that V2G services without battery life optimisation strategies will shorten battery life, the impact of V2G services available in the Netherlands on battery life has yet to be researched. The most extensive study on the impact of VIPV on battery life found that solar panels could elongate battery cycle life [50]. However, the researchers neglected the impact of VIPV on battery calendar life and considered only one battery ageing stress factor, while multiple stress factors impact ageing. Additionally, the model-based study used a simplistic battery model to simulate EV battery data. Furthermore, researchers have studied methods to extend battery life by lowering the average battery state of charge (SoC) [18, 33, 98], which is considered beneficial for Li-ion batteries [5, 18, 81, 84, 102]. Moreover, while increased battery temperatures also heavily impact Li-ion battery life, methods to reduce battery ageing through VIPV and V2G-powered thermal battery management have yet to be researched [5, 81, 102]. Generally, it appears that studies on the impact of VIPV and V2G on battery life either use unrealistic load profiles or simplistic ageing models to determine the impact on battery life. Moreover, methods to extend battery life using VIPV have not been investigated.

To fill this research gap, this study determines the impact of VIPV and V2G on EV battery life using validated models. First, Lightyear's Vehicle Performance Model (VPM) is used to simulate realistic EV battery data. Following this, Lightyear's SolarSimulator tool is used to model VIPV power generation profiles for the Netherlands and Spain. Subsequently, V2G data from the Netherlands is used to model the V2G electricity demand and response load profile. Afterwards, the generated EV battery datasets are consequently implemented in validated semi-empirical ageing models from literature to quantify the impact of VIPV and V2G on battery calendar and cycle life. Finally, methods to reduce battery ageing using VIPV and V2G are proposed.

This work is conducted in collaboration with Delft University of Technology and Lightyear, the SEV manufacturer based in Eindhoven, the Netherlands. For illustration purposes, Figure 1.2 shows the energy flows of a Lightyear 0 vehicle charging its battery using VIPV and discharging it into the power grid using V2G.

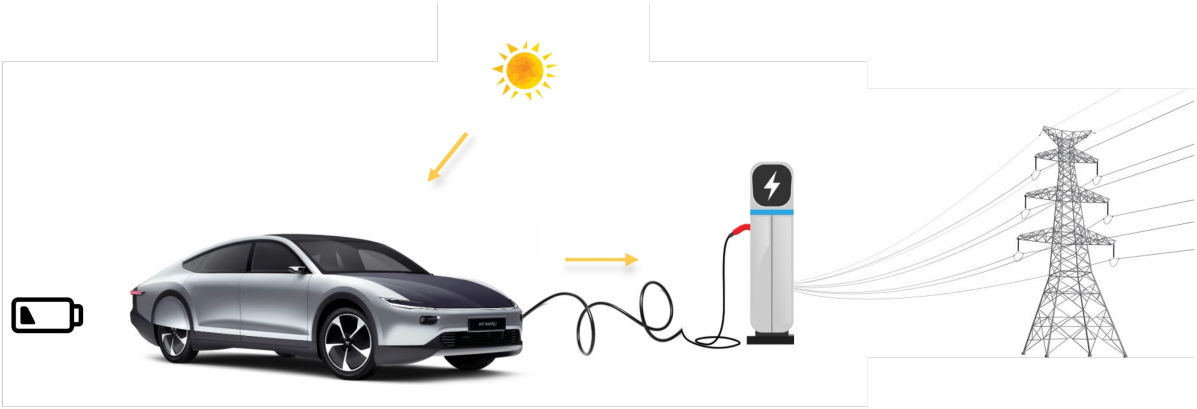

Figure 1.2: Illustration of the energy flows of a Lightyear 0 vehicle that is charging its battery using VIPV and discharging it using V2G.

1.1. Motivation

Despite the widespread benefits of VIPV and V2G, the potential impact of VIPV and V2G on battery life present economic and regulatory implications for EV owners, original equipment manufacturers (OEMs) and policymakers [41, 98]. Established EV manufacturers like Hyundai and EV scale-ups like Lightyear are currently developing V2G technology. Lightyear is also developing a VIPV system certified for automotive standards and designed for mass customisation. Researchers suggest that an appropriate compensation model for V2G and a cost-effective integration of VIPV are necessary to enforce the expansion of these technologies [41, 91].

To support OEMs and policymakers with the development of business models and appropriate compensation models for VIPV and V2G, this work investigates the impact of these technologies on EV battery life. Additionally, methods to extend battery calendar life using VIPV and V2G are investigated. This work is conducted to support the further development of VIPV and V2G with the ultimate goal of accelerating the decarbonisation of the transportation sector.

1.2. Research objective

Based on the existing literature and the motivation, the research objective is formulated as follows:

Determine the impact of vehicle-integrated photovoltaics and vehicle-to-grid on electric vehicle battery life.

To fulfil the research objective, four sub-objectives are addressed. The sub-objectives are shown schematically in Figure 1.3 and are elaborated on below.

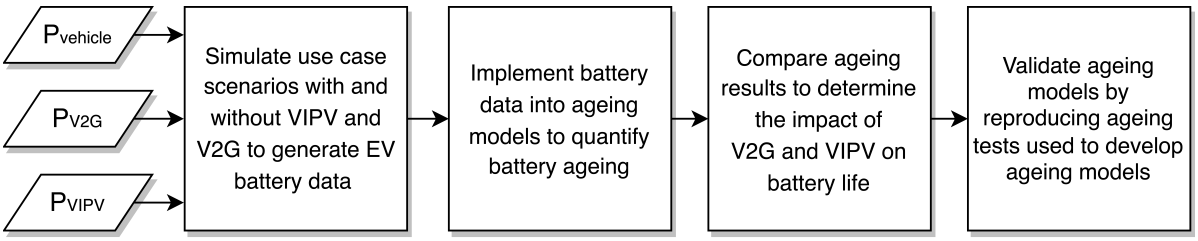

Figure 1.3: Flow diagram depicting the steps required to fulfil the proposed research objective.

i Simulate use case scenarios with and without VIPV and V2G to generate one-year EV battery datasets.

ii Implement the EV battery datasets into battery ageing models from literature to quantify battery calendar and cycling ageing for each use case scenario.

iii Compare the ageing results of the use case scenarios to analyse the impact of VIPV and V2G on battery calendar and cycling ageing.

iv Validate the ageing models by simulating ageing tests performed to develop the ageing models.

1.3. Methodology

The following methodology is defined to fulfil the research objectives stated in Section 1.2.

Literature review

The literature review uses papers found predominantly in the fields of electrochemistry and power. It provides insight into the characteristics and electrochemistry of commonly used Li-ion EV battery. Li-ion battery ageing causes, mechanisms, degradation modes and subsequent effects on battery capacity and power capability are described. The developments in VIPV technology are discussed and he mechanism of V2G day-ahead electricity trading and V2G grid-balancing services are explained.

EV battery ageing modelling

Realistic driving and charging profiles are designed based on EV driving data in the Netherlands and Germany. A modelled version of the Lightyear 0, the world's first production-ready SEV, is used to simulate EV battery data. Various driving cycles are simulated to generate realistic one-year EV power profiles. These modelled power profiles follow the mobility and charging behaviour of EV drivers. Power profiles of VIPV and V2G are integrated with the EV power profiles to simulate various use case scenarios. These power profiles form the basis for deriving the factors that stress battery life. The battery datasets are consequently implemented in battery ageing models found in literature. These models integrate the battery data into ageing equations derived from empirical ageing tests to determine the capacity loss due to calendar and cycling ageing.

Validation and results

The capacity loss due to battery calendar and cycling ageing is determined for realistic use case scenarios, with and without VIPV and V2G. The battery ageing results of the use case scenarios are compared with each other to determine how certain applications of VIPV and V2G affect battery life. The model that generates EV battery data is validated by comparing its output with battery data from the VPM. Finally, the ageing models are validated by simulating the ageing tests used by the authors to develop the ageing models, to compare the modelled results with results from the ageing tests.

1.4. Scope

The scope of this work is limited to one passenger EV, two geographical areas, two Li-ion battery technologies, two different kinds of V2G services with two different configurations, and three battery ageing models from literature. The EV used for simulations and data modelling is the Lightyear 0. The locations used to model VIPV power generation potential are Amsterdam, the Netherlands and Madrid, Spain. Both V2G day-ahead electricity trading and V2G grid balancing services are simulated for the Netherlands. The battery technologies researched in terms of ageing are lithium nickel manganese cobalt oxide (NMC) and lithium iron phosphate (LFP). The scope of this work results in eight different use case scenarios, which are summarised in Table 1.1. These scenarios correspond to driving and charging scenarios of an EV with and without VIPV and V2G, with variations in VIPV power generation, type of V2G service and with battery capacity retention limits during V2G of 50% SoC and 20% SoC. One-year EV load profiles are modelled per second for each use case scenario. These load profiles portray the net power load acting on the battery and form the basis for deriving the profiles for the battery SoC, temperature, voltage, current, C-rate, number of cycles, and throughput. The EV battery datasets are implemented in two of the three semi-empirical ageing models from literature. Due to the limitations of the LFP ageing model, the results from the NMC ageing model are the main focus of this work.

Table 1.1: Use case scenarios researched with respect to battery ageing. 'Standard' corresponds to the standard EV battery load which consists of power for forward traction, grid charging, regenerative braking, and the necessary auxiliaries.

	Load profiles			
Use case scenario	Standard	VIPV	$V2G_{Day\text{-}Ahead}$	$V2G_{aFRR}$
Base	V			
$VIPV_{NL}$	V	V		
$VIPV_{ESP}$	V	V		
$VIPV_{NL}$ & $V2G_{DA}^{50\%\ SoC}$	V	V	V	
$V2G_{DA}^{50\%\ SoC}$	V		V	
$V2G_{DA}^{20\%\ SoC}$	V		V	
$V2G_{aFRR}^{50\%\ SoC}$	V			V
$V2G_{aFRR}^{20\%\ SoC}$	V			V

2

Background

This chapter elaborates on EV batteries, VIPV and V2G. In Section 2.1, the working principle of Li-ion batteries is explained, battery chemistries commonly found in EVs are compared, and factors that impact battery ageing are explained. Afterwards, Section 2.2 provides an overview of the types of battery ageing models. Finally, the workings of VIPV and V2G are described in Sections 2.3 and 2.4, respectively.

2.1. EV batteries

Over the years, various rechargeable battery chemistries have been used to power EVs, with the three main types being lead-acid, nickel-metal hydride (NiMH) and Li-ion. Li-ion batteries have taken the stage due to their high volumetric energy density, high gravimetric energy density (specific energy), high gravimetric power density (specific power), and low self-discharge rate [37, 105]. Several EV manufacturers have also shown interest in solid-state batteries (SSB), which uses a solid-state electrolyte instead of a liquid electrolyte and a carbon anode. While SSBs could result in a 20% energy density improvement, the technical challenges of SSBs, coupled with the decreasing cost of liquid electrolytes leads researchers to conclude that Li-ion batteries will likely remain the favoured technology in the foreseeable future [99].

2.1.1. Working principle of a Li-ion battery

Li-ion batteries consist of a positive and negative electrode, an electrolyte, and a separator. The electrodes lay in the electrolyte, a chemical liquid that allows the flow of Li-ions but not of electrons. The separator is a porous plastic that separates the two electrodes to prevent them from short-circuiting.

The anode is the electrode that releases the positively charged Li-ions during discharging, and the cathode is the electrode that then absorbs Li-ions. Figure 2.1 shows how the Li-ions intercalate through the electrolyte and the separator towards the cathode. The Li-ions create a flow of negatively charged electrons (e^-) from the anode through the external circuit towards the cathode to neutralise the charge of the electrons. The flow of electrons created by the flow of Li-ions creates an opposite flow of electrical current, which can power an electric device or system. During charging, the flow reverses. The electrode that releases Li-ions is the cathode, and the electrode that the Li-ions intercalate into is the anode.

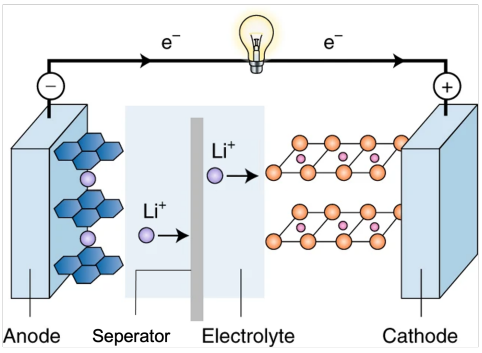

Figure 2.1: Discharging process of a Li-ion battery [29]. The original figure has been adjusted.

2.1.2. Analysis of common Li-ion batteries

The characteristics of Li-ion batteries differ due to the chemistry of their electrodes. While lithium-titanate oxide and silicon are sometimes used as anode materials in Li-ion batteries, graphite is the most commonly used anode material. Graphite is abundant, low cost, has a long cycle life, high specific energy and high specific power.

Therefore, Li-ion batteries are mainly classified according to the chemical composition of their cathode. Currently, the most common chemistries are lithium cobalt oxide or LCO ($LiCoO_2$), lithium manganese oxide or LMO ($LiMn_2O_4$), NMC ($LiNiMnCoO_2$), LFP ($LiFePO4_4$), lithium nickel cobalt aluminium oxide or NCA ($LiNiCoAlO_2$), and lithium titanate oxide or LTO (Li_2TiO_3) [6]. These five chemistries are analysed below according to the following six battery characteristics:

- Specific energy corresponds to energy per unit weight [Wh/kg], which reflects the driving range.
- Specific power corresponds to power per unit weight [W/kg], which reflects the potential acceleration.
- Safety corresponds to the battery's ability to remain safe (e.g., not to catch fire or explode).
- Performance corresponds to the battery's ability to withstand extreme temperature conditions.
- Lifespan corresponds to the battery's resistance to ageing.
- Cost corresponds to the battery's technological feasibility and cost of ownership.

LCO

The main advantages of the LCO battery are its high specific energy and low self-discharge rate [66]. Cobalt increases the battery's specific energy, thermal stability, lifespan, and safety [11]. The disadvantages of the LCO battery are its low thermal stability which leads to safety risks, its limited specific power, its relatively short lifespan, and the use of cobalt, a rare element with a controversial supply chain [42, 85].

LMO

The advantages of the LMO battery are its low internal resistance, good current handling, and high safety [17]. The main disadvantage is its short lifespan, average specific power, average specific energy, low performance and short lifespan [95]. However, its design flexibility allows for it to be optimised for a high specific energy, high specific energy, or long lifespan.

LFP

LFP batteries are implemented in half of Tesla's produced EVs. Partly because choosing LFP batteries reduces cobalt and nickel supply chain challenges and partly due to its overall performance, which is shown in Figure 2.2 [40]. The main advantages of the LFP battery are its safety due to its thermal stability, long lifespan, and lack of cobalt. Its performance is attributed to limiting the battery's high self-discharge by using costly, high-quality cells or expensive control electronics. Its main disadvantage is the battery's low specific energy [17].

NMC

The main advantage of the NMC battery is that it can be optimised to serve a particular purpose. Nickel provides high specific energy but poor stability, and manganese provides low internal resistance but low specific energy. By blending nickel and manganese, the strengths of the two materials are enhanced, which according to Miao et al. (2019) makes NMC the winner among the Li-ion batteries. Blends of nickel, cobalt and manganese in proportions of 5:3:2 and 8:1:1 instead of 1:1:1 have proven to offer useful combinations of qualities while reducing the amount of cobalt in the battery [6, 60].

NCA

The advantages of the NCA battery, in which aluminium is used to improve stability, are similar to that of NMC. NCA batteries provide high specific energy, average specific power and long lifespan [6, 32]. Its disadvantages are its high cost and lack of safety. NCA is also used by Tesla, who claims that their NCA battery uses even less cobalt than the NMC 8:1:1 battery [55].

LTO

The LTO battery uses titanate for its anode instead of graphite, which all the aforementioned battery chemistries use. The advantages of LTO are its safety due to its thermal stability and long lifespan [66]. The disadvantages of LTO are its low specific energy and high cost due to the expensive raw material titanate.

Comparative overview

Figure 2.2 and Figure 8.1 of the appendix show a similar comparative overview of the battery chemistries mentioned above. The information in the two figures closely corresponds, with the only significant difference being the cost of the LTO battery. The outer hexagons in the two comparative overviews correspond to the most desirable quality. Figure 8.1 shows that the LTO battery chemistry scores well in terms of cost, which is likely incorrect due to the high cost of titanium [66, 107].

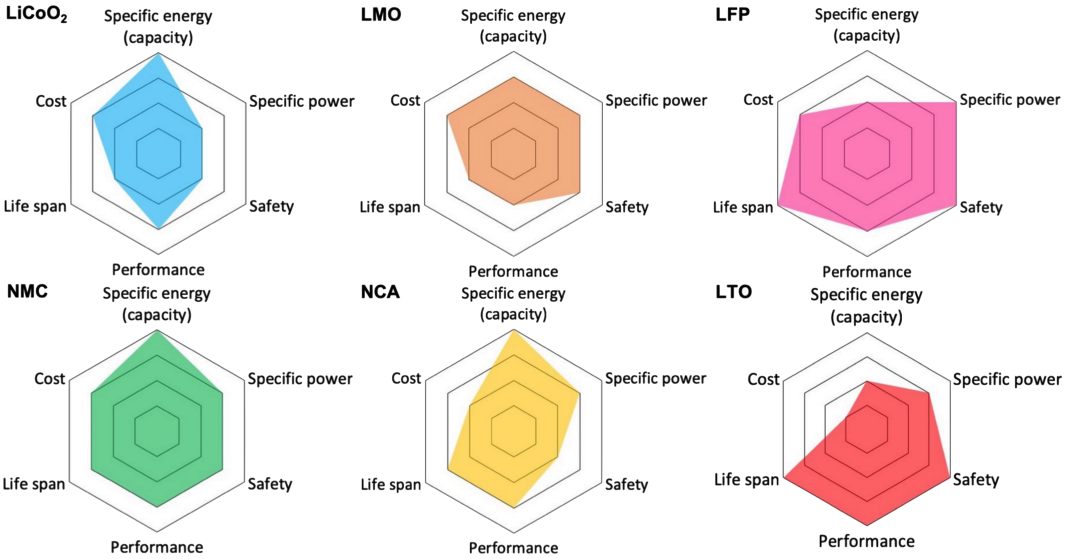

Figure 2.2: Overview of Li-ion batteries. (a) LCO ($LiCoO_2$); (b) LMO; (c) LFP; (d) NMC; (e) NCA; (f) LTO [55].

According to McKinsey & Company (2022), NMC and LFP are expected to remain the most prominent battery chemistries [54]. The left graph of Figure 2.3 shows the expected capacity demand for common EV batteries in 2030. The right graph of Figure 2.3 shows the specific energy of the currently mass-produced Li-ion battery chemistries. While the LFP battery outperforms NMC in most of the considered battery characteristics, it is inferior in terms of specific energy. The specific energy of a battery plays an important role as it heavily impacts vehicle weight. Vehicle weight plays a large role in improving driving range, which has long been considered a significant barrier to the acceptance of electric mobility (e-mobility) [7, 26, 38]. Considering their widespread implementation, both NMC and LFP batteries are researched in terms of degradation.

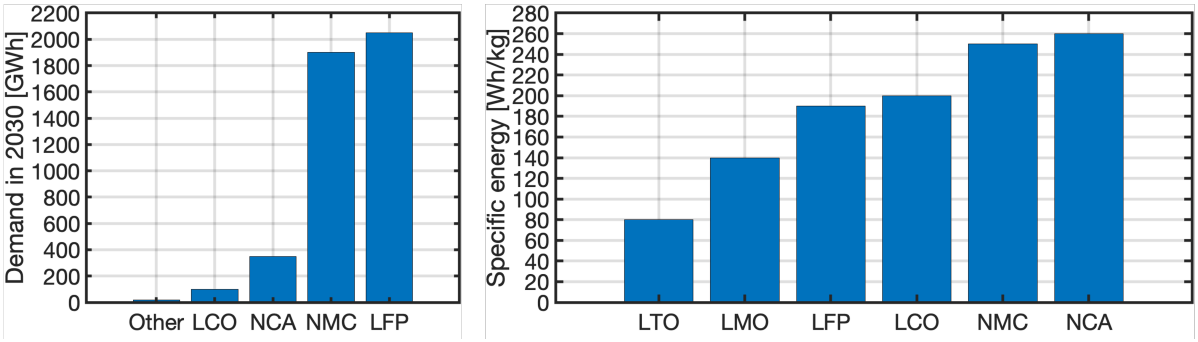

Figure 2.3: The left graph shows the expected capacity demand for different Li-ion battery chemistries in 2030 [54]. The right graph shows a comparison of the mass-produced EV Li-ion batteries in terms of specific energy [6, 34, 40, 51, 88].

2.1.3. Li-ion battery ageing

Li-ion batteries undergo ageing during usage and rest [80, 103]. Calendar ageing occurs both during usage and at rest and cycling ageing occurs during usage due to the intercalation of Li-ions during charging and discharging [102]. Therefore, battery researchers distinguish between cycling and calendar ageing [73, 81, 84]. The terms 'degradation' and 'ageing' are used interchangeably.

The causes of battery degradation mechanisms, associated degradation modes, and the subsequent effects on the battery are shown schematically in Figure 2.4 and in a similar diagram in Figure 8.2 of the appendix.

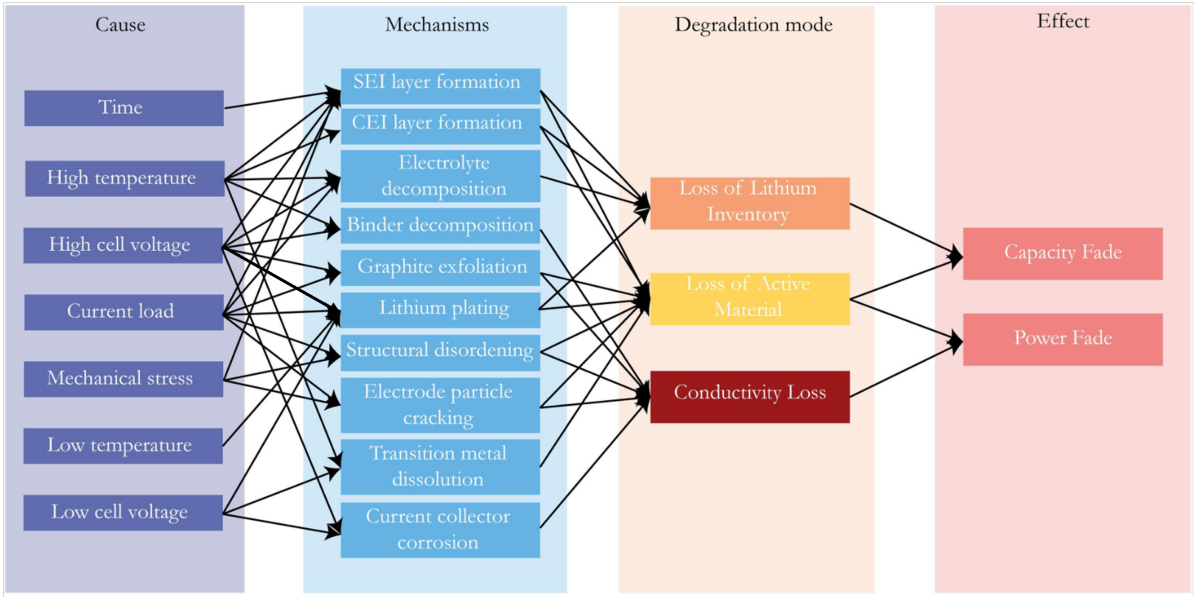

Figure 2.4: Causes of battery degradation mechanisms, associated degradation modes and subsequent effects on the battery [5, 102]. A connection has been added between high cell voltage and lithium plating, which is explained in the *Degradation mechanisms* subsection.

Ageing stress factors

So-called 'ageing stress factors' cause or accelerate the physical degradation mechanisms of the battery. The ageing stress factors for calendar ageing are time (t), SoC, and temperature (T), while the ageing stress factors for cycling ageing are SoC, T, depth of discharge (DoD), capacity throughput (Ah), and current rate (C-rate) [96, 102].

Time causes the formation of the solid electrolyte interface (SEI) layer, which will be elaborated on in the next subsection.

High temperatures impact ageing mainly due to the Arrhenius reaction rate dependence on temperature. The Arrhenius reaction rate increases with temperature, which is shown in Equation 2.1:

$$\Phi = \Phi_{ref} \cdot \exp\left[\frac{E_a(\Phi)}{R}\left(\frac{1}{T_{ref}} - \frac{1}{T}\right)\right] \tag{2.1}$$

where Φ is the reaction rate, subscript *ref* denotes the reaction rate value at a reference temperature, $E_a(\Phi)$ is the activation energy whose magnitude determines the sensitivity of temperature on Φ, R is the gas constant with value 8.3144 J K^1 mol^1, and T is the ambient temperature in degree centigrade [114]. The Arrhenius equation shows that the reaction rate increases with temperature. For batteries, this means that the parasitic side reactions occur faster at elevated temperatures. These parasitic side reactions accelerate degradation due to the formation of the SEI layer. Temperatures above 60 °C can cause thermal runaway [102]. During thermal runaway, the battery cell enters a self-heating state which could cause the cell to catch fire or explode [4]. Low temperatures can cause the diffusion rate of Li-ions to decrease, which causes lithium plating as will be elaborated on in the following subsection.

SoC is the level of charge relative to the battery's full capacity, and effectively describes the difference in voltage between the two electrodes. The bigger the voltage difference, the larger the imbalance between the two electrodes. High SoC can cause parasitic side reactions to occur, which grow the SEI layer. Low SoC can cause lithium plating [102]. Several studies have found that NMC batteries age the least when kept at 50% SoC [14, 19, 84, 109]. LFP ageing studies show that LFP batteries age the least when stored at lower SoC levels [57, 81, 113].

DoD is defined as the percentage of battery capacity that is discharged relative to the available storage capacity during that cycle. For many Li-ion batteries, shallower cycle depths cause less ageing compared to deeper cycle depths [14, 45]. Figure 8.3 of the appendix illustrates the relation between cycle depth and capacity loss.

Ah refers to the capacity throughput, or throughput, of the cell. The higher the throughput, the more Li-ions intercalate between the electrodes, causing cycling ageing. Equation 2.2 can be used to describe the cumulative throughput [107].

$$Ah = N \cdot DoD \cdot Q_{full} \tag{2.2}$$

where N corresponds to the number of cycles N, DoD to the depth of the corresponding cycles, and Q_{full} to the cell's usable capacity [102]. The impact of throughput can be described using the following relation: Ah^z, with $0 \leq z \leq 1$ [102]. While most researchers argue that z = 0.5 best follows the ageing pattern, Schmalstieg et al. (2014) found z = 0.75 to give the best fit to measured ageing data.

C-rate is the rate at which a battery is being charged or discharged. A C-rate of 1C means that the battery's rated Ah would be discharged in one hour, a C-rate of 2C means it would discharge its rated Ah at double the current in 30 minutes, and a C-rate of C/2 means it would discharge its rated Ah at half the current in 2 hours. C-rate has a strong interdependency with temperature. Above 2C, cycling ageing is thought to be exponentially dependent on C-rate [102].

Degradation mechanisms

In Li-ion batteries with a graphite anode, the main calendar ageing mechanism is the growth of a thin layer on the surface of an electrode, called the SEI layer [74]. The SEI layer is a lithium-containing passivating film that results from irreversible side reactions between the electrode and the electrolyte [37, 65]. The function of the SEI layer is that it prevents further electrolyte decomposition to maintain cycling ability [25]. However, the SEI layer causes undesired degradation effects as it consumes cyclable Li-ions during formation and creates an increasing resistance layer due to the growing layer thickness [37, 84, 103]. The electrolyte interface layer on the anode mainly forms in the first few cycles. Its growth scales with the square root of time and accelerates with higher SoC and higher temperatures. According to the Arrhenius reaction rate, high temperature increases the rate at which parasitic side reactions occur, as discussed in the previous subsection.

An electrolyte interface layer can form on both the anode and the cathode. The interface layer on the cathode, called the cathode electrolyte interface (CEI), grows due to electrolyte oxidation and salt deposition [102]. According to the Li-ion battery, manufacturer Forge Nano and to Vermeer et al. (2022), the layer formed on the cathode has a more limited passivation ability than the layer on the anode [25].

High SoC mainly causes electrolyte dissolution, which results in further growth of the SEI layer. High SoC might also lead to increased ageing due to electrolyte oxidation, structural damage to the cathode and transition-metal dissolution [102].

Cycling ageing also causes the SEI layer to grow due to Li-ion intercalation. A dominant cycling ageing mechanism is lithium plating, or dendrite formation. Lithium plating is caused by spiny-structured piles of Li-ions that during charging cannot be absorbed into the anode in time, subsequently stacking unevenly on the surface of the anode [44, 74, 105]. Figure 2.4 shows that lithium plating is caused due to a high current load, low temperature, and low cell voltage. At temperatures below 20 °C, the rate at which Li-ions diffuse into the anode or electrolyte reduces, causing them to stack on the anode. According to scientists at NASA and researchers at the Battery Research Group at the University of Maryland, lithium plating is also caused due to a high cell voltage [43, 115]. Therefore, an arrow between high cell voltage and lithium plating has been added to Figure 2.4. As shown in Figure 2.4, the compounds that make up the electrolyte and the binder decompose due to, among other things, high temperatures and high SoC, which also causes degradation. Binder holds the active material together and ensures the connection between the electrode and the contacts. Graphite exfoliation is the separation of graphite layers. Loss of electric contact and electrode particle cracking are mainly caused by mechanical stress due to Li-ion intercalation [5]. Thus, it appears that both calendar and cycling ageing accelerate when the Li-ion battery is stored and cycled at extreme temperatures and voltage levels.

The causes, rates and interdependencies of these degradation mechanisms are challenging to model. Therefore, most physics-based models focus only on the dominant degradation mechanisms such as SEI growth, lithium plating and electrode particle cracking [5, 37, 105].

Degradation modes

The effects of the degradation mechanisms are categorised into three main degradation modes, namely loss of lithium inventory (LLI), loss of active material (LAM), and conductivity loss [5]. In contrast to the diagram in Figure 8.2 of the appendix by Birkl et al. (2017), the diagram in Figure 2.4 by Vermeer et al. (2022) groups LAM_{anode} and $LAM_{cathode}$ together. Uddin et al. (2018) defines kinetics limitations to be a separate degradation

mode, whereas Birkl et al. (2017) and Vermeer et al. (2022) have seemingly allocated kinetics limitations to the other degradation modes.

LLI is caused by the unavailability of active Li-ions, which become unavailable due to parasitic side reactions. These parasitic side reactions can occur during the formation and decomposition of the SEI and CEI layers, due to electrolyte decomposition, and lithium plating.

LAM is caused by the active mass of the electrodes no longer being available to take up Li-ions as a result of the structural degradation of the electrode material. According to Figure 8.2 in the appendix, the active anode material is lost due to binder decomposition, graphite exfoliation, lithium plating, loss of electric contact, electrode particle cracking due to mechanical stress and corrosion of current collectors. The active cathode material is lost due to binder decomposition, structural disordering, loss of electric contact, electrode particle cracking due to mechanical stress, transition metal dissolution and corrosion of current collectors. According to Figure 2.4, SEI and CEI layers can also cause LAM.

Conductivity loss, or contact loss (CL), is caused by binder decomposition, graphite exfoliation, and current collector corrosion.

Effects

Battery researchers quantify the physical degradation by the battery's capacity decrease (Q_{loss}), or capacity fade, and resistance increase, or power fade. Capacity fade is an irreversible loss of the ability of a battery to store charge, which reduces the storage capacity and thus driving range of the EV. Power fade is an irreversible reduction of the rate at which electrical energy can be accepted or released by the battery, which affects the power capability and decreases the efficiency of the EV [98]. Capacity and power fade indicate the battery's state of health (SoH) compared to its beginning of health (BoH), and can thereby indicate whether the battery has reached its end of life (EoL) [87]. Researchers often consider the EoL to be reached when 80% of the battery capacity is retained compared to its initial capacity [31, 50], or sometimes when resistance has increased by 50% or 100% [81]. LLI results in capacity fade, LAM results in both capacity and power fade, and conductivity loss results in power fade.

Graphical overview

Figure 2.5 graphically illustrates the possible degradation mechanisms and degradation modes of graphite-based Li-ion batteries. The degradation mechanisms are colour-coded to indicate their corresponding degradation mode.

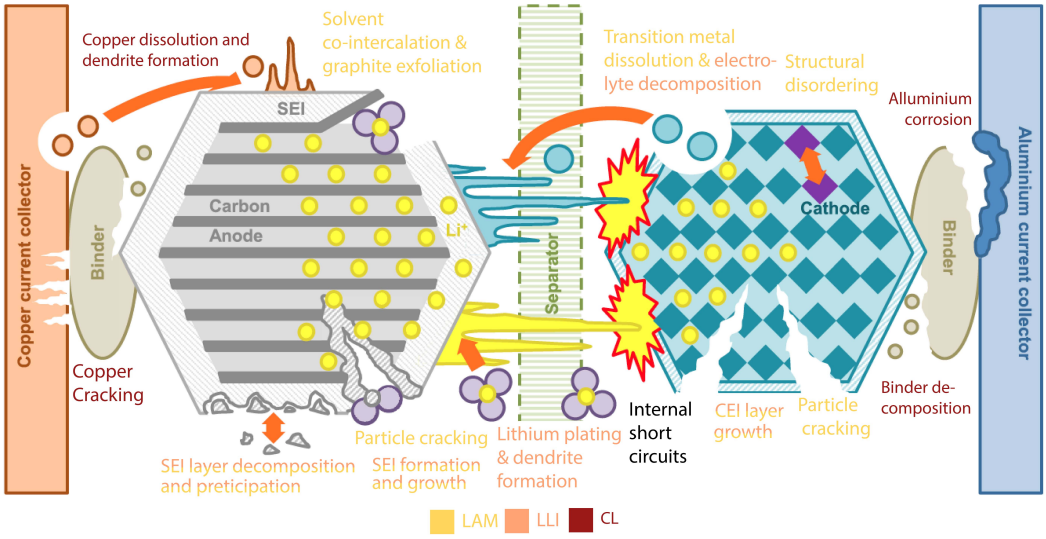

Figure 2.5: Graphical overview of the possible degradation mechanisms and degradation modes of Li-ion batteries with graphite-based anodes [5], adapted by Vermeer et al. (2022). LAM, LLI and CL are colour-coded.

Battery ageing modelling and limitations

Various battery ageing studies have been conducted to develop ageing models that can estimate how batteries will age [30, 45, 52, 81, 84, 87, 92]. As time also passes during Li-ion intercalation, calendar and cycling ageing are essentially intertwined and have a superposing effect on each other. Ageing modelling studies that only

research cycling ageing inherently incorporate calendar ageing effects in the mathematical expressions, or ageing equations, that describe cycling ageing [102]. Ageing models that are based on cycling tests and neglect calendar ageing effects will lead to ageing estimation errors when used with more realistic EV battery data, as realistic battery data includes rest periods between cycles. In an attempt to split the intertwined effects of calendar and cycling ageing, some researchers subtract the impact of calendar ageing from the impact of cycling ageing to be left with 'pure' cycling ageing [81, 84]. Essentially, these researchers assume that calendar and cycling ageing can be superpositioned.

Furthermore, a study by Raj et al. (2020) suggests that battery ageing is sensitive to the order and periodicity of calendar and cycling ageing, an effect called 'path dependence'. The study indicates that ageing models that do not consider path dependence of calendar and cyling ageing, but rather consider calendar and cycling ageing to be independent and cumulative, may yield inaccurate ageing results. Specifically, the researchers found that such ageing models are likely to underestimate ageing at higher C-rates and during continuous cycling [72].

2.2. Types of battery ageing models

Literature suggests that battery ageing models used for system design and control algorithm development should accurately measure the battery's degradation, be computationally efficient and easy to use. Jin et al. (2017) considers electrochemical models, semi-empirical models, and empirical models to be useful models to quantify Li-ion battery ageing. A study on ageing models found in literature by Vermeer et al. (2022) adds equivalent circuit models and machine learning models to the list of useful models for battery ageing applications. The different types of ageing models are described below.

Electrochemical models

Electrochemical models analyse physical and electrochemical processes in the battery to quantify ageing. The advantage of electrochemical models is that they require a small amount of data and their operating conditions are easily adjustable once a model is calibrated. Electrochemical models are, therefore, suitable for battery design. The disadvantage of electrochemical models is that they require a thorough understanding of the electrochemical and physical processes, which are described by many partial differential equations, making them computationally inefficient and thus unsuitable for system design and algorithm development.

Equivalent circuit models

Equivalent circuit models use the impedance data from passive circuit components such as a resistor (R), an inductor (L), and a capacitor (C) (RLC), to model the transient response of the battery. The operating conditions of the RLC components do not change with time, meaning that the impedance data can only determine the battery's state at that particular time. By varying the condition of the RLC components according to the defined ageing, the equivalent circuit models can be used as ageing models. These models are often used for SOH estimation due to their mathematical simplicity but require large test matrices for different operations conditions, making them unsuitable for system design.

Machine learning models

Machine learning ageing models feed an algorithm data for it to use simple parameters like voltage, current and temperature to estimate ageing, or combine empirical modelling methods with regression models to estimate ageing. While these models can accurately estimate ageing, they generally require large datasets to train the algorithms, making them unsuitable for system design. However, a machine learning-based ageing model recently showed increased predictive accuracy compared to current ageing models [39]. According to the authors, the model meets requirements regarding the applicability, generalisability and interpretability, which demonstrates the potential of machine learning ageing models in the near future.

(Semi-)empirical models

(Semi-)empirical ageing models curve-fit the relation of ageing stress factors onto empirical ageing data of a particular cell to derive ageing equations, that could estimate ageing. The idea is that these ageing models can consequently be used to estimate ageing of similar battery cells. The difference between the two is that semi-empirical models are physics-motivated, while empirical ageing models do not consider the physical and electrochemical ageing mechanisms, but use only experimental data to derive ageing equations.

The advantage of (semi-)empirical models is that their ageing equations provide intuitive insight into how the ageing stress factors affect ageing. In addition, they are computationally efficient due to their mathematical simplicity. Moreover, many (semi-)empirical ageing models can be found in literature. These models are therefore suitable for system design and algorithm development and are thus used for smart charging, feasibility, and cost analysis studies [102].

The disadvantage of these models is that once they are calibrated with specific data, the flexibility regarding their operating conditions is limited. The use of the ageing equations is therefore bounded to the range of the operating conditions used to design the ageing model. The operating conditions can be extended by considering the interdependency of ageing stress factors or by re-calibrating the models for new applications. However, this requires time-consuming and expensive experimental data collection. Moreover, the ageing equations defined in these models are often based on data derived from tests with accelerated ageing conditions and limited test conditions due to a lack of available equipment or time.

Nevertheless, (semi-)empirical ageing models are specifically suitable for system design as they are computationally efficient due to their mathematical simplicity, as well as their wide availability. Therefore, these types of models are applied in this work.

2.3. VIPV

The first vehicle-integrated solar panels were introduced in 1955 by William G. Cobb, who worked at General Motors. His so-called *Sunmobile* featured 12 selenium PV cells and a small electromotor that drove the small vehicle forward. Forty-six years later, in 2001, the TU Delft Dream Team 'Nuna' first participated in the World Solar Challenge, obtaining first prize in the competition through the Australian Outback. In 2011, students from the TU Eindhoven 'Solar Team Eindhoven' joined the competition. In 2016, their successors determined it was technically feasible to mass-produce SEVs and decided it was time to transform EVs. The team from Eindhoven founded 'Lightyear'. Sono Motors, the SEV manufacturer from Germany, and Lightyear, the SEV manufacturer from the Netherlands, are developing the first production-ready solar cars. In 2023, 68 years after the first appearance of a solar car, SEVs are being driven in the Netherlands, Germany and Spain. Other vehicle manufacturers, such as Mercedes, Fisker, and Hyundai, have added solar panels to their vehicle. These solar cars, however, either use solar panels to power the auxiliaries or are not designed for mass production. Kanz and Lim wrote a position paper on VIPV, proposing VIPV as a core source of electricity in road transport. The study estimates the economic and environmental viability of on-board solar panels from technical viewpoints, outlines strategies for integrated research and development (R&D) and clarifies the main bottlenecks to the introduction of VIPV.

2.3.1. Solar-powered mobility

SEVs use solar panels mounted on the roof and the sides of the vehicle to charge the battery. The SEV can thereby charge from the sun while driving and parking, adding additional range to the vehicle's driving range. Considering the small amount of energy solar panels can generate per unit area, SEVs are designed to be energy-efficient. Due to their efficient design, SEVs require less electricity compared to normal EVs. By demanding less electricity than standard EVs, SEVs could be considered a favourable alternative to standard EVs due to their self-charging capabilities and low life-cycle GHG emissions.

Lightyear's first vehicle, the Lightyear 0, has 5 m^2 of vehicle-integrated solar panels mounted on its roof. The patented double-curved crystalline silicon (c-Si) solar panels achieve an efficiency of 215 Wp/m^2. In contrast to most EVs on the market, the Lightyear 0 is designed with a focus on efficiency. Due to its in-wheel motors, drag coefficient of 0.17 Cd, highly efficient converters and other efficient components, the vehicle's driving efficiency ranges around 100 Wh/km. According to Lightyear, the SEV's efficiency allows it to charge up to 11,000 km per year from the sun in Amsterdam, the Netherlands [48].

2.3.2. Alliance for Solar Mobility

Lightyear and Sono Motors founded the Alliance for Solar Mobility (ASM) with the mission "to become the cooperative European platform to establish and foster the Solar Mobility Industry" [2]. As the solar mobility industry grows, various EV and PV manufacturers and research institutes have joined the alliance. Among them are TNO, Fraunhofer ISE, TU Eindhoven, and TU Twente.

2.3.3. Literature on the impact of VIPV on battery life

The impact of VIPV on EV battery life has barely been researched. The most extensive study found by the author was a study by Mallon et al. (2017). This study presents a model that analyses the impact of on-board solar panels on the battery cycle life of an electric bus. The simulation-based cycling ageing study suggests that as gradual PV charging reduces the required number of battery cycles, Li-ion battery cycle life may extend by up to 19% if VIPV are mounted on the roof and the sides of the bus. However, the battery model used by the researchers only considered the battery's DoD after a whole day of driving. According to the paper, the implemented ageing model "assumed that the battery is discharged from its initial charge to final charge, without significant charging in between" [50]. By only considering the difference in DoD at the start and end of each day, the authors assumed that gradual solar charging is not significant enough to impact cycling ageing during the day. In reality, gradual solar charging causes Li-ion intercalation from the cathode to the anode. According to literature, this causes further growth of the SEI layer and lithium plating, which should increase cycling ageing. Therefore, not considering the impact of gradual solar charging on cycle life inherently limits the analysis. Additionally, the authors defined the battery's EoL as if it is only influenced by cycling ageing, while in reality calendar ageing would add a share of capacity loss to the battery's total ageing until EoL. Thus, the estimated cycle life extension due to VIPV is likely to have been overestimated. Moreover, the authors did not validate the models used for the analysis.

2.4. V2G

V2G allows for EVs to feed power into the electricity grid. V2G enables EVs to, among other things, participate in day-ahead electricity trading and grid balancing services. Both these services balance the grid's electricity supply and demand and can be monetised by EV owners, EV manufacturers and utility companies, among others. Considering the current participation of EVs in these forms of electricity trading and the consequent effect on the EV batteries, the workings of day-ahead electricity trading and grid balancing services are explained below. The modelling methodology of V2G is elaborated on in Section 3.4.

2.4.1. Day-ahead electricity trading

Day-ahead electricity trading enables balancing groups to trade electricity one day before the actual delivery moment of the electricity [63]. Each balancing group has one balancing responsible party (BRP), responsible for supplying or demanding the contracted power bid. Day-ahead electricity trading occurs on the day-ahead electricity market [61]. The intermediate party that facilitates day-ahead electricity trading in the Netherlands is EPEX Spot [23]. Examples of balancing groups that can trade on the day-ahead electricity market are large power producers, utility companies and energy traders. EV companies can participate in day-ahead electricity trading by aggregating multiple EV batteries to supply and/or demand energy. Essentially, the aggregated EV batteries act as a virtual power plant, supplying and demanding energy from the grid when required.

2.4.2. Grid balancing services

The Dutch power grid should operate at a frequency of 50 Hz to function properly. If the frequency exceeds a 0.2 Hz deviation, a blackout may occur [62]. Power supply and demand must be in balance to reduce grid deviations. Transmission system operators (TSOs), such as TenneT in the Netherlands, are responsible for stabilising the grid frequency. TSOs activate balancing services to ensure that the power grid frequency is maintained at 50 Hz [64]. Balancing services in the Netherlands are the Frequency Containment Reserve (FCR), automatic Frequency Restoration Reserve (aFRR), and the manual Frequency Restoration Reserve (mFRR) [94]. The balancing services are provided by balancing service providers (BSPs) and are centrally controlled by the TSO. BSPs are market participants of FCR, aFRR or mFRR that can supply and/or demand power from the grid upon the TSO's request to support in balancing the grid.

FCR, aFRR, and mFRR have different requirements and rules. FCR is the primary reserve, aFRR the secondary reserve, and mFRR the tertiary reserve [93]. As mFRR is required for large or prolonged imbalances and must be pre-contracted, it is currently not viable for EV fleets to participate in. mFRR is therefore not explained in further detail. The characteristics of FCR and aFRR are summarised below.

FCR

- 30-second full activation time (FAT) to deliver contracted power.
- Requires 1 MW minimum contracted power capacity.
- Symmetric service meaning that if the BSP wants to supply 1 MW, the BSP must also be able to demand 1 MW.
- Block duration of product delivery is 4 hours. The BSP is not required to be able to supply continuous power for these 4 hours but needs to be continuously available to steer on minor frequency deviations. The minimum continuous delivery time within those 4 hours is 1 hour.
- If BSP cannot supply the minimum duration/capacity, BSP can be kicked out.
- Participation requires prequalification, which takes between 6 and 12 months.

aFRR

- 5-minute FAT to deliver contracted power (used to be 15 min FAT).
- The minimum ramp rate of the offered aFRR volume (up and/or down) should be at least 20% per minute of the energy bid volume.
- Requires 1 MW minimum contracted power capacity, with a 1 MW minimum granularity.
- Asymmetric service, meaning that the bid for upwards and downwards regulation does not need to be equal. For example, it is also possible to demand less power than the power supplied.

FCR allows aggregated EVs to participate in. However, because it is a symmetric balancing service and requires an extended prequalification time, it has a lower priority to research in terms of its impact on EV ageing compared to aFRR. Therefore, aFRR is considered in this work.

2.4.3. Literature on the impact of V2G on battery life

Roks et al. (2019) wrote a report for the Netherlands Enterprise Agency on vehicle-to-everything (V2X) in the Netherlands. The report sketches its current state of development and discusses battery ageing, institutional bottlenecks and economic aspects of V2X. Zhou et al. (2011) modelled the cost of EV battery ageing due to V2G. The research highlights the effect of DoD on ageing cost per kilowatt-hour (kWh) at peak electricity rate. In addition, the study compares the cost of battery ageing to the cost of energy purchased and to the benefits of energy sales to the utility grid. The researchers, however, disregarded the thermal management of the EV's battery, posing inherent limitations to the analysis. Steffen et al. (2020) researched optimal EV charging considering the effects of a financial incentive on battery ageing. The authors state that with an appropriate thermal strategy, no significant additional battery ageing should occur. Wang et al. (2016) quantified EV battery ageing from driving compared to using an EV for V2G services and driving. The simulations used for the research incorporated a detailed thermal management model. The study found that if V2G were only used 20 times per year, the 10-year average capacity losses would be a maximum of 1.18% more than without the V2G services. Dubarry et al. (2017) and Uddin et al. (2017) studied the ageing of similar Li-ion NCA battery technologies. Dubarry et al. (2017) found that additional cycling associated with V2G services reduces Li-ion battery lifespan, while Uddin et al. (2017) claimed that V2G could extend Li-ion battery lifespan. The researchers together reflected on their research of 2017 and published a paper in 2018, clearing up how battery ageing due to V2G can be managed to extend battery lifespan using a smart control algorithm that maximises battery lifespan [98]. Mouli et al. (2019) used a mixed integer linear program (MILP) to model the potential cost reduction of an EV fleet charging from PVs in different scenarios. Among other things, the simulations showed that V2G for grid regulation services is more cost-effective than V2G for energy sales due to the ageing of the EV's battery.

Literature demonstrates the importance of characterising the specific application of V2G, as different V2G services impact the battery lifespan to a greater extent than others [59, 106, 114].

3

EV battery data modelling

The following chapter elaborates on the EV battery data generation model as well as VIPV and V2G modelling. The EV battery data generation model is used to simulate the eight use case scenarios introduced in Chapter 1. Through the completion of this chapter, the first sub-objective is addressed:

i *Simulate use case scenarios with and without VIPV and V2G to generate one-year EV battery datasets.*

In Section 3.1, the methodology for modelling EV battery data and battery ageing is visualised and explained. Hereafter, Section 3.2 provides a detailed description of the workings of the EV battery data generation model. Following this, the methodologies for V2G and VIPV modelling are presented in Section 3.4 and Section 3.3, respectively. Finally, the EV battery data generation model is validated in Section 3.5.

3.1. Modelling methodology

The diagram shown in Figure 3.1 shows the methodology for EV battery ageing modelling. Lightyear's VPM, which is a modelled version of the Lightyear 0 vehicle, is used to simulate per-second battery data. A study by Centraal Bureau voor de Statistiek (CBS) and a study called Mobility in Germany (MiG) are used to develop a one-year mobility profile of a new EV. Charging data from ElaadNL is used to develop a charging profile for an EV. By simulating driving cycles in the VPM according to the constructed mobility and charging profiles, a realistic one-year EV load profile is derived. This one-year EV load profile data is consequently merged with VIPV and V2G load profiles to construct the use cases mentioned in the introduction.

The battery ageing stress factors, namely t [s], SoC(t)[%], T(t) [°C], U(t) [V], I(t) [A], C-rate, and Ah are derived mainly from the power profile. First, the power profile is integrated and subtracted from the full battery capacity to derive the SoC profile. Second, the temperature profile is modelled based on the power and SoC profiles and the EV characteristics derived from the VPM. Third, the voltage profile is derived from the SoC profile and the cell-specific V_{OC}(SoC) curve. Fourth, the current profile is derived from the power and voltage profiles. Finally, the C-rate and throughput profiles are derived from the current profile. These battery ageing stress factors form the inputs for the ageing models. Using the ageing stress factors, the ageing models determine the capacity decrease and resistance increase per time step and yield a lifetime prognosis.

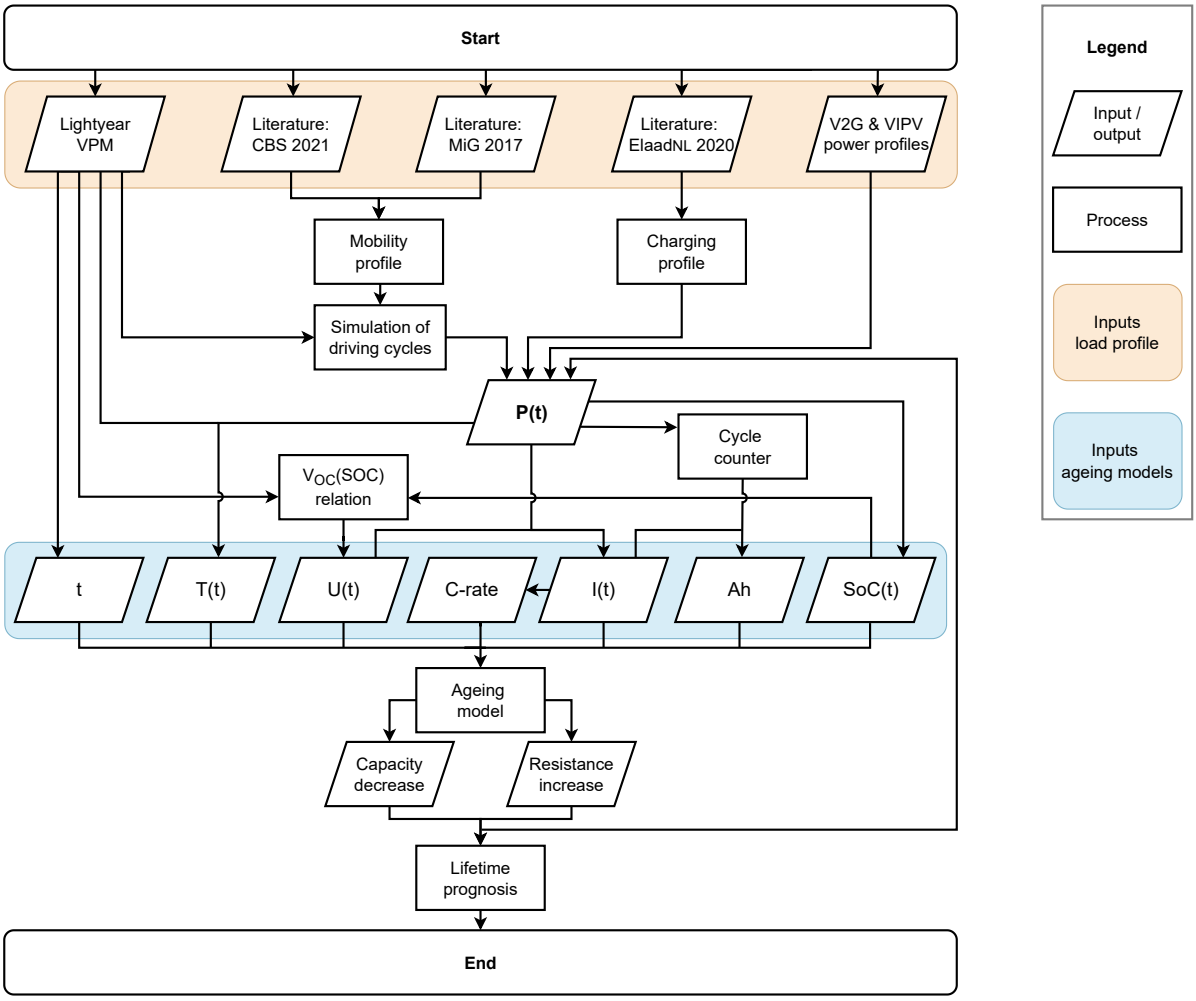

Figure 3.1: Flowchart illustrating the methodology applied to model EV battery ageing.

Ideally, the outputs of the ageing model, namely the capacity decrease and resistance increase, are looped back into the power profile. Thereby, the capacity decrease and resistance increase that the battery cell has suffered in the previous time step are integrated following the time step of the battery data. Due to the modelling complexity and required computational power, this step is omitted.

3.2. EV battery data generation model

Two approaches are widely used by researchers to model EV load profiles [1]. One approach is charger-centric and considers one EV charging station or aggregates multiple EV charging stations. The other approach is vehicle-centric, in which individual EV loads are modelled that can be combined to create one aggregated load. In literature, the vehicle-centric approach is preferred over the charger-centric approach, mainly because it allows exploration of the finer details of an EV load [1, 49]. To develop a holistic EV battery ageing model, the approach in this work combines the vehicle and charger-centric approach. The EV's mobility and charging profiles are constructed based on EV driving data in the Netherlands and Germany. Driving cycles are simulated in Lightyear's VPM, which generates power profile data of an EV battery. The battery power profile forms the basis for deriving the ageing stress factors that influence battery ageing.

3.2.1. Mobility profile

CBS (2022) gathered historical travel data for the Netherlands in 2019 and 2020. The data suggests that in 2019, the average one-year-old passenger vehicle had travelled 19,190 km. To simulate realistic travel behaviour, a mobility profile is constructed comprising variations in travel patterns due to leisure, weekend and holiday trips. The mobility profile includes a total of 260 commuting trips; 50 leisure trips for leisure, 13-weekend trips to the Veluwe, the Netherlands, one winter trip to Soelden, Austria and one summer trip to Biarritz, France. To model the work commuting distance, the total distance travelled for leisure, weekend and holiday trips is deducted from the one-year travelled distance and spread evenly over working days. It is assumed that the EV owner commutes to work every day of the work week and that the driver uses only one vehicle. The trips are composed of various driving cycles, elaborated on later in this section. It is assumed that the constructed mobility profile is sufficiently representative of average EV use in the Netherlands and Spain. An overview of the determined one-year mobility profile of a new EV driver in Amsterdam is shown in Table 3.1 and Figure 3.2.

Table 3.1: Modelled one-year mobility profile characteristics.

Specification	Journey	Frequency	Round trip distance [km]	Total distance [km]
Commuting	home - work	250	31.8	7,957
Leisure trips	home - leisure	50	101.7	5,087
Weekend trips	Amsterdam - Veluwe	13	121.1	1,574
Winter trip	Amsterdam - Soelden	1	1,876	1,876
Summer trip	Amsterdam - Biarritz	1	2,696	2,696
Total distance				**19,190**

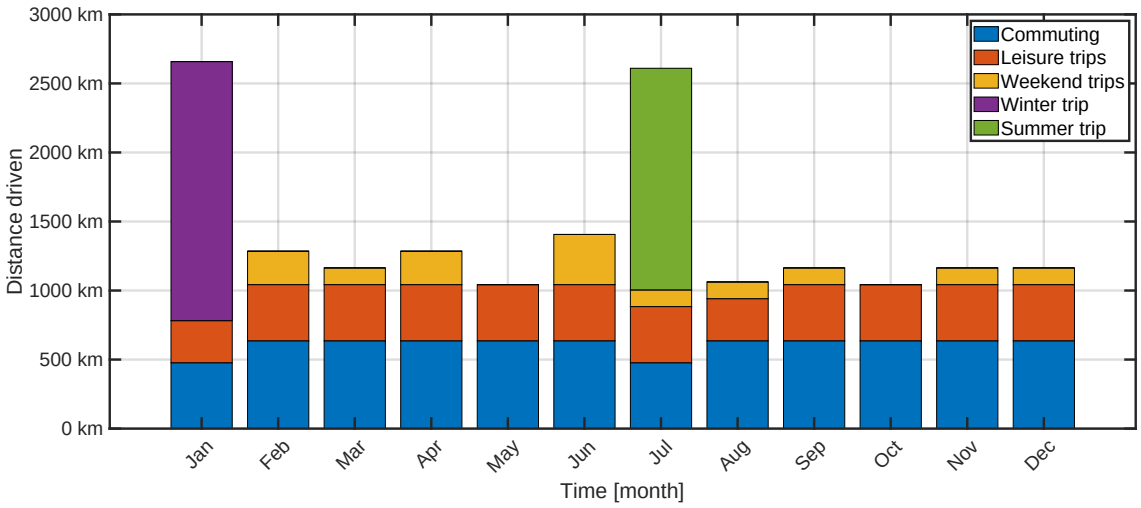

Figure 3.2: One-year mobility profile of a new EV driver defined using mobility statistics from the Netherlands and Germany.

The 2017 Mobility in Germany study used data from 155,000 participating households to describe the mobility behaviour of working people in Germany [28]. Schlund (2021) used data from the 2017 Mobility in Germany study to create a stochastic model that describes the mobility behaviour of a large fleet of working people with private EVs. Figure 3.3 visualises this weekly mobility behaviour. The figure shows a recurring pattern of commuting to work during the weekdays and more time spent at home during the weekends.

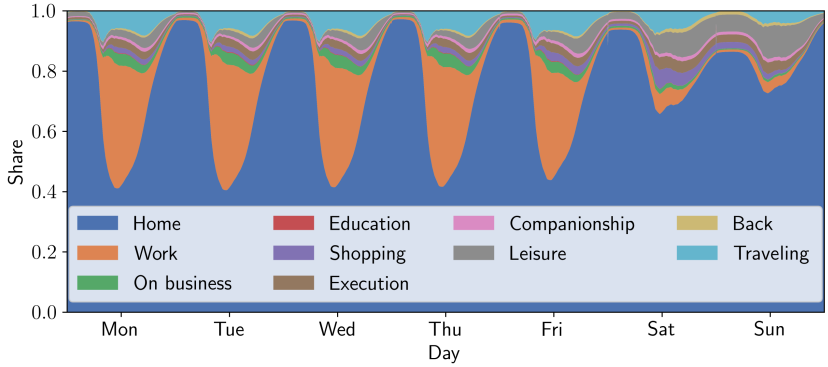

Figure 3.3: Weekly mobility behaviour of a large fleet of working people with EVs in Germany in 2017 [82].

3.2.2. Charging profile

ElaadNL (2020) gathered data on charger arrival times for weekdays and weekends based on a large volume of charging events in the Netherlands. Figure 3.4 shows the distribution of arrival times at private, public, and workplace charging stations on weekdays. Figure 3.5 shows the distribution of arrival times at private and public charging stations on weekends.

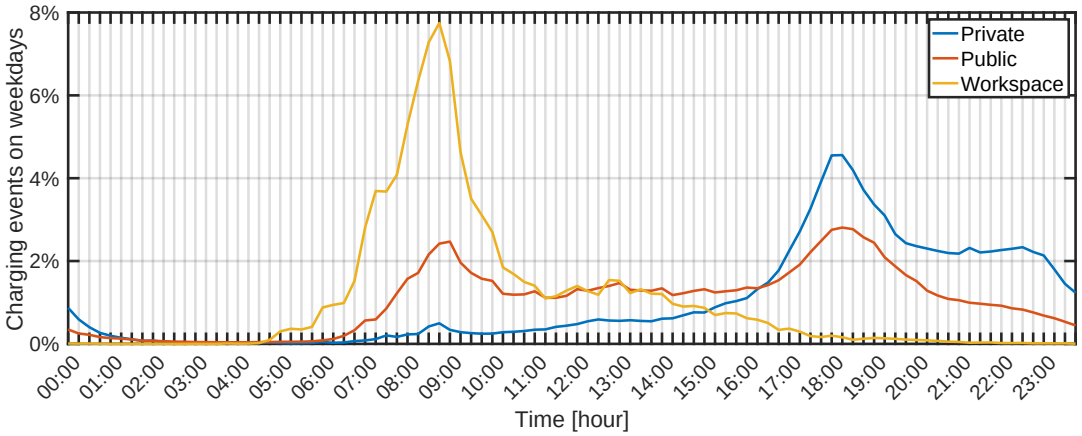

Figure 3.4: Normalised profiles of charger arrival times on weekdays based on large volumes in the Netherlands [21].

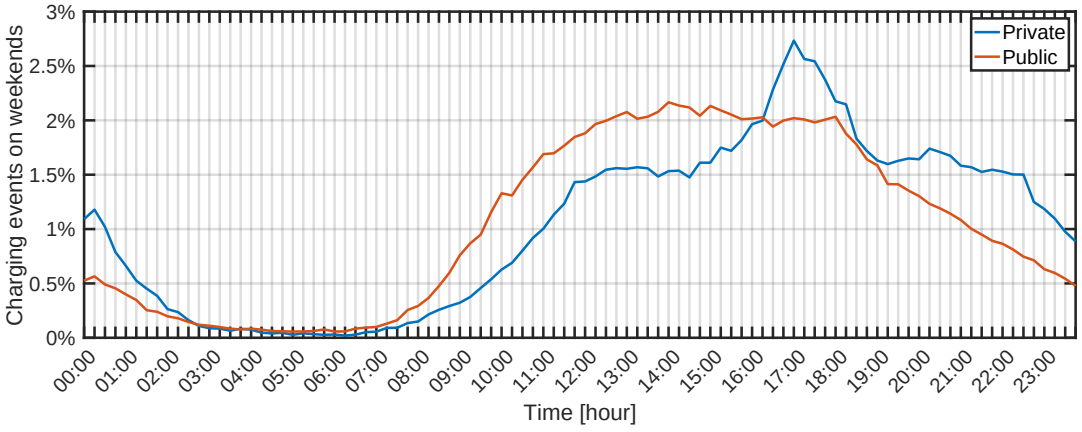

Figure 3.5: Normalised profiles of charger arrival times on weekends based on large volumes in the Netherlands [21].

Figure 3.4 shows that charging activity peaks during weekdays around 8:45 AM for private, public and workspace charging stations and around 18:15 PM for private and public charging stations. Figure 3.5 shows that charging activity peaks during weekends around 00:15 AM for both private and public charging stations, around 14:00 PM for public charging stations, and at around 17:15 PM for private charging stations. The same charger arrival times are used for the composition of the power profile.

3.2.3. Lightyear Vehicle Performance Model

Through system modelling, vehicle systems can be modelled in MATLAB and Simulink. These vehicle systems can be used to simulate driving cycles to generate EV battery load data [9]. As this method allows to closely imitate the characteristics of an SEV, Lightyear's VPM is used to model the EV load for the scenarios mentioned in Table 1.1. As explained in Section 3.1 Lightyear's VPM is a digital version of the Lightyear 0 vehicle designed in Simulink. The VPM is used to simulate the EV's behaviour and incorporates all aspects of the EV, including the aerodynamic drag, rolling resistance, in-wheel motors, converters, inverters, thermal management systems, high voltage (HV) and low voltage (LV) batteries. To ensure that the model is accurate and representative of real-world conditions, the VPM of the Lightyear 0 vehicle has been validated on subsystem level, after which the data has been fed back into the model [36].

Choice of time step

To decide on the unit time step for the modelled EV battery data, a trade-off is made between processing power and data accuracy. A smaller time step corresponds to higher accuracy of results but to more computational power. In contrast, a larger time step corresponds to lower accuracy of results but less required computational power. The ageing models that will be applied to the data are based on ageing measurements which are performed on a daily basis and thus do not consider minor deviations in the load profiles. Considering the required computational power, accuracy of data and of the ageing tests, the chosen time step is per second. The time step of the output of Lightyear's VPM simulations is 0.1 s, which is sampled per second.

Battery configurations

Lightyear's HV battery pack has a setup, with 10 modules in series, each having 10 cells in series and 34 cells in parallel (100s34p). To maximise battery life, researchers suggest that a Li-ion battery should not utilise the full 100% SoC range of the battery but should rather operate within a smaller SoC range. In other words, an EV Li-ion battery should be charged and discharged within a minimum and a maximum SoC limit. Battery manufacturers suggest discharging an EV battery up to 10% SoC [53]. The researchers determined that both charging current and power are controllable up to an SoC level of about 90%. The minimum and maximum SoC of the HV battery in the VPM is thus set to 10% and 90%, respectively. If the SoC of the battery reaches 90%, it is considered 'full' and cannot take any more energy. If the HV SoC approaches 10%, the battery is grid charged with AC power to 90%. Each power profile starts with an initial SoC of the battery (SoC_i) of 90%. While the Lightyear 0 has both an LV and an HV battery, for simplification, it is assumed that the SEV only uses an HV battery.

Charging power

Based on Lightyear's onboard charger (OBC) efficiency curve shown in Figure 8.4 of the appendix, the modelled AC grid charging is performed at a constant charging efficiency of 95%. Moreover, the modelled EV uses regenerative braking to recharge the battery using electricity generated during braking.

3.2.4. Simulation of driving cycles

To generate battery data, a variety of driving cycles are simulated in the VPM. By organising these driving cycles according to the mobility and charging profile, the travel patterns are simulated to imitate the EV travel behaviour designed in Subsections 3.2.1 and 3.2.2. The following subsections describe the characteristics of the simulated driving cycles. The driving cycles are simulated at a single battery temperature and with an initial SoC of 90%. In reality, varying SoC and battery temperatures would influence the battery cell's resistance, which would consequently impact the derived ageing stress factors. It is assumed that this effect does not heavily impact the ageing estimations of the ageing models.

WLTC driving cycle

The Worldwide harmonized Light vehicles Test Cycle (WLTC) procedure is used to determine light-duty vehicles' emissions and energy consumption [16]. The WLTC procedure is part of the Worldwide harmonised Light vehicles Test Procedures (WLTP). While WLTC and WLTP are used interchangeably, the WLTP procedures consist of more procedures than only the WLTC test cycles. The WLTP procedures act as the European vehicle homologation procedure to approve vehicles. The WLTP procedures differ per type of vehicle based on the vehicle's power-to-mass (PMR) ratio and maximum speed. The Lightyear 0 vehicle's maximum speed exceeds 120 km/h and, together with its weight, classifies it as a Class 3b vehicle. The characteristics of the WLTC cycle of Class 3b WLTP procedures are summarised in Table 3.2. The consumption breakdown of the Lightyear 0 covering one WLTC cycle can be found in Figure 8.5 of the appendix. The power profile data of the four phases, namely the low, medium, high, and extra high phases, are sampled per second and segmented per phase. The velocity of the WLTC driving cycle per phase is shown in Figure 3.6. The WLTC driving cycle is simulated at 10 °C as it will be simulated throughout the year in the Netherlands, where the average ambient temperature throughout the year is 10 °C.

Table 3.2: WLTC Class 3b driving cycle characteristics.

Phase	Duration [s]	Stop duration [s]	Distance [m]	v_{max} [km/h]	v_{avg} excluding stops [km/h]	a_{min} [m/s^2]	a_{max} [m/s^2]
Low	589	156	3,905	57	26	-1.5	1.5
Medium	433	48	4,756	77	46	-1.5	1.6
High	455	31	7,162	97	61	-1.5	1.6
Extra high	323	7	8,254	131	94	-1.2	1.0
Total	1,800	242	15,914				

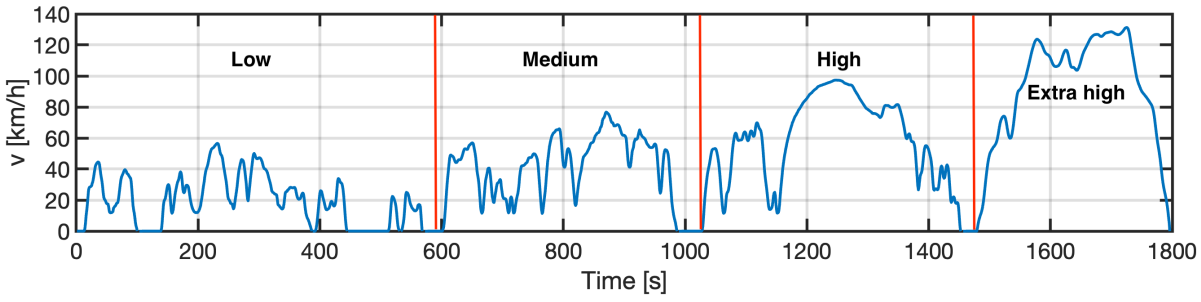

Figure 3.6: Velocity profile during a WLTC driving cycle. Data sourced from Lightyear VPM simulations. Plot composition inspired by DieselNet.

Artemis driving cycle

The Artemis driving cycles is based on a statistical analysis of an extensive database of European real-world driving patterns [15]. Figure 3.7 shows the velocity profile during the Artemis driving cycle. The characteristics of the Artemis cycle, which takes about 18 minutes in total, are summarised in Table 3.3. The Artemis driving cycle is simulated at 10 °C as it will be used throughout the year in the Netherlands, where the average ambient temperature is 10 °C.

Table 3.3: Artemis driving cycle characteristics.

Duration [s]	Distance [m]	v_{max} [km/h]	v_{avg} [km/h]
1,068	28,737	131	97

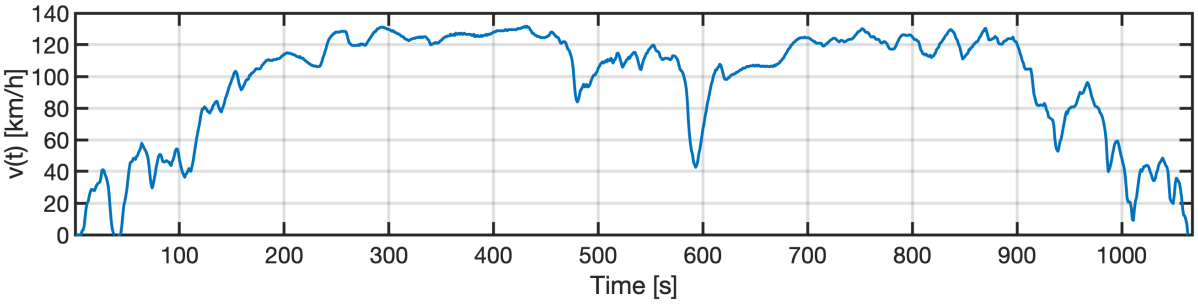

Figure 3.7: Velocity profile during the Artemis driving cycle. Data sourced from Lightyear VPM simulations.

Highway driving cycle

Figure 3.8 shows the velocity profile during the highway driving cycle. The highway driving cycle is simulated at 25 °C, as the battery temperature is assumed to range around 25 °C battery temperature when the EV is driving on the highway. The characteristics of the highway driving cycle, which takes 100 minutes in total, are summarised in Table 3.4.

Table 3.4: Highway driving cycle characteristics.

Duration [s]	Distance [m]	v_{max} [km/h]	v_{avg} [km/h]
5,844	244,740	160	151

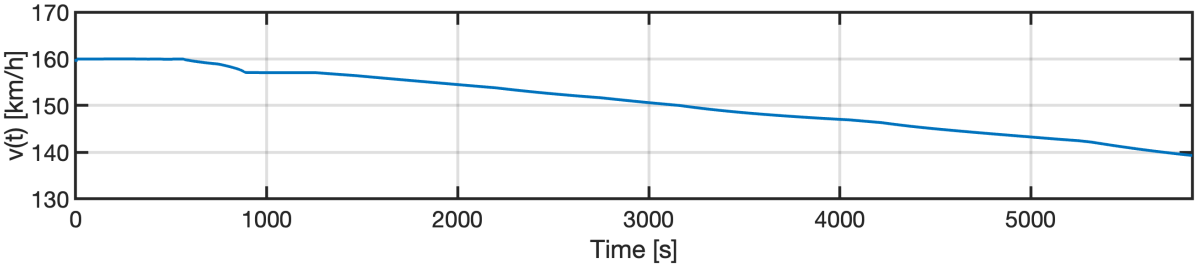

Figure 3.8: Velocity profile during the highway driving cycle. Data sourced from Lightyear VPM simulations.

Overtaking driving cycle

Figure 3.9 shows the velocity profile during the overtaking driving cycle. The overtaking driving cycle is simulated at 25 °C, as the battery temperature is assumed to range around 25 °C battery temperature when the EV is overtaking other vehicles on the highway. The characteristics of the overtaking driving cycle, which takes 100 minutes in total, are summarised in Table 3.5.

Table 3.5: Overtaking driving cycle characteristics.

Duration [s]	Distance [m]	v_{max} [km/h]	v_{avg} [km/h]
1,068	42,720	154	144

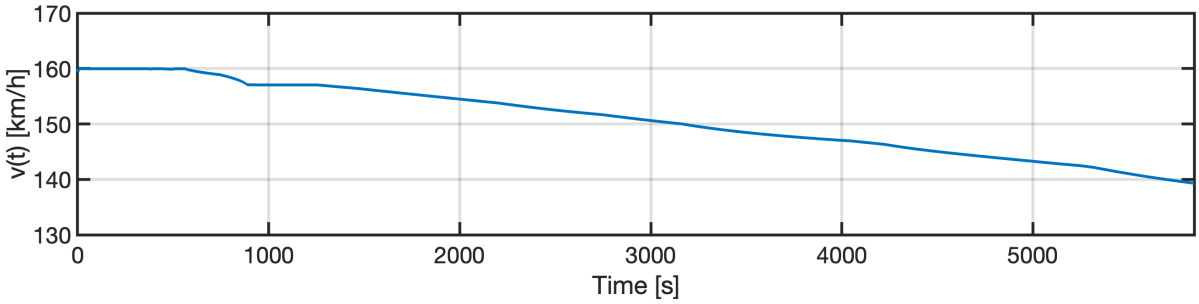

Figure 3.9: Velocity profile during the overtaking driving cycle. Data sourced from Lightyear VPM simulations.

Brenner pass driving cycle

Figure 3.8 shows the velocity profile during the Brenner pass driving cycle. The Brenner pass towards Soelden passes from Bolzano to Innsbruck. Figure 8.6 of the appendix shows the elevation profile of the Brenner pass. The Brenner pass driving cycle is simulated at 35 °C, as it is assumed that the EV battery temperature will be high when approaching the Brenner pass. The characteristics of the Brenner pass driving cycle, which takes about 75 minutes in total, are summarised in Table 3.6.

Table 3.6: Brenner pass driving cycle characteristics.

Duration [s]	Distance [m]	Elevation [m]	v_{max} [km/h]	v_{avg} [km/h]
4,593	132,500	1,370	111	104

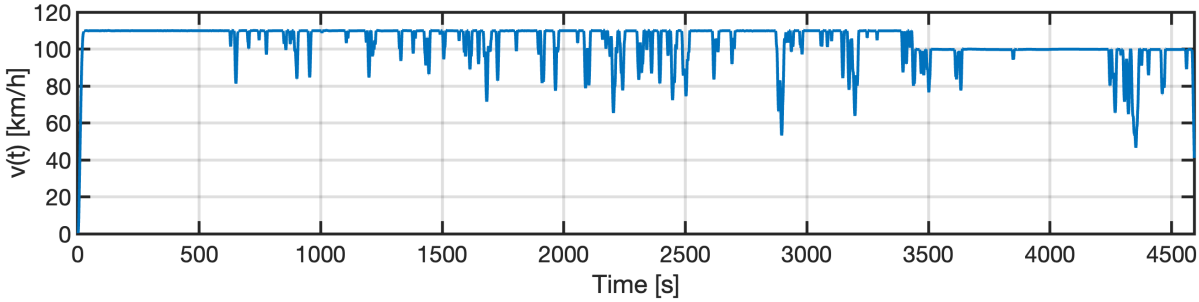

Figure 3.10: Velocity profile for the Brenner pass driving cycle. Data sourced from Lightyear VPM simulations.

3.2.5. Power profile modelling

A one-year power profile is modelled per second using the mobility profile shown in Figure 3.2, the charging profiles shown in Figures 3.4 and 3.5, and the vehicle configurations and driving cycles described in Subsection 3.2.3. The modelled one-year power profile consists of four alternating one-week power profiles. The four one-week and one-year power profiles are described in detail below. The corresponding SoC profiles are described in Subsection 3.2.6. In the power profiles, positive values correspond to the power output required to drive the vehicle forward and to power the necessary auxiliaries, and negative values correspond to power input due to grid charging and regenerative braking. Grid charging always charges the battery up to 90% SoC with a charging power of $P_{charging}$ = 11 kW and a charging efficiency of $\eta_{charging}$ = 0.95. While the power profiles depend on the battery temperature, the driving cycles are simulated at one single temperature depending on the EV's situation. The battery temperatures at which each driving cycle is simulated are described in Subsection 3.2.4.

Composition of a working week with a weekend trip

Figure 3.11 shows a one-week power profile during a working week with a weekend trip. The modelled one-week power profile with a weekend trip consists of the following:

- Commuting trips during workdays, from 8:30 AM to 9:00 AM and from 17:30 PM to 18:00 PM (31.8 km round trip). A commuting trip consists of one WLTC cycle in a regular phase sequence, as it is shown in Figure 3.6, and another WLTC cycle with the phase sequence reversed.
- A leisure trip on Wednesday afternoon from 19:00 PM to 20:30 PM and from 22:00 PM to 23:30 PM (101.7 km round trip). The leisure trip consists of a low and a high WLTC phase followed by an Artemis cycle, and a high and low WLTC phase.
- A weekend trip towards the Veluwe on Saturday from 12:00 PM to 13:17 PM with a return trip on Sunday from 16:00 PM to 17:17 PM (121.1 km round trip). The weekend trip consists of one regular WLTC cycle followed by an Artemis cycle and a second WLTC cycle with the phase sequence reversed.
- Grid charging takes place at the workplace on Thursday at 9:00 AM and at home on Sunday at 17:17 PM.
- Battery preheating to 5 °C before each commuting trip and before the trips towards and back from the Veluwe.

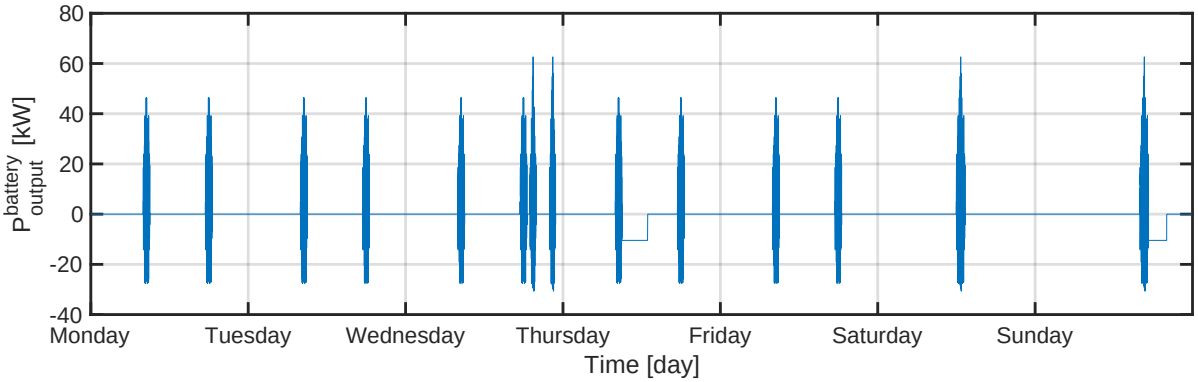

Figure 3.11: Modelled one-week EV battery power profile with workday commuting, an extra trip on Wednesday afternoon, grid charging on Thursday morning, a weekend trip, and grid charging on Sunday afternoon.

According to literature, average EV drivers charge their vehicles between two and three times a week, with a lower charging frequency for EVs with a larger battery capacity. Considering the Lightyear 0 has a large battery compared to its curb weight, the literature validates the two times per week charging behaviour portrayed in Figure 3.11 [101]. In this power profile, the EV is not equipped with VIPV, does not participate in V2G services, and does not use an air conditioning system.

Composition of a working week without a weekend trip

Figure 3.12 shows a one-week power profile with the same composition as the profile described in the subsection above, but excludes the weekend trip to the Veluwe and battery preheating to 5 °C during the weekend. Grid charging to 90% takes place on the same occasions as in the working week with a weekend trip.

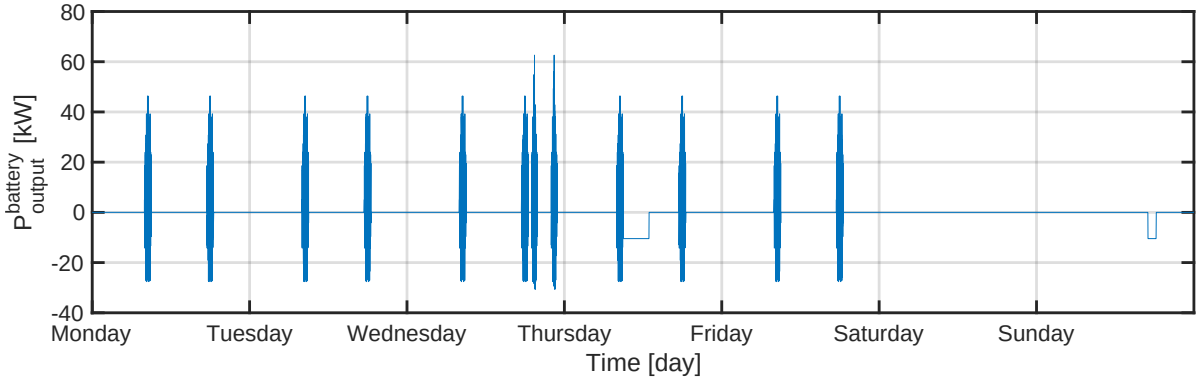

Figure 3.12: Modelled one-week EV battery power profile with workday commuting, an extra trip on Wednesday afternoon, grid charging on Thursday morning, and grid charging on Sunday afternoon.

Composition of the winter trip

Figure 3.13 shows the modelled one-week power profile of the winter trip from Amsterdam to Soelden. The power profile of the winter trip consists of the following:

- An outward trip from Amsterdam to Soelden covering 938 km. The outward trip consists of the driving cycles in the following sequence: five continuous Artemis driving cycles - one WLTC driving cycle - one Artemis driving cycle - grid charging - one highway driving cycle - one overtaking driving cycle - one Artemis driving cycle - one Brenner pass elevation driving cycle - grid charging.
- Parking from Tuesday to Saturday at a 1,368 m elevation at a low ambient temperature (T_{avg} = 7 °C for this particular week in Soelden), without thermal battery management.
- A return trip from Soelden to Amsterdam covering 938 km. The return trip consists of the driving cycles in the following sequence: five continuous Artemis driving cycles - grid charging - one Artemis driving cycle - one overtaking driving cycle - one highway driving cycle - one overtaking driving cycle - one highway driving cycle - grid charging - one Artemis driving cycle - one WLTC driving cycle - five Artemis driving cycles - grid charging.
- Battery preheating to 15 °C before the departure and return trip as it is considered that the EV owner will additionally preheat the battery before a long trip.

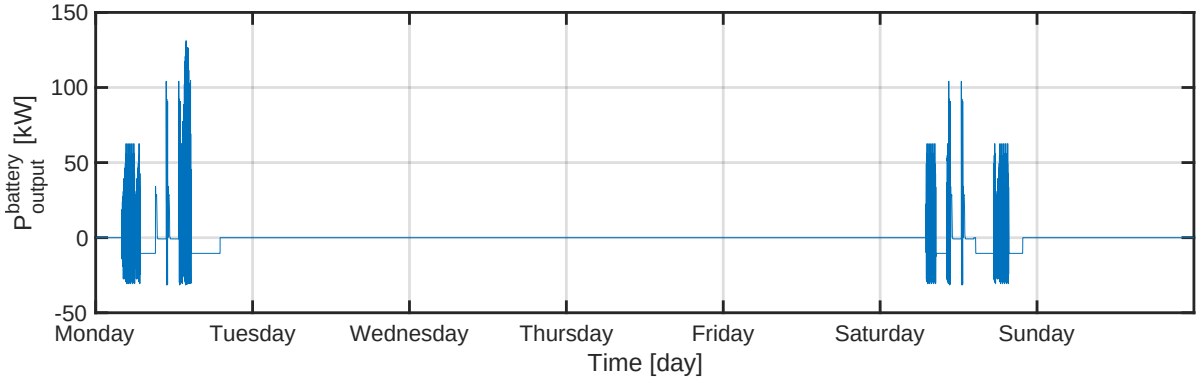

Figure 3.13: Modelled one-week EV battery power profile for a winter return trip from Amsterdam, the Netherlands to Soelden, Austria.

Composition of the summer trip

Figure 3.14 shows the modelled one-week power profile of the summer trip from Amsterdam, the Netherlands to Biarritz. The power profile of the summer trip consists of the following:

- An outward trip from Amsterdam to Biarritz covering 1,348 km. The outward trip consists of the driving cycles in the following sequence: one WLTC driving cycle - five Artemis driving cycles - one WLTC driving cycle - one Artemis driving cycle - grid charging - one highway driving cycle - one overtaking driving cycle - one highway driving cycle - one overtaking driving cycle - two Artemis driving cycles - one highway driving cycle - one overtaking driving cycle - grid charging - one highway driving cycle - one overtaking driving cycle - one Artemis driving cycle - grid charging.
- Parking from Tuesday to Saturday at a high ambient temperature without thermal battery management. T_{avg} = 24 °C for this particular week in Biarritz.
- A return trip from Biarritz to Amsterdam covering 1,348 km. The return trip consists of the driving cycles in the following sequence: one highway driving cycle - one overtaking driving cycle - one Artemis driving cycle - grid charging - one highway driving cycle - one overtaking driving cycle - one highway driving cycle - one overtaking driving cycle - two Artemis driving cycles - one highway driving cycles - one overtaking driving cycle - grid charging - one WLTC driving cycle - five Artemis driving cycles - one WLTC driving cycle - one Artemis driving cycle - grid charging.

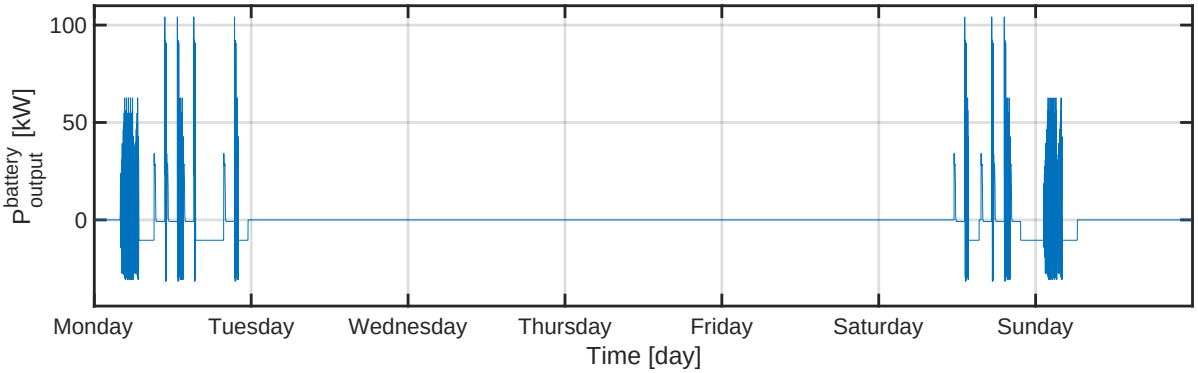

Figure 3.14: Modelled one-week EV battery power profile for a winter return trip from Amsterdam, the Netherlands to Biarritz, France.

Composition of the one-year power profile

Figure 3.15 shows the modelled one-year power profile, which comprises the four aforementioned power profiles. This one-year power profile consists of 13 working weeks with a weekend trip, 37 working weeks without a weekend trip, a winter trip and a summer trip. This power profile forms the base scenario. The other ageing stress factors, as well as the VIPV and V2G power profiles, are derived from this power profile.

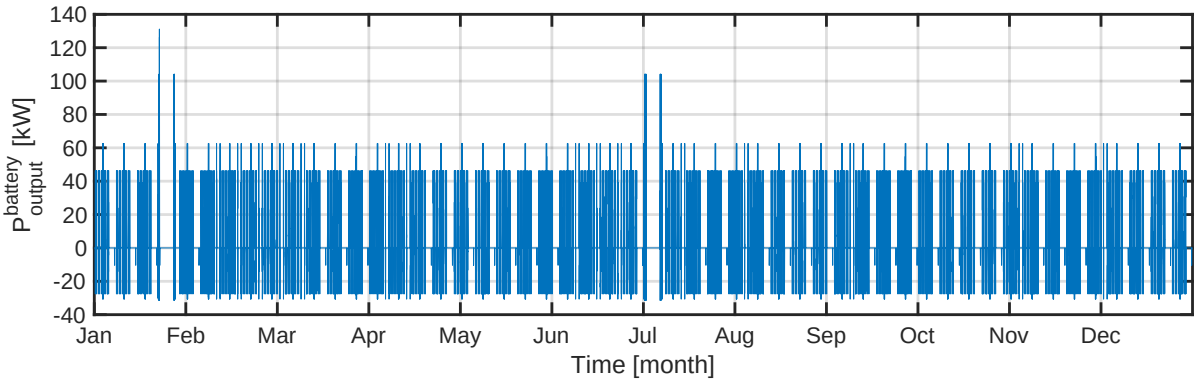

Figure 3.15: Modelled one-year EV battery power profile in the base scenario, comprising of 13 working weeks with a weekend trip, 37 working weeks without a weekend trip, a winter trip in January and a summer trip in July. Positive power values correspond to power output.

3.2.6. SoC profile modelling

The battery energy profile is derived from the modelled power profile subtracting the integration of the power profile from the battery capacity, since E = P · t. The SoC profile is consequently derived by dividing the remaining battery capacity by the total battery capacity. Figure 3.16 illustrates the relation between a 30-minute power profile (on the left y-axis) and the corresponding SoC profile (on the right y-axis). In this figure, the 5 kW power output at the start of the positive power profile corresponds to battery power output, enabling the HV heater to preheat the battery to 5 °C. The following positive battery power values correspond to powering the electric drivetrain, and the negative battery power values correspond to charging the EV using regenerative braking. Since the net power output in this 30-minute profile corresponds to 4.36 kWh, which is overwhelmingly positive, the battery SoC drops from about 68% to 61%. This drop in SoC correlates with a 4.36 kWh energy capacity drop in a 59.42 kWh battery.

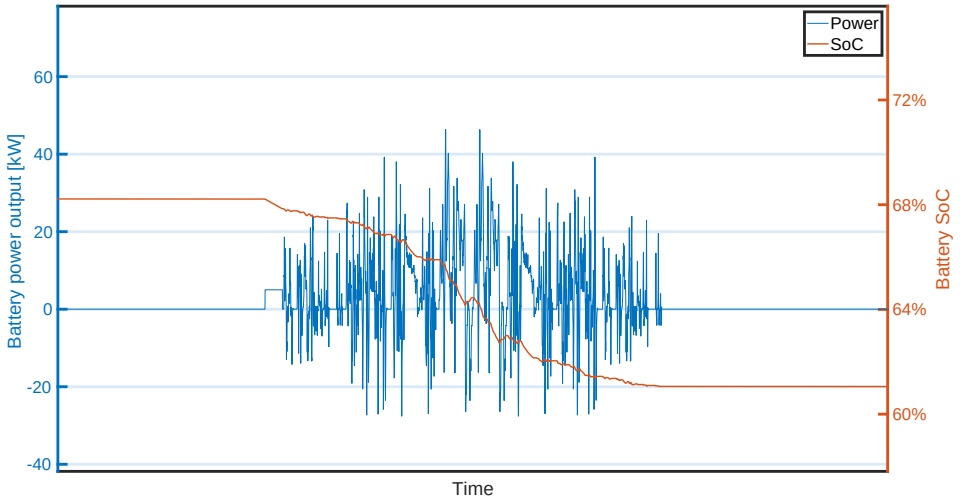

Figure 3.16: Zoomed-in image of Figure 3.17 illustrating the power and SoC profile on Tuesday evening. The image shows the impact of the power profile (left y-axis) on the battery SoC profile (right y-axis). The time period is 30 minutes from the first power deviation to the last. Positive power values correspond to power output.

As the battery cell's internal resistance depends on battery SoC and battery cell temperature, the actual SoC traces differ from the SoC profile derived from integrating the power profile. The dependency of the battery cell's internal resistance on SoC and cell temperature is shown in Figures 8.9 and 8.8 of the appendix. While the internal resistances are not considered in the modelled SoC profile, they are considered in the derived voltage profile which is used as input for the ageing models, on which is elaborated in Subsection 3.2.8.

Modelled one-week and one-year SoC profiles

Figures 3.17 - 3.20 show the power profiles on the left y-axes with their corresponding SoC profiles on the right y-axes. Figure 3.21 shows the modelled one-year SoC profile for the base scenario.

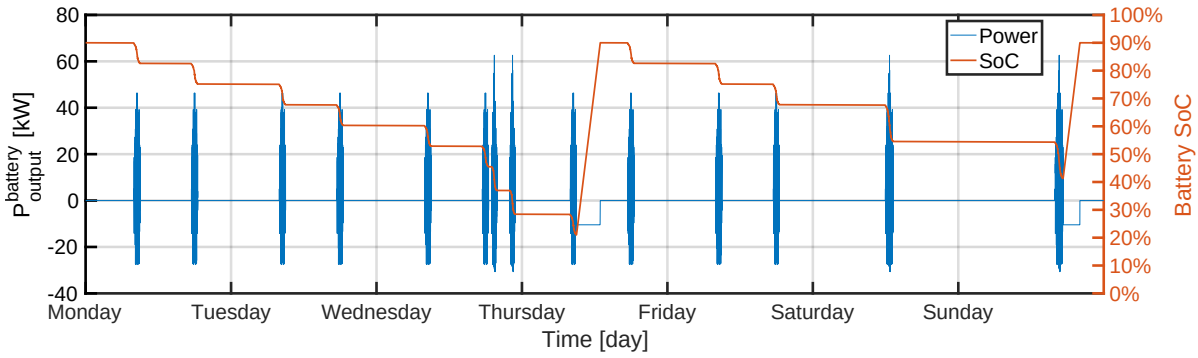

Figure 3.17: Modelled one-week EV power profile (left y-axis) with its corresponding SoC profile (right y-axis) during a working week with a weekend trip. Positive power values correspond to power output.

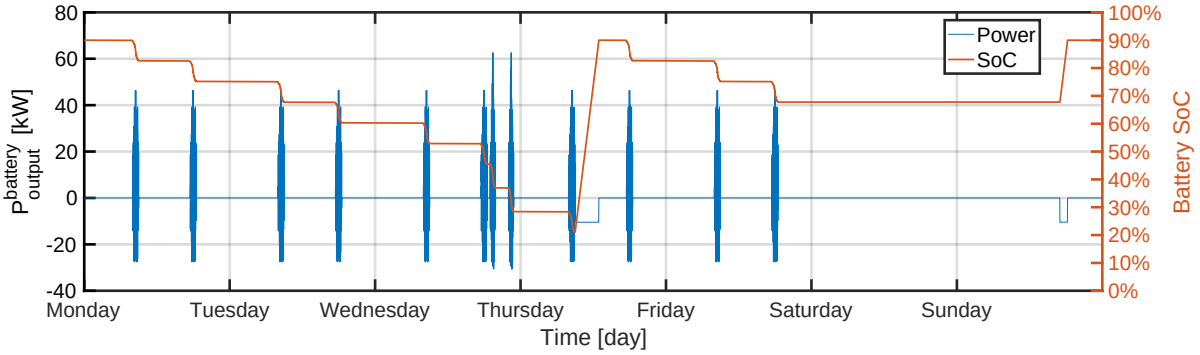

Figure 3.18: Modelled one-week EV power profile (left y-axis) with its corresponding SoC profile (right y-axis) during a working week with a weekend trip. Positive power values correspond to power output.

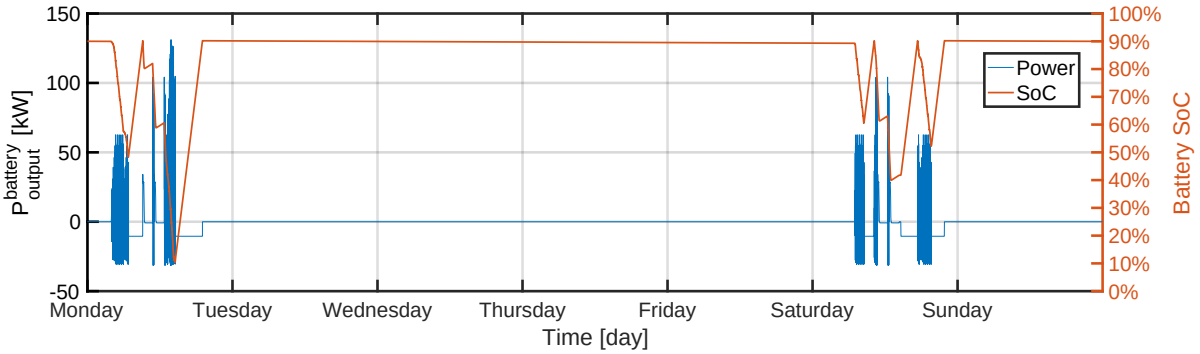

Figure 3.19: Modelled one-week EV power profile (left y-axis) with its corresponding SoC profile (right y-axis) during a winter trip. Positive power values correspond to power output.

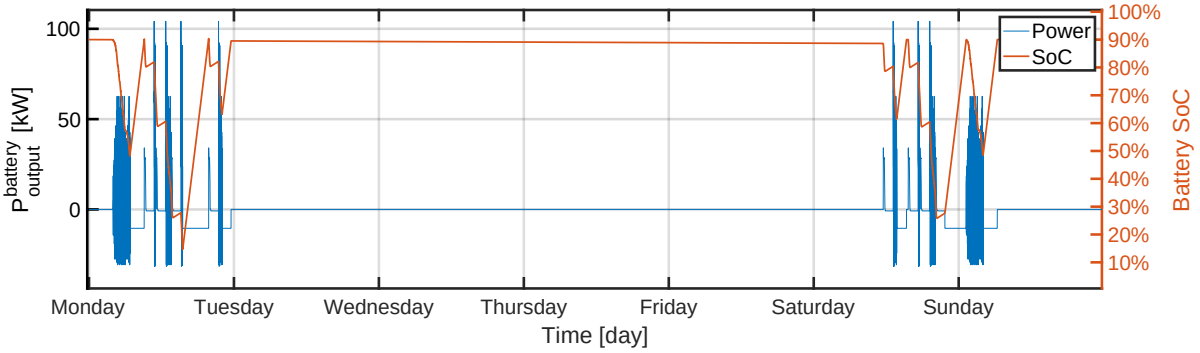

Figure 3.20: Modelled one-week EV power profile (left y-axis) with its corresponding SoC profile (right y-axis) during a summer trip. Positive power values correspond to power output.

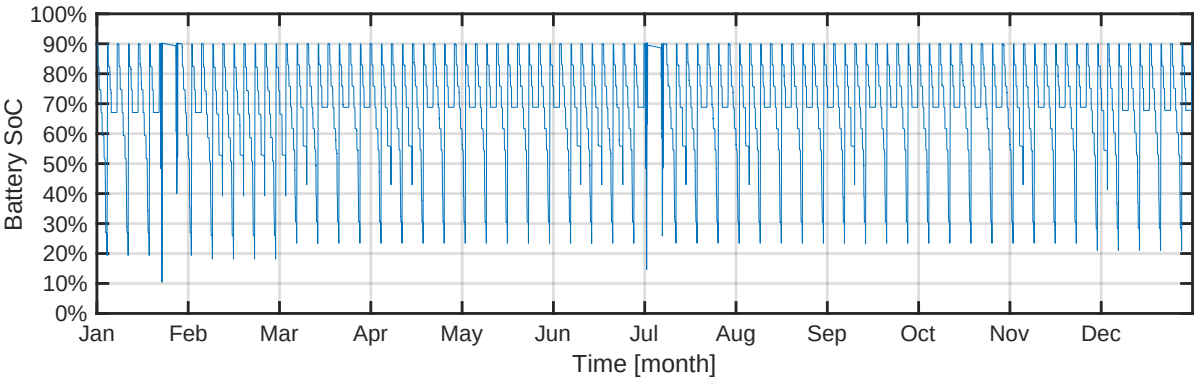

Figure 3.21: Modelled one-year EV battery SoC profile in the base scenario, comprising 13 working weeks with a weekend trip, 37 working weeks without a weekend trip, a winter trip in January and a summer trip in July.

3.2.7. Temperature profile modelling

This section addresses the main factors that impact the battery temperature profile throughout the year and explains the battery temperature modelling methodology used in this work.

Temperature increase during driving

There are several ways to determine how the battery temperature increases during driving. The most accurate method is to implement an electro-thermal model for Li-ion batteries that uses a power profile as an input, like the one designed by Huang et al. (2021). Another method is to use Lightyear's VPM to simulate either the battery temperature increase during driving over time, or the battery temperature increase over the distance travelled. It is assumed that the battery temperature increase over the distance travelled will result in a disproportionate increase of battery temperature during highway driving compared to city driving and that this effect is less if the battery temperature increase during driving over time is considered.

Lightyear's VPM is therefore used to analyse how the vehicle's battery temperature behaves over multiple hours of driving. 15 WLTC cycles are continuously looped for three different ambient temperatures. In all three simulations, the starting battery temperature equals the ambient temperature of that simulation. The velocity and battery temperature profiles for one simulation are visualised in Figure 3.22. In this figure, the left y-axis shows the vehicle velocity and the right y-axis shows the battery temperature in degree centigrade. The figure shows that at a starting battery temperature of 25 °C, in the first 12 WLTC cycles (from 0 s to 19,801 s (5.5 h)) the battery temperature increases from 25 °C to 35.4 °C. This temperature increase of ΔT = 10.44 °C corresponds to an average temperature increase of 1.90 °C per hour. In the second simulation, the ambient temperature and thus the starting battery temperature is set at 15 °C. The temperature increase in the second simulation is 2.35 °C per hour. In the third simulation, the ambient temperature and thus the starting temperature is set at 10 °C. The temperature increase in the third simulation was 2.58 °C per hour.

It appears that compared to the battery temperature increase rate at a starting battery temperature of 25 °C, the battery temperature increase rate is 24% higher at a starting temperature of 15 °and 36% higher at a starting temperature of 10 °C. The higher battery temperature increase rate at lower temperatures might be due to additional resistance in the battery cell at lower temperatures, which is also shown in Figure 8.9 of the appendix.

Considering that the ambient temperature in the Netherlands over the whole year averages 10.2 °C, an average temperature increase during driving of 2.58 °C per hour is considered throughout the modelling of the temperature profile [13].

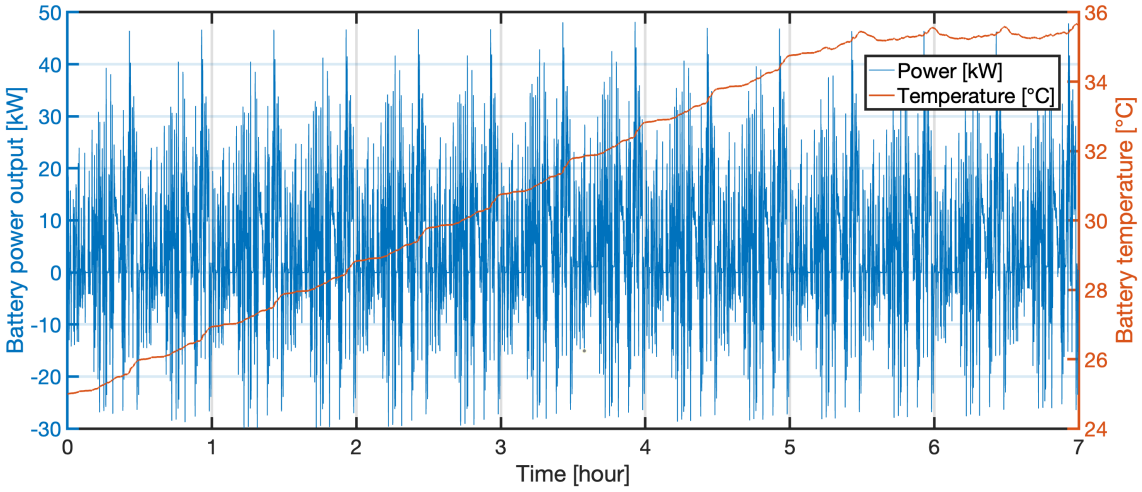

Figure 3.22: Velocity and battery temperature profile over 15+ full WLTC cycles with an ambient temperature of 25 °C.

Figure 3.23 shows the power profile on the left y-axis and the battery temperature profile on the right y-axis for a single WLTC cycle. As highlighted in the black rectangle at around t = 1,500 s, the battery temperature increases the most when the power output peaks. Figure 8.7 of the appendix, which shows the corresponding temperature and velocity profiles, shows that the vehicle accelerates at around t = 1,500 s. This correlation between temperature, power and velocity shows how the battery temperature increases the most during vehicle acceleration.

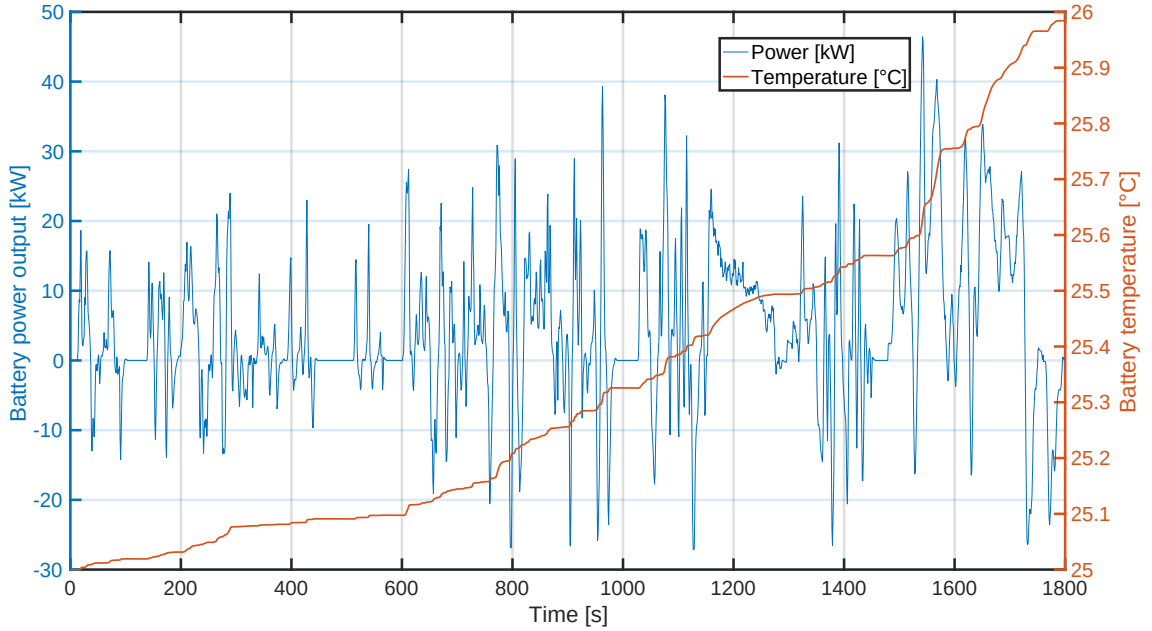

Figure 3.23: Power and temperature profile over one WLTC cycle with an ambient temperature of 25 °C.

Temperature decrease to ambient temperature during parking

To determine the heat loss rate of the battery during parking, Newton's law of cooling is used, as shown in Equation 3.1:

$$\frac{dT}{dt} = -\frac{h}{c} \cdot A \cdot (T_{\text{amb}} - T_{\text{batt}}) \tag{3.1}$$

where h corresponds to the heat transfer coefficient, c corresponds to the heat capacity of the battery pack, A corresponds to the area of the battery pack, T_{amb} corresponds to the ambient temperature to which the battery temperature will drop, and T_{batt} corresponds to the battery pack temperature at the start of the cooling period. The heat transfer coefficient is assumed to be 10 W / ($m^2 \cdot K$) at the bottom side of the battery pack, and 5 W / ($m^2 \cdot K$) at the cabin side. Lightyear's battery pack dimensions are approximately 1800x1600 mm, corresponding to an area of 2.88 m^2. Lightyear's battery cells, battery enclosure, and battery coolant, have heat capacity values of 206 kJ/K, 118 kJ/K, and 58 kJ/K, respectively, adding up to a total heat capacity of 380 kJ/K. It is assumed that the cabin temperature equals the ambient temperature. For simplification, it is assumed that the battery temperature decreases linearly instead of following an exponential decay. To model the linear temperature decrease, first, the cooling time period of the previous cooling session is used to estimate to what future ambient temperature the battery will drop. Then, to more accurately determine the temperature decrease per second during the cooling of the battery, Equation 3.2 is used.

$$dT_{\text{sec}}^{\text{cooling}} = -\left(c_{\text{total}} \cdot \frac{T_{\text{amb}}^{\text{est.}} - T_{\text{batt}}^{\text{start}}}{2}\right) \tag{3.2}$$

where $dT_{sec}^{cooling}$ is the temperature decrease per second, c is the heat capacity which is set at 380 kJ / K, $T_{amb}^{est.}$ is estimated ambient temperature to which the battery is expected to drop, T_{batt}^{start} is the battery temperature at the start of the considered cooling period, and the factor 2 is included to more-accurately approximate the exponential temperature decay using a linear temperature decay. Equation 3.3 is subsequently used to determine the actual cooling time period of the considered cooling session.

$$t_{\text{cooling}} = \left(\frac{T_{\text{batt}}^{\text{start}} - T_{\text{amb}}^{\text{est.}}}{dT_{\text{sec}}^{\text{cooling}}}\right) \tag{3.3}$$

where $t_{cooling}$ is the cooling time, $T_{amb}^{est.}$ is the estimated ambient temperature to which the battery will drop, T_{batt}^{start} is the battery temperature at the start of the considered cooling period, and dT_{sec} is the temperature decrease per second which is calculated using Equation 3.2.

The ambient temperature throughout the year for the Netherlands is interpolated from hourly measurements to per-second data. The hourly measurements are sourced from a typical meteorological year (TMY) dataset. TMY is a dataset selected from a longer time period, in this case, 12 years. For each month of the year, the most typical temperature values have been selected [13]. Figure 3.24 shows the TMY ambient temperature for Amsterdam, the Netherlands, sourced from the European Commission's Photovoltaic Geographical Information System [12]. The values in this ambient temperature profile are for T_{amb} in the temperature profile modelling equations.

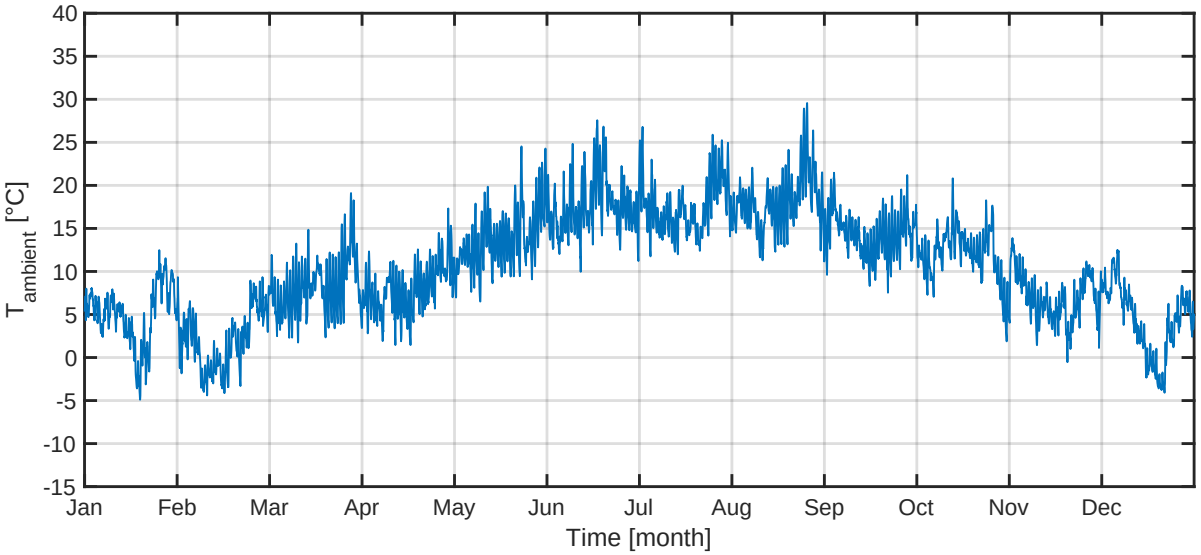

Figure 3.24: Ambient temperature in Amsterdam, the Netherlands. Data sourced from the European Commission's Photovoltaic Geographical Information System [12].

Thermal management system

EV manufacturers like Lightyear incorporate thermal battery management systems and strategies to improve the battery's performance to reduce battery ageing. For example, Lightyear performs active battery cooling and battery preconditioning. Battery preconditioning refers to battery preheating and precooling.

Active battery cooling

During active cooling a fan forces cool air over the batteries to withdraw heat, keeping the battery temperature within a certain desired range. Within the 5 °C - 25 °C temperature region, the battery cell resistance is considered reasonable. Outside this region, the resistance increases to undesired levels, decreasing the C-rate. This study assumes a desired battery temperature range of 5 °C - 25 °C. The C-rate is further discussed in Subsection 3.2.10. Active battery cooling ensures that the battery temperature remains under 35 °C during operation, as shown around t = 20,000 s in Figure 3.22. The battery is actively cooled at 35 °C to prevent higher battery temperatures from causing the growth of the SEI layer to further accelerate, which would accelerate ageing [102]. Due to slight temperature variations during active cooling, the battery temperature rises to a maximum of 35.4 °C.

Battery preconditioning

Before driving or charging, the battery is preheated or precooled to reach a reasonable operating temperature range. Battery preconditioning demands energy from the battery, for which an energy penalty is calculated. This energy penalty is incorporated in the modelling of the power profile.

Preheating is performed using an HV heater when the ambient temperature is lower than the desired battery operating temperature. The HV heater extracts up to 5 kW power from the HV battery. Therefore, it is assumed that the HV heater demands a constant power of 5 kW for preheating the battery. Several preconditioning tests from Lightyear show that it takes an average of 1070 s to heat the battery from -10 °C to 10 °C, 1300 s to heat up from -10 °C to 15 °C, and 1900 s to heat up from -10 °C to 25 °C. These heating rates imply a linear temperature increase of 0.0185 °C/s. This same preheating temperature increase is used throughout the temperature profile modelling. As the optimal operating range of the battery operating temperature is

between 5 °C and 35 °C, the battery is preheated to 5 °C. Equation 3.4 is used to determine the time required to preheat the battery from the ambient temperature to the desired battery temperature.

$$t_{\text{preheat}} = \frac{T_{\text{batt}}^{\text{desired}} - T_{\text{amb}}}{\frac{dT_{\text{heater}}}{dt}} \tag{3.4}$$

where $t_{preheat}$ is the time required to preheat the battery, $T_{batt}^{desired}$ is the desired battery temperature, which is 5 °C in this case, T_{amb} is the ambient temperature at the start of the considered preheating period, and $\frac{dT_{heater}}{dt}$ is the heating rate, set at 0.0185 °C/s in this case.

Precooling is performed when the ambient temperature is higher than the desired battery temperature. Equation 3.5 calculates the required energy to lower the temperature to the desired operating range.

$$E_{\text{req}}^{\text{HVAC}} = \frac{\Delta T \cdot c}{3{,}600 \cdot COP} \tag{3.5}$$

where E_{req}^{HVAC} corresponds to the energy required for the HV air conditioning (HVAC) system to cool the battery, ΔT corresponds to the difference in temperature, c corresponds to the sum of the heat capacity of the battery pack components, and COP stands for coefficient of performance, which is again a function of temperature. Precooling is not used for modelling the temperature profile of the Netherlands, as the ambient temperature in the Netherlands does not exceed 35 °C.

Modelled one-week battery temperature profiles

Figures 3.25 3.26 show the modelled battery temperature week profile for January and August, respectively. As shown in the graphs, the battery temperatures are governed by the ambient temperatures. Each morning and evening in January, the battery preheats to 5 °C, concurrently causing a constant 5 kW power output required to power the HV battery heater. As the ambient temperature in August exceeds 5 °C, no battery preheating is required. Following this, a constant battery temperature increase of 2.58 °C per hour is simulated during driving, after which the battery cools down to the ambient temperature in a linear matter according to Equations 3.2 and 3.3.

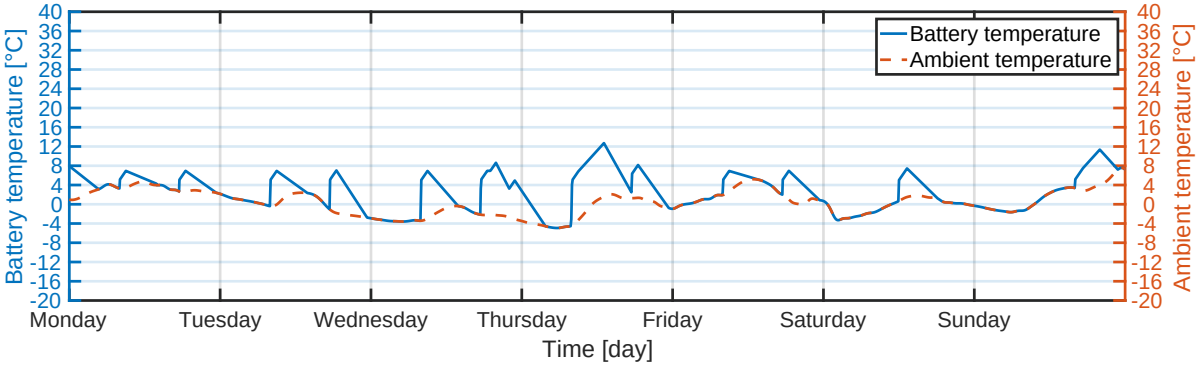

Figure 3.25: Modelled one-week battery temperature profile (left y-axis) and ambient temperature (right y-axis) during a working week with a weekend trip in January.

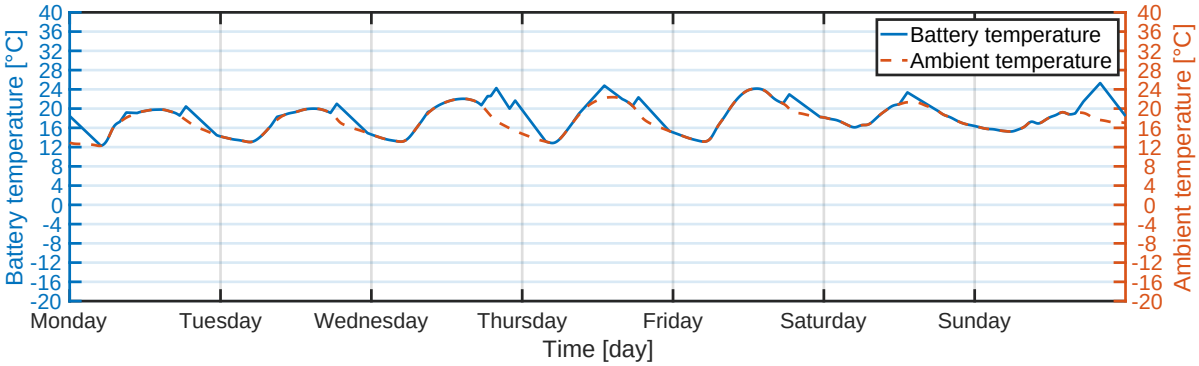

Figure 3.26: Modelled one-week battery temperature profile (left y-axis) and ambient temperature (right y-axis) during a working week with a weekend trip in August.

Figures 3.27 and 3.28 show the modelled battery temperature week profile during the winter and summer trips, respectively. In the winter trip, the EV driver travels from Amsterdam to Soelden on Monday and back on Sunday. In the summer trip, the EV driver travels from Amsterdam to Biarritz on Monday and back on Sunday. In the winter trip, the battery is preheated to 5 °C. Considering the higher ambient temperatures during the week of the summer trip, no battery heating is required. In both trips, the battery temperature increases at a rate of 2.58 °C per hour during driving. When the battery temperature reaches 35 °C, active cooling is activated to prevent the battery from reaching temperatures that reduce performance and accelerate ageing mechanisms in the battery. When the EV arrives at its destination, the battery cools down to the ambient temperature in a linear matter according to Equations 3.2 and 3.3. In the winter trip, the battery temperature during parking in Soelden averages around -6 °C. On the summer trip, the battery temperature during parking in Biarritz ranges around 24 °C.

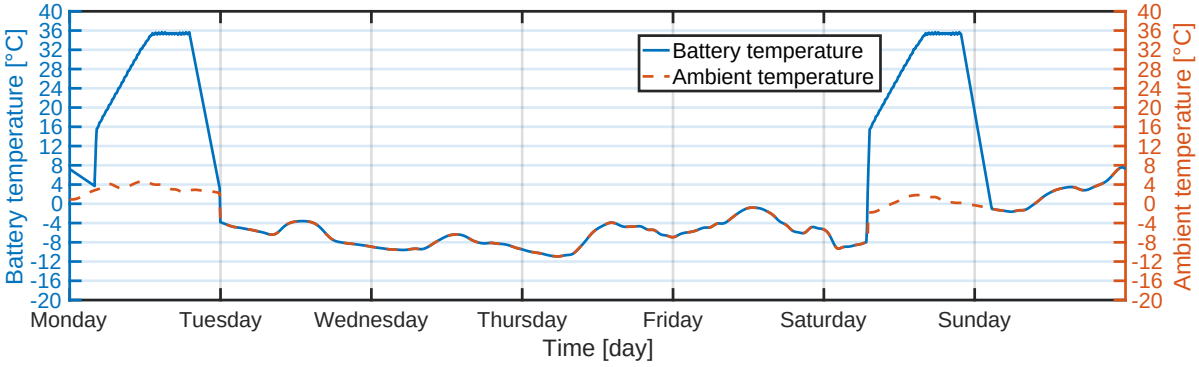

Figure 3.27: Modelled one-week battery temperature profile (left y-axis) and ambient temperature (right y-axis) during a winter trip.

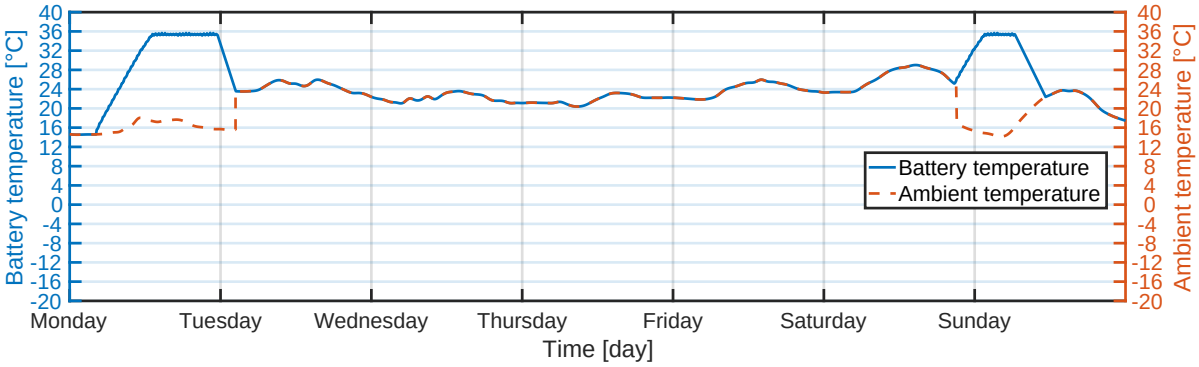

Figure 3.28: Modelled one-week battery temperature profile (left y-axis) and ambient temperature (right y-axis) during a summer trip.

Modelled one-year battery temperature profile

The red line in Figure 3.29 represents the ambient temperature of the Netherlands throughout the year, and the blue line represents the modelled battery temperature. The graph illustrates how the battery temperature is governed by the ambient temperature. For each month, the ambient temperature profile of a single week is taken to simulate the battery temperature throughout the month. The following weeks are used to simulate their corresponding months: 16/1 - 23/1; 6/2 - 13/2; 6/3 - 13/3; 3/4 - 10/4; 9/5 - 16/5; 6/6 - 13/6; 4/7 - 11/7; 16/8 - 23/8; 13/9 - 20/9; 11/10 - 18/10; 13/11 - 21/11 and 11/12 - 18/1. Therefore, the modelled ambient temperature profile slightly varies from the actual ambient temperature profile.

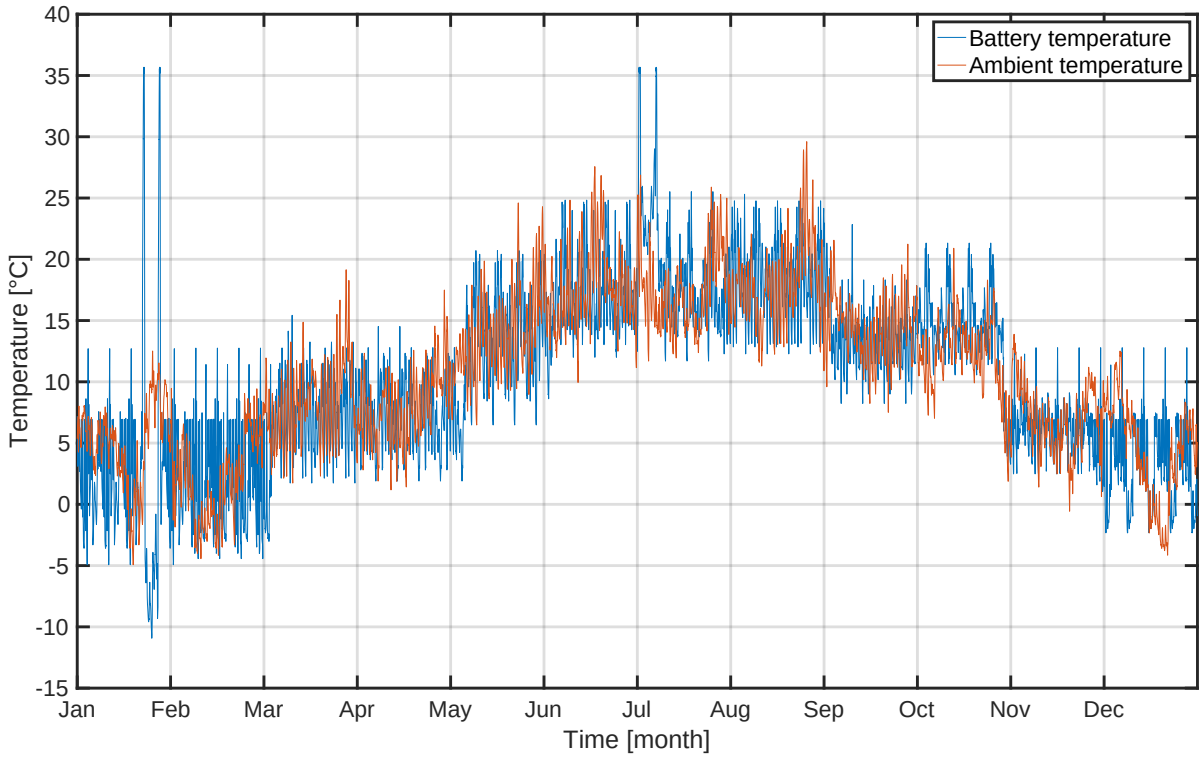

Figure 3.29: Modelled one-year battery temperature profile (left y-axis) and ambient temperature (right y-axis).

The same one-year battery temperature profile is applied throughout all the use case scenarios that simulate an EV in the Netherlands. The scenarios that simulate an EV in Spain contain a slightly different battery temperature profile, which is elaborated in Section 5.1.

3.2.8. Voltage profile modelling

The battery cell's voltage profile ($V_{cell}(t)$) is calculated using Equation 3.6:

$$V_{\text{cell}} = V_{OC} - \Delta V \tag{3.6}$$

where V_{OC} corresponds to the open-circuit voltage of the battery cell, which is the difference in electrical potential between the two electrodes of a battery when no current is applied and on which is elaborated below, and ΔV corresponds to the voltage drop over the battery's resistance. The corresponding battery circuit model is shown in Figure 3.30.

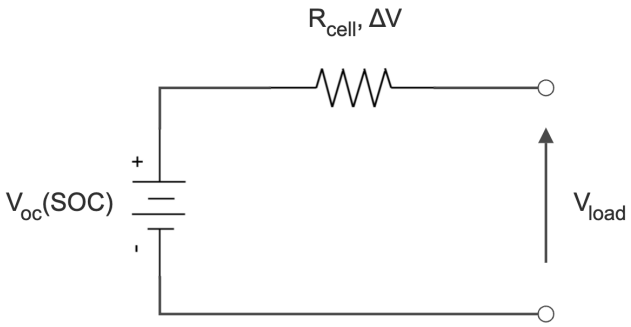

Figure 3.30: Battery equivalent circuit model. Own composition.

The voltage drop over the resistance is calculated using Equation 3.7:

$$\Delta V = R_{\text{cell}} \cdot I_{\text{cell}} \tag{3.7}$$

where R_{cell} is the resistance of the battery cell, and I_{cell} is the current running through the battery cell [96]. R_{cell} varies with SoC and temperature. Figure 8.9 of the appendix shows the battery sheet provided by Lightyear's battery manufacturer with the battery cell resistance in mΩ for various temperatures and SoC values. For simplicity, the R_{cell} is assumed constant. As the average battery temperature over the full year is 10.2 °C, the cell's resistance is set at 20.0 mΩ, which corresponds to the discharging resistance around 10 °C according to Figure 8.9. I_{cell} depends on the voltage drop and is calculated by dividing the power output of one cell by the cell's voltage, as shown in Equation 3.8.

$$I_{\text{cell}} = \frac{P}{N_{\text{cells in parallel}} \cdot N_{\text{cells in series}} \cdot V_{\text{cell}}} \tag{3.8}$$

where P corresponds to the battery's power output, shown in Figure 3.11, and n corresponds to the number of cells in series, which add up the cell's operating voltage.

As shown in the battery circuit model in Figure 3.30, the battery's V_{OC} depends on the battery's SoC. The relation between the two can be derived from the battery's datasheet. Lightyear's battery manufacturer has provided a look-up table (LUT) that states the battery cell's V_{OC} for every SoC value. The LUT is plotted in Figure 8.10 of the appendix, portraying a typical V_{OC}(SoC) curve of an NMC battery. The LUT is expanded using 1D-interpolation to match V_{OC} values with exact SoC values from the modelled SoC profile. The resulting V_{OC} values per time step are used in Equation 3.6 to determine the battery cell's operating voltage per time step. The constant V_{OC}(SoC) values between 0% and 2% SoC, and 99% and 100% SoC, are likely to be incorrect values provided by the battery manufacturer. However, due to the set battery SoC limits of 10% and 90% stated in Subsection 3.2.3, these values are neglected.

A single cell resistance R_{cell} is considered for every battery temperature and SoC value. In reality, the cell resistance depends on the cell's SoC and temperature, as can be seen in Figures 8.8 and 8.9 of the appendix. Therefore, at elevated temperatures or different SoC levels, the simulated voltage profile will likely inaccurately follow the actual EV voltage profile.

Modelled one-week and one-year voltage profiles

Figure 3.31 shows a one-week V_{OC} profile on the left y-axis and the corresponding SoC profile on the right y-axis. The corresponding one-week cell voltage profile is shown in Figure 3.32. Figure 3.33 shows the modelled one-year voltage profile for the base scenario.

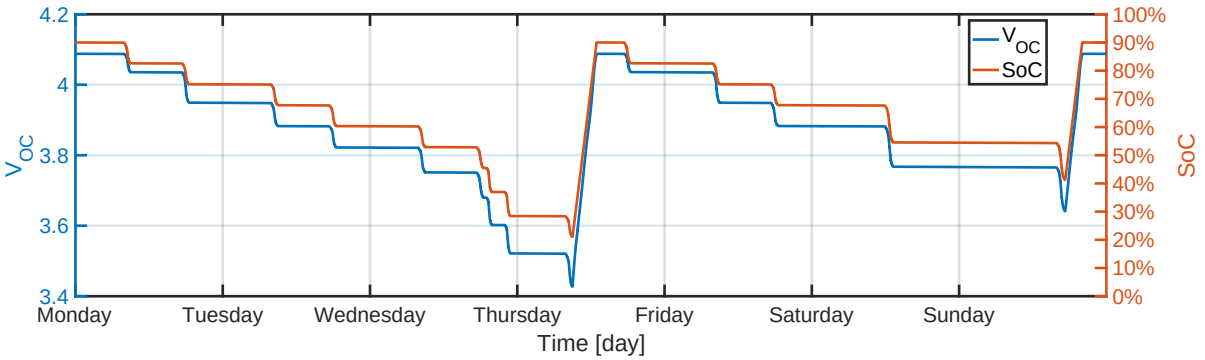

Figure 3.31: The V_{OC} profile derived from the modelled SoC profile and the battery's V_{OC}(SoC) curve shown in Figure 8.10 of the appendix.

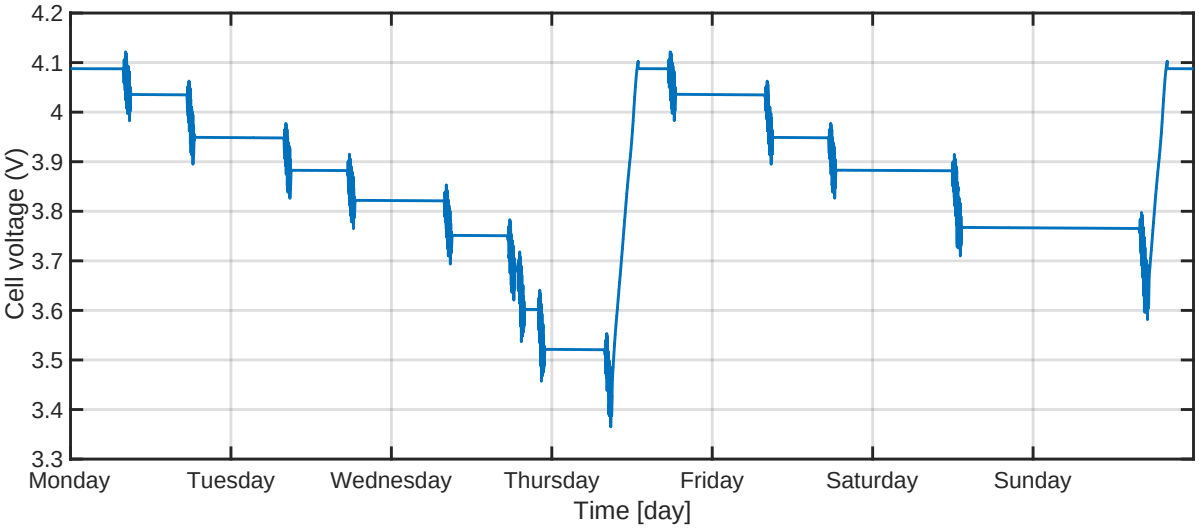

Figure 3.32: Cell voltage profile for one week determined using Equations 3.6 - 3.8.

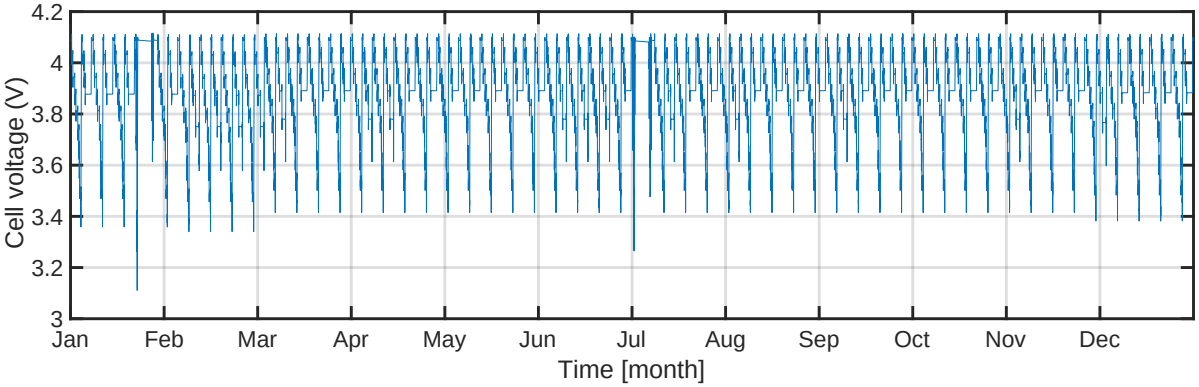

Figure 3.33: Modelled one-year battery voltage profile for the base scenario.

3.2.9. Current profile modelling

The current profile is derived by dividing the power profile by the voltage profile values, as shown in Equation 3.9, and scaling it accordingly to the battery pack setup. Figure 3.34 shows a one-week current profile and Figure 3.35 shows the modelled one-year current profile for the base scenario.

$$I = \frac{P}{V} \tag{3.9}$$

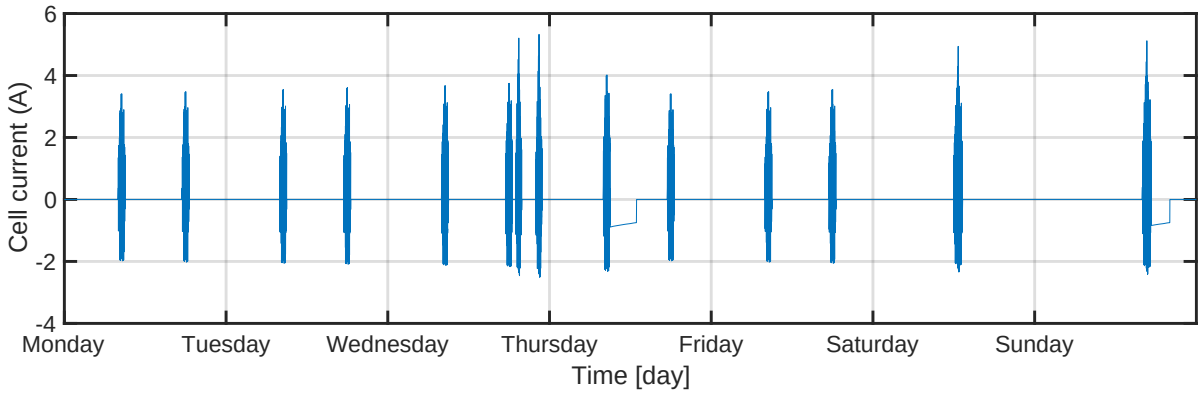

Figure 3.34: Current profile derived from the power profile shown in Figure 3.11 and the voltage profile shown in Figure 3.32.

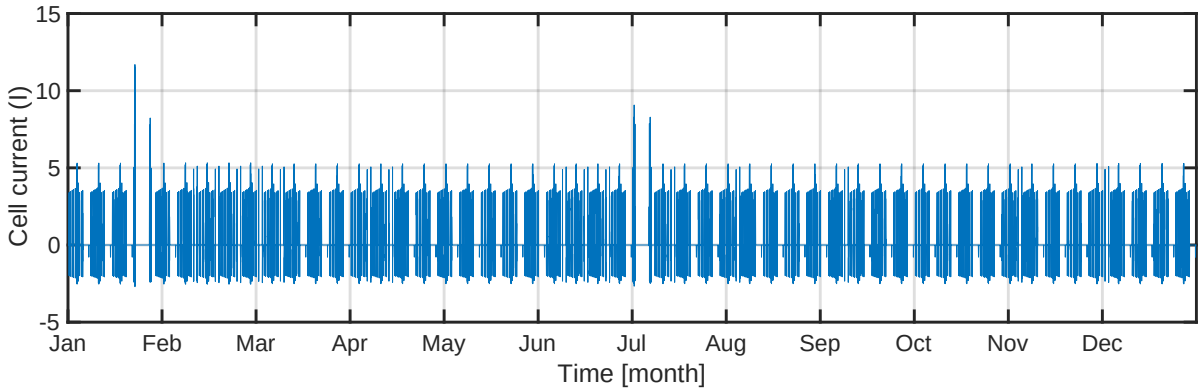

Figure 3.35: Modelled one-year battery current profile for the base scenario.

3.2.10. C-rate profile modelling

In the VPM, the battery's C-rate is specified as a function of SoC and cell temperature. For simplification, the C-rate profile is derived by dividing the absolute cell current by the useful cell capacity at each second. The useful cell capacity of Lightyear's NMC battery is 4.85 A. Figure 3.36 shows a one-week C-rate profile and Figure 3.37 shows the modelled one-year current profile for the base scenario.

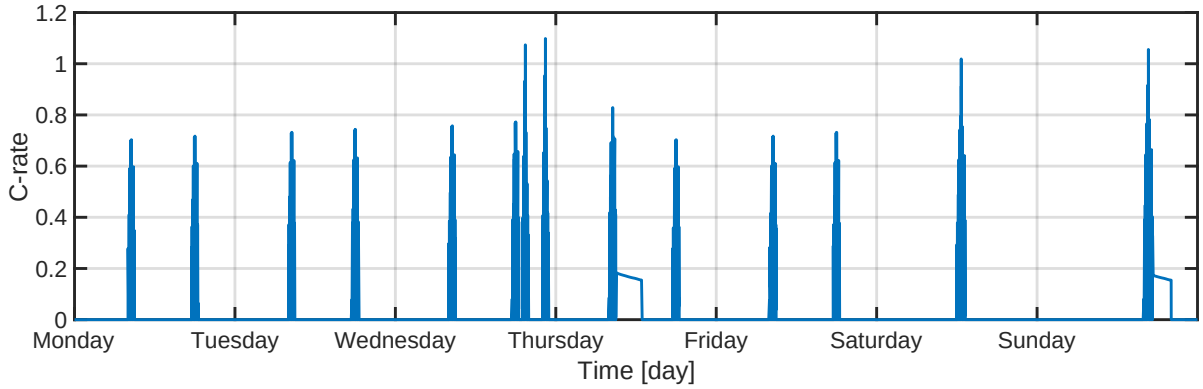

Figure 3.36: Modelled one-week C-rate profile derived from the cell current profile shown in Figure 3.34 and the full cell capacity.

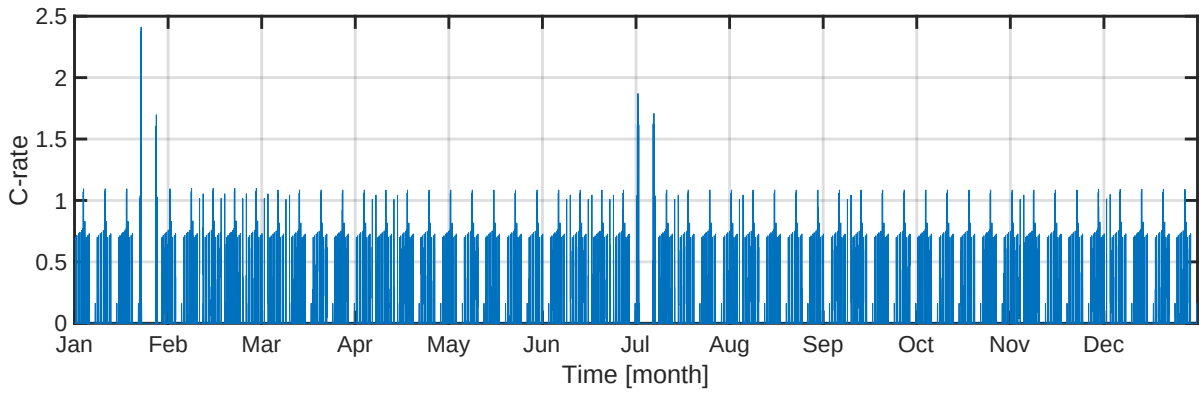

Figure 3.37: Modelled one-year C-rate profile derived from the cell current profile shown in Figure 3.35 and the full cell capacity.

3.2.11. Cycle counting method and capacity throughput definition

Rainflow cycle counting

In engineering, rainflow cycle-counting is used to accurately determine the combined fatigue of individual stress cycles. Figure 8.12 in the appendix shows the working of the rainflow cycle-counting method. Rainflow cycle counting is based on the assumptions that the specific sequence of different-sized cycles does not influence the fatigue, and that the impact of a cycle on fatigue is the same over the period of time over which the cycle counting is performed [47]. Close analysis of the results from Matlab's built-in rainflow cycle counting algorithm on battery data shows that due to the nature of the algorithm, the algorithm does not accurately determine the start and end of each battery cycle. Thus, Matlab's built-in rainflow cycle counting algorithm shows to have limited applicability to battery data.

Load profile cycle counting

Instead, the load profile cycle counting method is used to determine the start and end of each charge and discharge 'partial cycle'. Each partial cycle's start and end points are determined by the moment in time that the power profile crosses the 0 value of the x-axis, which is named a 'zero crossover point'. Figure 3.38 illustrates this cycle-counting method. The first partial cycle in this illustration starts at point A and ends at point B, which is a partial discharge cycle considering the sign convention of the power profile on the left y-axis. The corresponding SoC profile on the right y-axis shows how the battery SoC drops from point A' to point B'. The second partial cycle in the illustration is considered a partial charging cycle, which starts at point B and ends at point C, with the SoC profile showing the drop in battery capacity from point B' to point C'. It appears that in literature, researchers do not share one common definition for a cycle. In this work, a full equivalent cycle is defined as the cell's discharged capacity divided by the cell's full capacity.

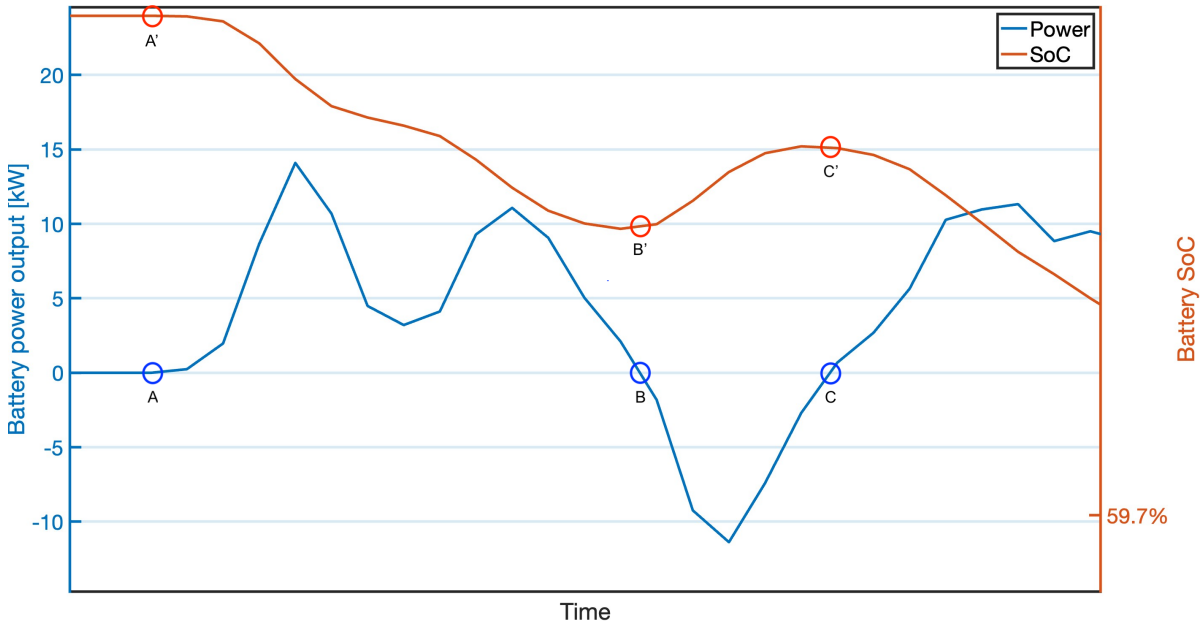

Figure 3.38: Illustration of the load profile cycle counting methodology.

Throughput definition

The definition of throughput appears inconsistent in literature. Throughput essentially describes the amount of energy managed by the battery. Vermeer et al. (2022) define throughput as the net amount of energy delivered by the battery. A researcher from RWTH Aachen affiliated with Schmalstieg et al. (2014) considers throughput to be the energy charged and discharged by a battery. Schimpe et al. (2018) define separately total throughput (Q_{Tot}) as the cumulative amount of energy charged and discharged by the battery, and define charge throughput (Q_{Ch}) as the throughput in charging direction. It thus appears that there is no single definition for throughput, but that it depends on the researcher's definition.

The throughput is determined for every second of the year using Equation 3.10.

$$Q(t) = \frac{I(t)}{3,600} \tag{3.10}$$

3.3. VIPV modelling

As described in Section 2.3, VIPV enable EVs to harness energy from the sun to consequently charge the vehicle's battery. Lightyear's SolarSimulator tool is used to simulate the potential VIPV power generation. A description of the model is given below.

3.3.1. Lightyear's SolarSimulator tool

Lightyear's SolarSimulator tool is developed to simulate the energy generated by photovoltaic solar cells based on weather and location input data. In order to do that, the model employs an optical, thermal and electrical model. First, the optical model retrieves the irradiance falling on the surface, where-after the combined thermal and electrical model determines the output power.

Two variables directly influence VIPV's performance, namely the temperature of the panel and the incident irradiance. These two parameters are consequently used in the electrical model. Standard test conditions (STC) of PV modules do not represent the working conditions because in real conditions, high irradiance causes an increase in the solar module's temperature, leading to lower voltage and lower power output. Therefore, both parameters are used as input for the thermal and electrical models.

Optical model

The optical model developed by Santbergen et al. (2016) and Regondi et al. (2017) was implemented to estimate the irradiance falling on the surface. In the optical model, ray-tracing tracks the light from the source to the surface investigated. The output of this simulation is combined with the all-weather model by Perez et al. (1993) for sky luminance distribution to determine the solar irradiance. As the SolarSimulator tool does not consider shading over the vehicle, it is assumed that the VIPV do not experience shading.

Thermal model

The thermal model evaluates the heat transfer processes, both internal and external to the PV module. The heat transfer model combines three heat transfer types, namely conduction, radiation, and convection.

Electrical model

The electrical model consists of a single diode model, which according to Mohamed et al. (2013) is the simplest approach for modelling a PV module. As shown in Figure 3.39, a single-diode model has a current source parallel to a diode. The output of the current source is directly proportional to the light falling on the cell. This electrical model requires only three parameters to completely characterise the current-voltage (I-V) characteristic curve: short-circuit current (I_{SC}), V_{OC} and the diode ideality factor n. Furthermore, because the single diode model does not adequately represent the cell's behaviour when subjected to environmental variation, especially at low voltage, the model includes a series resistance R_S. This model, also known as the R_S-model, is the most widely-used model in PV system simulations due to its simplicity and computational efficiency.

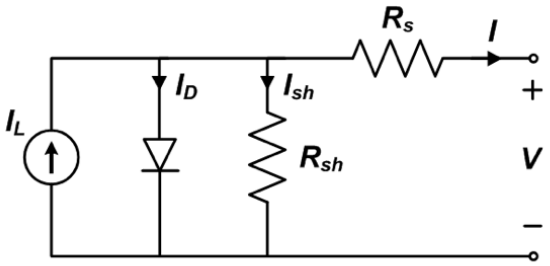

Figure 3.39: Single diode model equivalent circuit model [70].

In Figure 3.39, I_L represents the solar-generated current in the cell, I_0 is the diode reverse saturation current, R_S is the series resistance, R_{sh} is a shunt resistance, I_{sh} represents the current lost due to the shunt resistance.

3.3.2. VIPV power profile modelling

Lightyear's SolarSimulator tool simulates Lightyear's one-year VIPV power generation data for different geographical locations. The data gives the VIPV power generation profile at a 15-minute time step. In the simulation, the average VIPV power generation is taken for a Lightyear 0 vehicle driving in 28 different directions.

Modelled one-year VIPV power profiles

The top graph of Figure 3.40 shows the modelled one-year VIPV power generation profile for Amsterdam, the Netherlands and the bottom graph for Madrid, Spain.

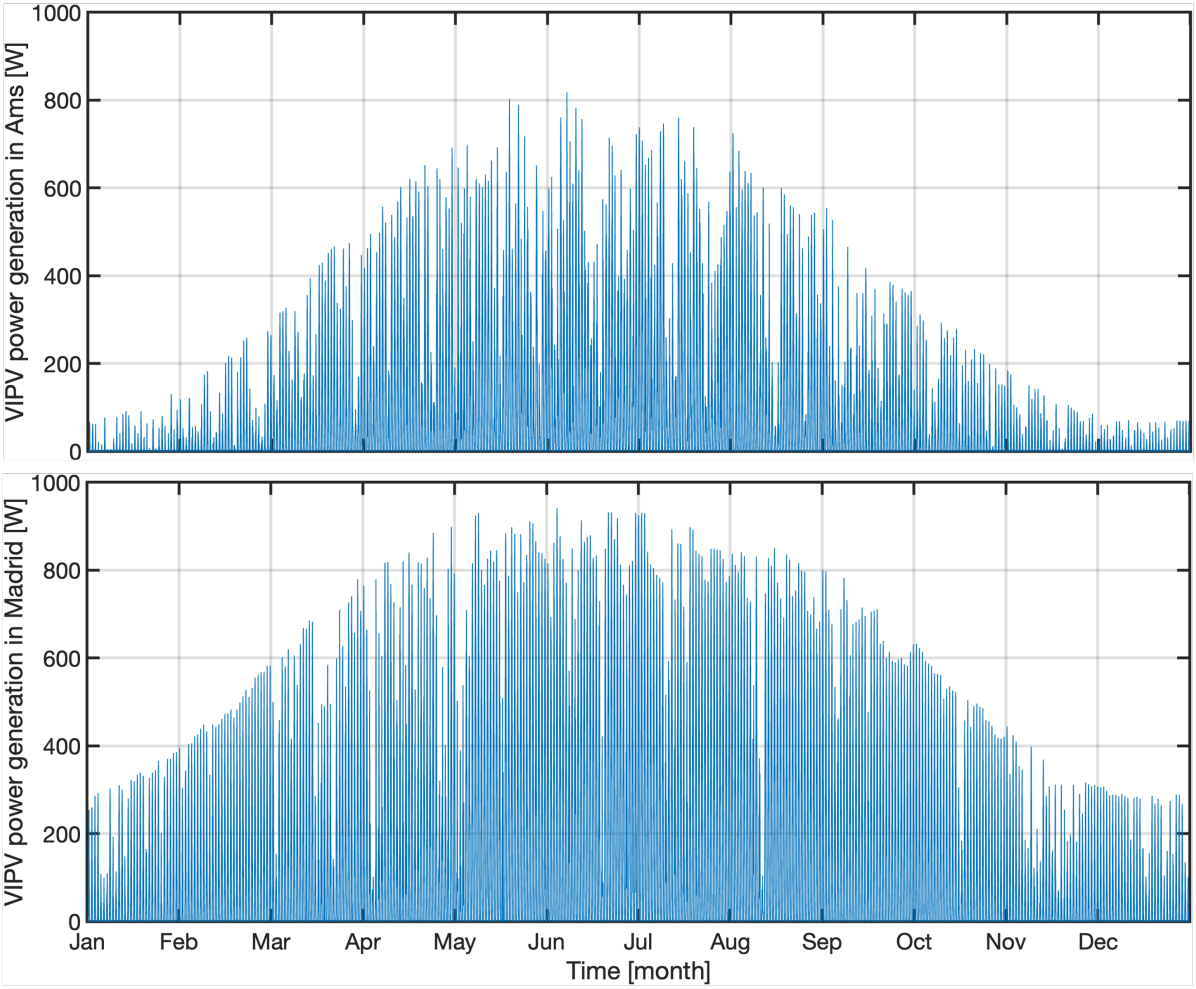

Figure 3.40: The top graph shows the modelled one-year VIPV power generation for the Netherlands and the bottom graph for Spain. Data sourced from Lightyear's SolarSimulator tool.

Annually, 5 m^2 of VIPV can generate 664 kWh of energy in the Netherlands and 1.27 MWh in Spain. In this scenario, 5 m^2 of VIPV would generate 91% more power in Spain compared to the Netherlands due to the difference in solar irradiance.

Modelled one-week VIPV power profiles

The 15-minute VIPV power generation data is consequently interpolated to per second data to fit to the power profile data modelled in Subsection 3.2.5. As an example, the top graph of Figure 3.41 shows the VIPV power generation profile for a week in May in Amsterdam, the Netherlands and the bottom graph for Madrid, Spain.

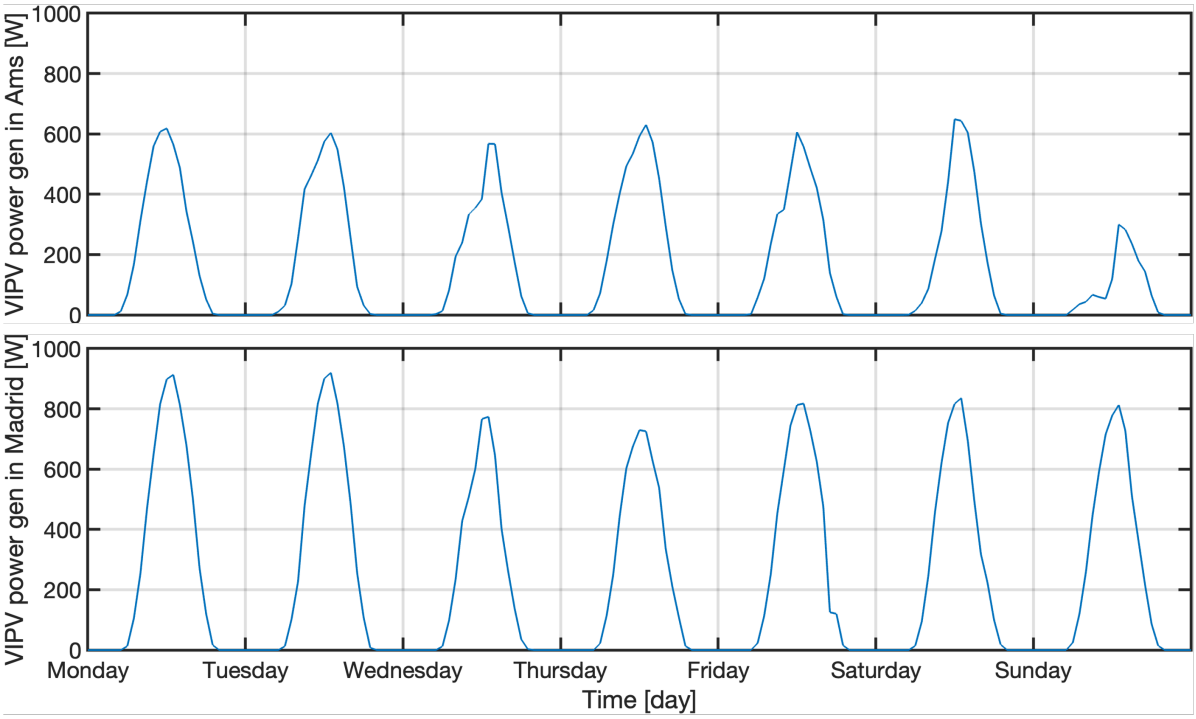

Figure 3.41: The top graph shows the VIPV power generation data for a week May in the Netherlands and the bottom graph for Spain. Data sourced from Lightyear's SolarSimulator tool.

Implementation of the VIPV power profile

The VIPV power generation is consequently applied on the power profile data modelled in Subsection 3.2.5. For illustration purposes, the top and bottom plots of Figure 3.42 show the power and SoC profile of the same week in May, without and with VIPV power generation, respectively. Both plots show the power profile on the left y-axis and the SoC profile on the right y-axis.

The bottom plot of Figure 3.42 shows slight power deviations during the day, which represent power generated by VIPV charging the battery. In comparison, these slight power deviations are absent in the top plot of Figure 3.42 as VIPV power generation is absent. These slight power input values in between the spikes of the power profile correspond to periods at which the EV is assumed to be parked in the sun, mostly during working hours. As a consequence of this VIPV power charging the battery, the red SoC line slightly increases, illustrating how the VIPV power generation provides battery capacity.

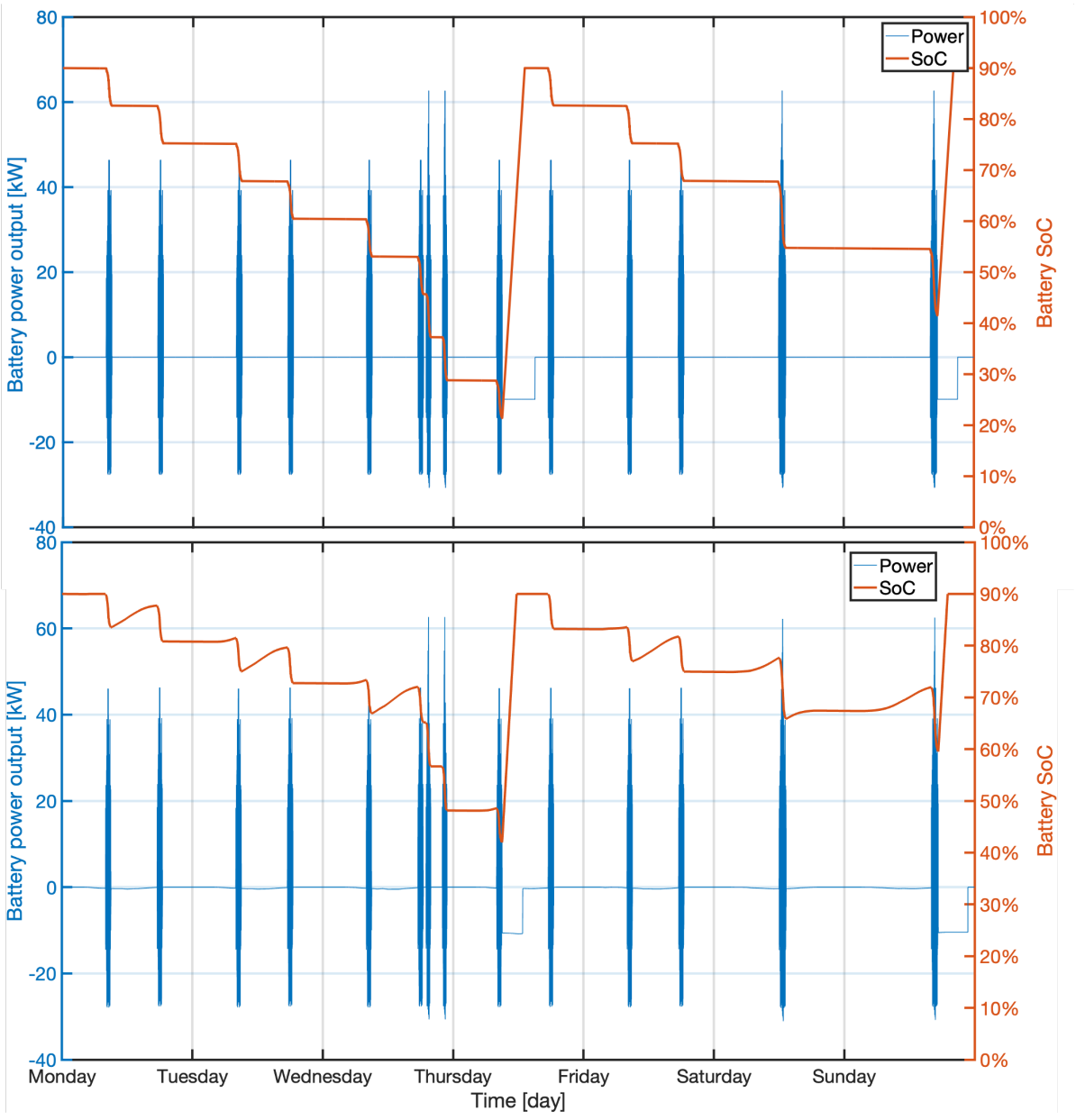

Figure 3.42: The top and bottom plots show the power profile (left y-axis) and SoC profile (right y-axis) for a week in May, without and with VIPV power generation, respectively.

Modelled one-year SoC profiles for the VIPV scenarios

The modelled one-year SoC profile for the VIPV scenario in the Netherlands is shown in Figure 3.43 and for Madrid, Spain in Figure 3.44. The modelled one-year SoC profile for the scenario in which an EV is equipped with VIPV is based in the Netherlands, and participates in V2G day-ahead electricity trading V2G with a battery capacity retention limit of 50% SoC during V2G is shown in Figure 3.45.

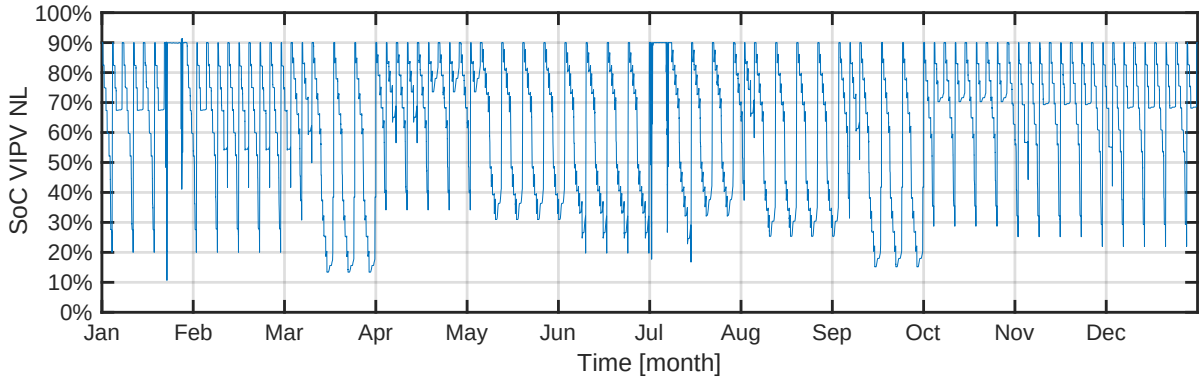

Figure 3.43: Modelled one-year battery SoC profile for an EV with VIPV in the Netherlands.

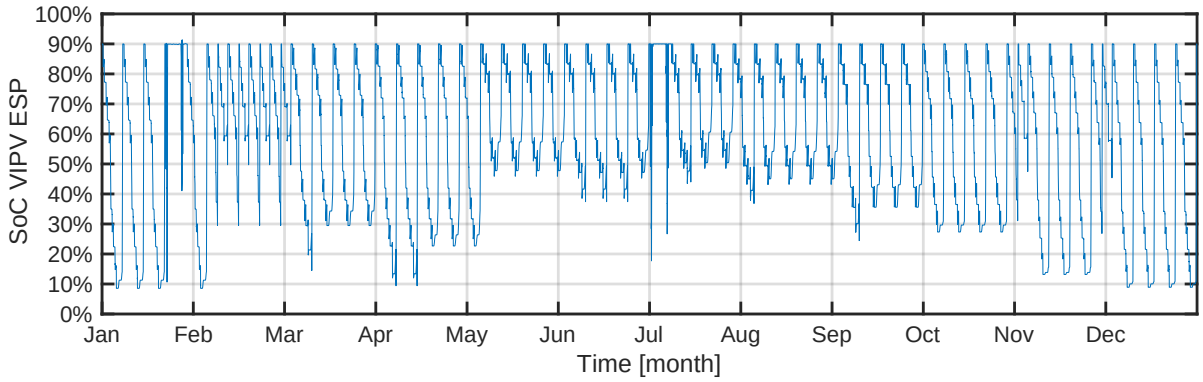

Figure 3.44: Modelled one-year battery SoC profile for an EV with VIPV in Spain.

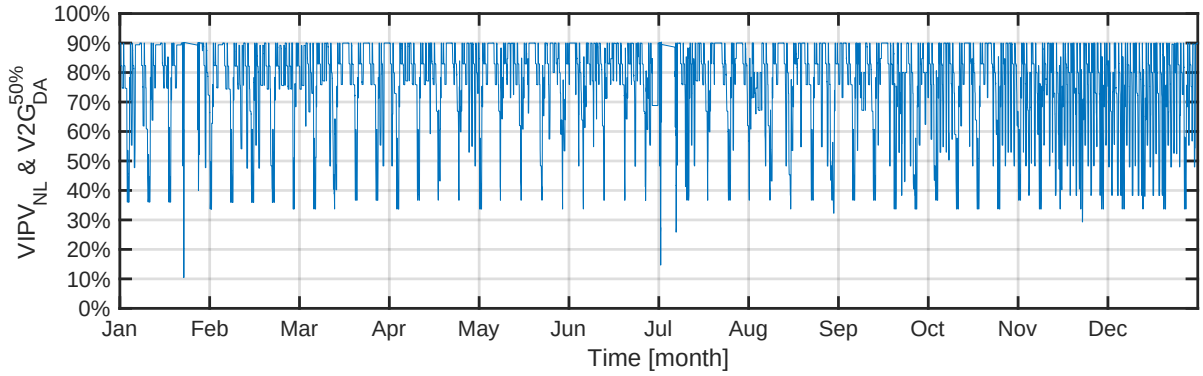

Figure 3.45: Modelled one-year battery SoC profile for an EV with VIPV in the Netherlands, that also participates in V2G day-ahead electricity trading and retains 50% SoC during V2G.

For each month, the VIPV power generation of a single week is taken to simulate the VIPV power generation throughout that month. The following weeks are used to simulate their corresponding months: 16/1 - 23/1; 6/2 - 13/2; 6/3 - 13/3; 3/4 - 10/4; 9/5 - 16/5; 6/6 - 13/6; 4/7 - 11/7; 16/8 - 23/8; 13/9 - 20/9; 11/10 - 18/10; 13/11 - 21/11 and 11/12 - 18/1. Therefore, the modelled VIPV power generation profile slightly varies from the actual VIPV power generation profile.

3.3.3. Impact on grid charging frequency

The top and bottom graphs of Figure 3.46 show the power and SoC profiles for the same week in May, with and without VIPV power generation, respectively. The top graph shows how for this modelled week in May, it takes an extended period of time for the battery to reach lower SoC levels. Thereby, VIPV effectively reduces the number of required grid charging sessions. In the VIPV power profile model, it is assumed that the EV owner will plug in only once a week if VIPV allows them to get through the week without depleting the battery Soc. Compared to the modelled base scenario in the Netherlands, VIPV can reduce the number of grid charging sessions from 102 to 79 per year, corresponding to a 23% decrease in grid charging frequency. Compared to the modelled base scenario in Spain, VIPV can reduce the number of grid charging sessions from 102 to 57 per year, corresponding to a 44% decrease in grid charging frequency.

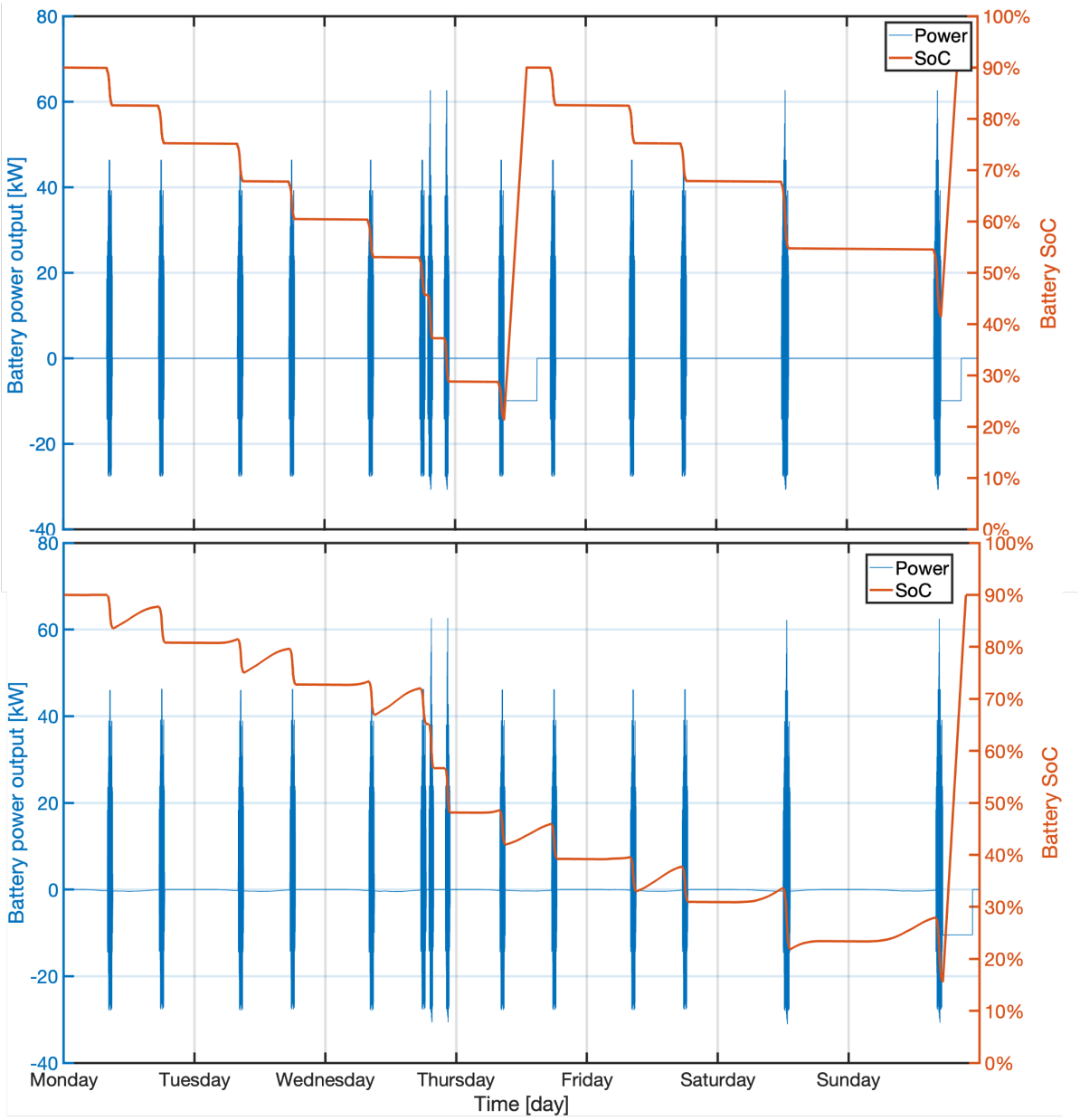

Figure 3.46: Power profile (left y-axis) and SoC (right y-axis) for a week in May, with VIPV power generation but with one charging occasion instead of two.

The average SoC in the top graph of Figure 3.46 is 66%, while the average SoC in the bottom graph is 54%. Thus, it appears that as VIPV reduces the grid charging frequency, VIPV reduces the battery's average SoC.

3.4. V2G modelling

As described in Section 2.4, currently, the most attractive V2G services for EVs participating in the Netherlands appear to be day-ahead electricity trading and aFRR grid balancing. Day-ahead electricity trading is elaborated on in Subsection 3.4.1 and aFRR grid balancing in Subsection 3.4.2. Considering the scope of this work, profits due to V2G are not investigated.

As mentioned in Section 2.1, driving range has long been considered a major barrier to the acceptance of e-mobility. The nature of V2G increases the probability that an EV is (partially) discharged due to V2G. Therefore, it assumed that EVs with V2G capabilities will allow EV owners to regulate the minimum battery capacity that they would like to retain during V2G. To determine its effect on battery ageing, the minimum battery capacity retention limit is set to 50% SoC and 20% SoC, where a 20% SoC retention limit would allow for more battery capacity during V2G services. Moreover, in the V2G use case scenarios, it is assumed that the EV connects to a charging point as soon as it is parked to perform V2G services, except during the summer and winter trips.

3.4.1. Day-ahead electricity trading

The mixed-integer linear programming objective function described in Equations 3.11 - 3.21 determines the energy supply and demand for V2G day-ahead electricity trading.

Day-ahead electricity trading model

Objective function

$$\text{minimise} \sum_{t}^{\tau} \epsilon_{\text{DA,t}} \cdot (P_{\text{charge,t}} - P_{\text{V2G,t}}) \tag{3.11}$$

subject to the following constraints and bounds:

Energy balance

$$E_{\text{stored,1}} = E_{\text{start}} \tag{3.12}$$

$$E_{\text{stored,t}} = E_{\text{start,t-1}} + (P_{\text{charge,t-1}} \cdot \eta_{\text{charge}} - \frac{P_{\text{V2G,t-1}}}{\eta_{\text{charge}}} - P_{\text{drive,t-1}}) \tag{3.13}$$

V2G minimum SoC binary

$$0 \leq P_{\text{V2G,t}} \leq P_{\text{max, V2G}} \cdot B_{\text{V2G, t}} \tag{3.14}$$

$$B_{\text{V2G, t}} \leq \frac{E_{\text{stored,t}} - 0.5 \cdot E_{\text{bat,max}}}{0.5 \cdot E_{bat,max}} + 1 \tag{3.15}$$

Connection requirement

$$P_{\text{charge,t}} = 0 \quad \forall \ t \in \mathbf{T}_{\text{disconnected}} \tag{3.16}$$

$$P_{\text{V2G,t}} = 0 \quad \forall \ t \in \mathbf{T}_{\text{disconnected}} \tag{3.17}$$

Energy requirement

$$E_{\text{stored,t}} \geq E_{\text{required}} \ \forall \ t \in \mathbf{T}_{\text{required}} \tag{3.18}$$

Non-negativity and maximum values

$$0 \leq P_{\text{charge,t}} \leq P_{\text{charge,max}} \tag{3.19}$$

$$0 \leq E_{\text{stored}} \leq E_{\text{bat,max}} \tag{3.20}$$

$$0 \leq P_{\text{V2G}} \leq P_{\text{V2G, max}} \tag{3.21}$$

where $\epsilon_{\text{DA,t}}$ is the electricity price on the day-ahead market in €/kWh, $P_{\text{charge,t}}$ is the charging power from the grid in kW, $P_{\text{V2G,t}}$ is discharging power to the grid in kW, E_{stored} is energy stored in the EV's battery in kWh, $E_{\text{bat,max}}$ is the maximum energy capacity of the battery in kWh, η_{charge} is the OBC's charging efficiency, $B_{\text{V2G, t}}$ is a binary constraint allowing V2G only if the battery's SoC is above 50%, $\mathbf{T}_{\text{disconnected}}$ is a vector containing times at which the EV is not connected to a charging point, and $\mathbf{T}_{\text{required§}}$ is a vector containing times at which the EV battery is required to have a minimum SoC for the owner to be able to drive off.

Modelled one-year SoC profiles for the V2G day-ahead electricity trading scenarios
The modelled one-year power profile of the base scenario described in Subsection 3.2.5 forms the base for modelling the one-year V2G power profiles. Using this base scenario power profile and the objective function described above, the one-year power and SoC profiles for the V2G day-ahead electricity trading scenarios are modelled. The two V2G profiles are modelled with a 50% and 20% SoC retention limit during V2G services, as described in the introduction of this section. The SoC profile for the V2G day-ahead electricity trading with a 50% SoC retention limit during V2G is shown in Figure 3.47, and with a 20% SoC retention limit in Figure 3.48.

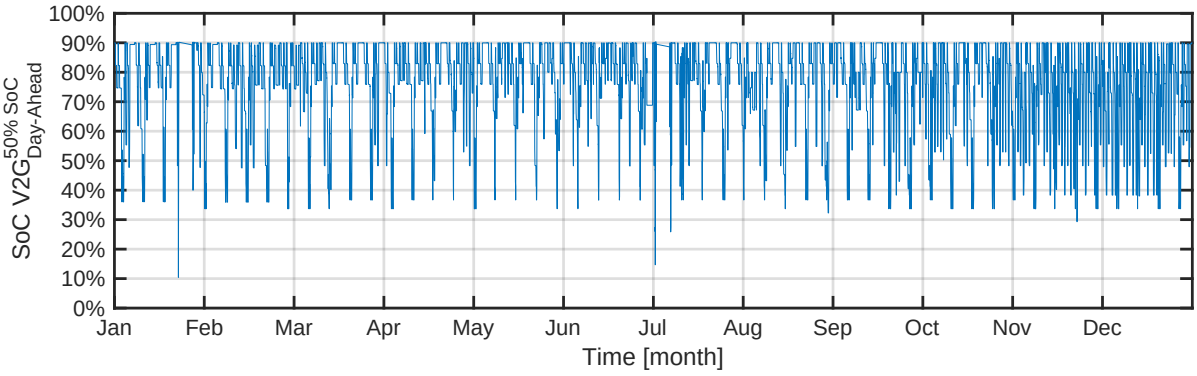

Figure 3.47: Modelled one-year EV battery SoC profile in the $V2G_{Day\text{-}Ahead}$ scenario with 50% SoC retention during V2G services.

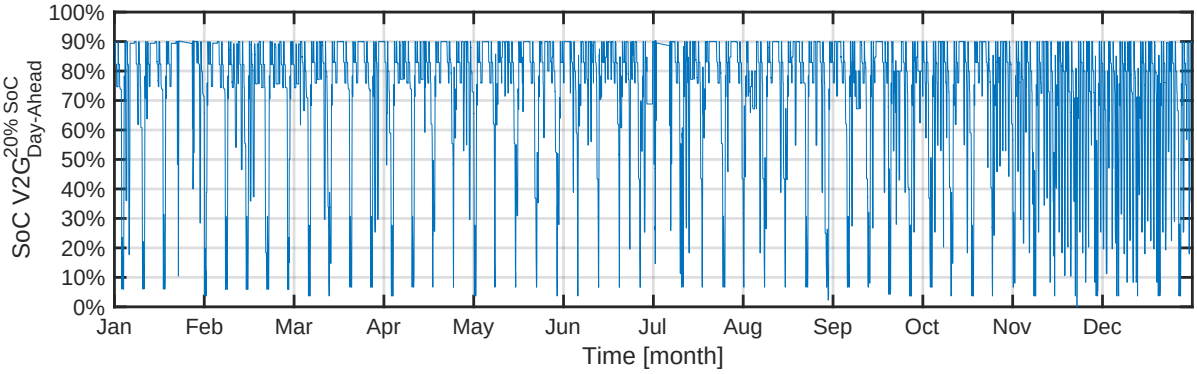

Figure 3.48: Modelled one-year EV battery SoC profile in the $V2G_{Day\text{-}Ahead}$ scenario with 20% SoC retention during V2G services.

3.4.2. aFRR grid balancing

As described in Section 2.4, on the aFRR market, revenue can be generated by counteracting imbalance. Imbalance can be in two directions. There is either too much or too little power fed into the grid. When too little power is fed into the grid, TenneT will activate bids for upwards regulation, or 'regulation state 1', starting at the lowest bid per kWh, to feed more power into the grid. TenneT will consequently pay the activated BSP an imbalance settlement price (ISP) for delivering a certain amount of energy. At the moment that there is an excess of power supply in the grid, or not enough power is demanded, TenneT will activate bids for downward regulation, or 'regulation state -1', starting at the highest bid per kWh, to demand power from the grid at that moment. The activated BSP will demand power from the grid, and pay TenneT the price of the lowest accepted bid within the ISP. If this accepted bid price is negative, TenneT will pay this negative of this negative amount (positive amount) to the BSP.

For an EV, upwards regulation can be provided by stopping grid charging or feeding power into the grid using V2G, with TenneT financially compensating the EV owner for supporting in balancing the grid. For an EV, downward regulation can be provided by charging additional energy. In case the electricity price is positive, the EV owner in this scenario benefits financially by charging with cheap electricity. However, the electricity price can also be negative, meaning that the EV owner will be paid in return for charging from the grid. The mixed-integer linear programming objective function described in Equations 3.22 - 3.25 determines the energy supply and demand for V2G day-ahead electricity trading.

Bid and acceptance model

The model consists of a numerical part which performs several precalculations and a sequential part which tracks the amount of energy delivered, the resulting revenues earned and the current SoC. For each time step the bid down is calculated as:

$$B_{\text{down},\tau} = \max(\epsilon_{\text{aFRR,t}}, 0) \tag{3.22}$$

where B_{down} is the bid placed for downward regulation. If accepted, a positive B_{down} will be a payment from the BSP to the TSO. The lowest bid to be placed is set at 0, which corresponds to free charging.

$$B_{\text{up},\tau} = \epsilon_{\text{aFRR,t}} \tag{3.23}$$

where B_{up} is the bid placed for upward regulation. If accepted, the payment will be from the TSO to the BSP.

Next, the minutes are counted in which a bid of this magnitude is accepted. It should be noted that this is an estimation. However, for computational purposes, the choice is made for this middle ground between the use of 4-second and 15-minute data. Still, in static pre-calculation, the following is performed:

$$A_{\text{down},\tau} = \frac{\Sigma_{\text{t}=\tau}^{\tau+14} B_{\text{down, accept, t}}}{15} \forall \tau \in T \tag{3.24}$$

where $b_{down,\ accept,\ t} = 1$ if and only if $B_{down,\tau} \leq \epsilon_{aFRR,\ down,\ t}$. Here, t enumerates the minutes and τ enumerates the 15-minute ISPs to avoid confusion. This results in that $A_{down,\tau}$ will have a value between 0 and 1. This is used to estimate the activated power of the aFRR per ISP.

The sequential part considers the EV's relevant parameters. It tracks the battery SoC to ensure that the aFRR can be provided in the required direction at each time step, without going under or over the desired SoC limits and based on the charging time availability. Just like in the DA model:

$$E_{\text{stored,t}} = E_{\text{start,t-1}} + (P_{\text{charge,t-1}} \cdot \eta_{\text{charge}} - \frac{P_{\text{V2G,t-1}}}{\eta_{\text{charge}}} - P_{\text{drive,t-1}}) \tag{3.25}$$

Modelled one-year SoC profiles for the V2G aFRR scenarios

The SoC profiles for V2G aFRR with 50% SoC and 20% retention are shown in Figure 3.49 and 3.50, respectively.

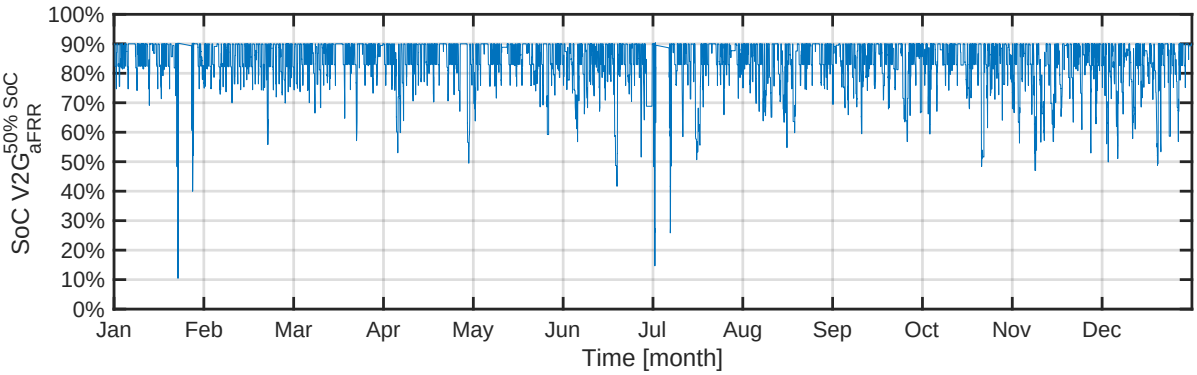

Figure 3.49: Modelled one-year EV battery SoC profile in the $V2G_{aFRR}$ scenario with 50% SoC retention during V2G services.

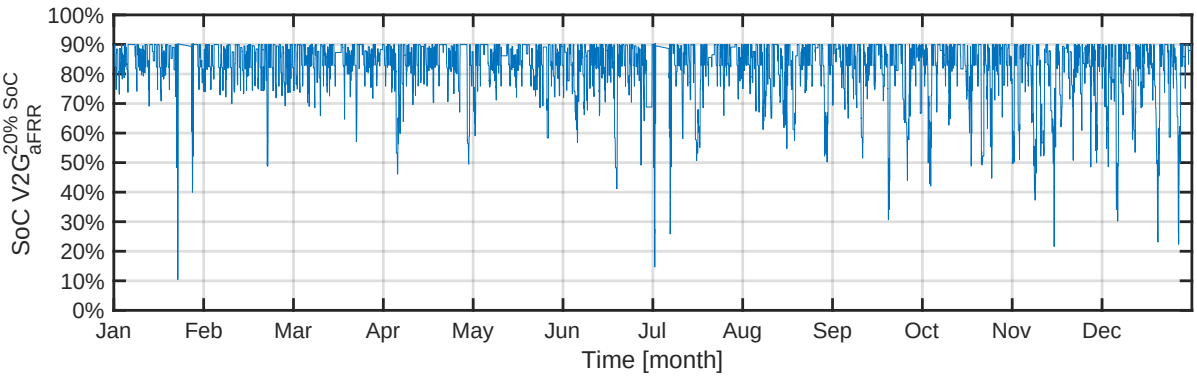

Figure 3.50: Modelled one-year EV battery SoC profile in the $V2G_{aFRR}$ scenario with 20% SoC retention during V2G services.

3.5. Validation of the EV battery data generation model

As described in Section 3.2, Lightyear's VPM is used to simulate driving profiles. The VPM generates a power profile which is sampled per second. This power profile forms the basis for modelling the rest of the battery ageing stress factors. These ageing stress factors, namely the battery's SoC, voltage, current, C-rate, throughput, and temperature are modelled using the EV battery data generation model. To validate the EV battery data generation model, its accuracy is determined by simulating a driving cycle and comparing the modelled battery's SoC, voltage, and current data with data sourced directly from the VPM. It should be noted that the modelled profiles are indirectly derived from the power profile. Validation of the EV battery data generation model on vehicle-level could further validate the accuracy of the data.

A commonly used method to determine the error between measured and modelled data is the root mean square error (RMSE), shown in Equation 3.26. The RMSE is a measure of accuracy, where an RMSE of 0 would indicate an identical fit of the measured and modelled data.

$$RMSE = \sqrt{\sum_{i=1}^{n} \frac{(y_i - \hat{y}_i)^2}{n}} \tag{3.26}$$

where y_i is the data from the VPM, $\hat{y}_i$ is the data modelled using the EV battery data generation model, i is a variable, and N is the number of data points.

SoC profile validation

The top graph of Figure 3.51 shows the SoC sourced from the VPM in a solid red line ('measured SoC') and the modelled SoC ('modelled SoC') in a solid blue line. The bottom graph shows the difference between the measured and modelled data in SoC charge percentage. The RMSE for the modelled SoC profile is 0.364, which suggests that the modelled SoC does not accurately follow the data from the VPM. As shown in Figure 3.51, the error appears to increase over time. The increasing error in the modelled SoC is likely because ΔV described in Subsection 3.2.8 is not considered in the SoC profile. Chapter 4 explains how the ageing models mainly use voltage as input, in which the error is resolved.

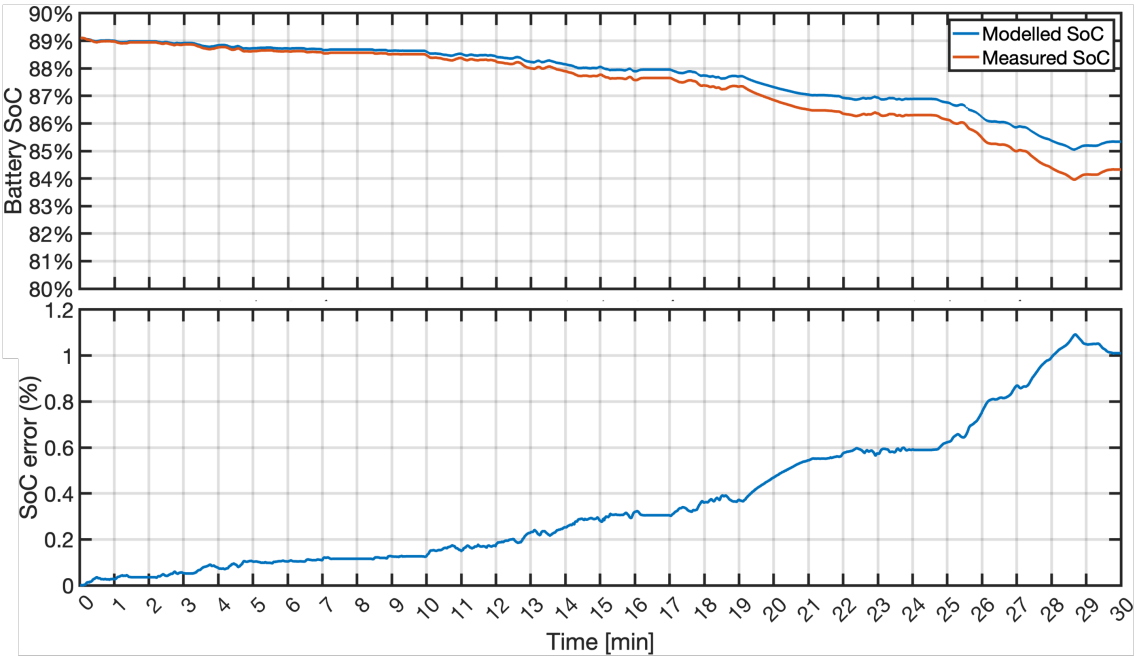

Figure 3.51: SoC profile error analysis for validation of the EV data generation model. The top graph shows the modelled battery SoC in a blue line and the measured VPM battery SoC in a red line. The bottom graph shows the absolute error between the two.

Voltage profile validation

The top graph of Figure 3.52 shows the measured cell voltage in a solid red line and the modelled cell voltage in a solid blue line. The bottom graph shows the difference between the measured and modelled data in voltage. The RMSE for the modelled voltage profile is 0.067, which suggests that the modelled voltage accurately follows the data from the VPM.

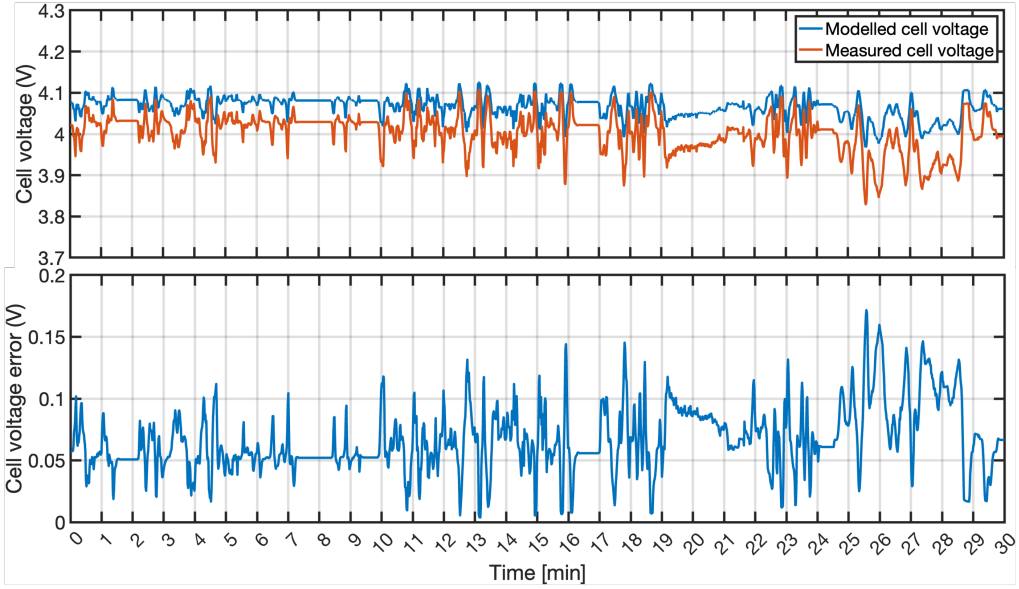

Figure 3.52: Voltage profile error analysis for validation of the EV data generation model. The top graph shows the modelled cell voltage in a blue line and the measured VPM cell voltage in a red line. The bottom graph shows the absolute error between the two.

Current profile validation

The top graph of Figure 3.53 shows the measured cell current in a solid red line and should show the modelled cell voltage in a solid blue line. However, considering the large y-axis range of the graph and that the error is small, the lines appear to superimpose each other, fading away the blue line. Nevertheless, the bottom graph of Figure 3.53 clearly shows the small difference between the measured and modelled data in voltage. The RMSE for the modelled current profile is 0.010, which suggests that the modelled current very accurately follows the data from the VPM.

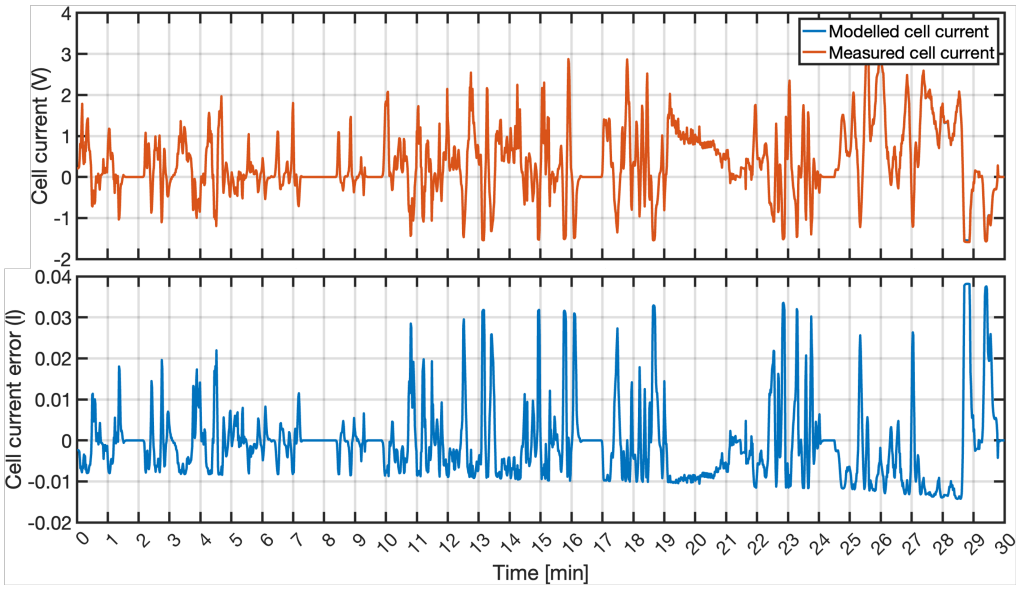

Figure 3.53: Current profile error analysis for validation of the EV data generation model. The top graph shows the modelled cell current in a blue line and the measured VPM cell current in a red line. The bottom graph shows the absolute error between the two.

4

Battery ageing modelling

The following chapter elaborates on EV battery ageing modelling. The reproduction of ageing models from literature allows for ageing analysis on the battery data modelled in the previous chapter. Thus, through the completion of this chapter, the second sub-objective can be addressed:

ii *Implement the EV battery datasets into battery ageing models from literature to quantify battery calendar and cycling ageing for each use case scenario.*

Section 4.1 presents an overview of the three ageing models used in this work to analyse ageing. Following this, Sections 4.2 - 4.4 thoroughly describe the ageing models by summarising the ageing tests on which they were built, depicting their ageing equations, and clarifying how they should be implemented to estimate ageing from battery data. Finally, the ageing models are validated in Section 4.5, which following the structure of this work, addresses the fourth sub-objective:

iv *Validate the ageing models by simulating ageing tests performed to develop the ageing models.*

4.1. Overview of the implemented ageing models

Semi-empirical models based on both NMC and LFP batteries are used to determine the ageing due to calendar and cycling ageing for each use case scenario. An overview of the three implemented semi-empirical ageing models, as well as their characteristics, is shown in Table 4.1. Ref. stands for literature reference, Cal. for calendar ageing, Cyc. for cycling ageing, Q for capacity loss, and R for resistance increase. 'Applicable' refers to whether the ageing model is applicable on battery data.

Table 4.1: Overview of the implemented semi-empirical ageing models for NMC and LFP battery cells.

Chemistry	Authors	Ref.	Cal.	Cyc.	Q	R	Applicable	Stress factors
NMC	Schmalstieg et al. (2014)	[84]	✓	✓	✓	✓	✓	time, V, T, DoD, Ah
NMC	Käbitz et al. (2013)	[45]	✓	X	✓	✓	X	time, T
LFP	Schimpe et al. (2018)	[81]	✓	✓	✓	X	✓	time, SoC, V, T, I, Ah

As shown in the table, the ageing model by Schmalstieg et al. (2014) describes both capacity and power fade due to calendar and cycling ageing, and is applicable on battery data. The ageing model by Käbitz et al. (2013) offers only calendar ageing equations for four constant battery temperatures, limiting its applicability. Therefore, the model is used to benchmark NMC ageing determined by the model of Schmalstieg et al. (2014). The ageing model by Schimpe et al. (2018) describes capacity loss for both calendar and cycling ageing. As the LFP ageing model provides insight into the anode stoichiometry, it enables to transform NMC-based ageing stress factors into LFP-motivated ageing stress factors. Furthermore, considering that Schmalstieg et al. (2014) demonstrate large errors in resistance increase estimations, as well as that Schimpe et al. (2018) neglect resistance increase, in this work, only capacity decrease is considered as a battery EoL criterion.

4.2. NMC ageing model I (NMC-AM)

The first NMC-based semi-empirical ageing model (NMC-AM) was designed by Schmalstieg et al. (2014) from RWTH Aachen. The researchers used accelerated ageing tests to design an ageing model that addresses capacity decrease and resistance increase due to calendar and cycling ageing. The ageing tests were performed using 60 Sanyo UR18650E round Panasonic NMC cells (1:1:1) [68, 104]. These cells have a nominal capacity of 2.15 Ah, a maximum C-rate of 3C and a specific energy of 162 Wh/kg. The Sanyo UR18650E cell, of which its battery sheet can be found in Figure 8 of the appendix, is a high energy and high power battery cell ideal for e-bikes, smaller electrical appliances, and robotics. According to NMC-AM, calendar and cycling ageing can be superpositioned to determine total ageing.

Calendar and cycling ageing tests

Every 50 days, for 500 days, the calendar ageing capacity decrease and internal resistance increase were measured. To verify the Arrhenius dependency, three battery temperatures were researched, namely 35 °C, 40 °C and 50 °C. The authors verified that the Arrhenius equation as presented in Equation 2.1 held for their data by verifying a linear relation between the logarithm of the ageing rate and the inverse of the temperature. The main focus was on the voltage dependency, which was researched by measuring ageing over time at 10 different constant SoC levels and at 50 °C. Each combination was tested with three cells to demonstrate the consistency of the tests. Figure 4.1 shows the mean capacity decrease and resistance increase due to calendar ageing and includes an error bar plot to show the measurement deviations from the different cells. The calendar ageing test data shown in Figure 4.1 suggests that both the capacity decreases and the resistance increases faster when batteries are stored at high SoC values and slower when stored at lower SoC values, which is in line with literature [14, 19, 109].

A total of 22 cycling ageing tests were performed with a constant temperature of 35 °C, a C-rate of 1, a varying DoD and an average SoC. The batteries were cycled up to 12 full cycles per day. As calendar ageing also occurs during cycling ageing, the impact due to calendar ageing has been subtracted from the measured cycling ageing-induced capacity and power fade. Figure 4.2 shows the 'pure' capacity decrease and internal resistance increase due to cycling ageing. The cycling ageing test data shown in Figure 4.2 suggests that both the capacity decreases and the resistance increases more when the batteries are cycled between high SoC values (e.g. 90 - 100%) and low SoC values (e.g. 5 - 15%), and less when they are cycled between average SoC values (e.g. 45 - 55%), showing that SoC also impacts cycling ageing.

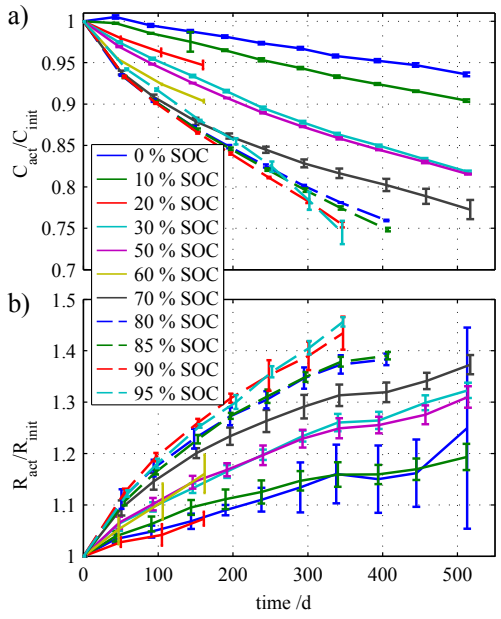

Figure 4.1: Calendar-led ageing: a) normalised capacity decrease and b) normalised internal resistance increase. Graphs show the mean calendar ageing of 3 cells with corresponding error bar plot for tests at 50 °C over 500 days [84].

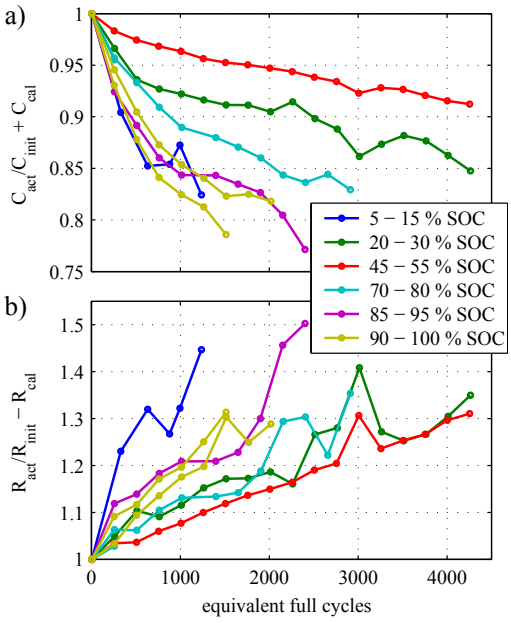

Figure 4.2: Cycling-led ageing: a) normalised capacity decrease and b) normalised internal resistance increase. Both graphs show the cycling ageing per equivalent full cycle for tests with a C-rate of 1 and a DoD of 10% [84].

Fit functions

The researchers determined ageing equations that best describe the ageing process. The ageing equations that define the capacity decrease and resistance increase due to calendar ageing are shown in Equations 4.1 - 4.4. Note that only the capacity loss ageing equations were used.

$$Q_{\mathrm{I}}^{\mathrm{calendar}} = 1 - \alpha_I^{\mathrm{Q}} \cdot t^{0.75} \tag{4.1}$$

$$R_{\mathrm{I}}^{\mathrm{calendar}} = 1 + \alpha_{\mathrm{I}}^{\mathrm{R}} \cdot t^{0.75} \tag{4.2}$$

with

$$\alpha_{\mathrm{I}}^{\mathrm{Q}} = (7.543 \cdot V - 23.75) \cdot 10^6 \cdot \exp\left(-\frac{6,976}{T}\right) \tag{4.3}$$

$$\alpha_{\mathrm{I}}^{\mathrm{R}} = (5.270 \cdot V - 16.32) \cdot 10^5 \cdot \exp\left(-\frac{5,986}{T}\right) \tag{4.4}$$

where t is time in days, T is the absolute temperature of the battery in Kelvin, and V is the voltage of the battery cell. The $t^{0.75}$ term indicates that calendar-led ageing follows an exponential decay over time, which is in line with the slowing growth of the SEI film [102]. As stated in Section 2, the SEI layer is commonly assumed to scale with the square root of time. For this ageing model, however, the researchers concluded that the $t^{0.75}$ factor better follows the trend of the ageing data. Thus, considered calendar ageing stress factors are time, temperature, and voltage. The ageing equations that define the capacity decrease and resistance increase due to cycling ageing are shown in Equations 4.5 - 4.8.

$$Q_{\mathrm{I}}^{\mathrm{cycling}} = 1 - \beta_{\mathrm{I}}^{\mathrm{Q}} \cdot \sqrt{Ah} \tag{4.5}$$

$$R_{\mathrm{I}}^{\mathrm{cycling}} = 1 + \beta_{\mathrm{I}}^{\mathrm{R}} \cdot Ah \tag{4.6}$$

with

$$\beta_{\mathrm{I}}^{\mathrm{Q}} = 8.175 \cdot 10^{-3} \cdot (\text{Ø}V - 3.683)^2 + 7.057 \cdot 10^{-4} + 4.198 \cdot 10^{-5} \cdot \Delta DoD \tag{4.7}$$

$$\beta_{\mathrm{I}}^{\mathrm{R}} = 2.673 \cdot 10^{-4} \cdot (\text{Ø}V - 3.741)^2 - 1.900 \cdot 10^{-5} + 2.837 \cdot 10^{-6} \cdot \Delta DoD \tag{4.8}$$

where $\text{Ø}V$ describes the dependency on the root mean square voltage of the cycle and ΔDoD describes the cycle depth. The $\sqrt{\mathrm{Ah}}$ term of Equation 4.5 indicates that cycling ageing capacity loss decreases with throughput or number of cycles. The $\sqrt{\mathrm{Ah}}$ term of Equation 4.6 indicates that cycling ageing resistance increases linearly with the number of cycles. Thus, considered cycling ageing stress factors are voltage, DoD, and throughput.

In 2014, shortly after the publication of the paper by Schmalstieg et al. (2013), Elsevier published a similar paper by the same authors. In the new publication, the authors seemingly revised Equations 4.7 and 4.8 [84]. Equations 4.9 and 4.10 below show the revised equations described in the paper.

$$\beta_{\mathrm{I,\,rev.}}^{\mathrm{Q}} = 7.348 \cdot 10^{-3} \cdot (\text{Ø}V - 3.667)^2 + 7.600 \cdot 10^{-4} + 4.081 \cdot 10^{-3} \cdot \Delta DoD \tag{4.9}$$

$$\beta_{\mathrm{I,\,rev}}^{\mathrm{R}} = 2.153 \cdot 10^{-4} \cdot (\text{Ø}V - 3.725)^2 - 1.521 \cdot 10^{-5} + 2.798 \cdot 10^{-4} \cdot \Delta DoD \tag{4.10}$$

The superposition of the calendar and cycling result in two ageing equations that holistically describe capacity decrease and resistance increase, namely Equations 4.11 and 4.12, respectively.

$$Q_{\mathrm{I}}^{\mathrm{total}} = 1 - \alpha_{\mathrm{I}}^{\mathrm{Q}} \cdot t^{0.75} - \beta_{\mathrm{I,\,rev}}^{\mathrm{Q}} \cdot \sqrt{Ah} \tag{4.11}$$

$$R_{\mathrm{I}}^{\mathrm{total}} = 1 + \alpha_{\mathrm{I}}^{\mathrm{R}} \cdot t^{0.75} + \beta_{\mathrm{I,\,rev}}^{\mathrm{R}} \cdot Ah \tag{4.12}$$

where again t is time in days and Ah is the throughput delivered.

Implementation

The model was implemented according to the explanation in the paper, supported by the flow chart shown in Figure 4.4. As the ageing process is iterative, they should work in a loop, as shown in the graphical representation of the model in Figure 4.3. Thereby, capacity and power fade after each time step are considered in the next time step. In the implementation by the author of this study, the capacity decrease and resistance increase are not looped back into the model, which can lead to ageing estimations. The model uses a load profile and a temperature profile as input. Together with the impedance parameters of the cell, the load profile and temperature profile form an electric-thermal model. Hildenbrand mentioned to use Matlab's built-in rainflow cycle counting algorithm to count cycles from the load profile. As mentioned in Subsection 3.2.11, the rainflow cycle counting algorithm has been found to inaccurately determine the start and end of each cycle, but proved useful for determining the cell throughput over multiple cycles. Hildenbrand mentioned that as the capacity and resistance measurements for the cycling battery ageing tests were performed on a multiple-day basis, the NMC-AM is not specifically designed for applications that determine ageing on a small timescale. Therefore, smaller cycles could aggregated into larger cycles. According to Hildenbrand, the results of the rainflow cycle counting algorithm appear to be accurate enough. The electric-thermal model calculates the values of the ageing stress factors such as cycle depth and average SoC, which is calculated only during current flow and neglects rest periods. The stress factors are derived using the flow chart shown in Figure 4.4.

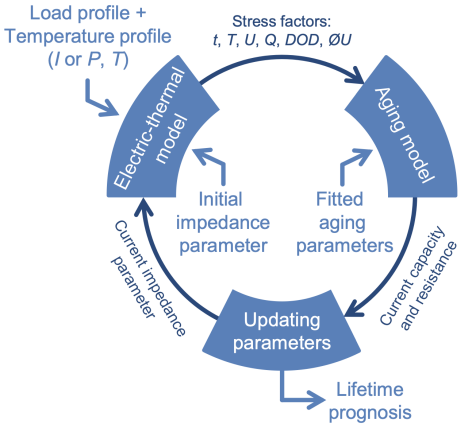

Figure 4.3: Graphical overview of the ageing model. Inputs are load and temperature profile and output is the lifetime prognosis [84].

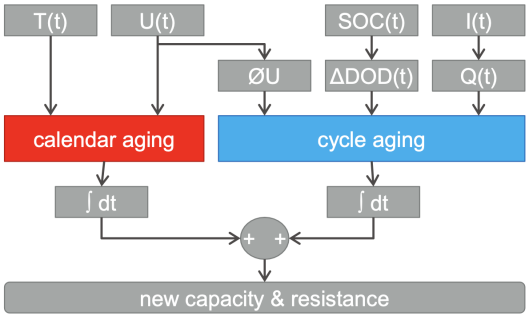

Figure 4.4: Flow chart illustrating the process of deriving the ageing stress factors for the ageing model. Inputs are stress factors and outputs are capacity and power fade [84].

NMC-AM inputs the ageing stress factors into the ageing equations of Equations 4.7 - 4.12 to determine the capacity decrease and resistance increase.

In the implementation of this work, calendar ageing capacity loss is determined by scaling up modelled per-second data to per-day data, and subsequently accumulating the calendar ageing capacity loss over time. Cycling ageing capacity loss is determined per partial cycle, after which the capacity loss caused by all the partial cycles is summed. Cycling ageing capacity loss is determined per partial cycle and accumulated over charge throughput cycles and total throughput cycles according to Equation 4.11.

Equations 4.7 shows that the capacity loss follows an exponential decay over time, which is considered through linearisation of the ageing equations over time. Furthermore, the capacity decrease and resistance increase are not looped back into the model, which may lead to ageing estimations.

Surprisingly, the cycling equations NMC-AM only correlate temperature with calendar ageing, while literature suggests that increased temperatures also impact cycling ageing. Schmalstieg et al. (2014) assumed that there is little to no temperature dependency on cycling ageing, which they validated using verification tests with irregular load profiles.

4.3. NMC ageing model II (NMC-AMII)

The second semi-empirical NMC ageing model (NMC-AMII was designed by Käbitz et al. (2013), also from RWTH Aachen. The researchers performed accelerated calendar and cycling ageing tests to independently analyse capacity decrease and resistance increase due to calendar and cycling ageing. The accelerated ageing tests were performed using a high-energy NMC (1:1:1) pouch cell with a nominal capacity of 10 Ah and a nominal voltage of 3.6 V.

Calendar and cycling ageing tests

The calendar ageing tests were performed over a course of 450 days and at four different temperatures, namely 25 °C, 40 °C, 50 °C, and 60 °C. All calendar ageing tests were performed at an SoC of 50%, corresponding to a voltage of 3.72 V. The voltage was kept constant using a power supply unit. The authors found the voltage dependency on calendar ageing between 50% and 90% to be quite small, while 20% SoC showed to be beneficial for battery life. Thus, considered calendar ageing stress factors are time and temperature.

The cycling ageing tests were performed to analyse the impact of various mean SoC values and temperature on ageing. Although cycling ageing tests were performed, the researchers only derived a regression function to describe calendar ageing.

Fit function

The ageing equation for capacity decrease due to calendar ageing is shown in Equation 4.13.

$$Q_{\text{calendar}} = 1 - \alpha_{\text{II}} \cdot \sqrt{t} \tag{4.13}$$

with $\alpha_{\text{II}} = 0.0017$ for T = 25 °C, $\alpha_{\text{II}} = 0.0038$ for T = 40 °C, $\alpha_{\text{II}} = 0.0061$ for T = 50 °C, and $\alpha_{\text{II}} = 0.0109$ for T = 60 °C. t corresponds to time in days. The authors expected SEI formation on the anode to mainly cause calendar ageing capacity loss, following a square root of time ageing pattern.

Unfortunately, no ageing equations for cycling ageing were derived by Käbitz et al. (2013).

Implementation

Only the calendar ageing capacity loss over time for four different constant battery temperatures can be determined using this 'ageing model'. Thus, NMC-AMII is not applicable to EV data. Nevertheless, the results of NMC-AMII can be used to benchmark the calendar ageing capacity loss results determined by NMC-AM, as elaborated on in Subsection 4.5.2.

4.4. LFP ageing model (LFP-AM)

The LFP-based semi-empirical ageing model (LFP-AM) was designed by Schimpe et al. (2018). The researchers performed accelerated ageing tests over a period of 234 days to analyse the capacity decrease due to calendar and cycling ageing. The ageing tests were performed on commercial cylindrical 26650-format Sony US26650FTC1 LFP cells. The Sony US26650FTC1 LFP cell has a nominal capacity of 3.0 Ah, a nominal voltage of 3.2 V, and is designed for stationary applications.

Calendar and cycling ageing tests

The calendar ageing tests were performed at 10 °C, 15 °C, 25 °C, 35 °C, and 55 °C, and were tested at a variety of SoC values, ranging from 0% to 100% in steps of 12.5%. Thus, considered calendar ageing stress factors were time, temperature, and voltage.

The cycling ageing tests were performed at 0 °C, 10 °C, 15 °C, 25 °C, 35 °C, and 55 °C, and were based on constant current (CC) full cycle tests at C-rates of 0.25C, 0.5C, and 1C, with and without constant voltage (CV) phases at the end of charging. Thus, considered cycling ageing stress factors are temperature, current and SoC.

Open-circuit anode potential

LFP-AM was used in this work as it provides insight into the anode stoichiometry on which the model is based, from which the anode open-circuit potential can be determined. This is elaborated on in the subsection below.

The anode stoichiometry is calculated as a function of SoC through linear interpolation between 0% and 100% SoC, as shown in Equation 4.14.

$$x_{\mathrm{a}}(SoC) = x_{\mathrm{a}}(SoC = 0\%) + SoC \cdot [x_{\mathrm{a}}(SoC = 100\%) - x_{\mathrm{a}}(SoC = 0\%)] \tag{4.14}$$

where the degree of lithiation at 0% SoC and 100% SoC is derived by fitting the half-cell open circuit potentials of both electrodes (Anode Li-C and cathode $LiFePO_4$) to full-cell open circuit potential data.

The anode stoichiometry is subsequently used to determine the open circuit potential of the anode, as shown in Equation 4.15.

$$\begin{aligned} U_{\mathrm{a}}(x_{\mathrm{a}}) = {} & 0.6379 + 0.5416 \cdot \exp(-305.5309 \cdot x_{\mathrm{a}}) + 0.044 \cdot tanh\left(-\frac{x_{\mathrm{a}} - 0.1958}{0.1088}\right) \\ & - 0.1978 \cdot tanh\left(\frac{x_{\mathrm{a}} - 1.0571}{0.0854}\right) - 0.6875 \cdot tanh\left(\frac{x_{\mathrm{a}} + 0.0117}{0.0529}\right) - 0.0175 \cdot tanh\left(\frac{x_{\mathrm{a}} - 0.5692}{0.0875}\right) \end{aligned} \tag{4.15}$$

where U_{a} is the anode open circuit potential, and x_{a} is the degree of lithiation, taken from Safari and Delacourt (2011).

Fit functions

The ageing equation that determines the capacity decrease due to calendar ageing are described in Equations 4.16 and 4.17.

$$Q_{\mathrm{III}}^{\mathrm{calendar}} = k_{\mathrm{cal}} \cdot \sqrt{t} \tag{4.16}$$

where k_{cal} is determined using

$$k_{\mathrm{cal}} = k_{\mathrm{cal,\,ref}} \cdot \exp\left[\frac{-E_{\mathrm{a,\,cal}}}{R_{\mathrm{g}}}\left(\frac{1}{T} - \frac{1}{T_{\mathrm{ref}}}\right)\right] \cdot \left(\exp\left[\frac{\alpha \cdot F}{R_{\mathrm{g}}}\left(\frac{U_{\mathrm{a,\,ref}} - U_{\mathrm{a}}(SoC)}{T_{\mathrm{ref}}}\right)\right] + k_0\right), \tag{4.17}$$

where $k_{cal,\,ref}$ is the calendar reference stress factor which equals $3.694 \cdot 10^{-4}$ $h^{-0.5}$, $E_{a,\,cal}$ is the activation energy parameter which equals 20592 J/mol, T_{ref} is the reference temperature which equals 298.15 K, R_g is the universal gas constant which equals 8.314 J/(mol K), F is the Faraday constant which equals 96,485 C/mol, $U_{a,\,ref}$ is the reference potential set at $U_{a,}$(SoC = 50%) = 0.123 V, T is the battery temperature in Kelvin, and α and k_0 are fitting parameters set at 0.384 and 0.142, respectively.

In this ageing model, a distinction is made between cycling ageing effects that occur at low and high temperatures. The high temperature cycling ageing mechanism is assumed to occur both during charging and discharging and thus independently of the current direction. In contrast, the low temperature induced cycling ageing mechanism is assumed to occur only during charging. The researchers therefore distinguish charge throughput and total throughput defined as the sum of charge and discharge throughput. The ageing equations that define the capacity decrease due to cycling ageing are described in Equations 4.18 - 4.24. As

shown in Equation 4.18, the capacity loss due to cycling ageing is consists of three sub-equations. Equation 4.19 describes cycling ageing at high temperatures, Equation 4.20 describes cycling ageing at low temperatures and SoC values beneath 83%, and Equation 4.21 describes cycling ageing at low temperatures and SoC values above 83%. The reference parameters used in these equations are calculated using Equations 4.20 - 4.24.

$$Q_{\text{III}}^{\text{cycling}} = Q_{\text{high T}}^{\text{cycling}} + Q_{\text{low T, SoC<83\%}}^{\text{cycling}} + Q_{\text{low T, SoC>83\%}}^{\text{cycling}} \tag{4.18}$$

with

$$Q_{\text{high T}}^{\text{cycling}} = k_{\text{cyc, high T}} \cdot \sqrt{Ah_{\text{total}}} \tag{4.19}$$

$$Q_{\text{low T, SoC<83\%}}^{\text{cycling}} = k_{\text{cyc, low T, SoC<83\%}} \cdot \sqrt{Ah_{\text{charge}}} \tag{4.20}$$

$$Q_{\text{low T, SoC>83\%}}^{\text{cycling}} = k_{\text{cyc, low T, SoC>83\%}} \cdot Ah_{\text{charge}} \tag{4.21}$$

with

$$k_{\text{cyc, high T}} = k_{\text{cyc, high T, ref}} \cdot \exp\left[\frac{-E_{\text{a, cyc, high T}}}{R_{\text{g}}}\left(\frac{1}{T} - \frac{1}{T_{\text{ref}}}\right)\right] \tag{4.22}$$

$$k_{\text{cyc, low T, SoC<83\%}} = k_{\text{cyc, low T, SoC<83\%, ref}} \cdot \exp\left[\frac{-E_{\text{a, cyc, low T}}}{R_{\text{g}}}\left(\frac{1}{T} - \frac{1}{T_{\text{ref}}}\right)\right] \tag{4.23}$$

$$\begin{aligned} k_{\text{cyc, low T, SoC>83\%}} = {} & k_{\text{cyc, low T, SoC>83\%, ref}} \cdot \exp\left[\frac{-E_{\text{a, cyc, low T, SoC>83\%}}}{R_{\text{g}}}\left(\frac{1}{T} - \frac{1}{T_{\text{ref}}}\right)\right] \\ & \cdot \exp\left[\beta_{\text{cyc, low T, SoC>83\%}} \cdot \frac{I_{\text{charge}} - I_{\text{charge, ref}}}{C_0}\right] \cdot \left(\frac{sgn(SoC - SoC_{\text{ref}}) + 1}{2}\right) \end{aligned} \tag{4.24}$$

where k_{ref} are reference parameters set at T_{ref} = 298.15 K, with values $k_{\text{cyc, high T, ref}} = 1.456 \cdot 10^{-4} \cdot Ah^{-0.5}$, $k_{\text{cyc, low T, SoC<83\%, ref}} = 4.009 \cdot 10^{-4} \cdot Ah^{-0.5}$, and $k_{\text{cyc, low T, SoC>83\%, ref}} = 2.031 \cdot 10^{-6} \cdot Ah^{-1}$. The temperature dependence is implemented through the Arrhenius equation where $E_{\text{a, cyc, high T}}$ = 32,699 J/mol, $E_{\text{a, cyc, low T, SoC<83\%}}$ = 55,546 J/mol, and $E_{\text{a, cyc, low T, SoC>83\%}} = 2.3 \cdot 10^5$ J/mol. Furthermore, $I_{\text{charge, ref}}$ = 3 A, $\beta_{\text{cyc, low T, SoC>83\%}}$ = 7.8 h, and SoC_{ref} = 82%. Due to its sign function (*sgn*), Equation 4.23 is only included when the SoC exceeds 82%.

Limitation

The anode stoichiometry given by Safari and Delacourt (2011) and used by Käbitz et al. (2013) to develop the model describes the relation between SoC and the degree of lithiation of the LFP anode. The LFP anode stoichiometry is used to derive the anode open circuit voltage (U_{a}) from the NMC-based SoC profile modelled in Subsection 3.2.6. As this SoC profile originates from NMC-based simulations of the VPM, essentially, the derived U_{a} is NMC-motivated. Furthermore, no relation is given on the LFP's V_{OC}(SoC) curve shown in Figure 8.11 of the appendix. Therefore, the other ageing stress factors used in Equations 4.19 - 4.24 could not be derived from the LFP's open-circuit potential, and thus remain NMC-based. Consequently, the cycling ageing equations of the LFP model use the NMC-based ageing stress factors to estimate cycling ageing, which limits LFP-AM's applicability. Ideally, Lightyear's VPM with an LFP battery would simulate the same power profile to generate LFP-based ageing stress factors, which could be implemented in this ageing model to improve the ageing estimations. Nevertheless, the ageing model is implemented in this work as it is assumed that useful comparisons can be made from NMC-motivated LFP-AM ageing results.

Implementation

The implementation of LFP-AM follows a similar implementation as NMC-AM. The calendar ageing capacity loss is determined by scaling up modelled per-second data to per-hour data, and subsequently accumulating the calendar ageing capacity loss over time. Cycling ageing capacity loss is determined per partial cycle and accumulated over charge throughput cycles and total throughput cycles according to Equation 4.18. The researchers assumed that calendar ageing at a storage temperature of 0 °C would be negligible, which is remarkable considering that the authors demonstrated 3.6% calendar ageing at 10 °C after 200 days and a significant cycling ageing capacity loss during cycling at 10 °C.

4.5. Validation of the implemented ageing models

The following section presents the methods and results for the validation of the ageing models. In Subsection 4.5.1, the implementation of NMC-AM is validated by simulating the validation tests performed by Schmalstieg et al. and comparing modelled results with measurements of the validation tests. Following this, Subsection 4.5.1 compared Lightyear's NMC calendar ageing tests with modelled calendar ageing results from NMC-AM. Moreover, Subsection 4.5.2 compares ageing results from NMC-AM with ageing results from NMC-AMII. Finally, in Subsection 4.5.3, the implementation of LFP-AM is validated by simulating the ageing tests performed by Schimpe et al. (2018) and comparing modelled results with measurements of the ageing tests.

4.5.1. NMC-AM validation

To validate the implementation of NMC-AM by Schmalstieg et al. (2014), the validation test performed by the authors are simulated and modelled ageing results are compared with measurements taken during their validation tests.

Validation tests performed by Schmalstieg et al. (2014)

Schmalstieg et al. validated their ageing model using the following method. First, the authors repeatedly applied a 30-minute semi-irregular load profile on an NMC battery at different ambient temperatures to imitate real driving behaviour of an EV battery. Subsequently, the authors measured the capacity decrease and resistance increase during these validation tests. Following this, the authors implemented the same load profile in their ageing model (NMC-AM). Finally, the authors compared the ageing measurements with the results from NMC-AM. The semi-irregular load profile, which included both city and highway driving, was taken from EV measurements in Aachen, Germany, and was scaled down to match the specifications of a single battery cell.

The top graph of Figure 4.5 shows the 30-minute load profile and the bottom graph shows a 24-hour load profile. The 24-hour load profile consists of two of the 30-minute load profiles, each one followed by grid charging to 100% SoC. Note that the sign convention for the load profile is different than in Section 3.2. Here, positive battery power values correspond to battery power input.

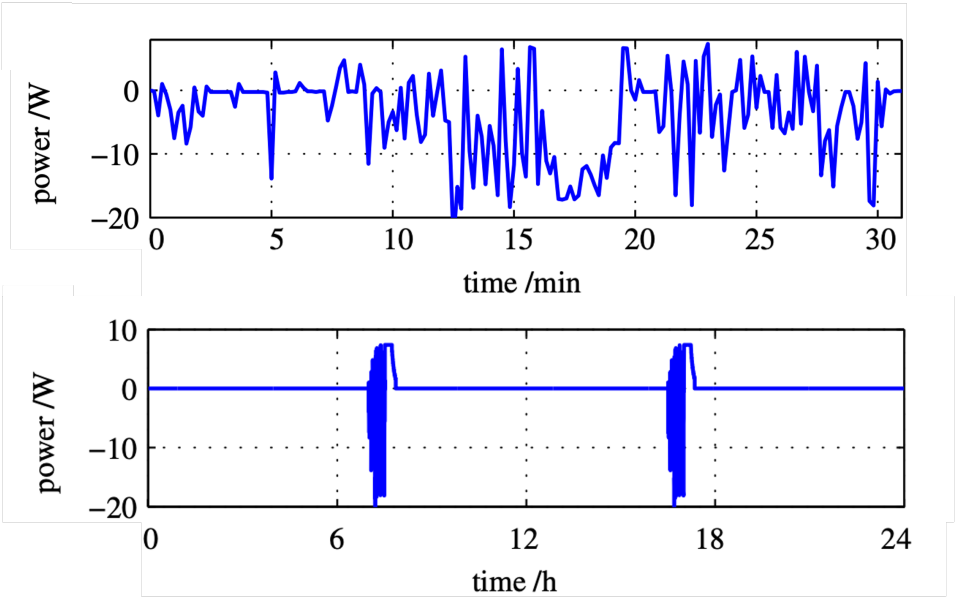

Figure 4.5: 30-minute and 24-hour load profiles of the ageing model verification tests by Schmalstieg et al. (2014) [84].

Simulation of validation tests

To simulate the ageing modelling tests performed by Schmalstieg et al., these load profiles are reproduced using WebPlotDigitizer [108]. Figure 4.6 illustrates this process. The three graphs on the left illustrate the process for the 30-minute load profiles and the three graphs on the right illustrate the process for the 24-hour load profiles. The top graphs are the validation profiles from the ageing model paper [84], the graphs between the top and bottom illustrate the dataset extraction process by WebPlotDigitizer, and the bottom graphs show the reproduced profiles simulated in Matlab.

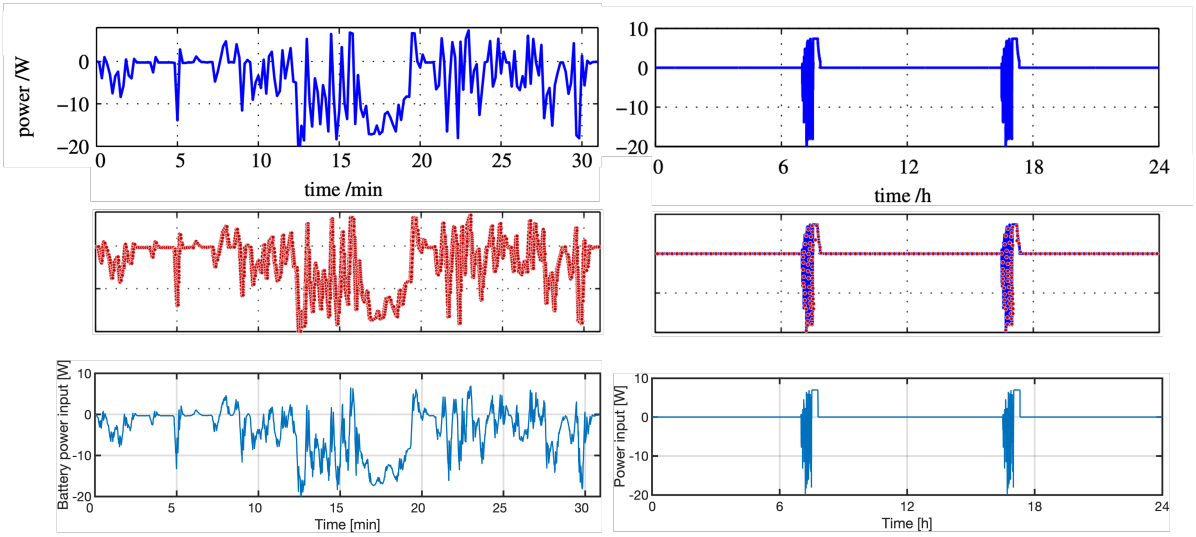

Figure 4.6: Reproduction of 30-minute and 24-hour load profiles used by Schmalstieg et al. (2014) to validate their ageing model. The top graphs show the model validation plots by Schmalstieg et al. (2014), the middle graphs show the dataset reproduction by WebPlotDigitizer, and the bottom graphs show the reproduced graphs.

From top to bottom, the left graphs of Figure 4.7 show the load profile, corresponding SoC profile, and voltage profiles. The three graphs on the right show how the EV data generation model reproduces the profiles. Slight deviations are seen in the voltage profile, but overall the profiles seem alike.

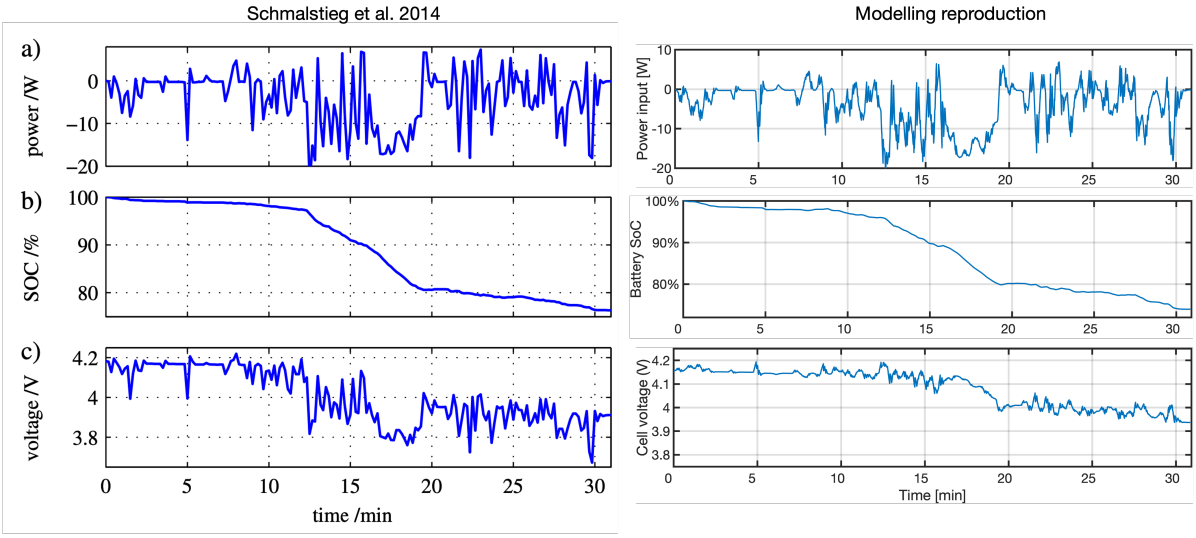

Figure 4.7: Comparison of the reproduced power, SoC, and temperature profiles and the original profiles used by Schmalstieg et al. (2014) to validate their own ageing model.

The 24-hour load profile is repeated on a daily basis throughout seven months, with varying battery temperatures based on average ambient temperatures from 2001-2010 in Germany. The varying ambient temperature is modelled as if it is equal to the battery temperature. The left graph of Figure 4.8 shows the

monthly temperature variations from the paper [84]. The initial month is September. The right graph of Figure 4.8 shows the modelled seven-month SoC profile.

To analyse the accuracy of the model at elevated battery temperatures, the seven-month load profiles were tested for three different battery heating scenarios. In the first scenario, the additional battery temperature is 0 °C. Thus, the battery temperature throughout the seven months is identical to the ambient temperature. In the second scenario, 10 °C is added at every time step of the seven-month ambient temperature profile. In the third month, 20 °C is added on every time step of the seven-month ambient temperature profile.

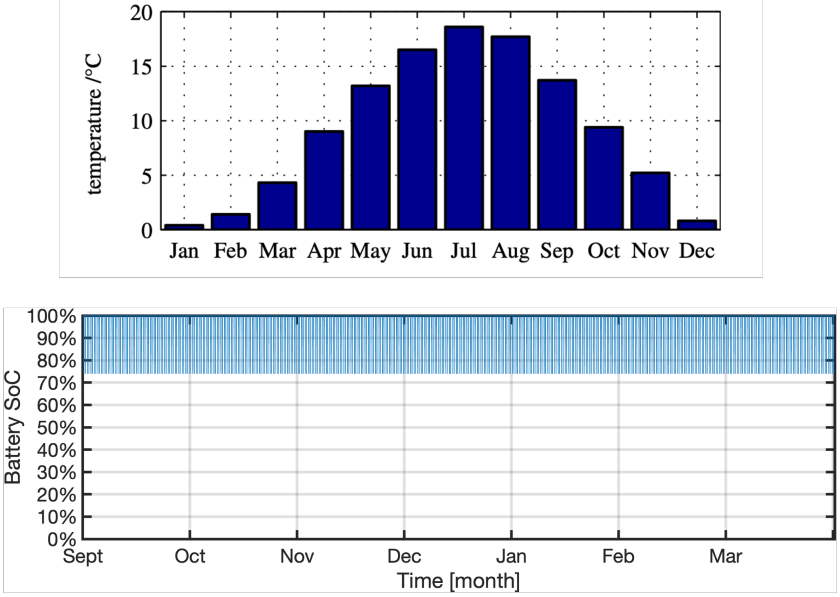

Figure 4.8: Temperature and SoC profiles of the validation tests used by Schmalstieg et al. (2014) to validate their own ageing model.

Ageing modelling results of the validation tests

Consequently, NMC-AM is applied on the seven-month data, which yields the modelled ageing results. The table in Figure 4.9 shows the comparison between the modelled ageing results and the measured ageing results. The left column shows the three different heating scenarios. The second column shows the ageing modelling results of the reproduced load profiles for each scenario. The third column shows both the modelled and the measured ageing results of Schmalstieg et al. for each scenario. In the graphs of the right column, the striped and solid red lines show the modelled resistance increase and the red squares show the measured resistance increase. As shown, the modelled resistance increase results do not closely follow the measured results. Resistance increase is therefore not determined. The striped and solid blue lines show the modelled capacity decrease and the blue circles show the measured capacity decrease. As shown, the modelled capacity decrease are in line with the measured capacity decrease.

Finally, the ageing modelling results of the reproduced load profiles in column two are compared with the measured and modelled ageing results by Schmalstieg et al. in column three to determine the accuracy of the implementation of NMC-AM. The modelled ageing results appear to imitate the measured ageing results surprisingly well, with a maximum deviation of 0.2% in ageing after six months.

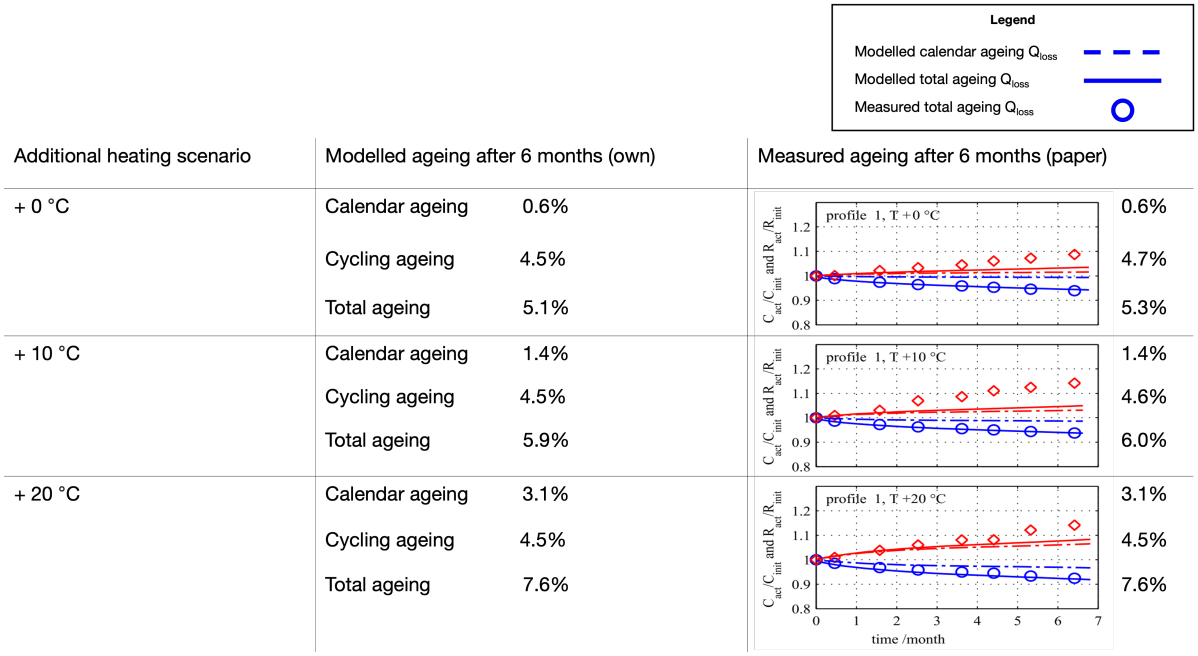

Figure 4.9: Comparison of modelled ageing and the actual ageing measurements for the validation of NMC-AM.

Figure 4.10 shows how the measured ageing is determined from the graphs using WebPlotDigitizer [108]. The figure illustrates a close-up comparison of the modelled ageing results and the ageing measurements for the validation tests. The implementation and validation method have been presented to Felix Hildenbrand who, as explained in Section 4.2, was trained by Johannes Schmalstieg to work with the ageing model. Hildenbrand approved of the implementation method and agreed with the validation methodology during an online meeting.

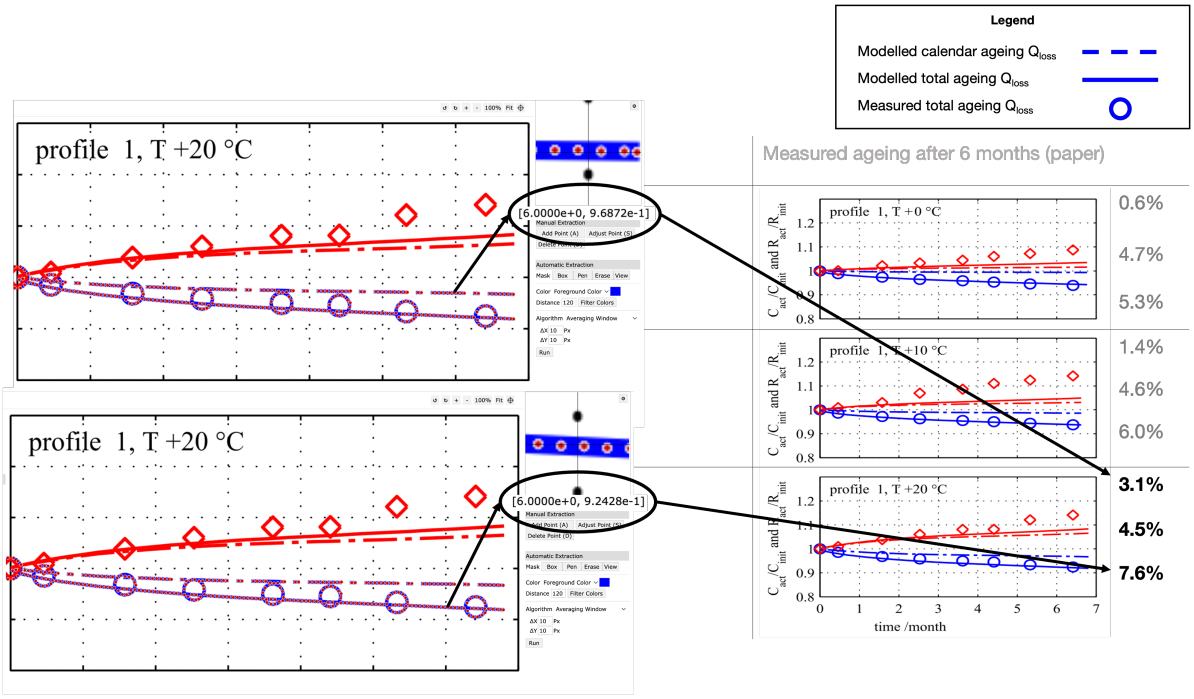

Figure 4.10: Close-up comparison of modelled ageing and the actual ageing measurements for the validation of NMC-AM.

Comparison with Lightyear's NMC ageing tests

Lightyear performed calendar ageing tests on three battery cells over the course of 12 months to determine the cell's capacity retention rate. Both accelerated ageing tests and more realistic use case tests were performed.

The realistic use case tests were performed using two cells stored at a constant battery temperature of 23 °C and 60% SoC. Capacity measurements were performed after 0, 109, 300 and 369 days. After 369 days of storage, one cell showed to have retained 98.2% of its capacity, while the other cell retained 98.4% of its capacity. Therefore, the average one-year capacity loss of the two NMC cells stored at a constant battery temperature of 23 °C and 60% SoC, appears to be 1.7%.

NMC-AM by was used to reproduce the realistic use case calendar ageing tests conducted by Lightyear. The 370-day calendar ageing capacity loss of a cell stored at a constant battery temperature of 23 °C and 60% SoC (V_{cell} = 3.81 V) is determined by the ageing model to be 1.9%.

Figure 4.11 compares the modelled calendar ageing results using the ageing model by Schmalstieg et al. (2014) and the measurements from Lightyear's calendar ageing tests, performed at a constant battery temperature of 23 °C and 60% SoC.

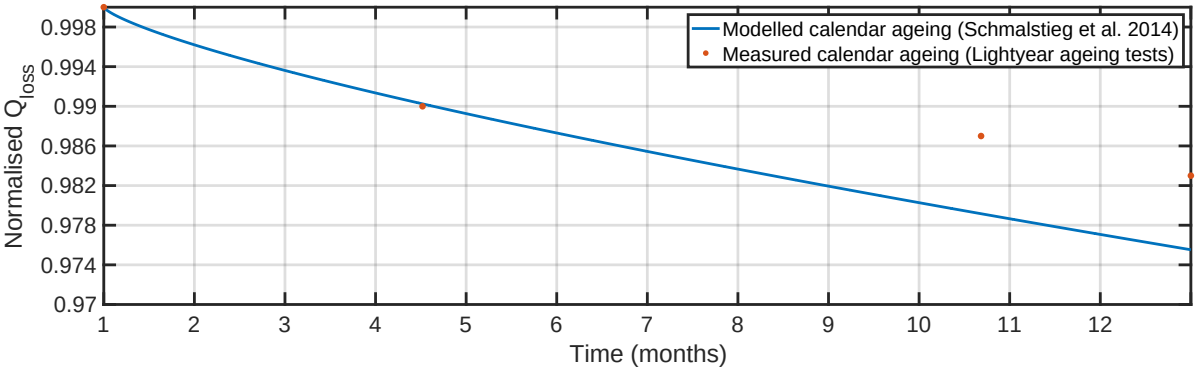

Figure 4.11: Modelled calendar ageing results using NMC-AM [84], and the measurements from Lightyear's calendar ageing tests, both performed at a constant battery temperature of 23 °C and at a 60% SoC.

The modelled capacity loss results slightly differ from the measurements, which may be due to several reasons. The ageing tests conducted by Schmalstieg et al. (2014) were performed on different battery cells, namely Sanyo UR18650E by Panasonic. The final section of the appendix 8 shows the battery datasheet for the Sanyo UR18650E battery cell by Panasonic [68], which states that the cell is ideal for e-bikes, radios, medical devices and robotics. The fact that the Sanyo UR18650E cell is not specifically designed for EV applications and that it originates from 2012 could explain the higher calendar ageing capacity loss compared to Lightyear's battery cells. It also seems that Lightyear's third and fourth capacity measurements, which took place on day 300 and day 369, respectively, deviate from the regression pattern. Nevertheless, Lightyear's battery cell appears to experience less calendar ageing than the Sanyo UR18650E used in the ageing model by Schmalstieg et al. (2014).

4.5.2. NMC-AMII comparison with NMC-AM

As described in Subsection 4.3, NMC-AMII has limited applicability on actual battery data. Instead, the ageing model gives parameters to estimate calendar ageing for four different storage temperatures and at one single SoC value. Like NMC-AM, NMC-AMII is also based on ageing tests of an NMC battery. Thus, under the same conditions, NMC-AMII can be used to benchmark results from NMC-AM. Thus, both NMC-AM and NMC-AMII are used to model the one-year calendar ageing capacity loss for an NMC cell stored under the same conditions, namely 25 °C, 40 °C, 50 °C, and 60 °C, and at an SoC of 50% SoC. In NMC-AM, 50% SoC corresponds to a voltage of 3.69 V.

Table 5.3 shows the modelled calendar ageing results from NMC-AM in the second column and from NMC-AMII in the third column for the four temperature scenarios.

Table 4.2: Comparison of one-year ageing capacity loss results from NMC-AM [84] and NMC-AMII [45]. The same temperature and SoC conditions are used in each temperature scenario - NMC battery.

Temperature scenario	NMC-AM one-year $Q_{loss}^{calendar}$	NMC-AMII one-year $Q_{loss}^{calendar}$
T = 25 °C	2.4%	3.2%
T = 40 °C	7.2%	7.3%
T = 50 °C	14.3%	11.6%
T = 60 °C	27.4%	20.8%

The calendar ageing capacity loss results of two models are similar in the T = 40 °C scenario. However, for higher and lower temperatures than 40 °C, the capacity loss determined by NMC-AM appears to deviate more than the capacity loss determined by NMC-AMII. This might be due to a difference in size or quality of the cell, which alters their performance. For example, the cell on which NMC-AM is baded comprises 2.15 Ah, while the cell on which NMC-AMII is based comprises 10 Ah.

4.5.3. LFP-AM validation

To validate the implementation of LFP-AM by Schimpe et al. (2018), the capacity loss measured during the calendar and cycling ageing experiments is compared with the capacity loss modelled for the base scenario under the same temperature and SoC conditions. The following two subsections describe the validation of LFP-AM for calendar and cycling ageing.

Calendar ageing validation

Figure 4.12 shows the measured capacity loss during calendar ageing tests by Schimpe et al. (2018). The authors performed these calendar ageing tests to determine the influence of temperatures ranging from 10 °C to 55 °C, at a constant 100% SoC, which corresponds to a voltage of 3.42 V.

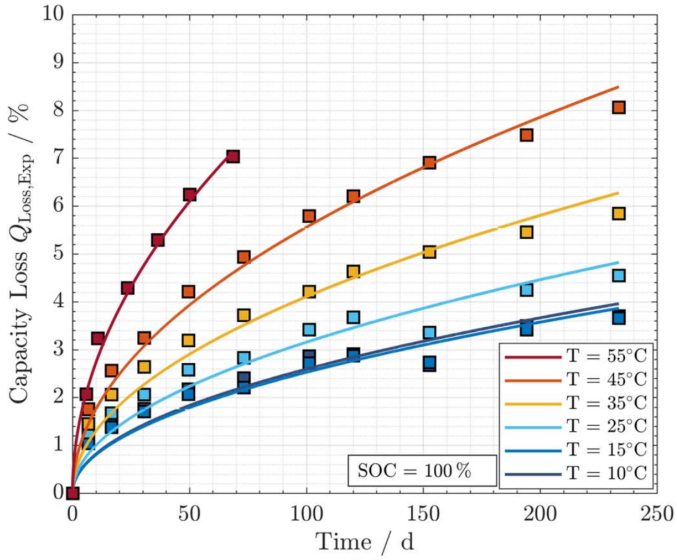

Figure 4.12: Capacity loss during the calendar ageing experiments by Schimpe et al. (2018). The squares represent experimental data and the curves represent simulations by the authors.

Figure 4.13 shows the modelled capacity loss for calendar ageing for battery temperatures at 10 °C, 25 °C, and 45 °C and at a constant 100% SoC. The figure shows that the 200-day measured capacity loss at battery temperatures of 10 °C °C, 25 °C, and 45 °C were 3.6%, 4.5%, and 7.9%, respectively. Comparing the capacity loss curves from Figures 4.12 and 4.13 at the same battery temperatures, the modelled results seem to reasonably follow the measured calendar ageing capacity loss results. Figure 4.13 shows that the 200-day modelled capacity loss at battery temperatures of 10 °C °C, 25 °C, and 45 °C were 3.1%, 4.8%, and 8.1%, respectively.

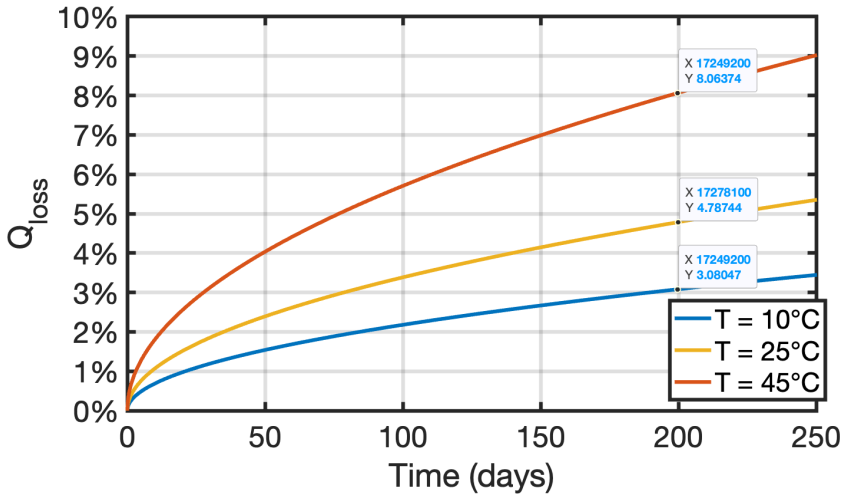

Figure 4.13: Modelled capacity loss for battery temperatures at 10 °C, 25 °C, and 45 °C and at a constant 100% SoC.

Cycling ageing validation

The top graphs of Figure 4.14 show the capacity loss during the cycling experiments at different temperatures, on which the model is based. The capacity loss measured during these cycling experiments also reflects a share of capacity loss due to calendar ageing. The authors of the ageing model assumed that cycling and calendar ageing can be superpositioned, and thus subtracted the capacity loss due to calendar ageing from the total capacity loss to determine the 'pure' cycling ageing capacity loss. The subtracted calendar ageing capacity loss was calculated using the average battery temperature measured during the experimental cycling tests and at an average SoC of 50%. The researchers thereby neglected the impact of the intercorrelation of temperature and SoC, as well as the fact that the average SoC does not equal 50%. The bottom graphs of Figure 4.14 show the capacity loss due to 'pure' cycling ageing.

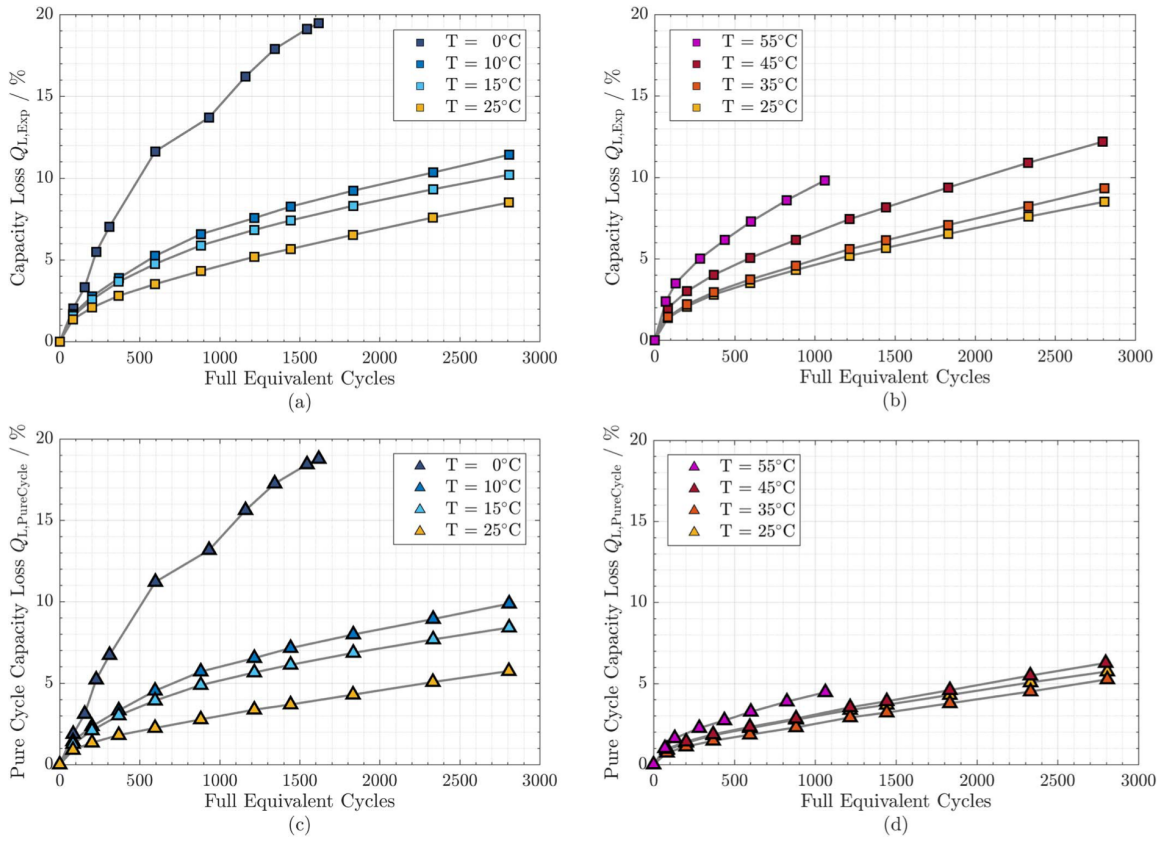

Figure 4.14: The top graphs show the capacity loss during the cycling ageing experiments by Schimpe et al. (2018). The bottom graphs show the 'pure' cycling ageing capacity loss during the same measurements.

The left bottom graph of Figure 4.14 shows that after 700 cycles and at a constant battery temperature of 25 °C, 10 °C and 0 °C the 'pure' cycling ageing capacity loss was measured to be 3.1%, 5.1%, and 15%, respectively. The base scenario modelled in Section 3.2 is simulated for 10 consecutive years to accumulate cycles at a constant temperature of 0 °C, 10 °C and 25 °C. In the base scenario, the throughput after one year is 342 Ah. As the battery cell capacity in the modelled profile comprises 4.85 Ah, this throughput would amount to 70.5 cycles per year. Thus, after 10 years, the battery will have discharged 750 full equivalent cycles. Figure 4.15 shows the simulated cycling ageing capacity loss for the different temperatures. Here, NMC-AMII has determined that after 705 cycles and at a constant battery temperature of 25 °C, 10 °C and 0 °C, the battery will have suffered a cycling ageing capacity loss of 2.8%, 4.9%, and 9.1%, respectively.

It appears that the modelled cycling ageing results at a constant battery temperature of 25 °C and 10 °C accurately follow the results from the authors, but give a relatively large error for a battery temperature of 0 °C. Schimpe et al. (2018) do not describe whether the trend deviation of the capacity loss graph for a battery temperature of 0 °C is incorporated in the derivation of the cycling ageing equations. Nevertheless, for battery temperatures of 10 °C and 25 °C, the simulated results appear to accurately follow the results of the ageing

measurements conducted by the authors. Thus, LFP-AM could essentially underestimate ageing at battery temperatures lower than 10 °C.

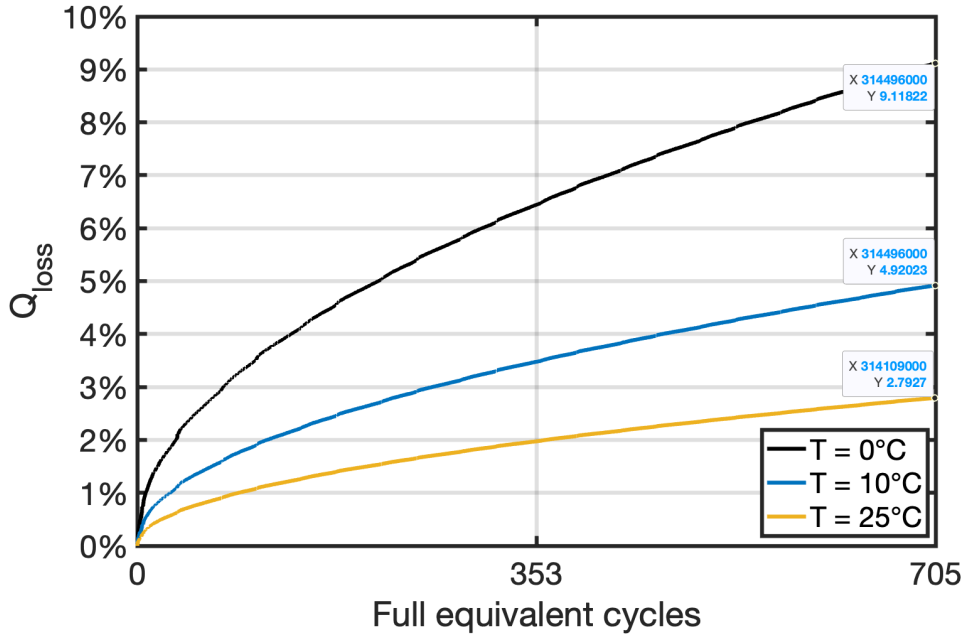

Figure 4.15: NMC-AMII cycling ageing capacity loss for a 10-year repeated base scenario at three constant battery temperatures.

5

EV battery ageing results

The following chapter presents the results from implementing the EV battery datasets developed in Chapter 3 into the ageing models described in Chapter 4. Thus, in this chapter, the third sub-objective is addressed:

iii *Compare the ageing results of the use case scenarios to analyse the impact of VIPV and V2G on battery calendar and cycling ageing.*

The results of NMC-AM, NMC-AMII and LFP-AM are presented in Sections 5.1, 5.2, and 5.3, respectively. The one-year capacity loss due to calendar and cycling ageing for the eight use case scenarios are thoroughly analysed for NMC-AM and LFP-AM. The differences in ageing are substantiated using the one-year use case characteristics of each scenario, Consequently, ageing patterns of calendar and cycling ageing are supported by describing the electrochemical ageing mechanisms thought to occur in the battery cells. Finally, in Section 5.4, the ageing results of NMC and LFP according to NMC-AM and LFP-AM are compared. For reference, Figure 8.13 of the appendix provides an overview of the SoC profiles for the eight scenarios.

5.1. Results from NMC-AM

Table 5.1 provides an overview of the results from NMC-AM for each use case scenario with its corresponding one-year use case characteristics. The table shows the one-year calendar, cycling and total ageing. $Q^{cell}_{throughput}$ is the net energy delivered by a single NMC cell throughout the whole year. $N_{eq.\ full\ cycles}$ is the corresponding full equivalent discharge cycles, given that the cell on which the ageing stress factors are based comprises a usable capacity of 4.85 Ah, even though NMC-AM is based on a cell that comprises 2.15 Ah. $N_{partial\ cycles}$ is the number of partial cycles as defined in Subsection 3.2.11. SoC_{avg} is the average SoC. DoD_{avg} is the average cycle depth of the partial cycles. EoL is the year in which the battery has retained 80% of its initial capacity after calendar and cycling ageing capacity loss. The temperature profiles are identical in all the scenarios. Furthermore, all scenarios model a Lightyear 0 vehicle covering a distance of 19,190 km per year, as described in Section 3.2. The share of calendar and cycling ageing at the battery's EoL as determined by NMC-AM are described in the discussion below the table.

Table 5.1: Overview of NMC-AM results and use case characteristics.

Scenario	One-year capacity loss		One-year use case characteristics			
Base	Calendar ageing	1.05%	$Q^{cell}_{throughput}$	342 Ah	SoC_{avg}	69%
	Cycling ageing	2.80%	$N_{eq.\ full\ cycles}$	70.4	DoD_{avg}	0.18%
	Total ageing	3.85%	$N_{partial\ cycles}$	70,797	EoL	16.2 years
$VIPV_{NL}$	Calendar ageing	0.97%	$Q^{cell}_{throughput}$	340 Ah	SoC_{avg}	63%
	Cycling ageing	2.81%	$N_{eq.\ full\ cycles}$	70.1	DoD_{avg}	0.13%
	Total ageing	3.78%	$N_{partial\ cycles}$	73,642	EoL	16.8 years
$VIPV_{ESP}$ with T_{ESP}	Calendar ageing	1.26%	$Q^{cell}_{throughput}$	339 Ah	SoC_{avg}	58%
	Cycling ageing	2.86%	$N_{eq.\ full\ cycles}$	69.9	DoD_{avg}	0.14%
	Total ageing	4.12%	$N_{partial\ cycles}$	74,098	EoL	14.3 years
$VIPV_{NL}$ & $V2G^{50\%\ SoC}_{DA}$	Calendar ageing	1.14%	$Q^{cell}_{throughput}$	606 Ah	SoC_{avg}	76%
	Cycling ageing	5.46%	$N_{eq.\ full\ cycles}$	125	DoD_{avg}	0.30%
	Total ageing	6.60%	$N_{partial\ cycles}$	71,686	EoL	7.1 years
$V2G^{50\%\ SoC}_{DA}$	Calendar ageing	1.14%	$Q^{cell}_{throughput}$	607 Ah	SoC_{avg}	76%
	Cycling ageing	5.48%	$N_{eq.\ full\ cycles}$	125	DoD_{avg}	0.31%
	Total ageing	6.62%	$N_{partial\ cycles}$	71,695	EoL	7.1 years
$V2G^{20\%\ SoC}_{DA}$	Calendar ageing	1.08%	$Q^{cell}_{throughput}$	772 Ah	SoC_{avg}	71%
	Cycling ageing	8.78%	$N_{eq.\ full\ cycles}$	159	DoD_{avg}	0.36%
	Total ageing	9.86%	$N_{partial\ cycles}$	71,529	EoL	3.8 years
$V2G^{50\%\ SoC}_{aFRR}$	Calendar ageing	1.23%	$Q^{cell}_{throughput}$	459 Ah	SoC_{avg}	84%
	Cycling ageing	4.83%	$N_{eq.\ full\ cycles}$	95	DoD_{avg}	0.24%
	Total ageing	6.06%	$N_{partial\ cycles}$	72,459	EoL	8.2 years
$V2G^{20\%\ SoC}_{aFRR}$	Calendar ageing	1.22%	$Q^{cell}_{throughput}$	477 Ah	SoC_{avg}	83%
	Cycling ageing	4.80%	$N_{eq.\ full\ cycles}$	98	DoD_{avg}	0.25%
	Total ageing	6.02%	$N_{partial\ cycles}$	72,368	EoL	8.4 years

5.1.1. Scenario comparison

Base scenario

- The battery's EoL is reached after 16.2 years, with a share of calendar and cycling ageing of 8.5% and 11.5%, respectively.

$VIPV_{NL}$ scenario

- As VIPV gradually charges the battery, in the Netherlands, VIPV can reduce the number of annual grid charging sessions from 102 to 79 compared to the base scenario, corresponding to a 23% decrease in grid charging frequency. By reducing the grid charging frequency, the battery ranges at lower SoC for an extended period of time, reducing the average SoC by 9%. As higher SoC accelerate the growth of the SEI layer, which causes calendar ageing, lower SoC is beneficial for battery life.
- Compared to the base scenario, one-year calendar ageing reduced by 8% due to VIPV, and cycling ageing is similar. 20-year ageing simulations show that VIPV can reduce calendar ageing by 9% in the Netherlands. Thus, NMC-AM suggests that VIPV can reduce calendar ageing by reducing the battery's average SoC, due to a decrease in grid charging frequency.
- The battery's EoL is reached after 16.8 years, with a share of calendar and cycling ageing of 8.5% and 11.5%, respectively. NMC-AM suggests that VIPV can extend EoL by 6 months. This is thought to be an underestimation of the potential benefit of VIPV on battery life for reasons mentioned below.
- Figure 5.1 illustrates the cycle depths in the base scenario in the top graph and in the $VIPV_{NL}$ scenario in the bottom graph. The graphs suggests that VIPV decreases cycle depth, which is in line with the 28% decrease in average DoD shown in Table 5.1. As shown in Figure 8.3 of the appendix, shallower cycle depths cause less ageing than deeper cycle depths, which suggests that VIPV is beneficial for cycle life.

  Moreover, the one-year cell throughput decreased by 2 Ah compared to the base scenario, which according to the composition of Lightyear's battery pack is equivalent to an annual energy throughput of $E = Q \cdot V_{\text{avg, working}} \cdot N_{\text{cells}} = 2\ \text{Ah} \cdot 3.6\ \text{V} \cdot 3{,}400 = 26\ \text{kWh}$. This suggests that VIPV occasionally powers the EV's drivetrain directly, which could slightly reduce cycling ageing.

  In contrast, the results in Table 5.1 suggest an increase in cycling ageing in the $VIPV_{NL}$ scenario compared to the base scenario. This increase in cycling ageing is due to the 4% increase in the number of partial cycles due to gradual VIPV charging. As NMC-AM is not based on irregular load profiles, it is suspected that the increase in partial cycles causes NMC-AM to overestimate cycling ageing.
- Considering the complexity of the various effects of VIPV on cycling ageing, further analysis is required to determine the impact of VIPV on battery cycle life.

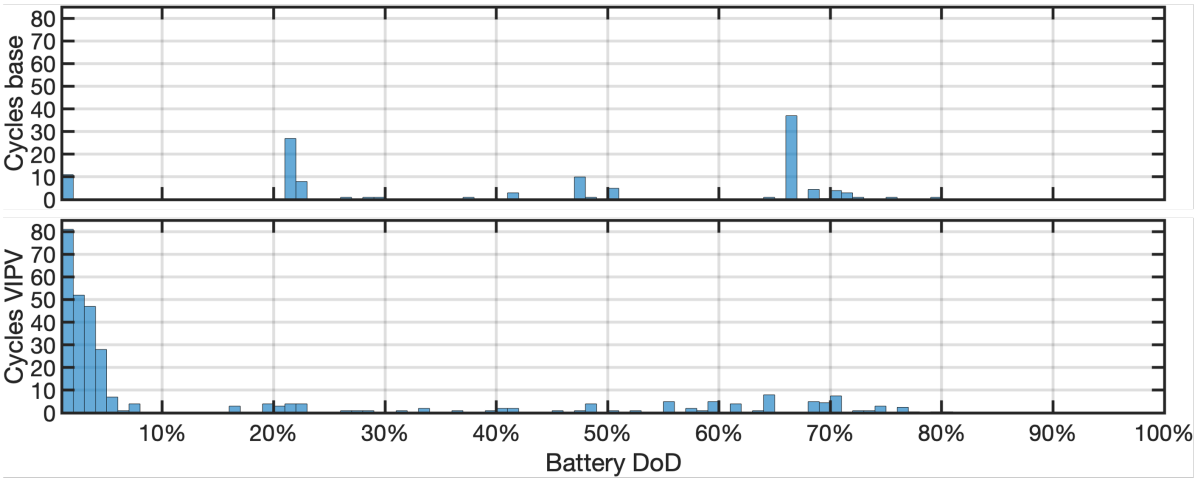

Figure 5.1: Two graphs illustrating the difference in the number of cycles per cycle depth according to Matlab's rainflow cycling counting algorithm for the base scenario (top graph) and the $VIPV_{NL}$ scenario (bottom graph).

VIPV$_{ESP}$ scenario

The impact of VIPV on battery life for an SEV in Spain is determined by accounting for higher ambient temperatures in Spain. Therefore, an ageing comparison is made between an EV in Spain with and without VIPV. According to the difference in ambient temperatures between the Netherlands and Spain [13], an additional scenario is modelled in which 3.3 °C is added to every time step of the battery temperature profile. The battery temperature is again capped at a maximum battery temperature of 35.4 °C to simulate the effect of active battery cooling, as discussed in Subsection 3.2.7. For simplification, it is assumed that the higher ambient temperatures in Spain do not cause additional power to be used by the HVAC system and do not impact the rest of the ageing stress factors. Figure 5.2 shows the modelled battery temperature profiles for the Netherlands and Spain. The ageing results according to NMC-AM for an EV in Spain with and without VIPV are depicted in Figure 5.2.

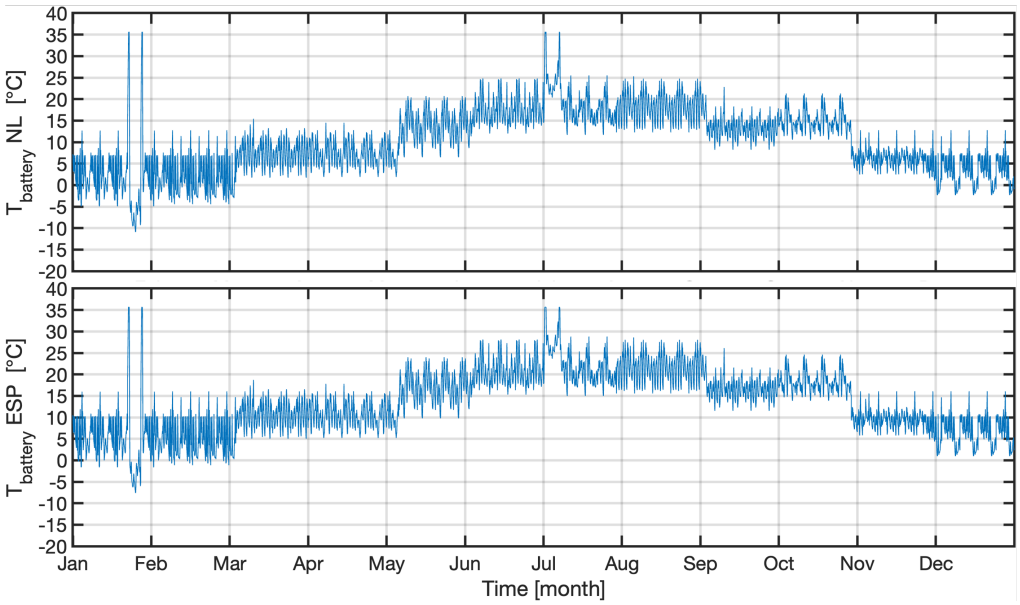

Figure 5.2: The top graph shows the modelled battery temperature profiles for the Netherlands and the bottom graph for Spain, where the average ambient temperature is 3.3 °C higher. The same maximum battery temperature is considered in both temperature profiles.

Table 5.2: NMC-AM results on the impact of VIPV on battery life for an EV in Spain.

Scenario	One-year capacity loss		One-year use case characteristics			
Base with T_{ESP}	Calendar ageing	1.39%	$Q^{cell}_{throughput}$	342 Ah	SoC_{avg}	69%
	Cycling ageing	2.80%	$N_{eq.\ full\ cycles}$	70.4	DoD_{avg}	0.18%
	Total ageing	4.19%	$N_{partial\ cycles}$	70,797	EoL	13.1 years
$VIPV_{ESP}$ with T_{ESP}	Calendar ageing	1.26%	$Q^{cell}_{throughput}$	339 Ah	SoC_{avg}	58%
	Cycling ageing	2.86%	$N_{eq.\ full\ cycles}$	69.9	DoD_{avg}	0.14%
	Total ageing	4.12%	$N_{partial\ cycles}$	74,098	EoL	13.7 years

- As VIPV gradually charges the battery, in Spain, VIPV can reduce the number of annual grid charging sessions from 102 to 57, corresponding to a 44% decrease in grid charging frequency. The reduced grid charging frequency causes the average SoC to reduce by 16%.
- Compared to the base scenario in Spain, VIPV in Spain caused the one-year calendar ageing to decrease by 9% due to the 44% reduction in grid charging frequency. 20-year ageing simulations show that VIPV can reduce calendar ageing by 8% in Spain. It is expected that additional VIPV power generation would

further decrease calendar ageing up to a certain threshold. If this threshold is crossed, VIPV charging can cause the SoC to increase, which could increase calendar ageing.

- In the base scenario in Spain, the battery's EoL is reached after 13.1 years, with a share of calendar and cycling ageing of 10.0% and 10.0%, respectively. In the $VIPV_{ESP}$ scenario, the battery's EoL is reached after 13.7 years, with a share of calendar and cycling ageing of 8.5% and 11.5%, respectively. Thus, NMC-AM suggests that VIPV can extend EoL by 6 months.

$VIPV_{NL}$ & $V2G_{DA}^{50\% SoC}$ scenario

- Compared to the $VIPV_{NL}$ scenario, the one-year calendar ageing is 18% higher and cycling ageing 94% higher in the $VIPV_{NL}$ & $V2G_{DA}^{50\% SoC}$ scenario. The 18% increase in calendar ageing is because the required grid connection for V2G services causes the vehicle to charge more often in the modelled scenario, increasing the average SoC by 21% in the $VIPV_{NL}$ & $V2G_{DA}^{50\% SoC}$ scenario. The significant 94% increase in cycling ageing is due to the 44% increase in throughput compared to the $VIPV_{NL}$ scenario. The increase in throughput is due to additional cycling for V2G day-ahead electricity trading. Furthermore, Equation 4.9 of NMC-AM suggests that the 131% increase in average DoD in the $VIPV_{NL}$ & $V2G_{DA}^{50\% SoC}$ scenario compared to the $VIPV_{NL}$ scenario contributes to the increase in cycling ageing.

- NMC-AM suggests that V2G day-ahead electricity trading, with the goal of maximising profits for the EV owner, can significantly harm battery life as V2G increases calendar ageing due to increased SoC, as well as increase cycling ageing due to additional throughput and increasing cycle depth.

- The results suggest that due to the increased grid connection required for V2G services, the battery's average SoC can increase, which increases calendar ageing. Thus, NMC-AM suggests that a controlled V2G strategy can lower the average SoC to reduce calendar ageing.

- The battery's EoL is reached after 7.1 years, with a share of calendar and cycling ageing at EoL of 5.1% and 14.9%, respectively.

$V2G_{DA}^{50\% SoC}$ scenario

- In the $V2G_{DA}^{50\% SoC}$ scenario, the one-year calendar and cycling ageing, throughput, number of partial cycles, and average SoC is are similar compared to the $VIPV_{NL}$ & $V2G_{DA}^{50\% SoC}$ scenario. This indicates that V2G governs ageing when combined with VIPV.

- Compared to the base scenario, the average SoC is 10% higher, which causes a calendar ageing increase of 9%. The SoC increased due to the increased grid connection required for V2G services.

- The battery's EoL is reached after 7.1 years, with a share of calendar and cycling ageing at EoL of 5.1% and 14.9%, respectively.

$V2G_{DA}^{20\% SoC}$ scenario

- Compared to the base scenario, the one-year calendar ageing is 3% higher and the one-year cycling ageing is 214% higher in the $V2G_{aFRR}^{20\% SoC}$ scenario, shortening battery life by up to 12.5 years. The 3% higher calendar ageing is due to the 3% increase in average SoC, as V2G increases the grid charging frequency. The 214% increase in cycling ageing is due to the 126% increase in throughput, which harms the battery due to additional intercalation of Li-ions. Thus, NMC-AM suggests that V2G services, with the goal of maximising profits for the EV owner, can be very harmful to battery life.

- Compared to the $V2G_{DA}^{50\% SoC}$, the one-year calendar ageing is 5% lower and the one-year cycling ageing is 60% higher in the $V2G_{DA}^{20\% SoC}$ scenario. The 5% lower calendar ageing is due to the 7% lower average SoC, as the V2G services allow the battery to be discharged to 20% SoC in this scenario, which lowers the average SoC. Thus, NMC-AM suggests that calendar ageing can be reduced by V2G by reducing the average SoC, which naturally occurs with a lower SoC retention limit during V2G services.

- The 60% increase in cycling ageing is mainly due to additional capacity being discharged in the $V2G_{DA}^{20\% SoC}$ scenario. The reason that additional capacity is being discharged, namely 27% more than in the $V2G_{DA}^{50\% SoC}$ scenario, is a result of more capacity being available due to the lower SoC retention limit

during V2G services. Part of the increase in cycling ageing is due to the X increase in average DoD. As described above, larger DoD can result in more ageing, suggesting that the larger average cycling DoD in the $V2G_{DA}^{20\%\ SoC}$ scenario compared to the $V2G_{DA}^{50\%\ SoC}$ adds to the increased cycling ageing.

- Thus, NMC-AM suggests that when EVs allow V2G services to cycle to a lower SoC retention limit, more capacity becomes available for cycling, increasing throughput cycle depth, which increases cycling ageing.
- The battery's EoL is reached after only 3.8 years, with a share of calendar and cycling ageing at EoL of 3.1% and 16.9%, respectively.

$V2G_{aFRR}^{50\%\ SoC}$ scenario

- Compared to the base scenario, the one-year calendar ageing is 17% higher and the one-year cycling ageing is 73% higher in the $V2G_{aFRR}^{50\%\ SoC}$ scenario. The 17% increase in calendar ageing is caused by a 22% increase in SoC, as high SoC accelerates the growth of the SEI layer. The significant 73% increase in cycling is caused by a 34% increase in throughput, which causes growth of the SEI layer and lithium plating.
- Compared to the the $V2G_{DA}^{50\%\ SoC}$ scenario, the one-year calendar ageing is 9% higher and the one-year cycling ageing is 12% lower in the $V2G_{aFRR}^{50\%\ SoC}$ scenario. It should be noted that two scenarios with different V2G services are being compared here, namely day-ahead electricity trading and aFRR.
- The 9% increase in calendar ageing is due to the 11% increase in average SoC, which accelerates calendar ageing. The high average SoC in the $V2G_{aFRR}^{50\%\ SoC}$ is due to the relatively low demand for aFRR grid balancing energy. In this modelled scenario, this causes the EV to charge from the grid whenever it is parked, increasing the average SoC and thus calendar ageing. Thus, NMC-AM suggests that due to the increased grid connection required for V2G services, the battery's average SoC can increase, which increases calendar ageing. As mentioned before, this suggests that a controlled V2G strategy can lower the average SoC to reduce calendar ageing.
- The 12% decrease in cycling ageing is due to the 24% lower throughput in the $V2G_{aFRR}^{50\%\ SoC}$ scenario compared to the $V2G_{DA}^{50\%\ SoC}$ scenario. In the simulated scenario, aFRR balancing services appear to demand less power compared to day-ahead electricity trading, naturally resulting in less cycling ageing due to reduced throughput.
- The battery's EoL is reached after 8.2 years, with a share of calendar and cycling ageing at EoL of 6.2% and 13.8%, respectively.

$V2G_{aFRR}^{20\%\ SoC}$ scenario

- Compared to the $V2G_{aFRR}^{50\%\ SoC}$ scenario, the one-year calendar ageing is 1% lower and the one-year cycling ageing is 1% lower in the $V2G_{aFRR}^{20\%\ SoC}$ scenario. Calendar ageing is lower in the $V2G_{aFRR}^{20\%\ SoC}$ scenario as the lower SoC retention limit lowers the average SoC, which is beneficial for calendar ageing.
- The battery's EoL is reached after 8.4 years, with a share of calendar and cycling ageing at EoL of 6.2% and 13.8%, respectively.
- Compared to the $V2G_{aFRR}^{50\%\ SoC}$ scenario, cycling ageing is lower while throughput is 4% higher in the $V2G_{aFRR}^{20\%\ SoC}$ scenario. An explanation for the increase in cycling ageing in the $V2G_{aFRR}^{50\%\ SoC}$ scenario is the slight increase in the number of partial cycles, which could cause NMC-AM to overestimate cycling ageing.

Notes and limitations

- According to Table 5.1, one-year cycling ageing is dominant in every scenario. Simulations using NMC-AM show that for the base scenario, calendar ageing becomes dominant above 22 °C.
- Capacity and power fade are not fed back into the data, which leads to ageing estimation errors.

- While NMC-AM is based on a cell comprising 2.15 Ah, the ageing stress factors used in the analysis are based on a cell comprising 4.85 Ah, which could lead to ageing estimation errors.
- NMC-AM is based on the rainflow cycling counting method to count cycles, which is shown to inaccurately determine the start and end of each cycle. The implementation of load profile cycle counting method described in Subsection 3.2.11 in combination with the increasing irregularity of the load profiles due to VIPV and V2G, can cause the NMC-AM to lead to ageing estimation errors. This demonstrates the limited applicability of semi-empirical ageing models on irregular load profiles.

5.1.2. Base scenario analysis

One-year SoC, temperature and capacity loss profiles
Figure 5.3 shows the one-year SoC, temperature and NMC-AM capacity loss profiles for the base scenario. Cycling ageing appears dominant, as also discussed in Subsection 5.1.1.

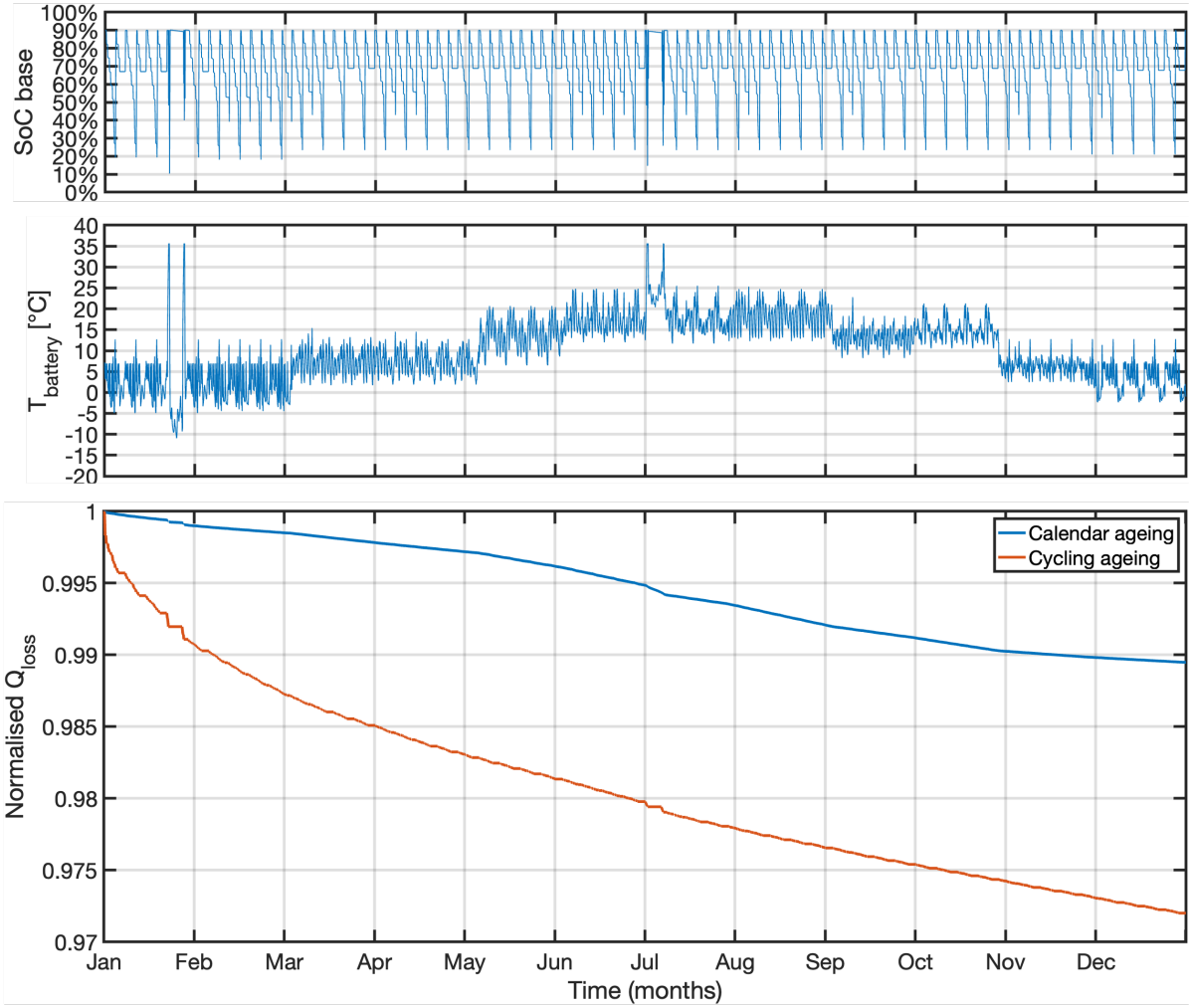

Figure 5.3: Base scenario: one-year SoC, temperature and Q_{loss} profiles for an NMC battery.

- The calendar ageing capacity loss profile follows a wavy curve, as well as an exponential decay. The exponential decay is not clearly visible in the calendar ageing curve and is therefore discussed in the *10-year capacity loss* subsection. Calendar ageing is governed by higher SoC and higher temperatures. The impact of higher temperatures is visible during the summer months, where calendar ageing capacity loss appears to occur at a higher rate compared to the winter months. The seasonal effect of temperature causes the wavy capacity loss pattern over the year, as higher temperatures increase the Arrhenius reaction rate, which causes electrolyte dissolution and parasitic side reactions to occur, which causes

the SEI layer to grow. The growth of the SEI layer causes LLI and LAM, resulting in capacity loss. The following subsection analysis how increased battery temperatures impact ageing.

- The cycling ageing capacity loss profile follows the following relation: $-x^z$, where $0 \leq z \leq 1$. This exponential decay follows from the $\sqrt{Ah}$ factor in Equation 4.5 of NMC-AM, and is in line with the electrochemical effects occurring in the cell. As discussed in Subsection 2.1.3, the SEI layer mainly forms in the first few cycles, after which its growth scales with the square root of time and accelerates with higher SoC and higher temperatures. The NMC-AM cycling ageing capacity loss curve shown in Figure 5.3 follows a similar pattern, where the most significant cycling ageing capacity loss occurs at the beginning of the year.

SoC, temperature and capacity loss profiles during summer trip

As mentioned above, both cycling ageing and calendar ageing capacity loss accelerates at higher SoC and higher temperatures. Figure 5.4 shows the one-week SoC, temperature and capacity loss profiles during the summer trip at the beginning of July.

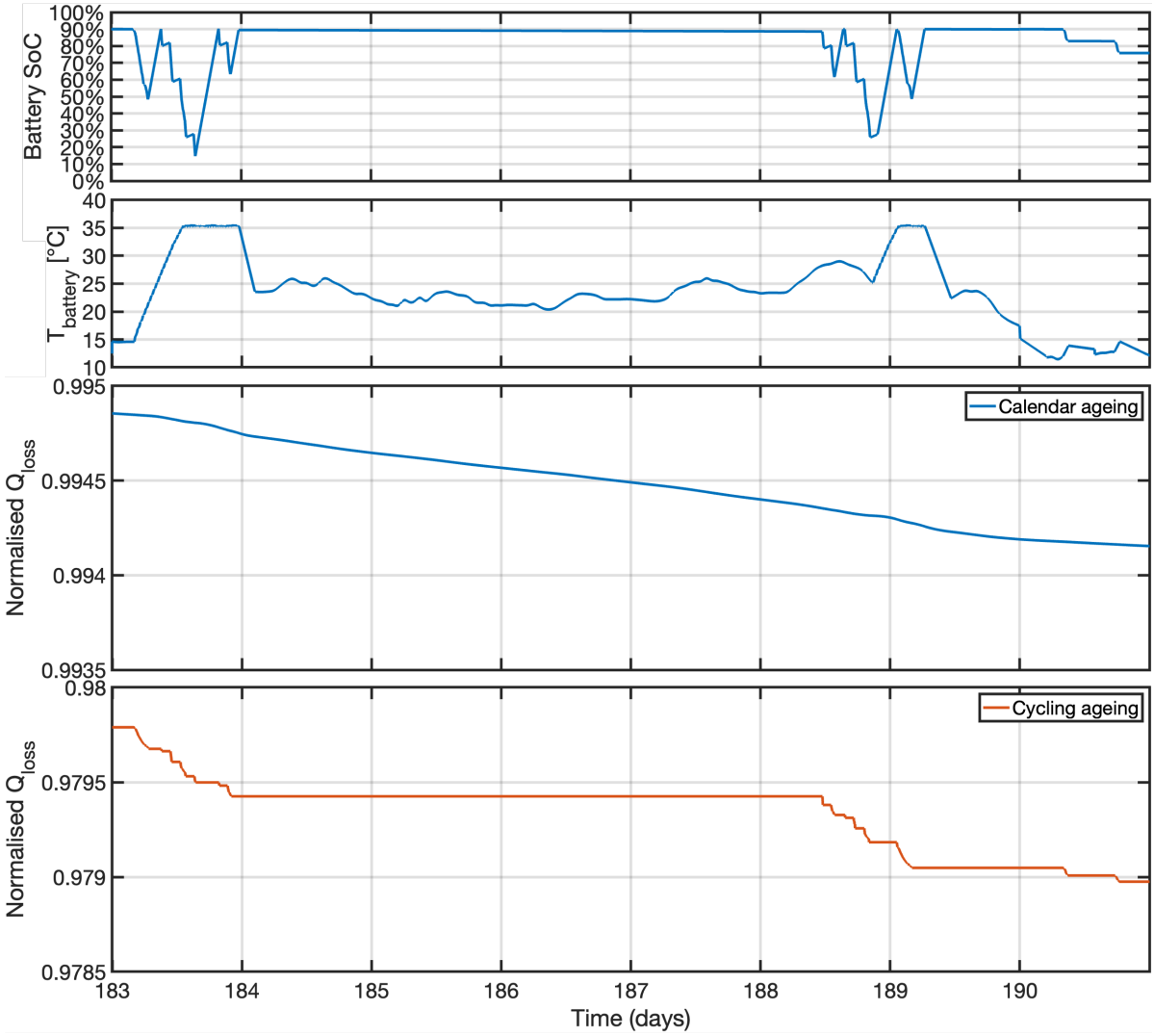

Figure 5.4: SoC, temperature and capacity loss profiles during the summer trip in the beginning of July.

- The calendar ageing capacity loss profile shows the steepest decline in the evening of day 183 and in the morning of 189, as the battery temperature peaks around 35 °C. The calendar ageing decline is also steep from day 184 to 189 when the SoC is high and the EV is exposed to high temperatures during parking in Biarritz, Spain, which illustrates the effect of increased SoC and temperatures on battery

life. As explained in Subsection 2.1.3, high SoC causes electrolyte dissolution and high temperatures accelerate the parasitic side reaction rate, which accelerate the growth of the SEI layer. The SEI layer consumes cyclable Li-ions, causing both LLI and LAM, resulting in capacity loss.

- The cycling ageing capacity loss profiles show step-wise capacity loss when the EV is driven to Biarritz on day 183 and back on days 188 and 189. This illustrates the effect of the increased throughput, or Li-ion intercalation, on battery life. As explained in Subsection 2.1.3, Li-ion intercalation causes, among other things, further growth of the SEI layer as well as lithium plating, which both cause LLI and LAM, resulting in capacity loss.

10-year capacity loss

To illustrate both the wavy pattern and exponential decay of the calendar ageing capacity loss, Figure 5.5 shows the 10-year capacity loss profile for the modelled base scenario. The blue solid line illustrates the wavy pattern of calendar ageing capacity loss. The blue dashed line illustrates how a hypothetical linear decay for calendar ageing would look, to contrast the exponential decay of calendar ageing capacity loss.

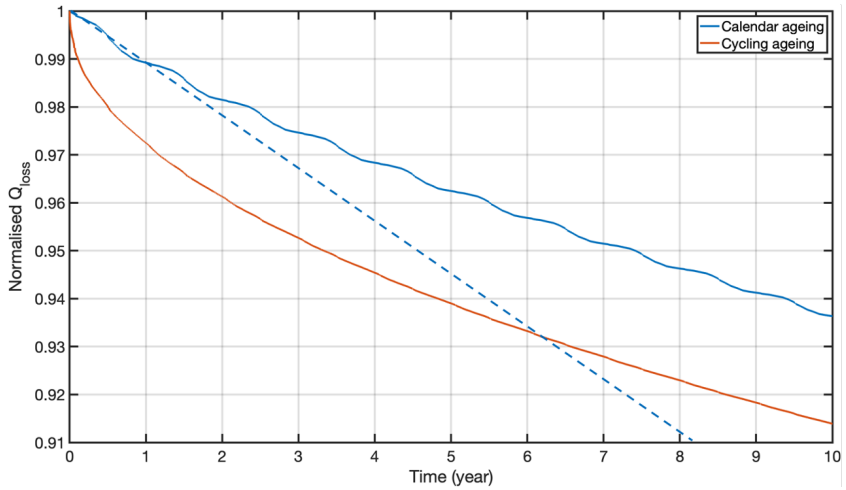

Figure 5.5: 10-year capacity loss profile resulting from NMC-AM. The blue dashed line is a hypothetical linear decay curve for calendar ageing capacity loss, to illustrate the exponential decay of the actual calendar ageing capacity loss.

- The exponential decay follows from the $t^{0.75}$ factor in Equation 4.1 of NMC-AM. The exponential decay in both the calendar and cycling ageing capacity loss curves illustrates how the slowing growth of the SEI layer impacts capacity loss. After 10 years, the EV will have covered a distance of 191,000 km while having retained 85% of its capacity.
- For comparison, battery ageing data from an extensive Tesla Model S battery ageing survey is shown in Figure 5.6. The battery size in the Tesla Model S varied over the years, ranging from 40 kWh to 100 kWh in newer models, but remained NCA. The data from the survey suggests that after 200,000 km the battery will have retained about 93% of its capacity, which is significantly higher than the capacity retention determined by NMC-AM for the same travelled distance. The difference is likely attributed to the difference in battery size, chemistry, and quality.

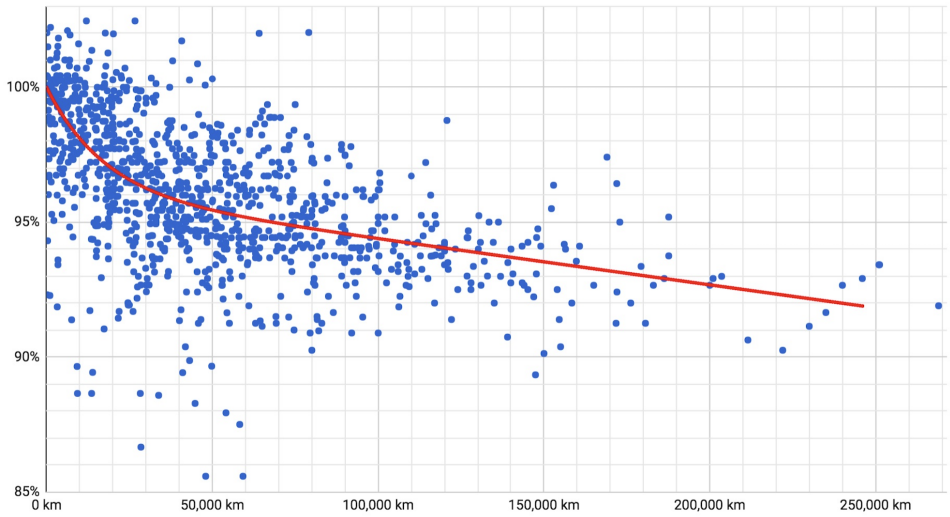

Figure 5.6: Y-axis shows the remaining NCA battery capacity and the x-axis shows the covered distance. The blue dots show capacity retention data from the survey and the red line shows the trend of the capacity ageing loss over the distance covered [90].

5.1.3. VIPV scenario analysis

Figure 5.7 shows the one-year SoC, temperature and NMC-AM capacity loss profiles for the VIPV scenario in the Netherlands.

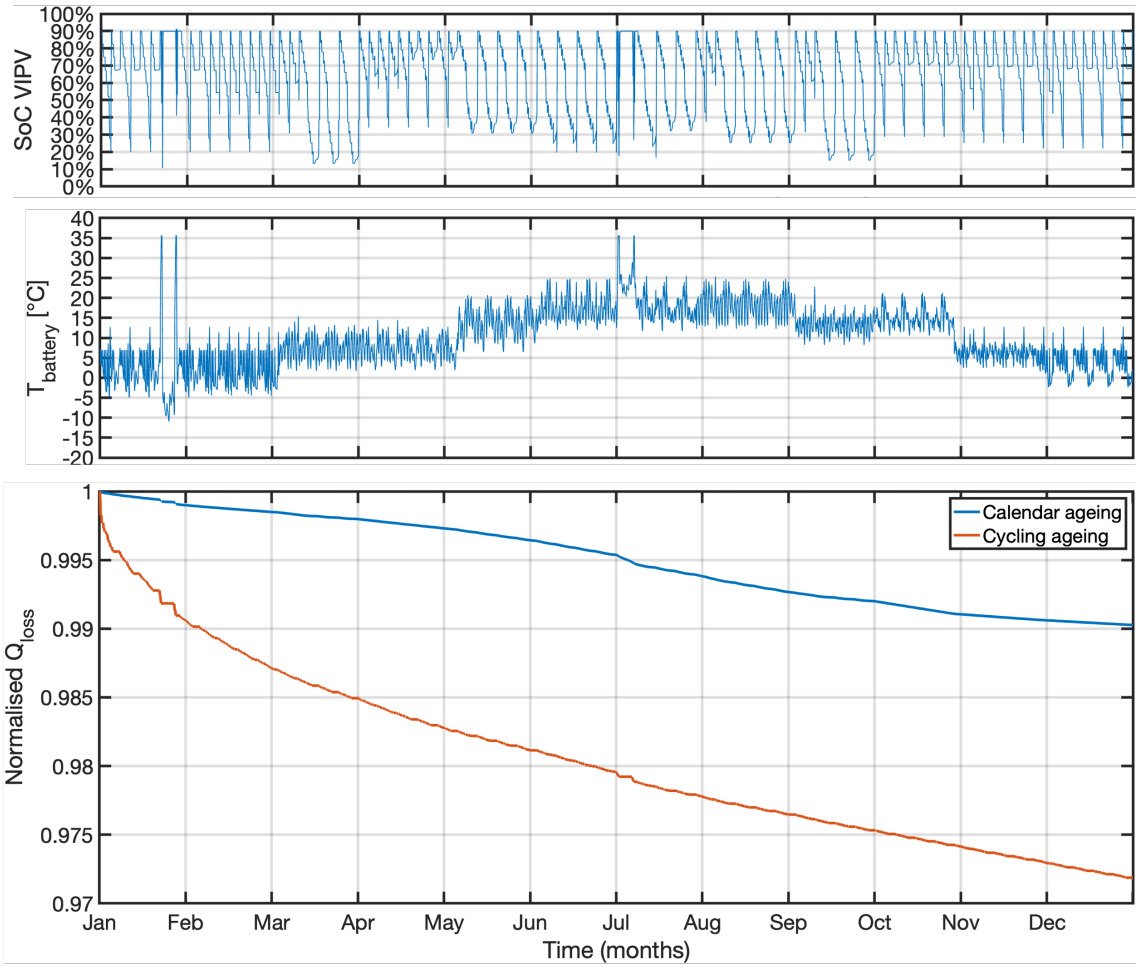

Figure 5.7: VIPV scenario: one-year SoC, temperature and Q_{loss} profiles for an NMC battery.

- Figure 5.7 shows how both the cycling and calendar ageing capacity loss profiles exhibit an exponential decay according to the growth pattern of the SEI layer.
- Compared to the base scenario, calendar ageing capacity loss is slightly less due to the lower average SoC. Figure 5.7 illustrates how VIPV impacts the SoC profile compared to the base scenario shown in Figure 5.3.

5.1.4. V2G scenario analysis

Figure 5.8 shows the one-year SoC, temperature and NMC-AM capacity loss profiles for the V2G scenario in the Netherlands.

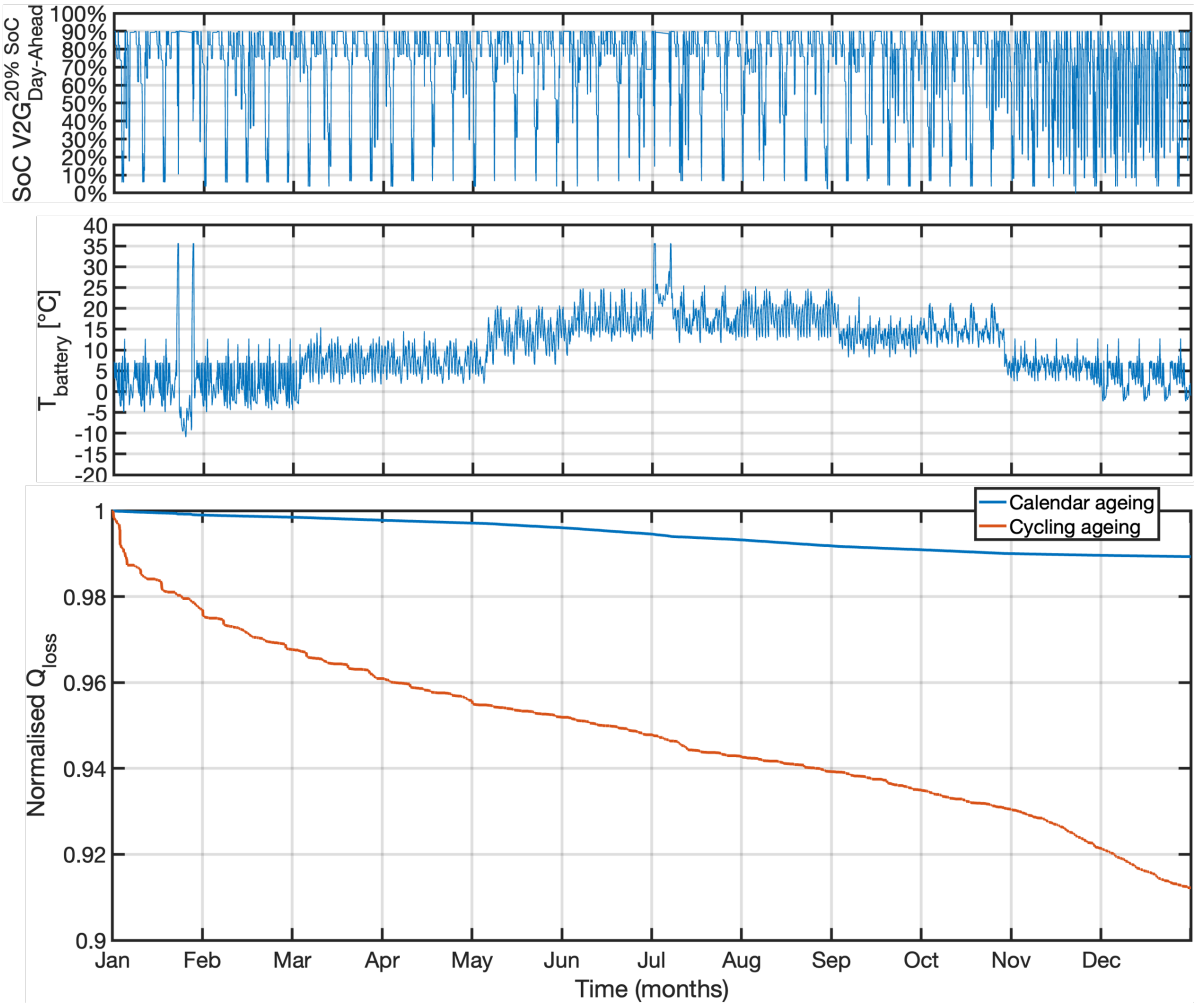

Figure 5.8: V2G scenario: one-year SoC, temperature and Q_{loss} profiles for an NMC battery.

- Figure 5.8 shows how the cycling ageing curve starts with an exponential decay governed by the decreasing growth of the SEI layer. Compared to the base scenario, especially in November and December, the SoC profile shows increased SoC variations due to increased battery cycling for V2G day-ahead electricity trading.
- The increased V2G cycling in the winter months could be due to an increase in electricity price variations due to the increased intermittency of RES during the winter.
- As illustrated in the capacity loss graph of Figure 5.8, the additional cycles due to V2G during the winter months cause a steeper cycling ageing capacity loss curve. The increased Li-ion intercalation due to additional V2G cycles causes, among other things, further growth of the SEI layer as well as lithium plating, which both cause LLI and LAM, resulting in capacity loss.

5.2. Results from NMC-AMII

As explained in Subsection 4.5.2, NMC-AMII is limited in its applicability as it can only determine the calendar ageing capacity loss for four different constant battery temperatures at 50% SoC. Nevertheless, NMC-AMII is used to determine the impact of temperature on calendar ageing capacity loss. Figure 5.9 shows the one-year capacity loss curves for the NMC battery stored at 50% SoC at different temperatures, namely 25 °C, 40 °C, 50 °C, and 60 °C. Table 5.3 shows the one-year NMC capacity loss and the expected EoL of the battery according to NMC-AMII, for each battery temperature scenario.

The capacity loss and EoL results of NMC-AMII demonstrate the significant impact of battery temperature on NMC battery life. Higher temperatures are thought to also impact cycling ageing. The fact that the impact of higher temperatures on cycling ageing is not considered in this EoL calculation accentuates the negative impact of higher temperatures on battery life.

Table 5.3: NMC-AMII results and use case characteristics.

Temperature scenario	One-year $Q_{loss}^{calendar}$	EoL
T = 25 °C	3.2%	19.9 years
T = 40 °C	7.3%	7.6 years
T = 50 °C	11.6%	2.9 years
T = 60 °C	20.8%	0.9 year

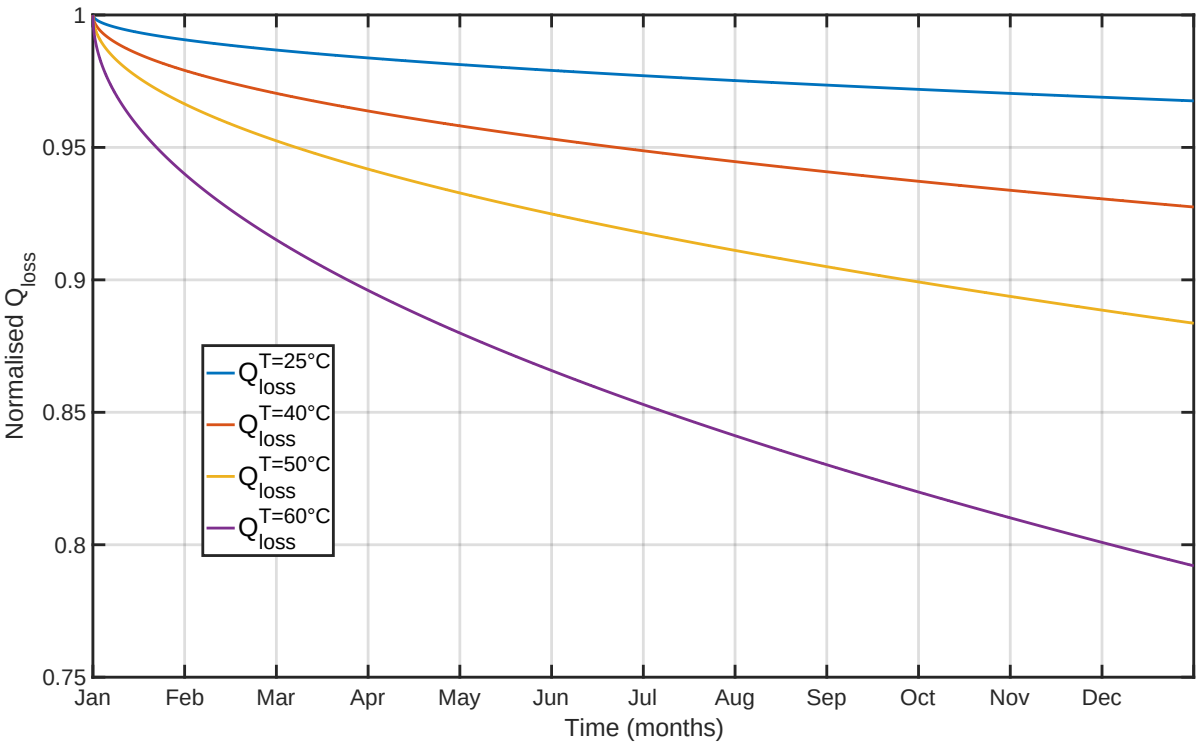

Figure 5.9: One-year Q_{loss} profiles for four different constant battery temperatures for an NMC battery.

5.3. Results from LFP-AM

Table 5.4 provides an overview of the results from LFP-AM for each use case scenario with its corresponding one-year use case characteristics. Like in Table 5.1, the table shows the one-year calendar, cycling and total ageing. $Q^{cell}_{throughput}$ is the net energy delivered by a single cell throughout the whole year. $N_{eq.\ full\ cycles}$ is the corresponding full equivalent discharge cycles given that the cell on which the ageing stress factors are based comprises a usable capacity of 4.85 Ah, even though LFP-AM is based on a cell that comprises 3.00 Ah. $N_{partial\ cycles}$ is the number of partial cycles as defined in Subsection 3.2.11. SoC_{avg} is the average SoC. DoD_{avg} is the average cycle depth of the partial cycles. EoL is the year in which the battery has retained 80% of its initial capacity after calendar and cycling ageing capacity loss. The temperature profiles are identical in all the scenarios. Moreover, all scenarios model a Lightyear 0 vehicle covering a distance of 19,190 km per year. The share of calendar and cycling ageing at the battery's EoL as determined by LFP-AM are described in the discussion below the table.

Table 5.4: Overview of LFP-AM results and use case characteristics.

Scenario	One-year capacity loss		One-year use case characteristics			
Base	Calendar ageing	3.04%	$Q^{cell}_{throughput}$	342 Ah	SoC_{avg}	69%
	Cycling ageing	2.03%	$N_{eq.\ full\ cycles}$	70.5	DoD_{avg}	0.18%
	Total ageing	5.07%	$N_{partial\ cycles}$	70,797	EoL	12.7 years
$VIPV_{NL}$	Calendar ageing	2.91%	$Q^{cell}_{throughput}$	340 Ah	SoC_{avg}	63%
	Cycling ageing	2.21%	$N_{eq.\ full\ cycles}$	70.1	DoD_{avg}	0.13%
	Total ageing	5.12%	$N_{partial\ cycles}$	73,642	EoL	12.6 years
$VIPV_{ESP}$ with T_{ESP}	Calendar ageing	3.02%	$Q^{cell}_{throughput}$	339 Ah	SoC_{avg}	58%
	Cycling ageing	2.07%	$N_{eq.\ full\ cycles}$	69.9	DoD_{avg}	0.14%
	Total ageing	5.09%	$N_{partial\ cycles}$	74,098	EoL	13.5 years
$VIPV_{NL}$ & $V2G^{50\%\ SoC}_{DA}$	Calendar ageing	3.36%	$Q^{cell}_{throughput}$	606 Ah	SoC_{avg}	76%
	Cycling ageing	2.40%	$N_{eq.\ full\ cycles}$	125	DoD_{avg}	0.30%
	Total ageing	5.76%	$N_{partial\ cycles}$	71,686	EoL	9.9 years
$V2G^{50\%\ SoC}_{DA}$	Calendar ageing	3.36%	$Q^{cell}_{throughput}$	607 Ah	SoC_{avg}	76%
	Cycling ageing	2.40%	$N_{eq.\ full\ cycles}$	125	DoD_{avg}	0.31%
	Total ageing	5.76%	$N_{partial\ cycles}$	71,695	EoL	9.9 years
$V2G^{20\%\ SoC}_{DA}$	Calendar ageing	3.19%	$Q^{cell}_{throughput}$	772 Ah	SoC_{avg}	71%
	Cycling ageing	2.94%	$N_{eq.\ full\ cycles}$	159	DoD_{avg}	0.36%
	Total ageing	6.13%	$N_{partial\ cycles}$	71,529	EoL	8.8 years
$V2G^{50\%\ SoC}_{aFRR}$	Calendar ageing	3.64%	$Q^{cell}_{throughput}$	459 Ah	SoC_{avg}	84%
	Cycling ageing	1.78%	$N_{eq.\ full\ cycles}$	95	DoD_{avg}	0.24%
	Total ageing	5.42%	$N_{partial\ cycles}$	72,459	EoL	11.5 years
$V2G^{20\%\ SoC}_{aFRR}$	Calendar ageing	3.63%	$Q^{cell}_{throughput}$	477 Ah	SoC_{avg}	83%
	Cycling ageing	1.83%	$N_{eq.\ full\ cycles}$	98	DoD_{avg}	0.25%
	Total ageing	5.46%	$N_{partial\ cycles}$	72,368	EoL	11.4 years

5.3.1. Scenario comparison

Base scenario

The battery's EoL is reached after 12.7 years with a share of calendar and cycling ageing at EoL of 11.3% and 8.7%, respectively.

$VIPV_{NL}$ scenario

- Similarly to NMC-AM, VIPV gradually charges the battery, which can reduce the grid charging frequency by 23% in the Netherlands. This decrease in grid charging frequency is based on NMC-based ageing stress factors, and could be different for LFP-based ageing stress factors due to the difference in the load profiles. Nevertheless, gradual VIPV charging is expected to lower the grid charging frequency by a similar order of magnitude, which can lower the average SoC. Lower SoC is also beneficial for LFP batteries as high SoC cause electrolyte dissolution, which accelerates SEI layer growth [57, 81, 113]. This implies that VIPV can reduce calendar ageing by reducing the battery's average SoC, due to a decrease in grid charging frequency.
- Compared to the base scenario, the one-year calendar ageing is 4% lower and the one-year cycling ageing is 9% higher in the $VIPV_{NL}$ scenario. Like for NMC-AM, the increase in cycling ageing is thought to be an ageing estimation error. 20-year ageing simulations indicate that VIPV can reduce LFP calendar ageing by 6% in the Netherlands. Considering the complexity of the various effects of VIPV on cycling ageing, further analysis is required to determine the impact of VIPV on battery cycle life.
- The battery's EoL is reached after 12.6 years, with a share of calendar and cycling ageing at EoL of 10.7% and 9.3%, respectively.

$VIPV_{ESP}$ scenario

Like for NMC-AM, the $VIPV_{ESP}$ scenario is compared to a base scenario in which increased battery temperatures are modelled. The ageing results according to NMC-AM for an EV in Spain with and without VIPV are depicted in Figure 5.5.

Table 5.5: LFP-AM results on the impact of VIPV on battery life for an EV in Spain.

Scenario	One-year capacity loss		One-year use case characteristics			
Base with T_{ESP}	Calendar ageing	3.37%	$Q^{cell}_{throughput}$	342 Ah	SoC_{avg}	69%
	Cycling ageing	1.67%	$N_{eq.\ full\ cycles}$	70.5	DoD_{avg}	0.18%
	Total ageing	5.04%	$N_{partial\ cycles}$	70,797	EoL	13.3 years
$VIPV_{ESP}$ with T_{ESP}	Calendar ageing	3.02%	$Q^{cell}_{throughput}$	339 Ah	SoC_{avg}	58%
	Cycling ageing	2.07%	$N_{eq.\ full\ cycles}$	69.9	DoD_{avg}	0.14%
	Total ageing	5.09%	$N_{partial\ cycles}$	74,098	EoL	13.5 years

- Similarly to NMC-AM, in Spain, VIPV can reduce the grid charging frequency by 44% decrease, causing a 16% decrease in SoC. The decrease in grid charging frequency is based on NMC simulations, but is expected to be similar for an LFP battery.
- In the base with T_{ESP} scenario, the battery's EoL is reached after 13.3 years, with a share of calendar and cycling ageing at EoL of 12.8% and 7.2%, respectively. In the $VIPV_{ESP}$ with T_{ESP} scenario, the battery's EoL is reached after 13.5 years, with a share of calendar and cycling ageing at EoL of 11.7% and 8.3%, respectively. Thus, LFP-AM suggests that VIPV can extend battery life by 2 months.

  Compared to the base scenario in Spain, the one-year LFP calendar ageing is 10% lower and the one-year cycling ageing is 24% higher in the $VIPV_{ESP}$ scenario. As explained in the *$VIPV_{NL}$ scenario* subsection, VIPV gradually charges the battery, reducing the grid charging frequency, which lowers the average SoC.

The lower average SoC is beneficial for calendar ageing, as shown in Table 5.5. 20-year ageing simulations indicate that VIPV can reduce LFP calendar ageing by 9% in Spain.

Thus, LFP-AM suggests that VIPV in Spain reduces calendar ageing by reducing the average SoC.

$VIPV_{NL}$ & $V2G_{DA}^{50\% SoC}$ scenario

- Compared to the $VIPV_{NL}$ scenario, the one-year calendar ageing is 11% higher and the one-year cycling ageing is 9% higher in the $VIPV_{NL}$ & $V2G_{DA}^{50\% SoC}$ scenario. The 11% increase in calendar ageing is due to the 131% increase in average DoD and the 21% increase in average SoC in the $VIPV_{NL}$ & $V2G_{DA}^{50\% SoC}$ scenario. The average SoC increased as the required grid connection for V2G services causes the vehicle to charge more often in the modelled scenario. The 9% increase in cycling ageing in the $VIPV_{NL}$ & $V2G_{DA}^{50\% SoC}$ scenario is due to the 44% increase in throughput compared to the $VIPV_{NL}$ scenario.
- The results suggest that uncontrolled V2G can be very harmful for cycle life, while controlled V2G could lower average SoC by regulating the SoC.
- In the $VIPV_{NL}$ & $V2G_{DA}^{50\% SoC}$ scenario, the battery's EoL is reached after 9.9 years, with a share of calendar and cycling ageing at EoL of 11.0% and 9.0%, respectively.

$V2G_{DA}^{50\% SoC}$ scenario

- In the $V2G_{DA}^{50\% SoC}$ scenario, the battery's EoL is reached after 9.9 years, with a share of calendar and cycling ageing at EoL of 11.0% and 9.0%, respectively.
- The results are similar to the $VIPV_{NL}$ & $V2G_{DA}^{50\% SoC}$ scenario, indicating that V2G governs ageing when combined with VIPV.

$V2G_{DA}^{20\% SoC}$ scenario

- Compared to the base scenario, the one-year calendar ageing is 5% higher and the one-year cycling ageing is 45% higher in the $V2G_{aFRR}^{20\% SoC}$ scenario, shortening battery life by up to 3.9 years. The 5% higher calendar ageing is due to the 3% increase in average SoC. The average SoC increases as V2G increases the grid charging frequency in the modelled scenario. The 45% increase in cycling ageing is due to the 126% increase in throughput, harming the battery due to extensive Li-ion intercalation. Li-ion intercalation causes, among other things, growth of the SEI layer as well as lithium plating. Thus, LFP-AM suggests that V2G services, with the aim of maximising profits for the EV owner, are also harmful to LFP battery life.
- Compared to the $V2G_{DA}^{50\% SoC}$, the one-year calendar ageing is 5% lower and the one-year cycling ageing is 23% higher in the $V2G_{DA}^{20\% SoC}$ scenario. The 5% lower calendar ageing is due to the 7% decrease in average SoC, as the V2G services allow the battery to be discharged to 20% SoC in this scenario. Thereby, a lower SoC retention effectively lowers the average SoC. The decrease in calendar ageing is the same as for the NMC battery. Thus, LFP-AM suggests that calendar ageing can be reduced using V2G by reducing the average SoC, which naturally occurs with a lower SoC retention limit during V2G services.
- In the $V2G_{DA}^{20\% SoC}$ scenario, the battery's EoL is reached after 8.8 years, with a share of calendar and cycling ageing at EoL of 9.9% and 10.1%, respectively.

$V2G_{aFRR}^{50\% SoC}$ scenario

- Compared to the $V2G_{DA}^{50\% SoC}$ scenario, the one-year calendar ageing is similar and the one-year cycling ageing is 39% lower in the $V2G_{aFRR}^{50\% SoC}$ scenario. It should be noted that two scenarios with different V2G services are being compared here.
- The 39% decrease in cycling ageing is due to the 24$ decrease in throughput in the $V2G_{aFRR}^{50\% SoC}$ compared to the $V2G_{DA}^{50\% SoC}$ scenario.

  While the cycle depth decreased by 20% decrease, which is beneficial for LFP cycle life [67], DoD is not considered as a stress factor in LFP-AM.

- The decrease in throughput suggests that with this aFRR modelling method, aFRR balancing services appear to demand less power compared to day-ahead electricity trading.
- The battery's EoL is reached after 11.5 years, with a share of calendar and cycling ageing at EoL of 12.9% and 7.1%, respectively.

$\mathbf{V2G_{aFRR}^{20\%\ SoC}}$ scenario

- Compared to the $V2G_{aFRR}^{50\%\ SoC}$ scenario, the one-year calendar ageing is similar and the one-year cycling ageing is 3% higher in the $V2G_{aFRR}^{20\%\ SoC}$ scenario. The 3% increase in cycling ageing is due to the 4% increase in throughput, which causes the lower SoC retention limit during V2G services.
- In the $V2G_{aFR}^{20\%\ SoC}$ scenario, the battery's EoL is reached after 11.4 years, with a share of calendar and cycling ageing at EoL of 12.7% and 7.3%, respectively. Thus, LFP-AM again suggests that additional battery cycling causes only a slight increase in cycling ageing capacity.

Notes and limitations

- According to Table 5.4, one-year calendar ageing appears to be dominant in the LFP battery. Simulations using LFP-AM show that calendar ageing remains dominant at higher battery temperatures.
- Capacity and power fade are not fed back into the data, which leads to ageing estimation errors.
- While LFP-AM is based on a cell comprising 3.00 Ah, the ageing stress factors used in the analysis are based on a cell comprising 4.85 Ah, which could lead to ageing estimation errors.
- The calendar ageing equations of the LFP model use LFP-motivated ageing stress factors and the cycling equations use NMC-based ageing stress factors to estimate ageing, which limits LFP-AM's applicability.

5.3.2. Base scenario analysis

Figure 5.10 shows the one-year SoC, temperature and LFP-AM capacity loss profiles for the base scenario. Calendar ageing appears dominant, as also discussed in Subsection 5.3.1.

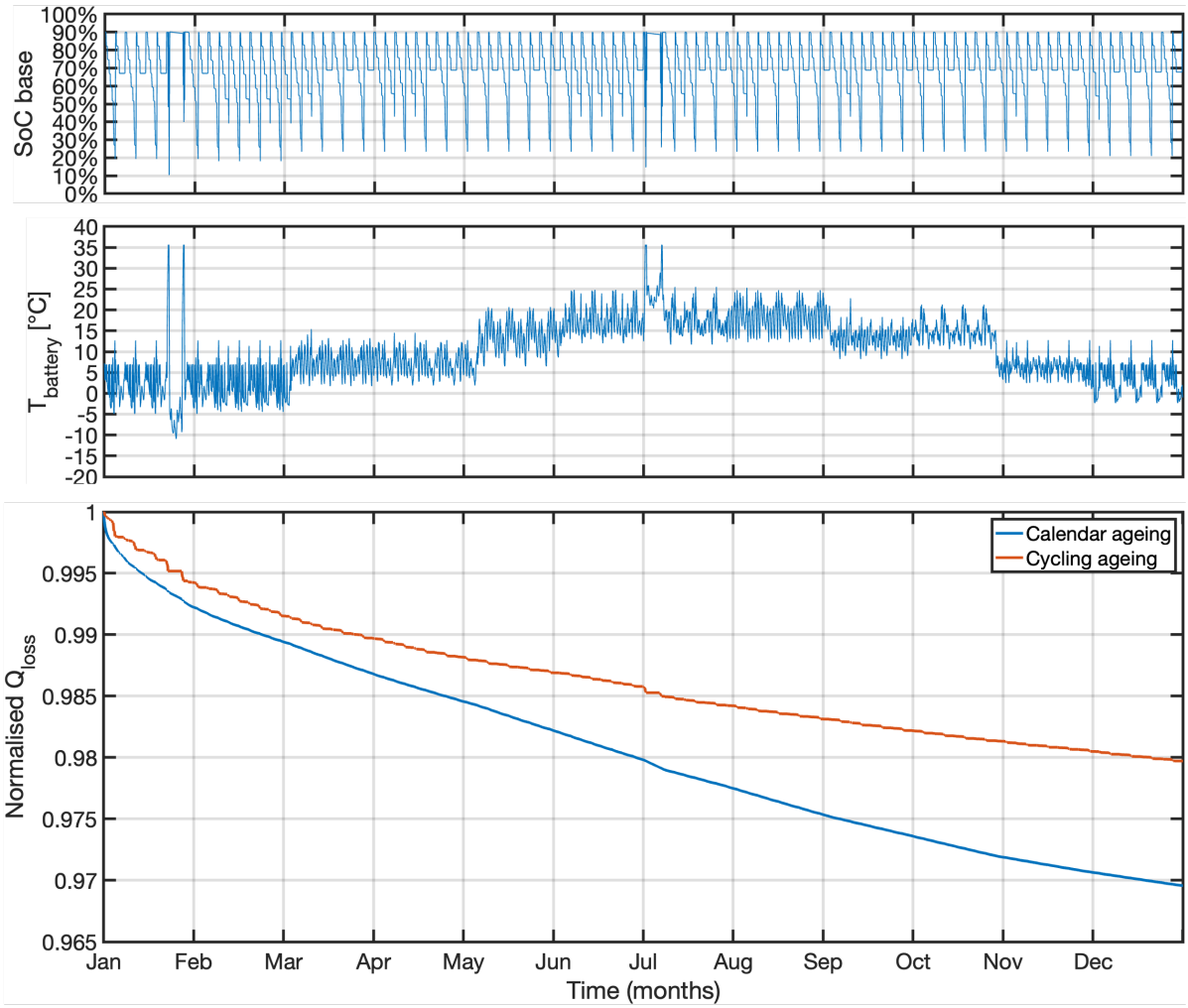

Figure 5.10: Base scenario: one-year SoC, temperature and Q_{loss} profiles for an LFP battery.

- Both the cycling and calendar ageing capacity loss profile follow the following relation: $-x^z$, where $0 \leq z \leq 1$. This exponential decay follows from the $\sqrt{t}$ factor in Equation 4.16 and the $\sqrt{Ah}$ factors in Equation 4.18 of LFP-AM.
- The exponential decay is in line with the electrochemical effects occurring in the battery cell. Like for NMC-AM, the SEI mainly forms in the first few cycles, after which the growth of the SEI layer scales with the square root of time and accelerates with higher SoC and higher temperatures. The growth of the SEI layer causes LLI and LAM, which causes capacity loss. A similar pattern can be seen in the calendar and cycling ageing capacity loss curves shown in Figure 5.10, where the most significant cycling ageing capacity loss occurs at the beginning of the year and eases over time.

5.3.3. VIPV scenario analysis

Figure 5.11 shows the one-year SoC, temperature and LFP-AM capacity loss profiles for the VIPV scenario in the Netherlands.

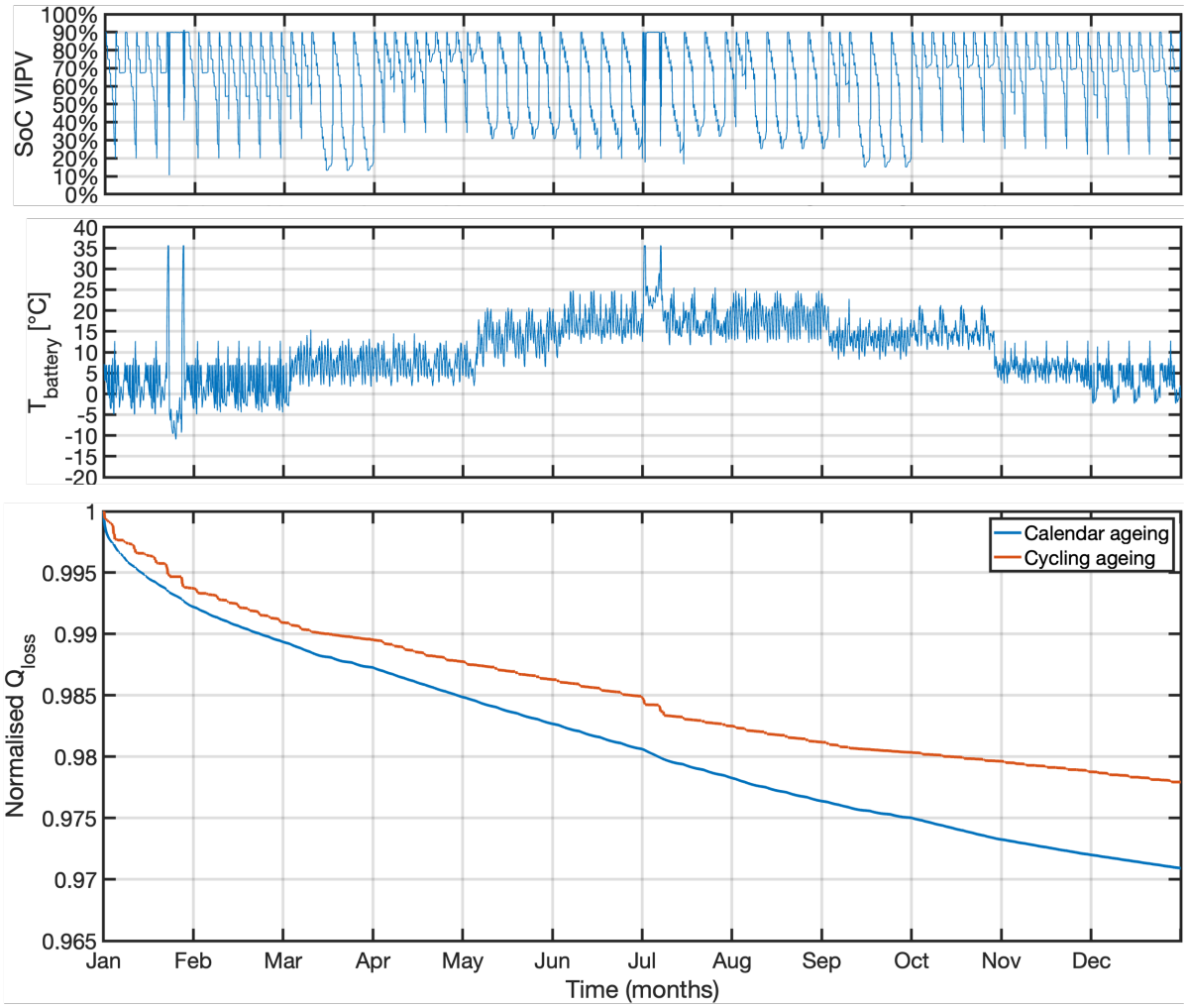

Figure 5.11: VIPV scenario: one-year SoC, temperature and Q_{loss} profiles for an LFP battery.

- Figure 5.11 illustrates shows how both the cycling and calendar ageing capacity loss profiles exhibit an exponential decay according to the growth pattern of the SEI layer.
- Compared to the base scenario, calendar ageing capacity loss is slightly less due to the lower average SoC and cycling ageing capacity loss is slightly more due to the increase in partial cycles, as discussed in Subsection 5.3.1.
- The decrease in calendar ageing capacity loss in the VIPV scenario illustrates how a lower SoC is also beneficial for LFP calendar life, as described in Subsection 2.1.3. Lower SoC is mainly beneficial because high SoC causes electrolyte dissolution. Electrolyte dissolution causes the SEI layer to grow further, which would cause LLI and LAM, resulting in capacity loss.

5.3.4. V2G scenario analysis

Figure 5.12 shows the one-year SoC, temperature and LFP-AM capacity loss profiles for the $V2G_{DA}^{20\%\ SoC}$ scenario in the Netherlands.

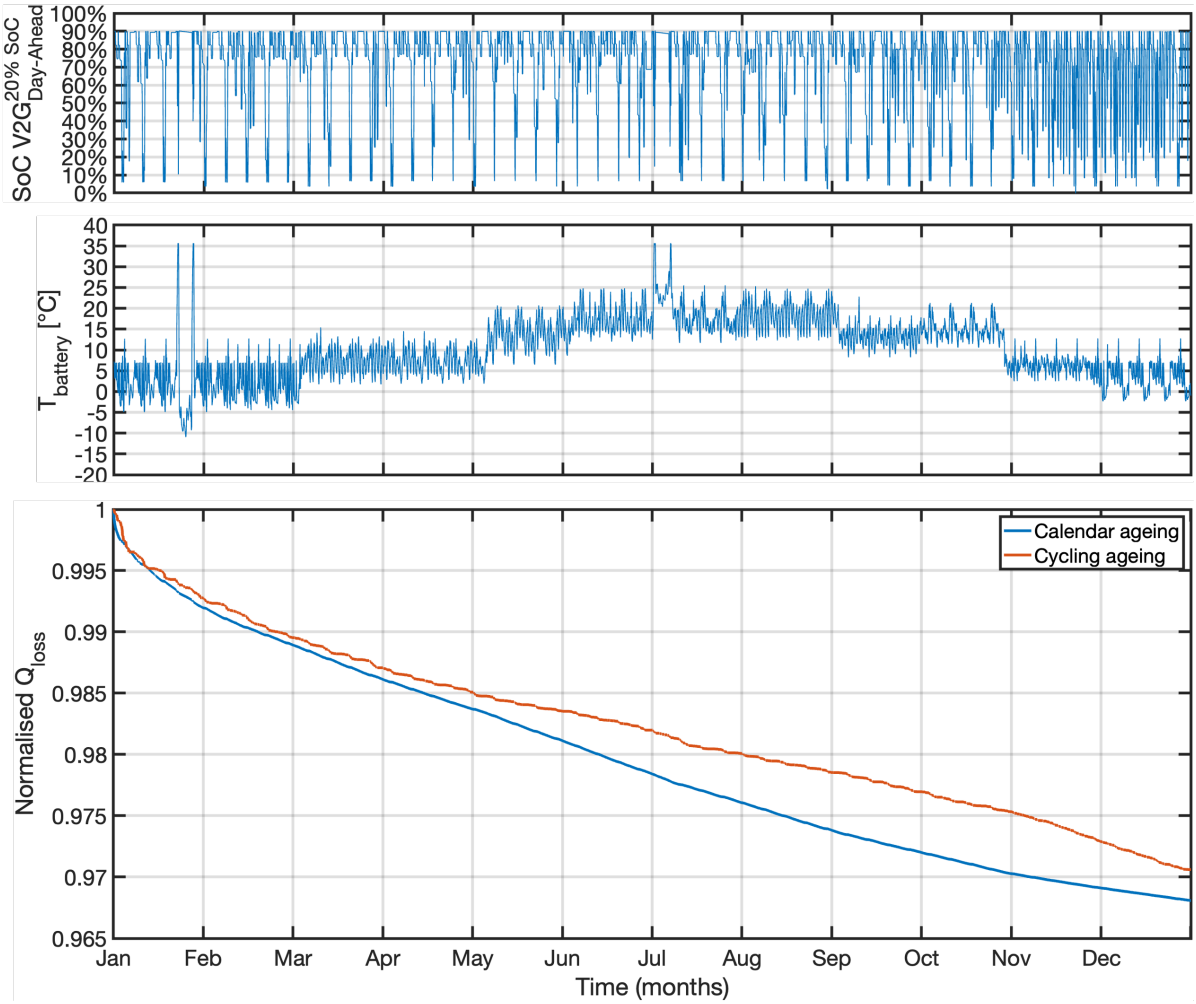

Figure 5.12: V2G scenario: one-year SoC, temperature and Q_{loss} profiles for an LFP battery.

- Figure 5.12 shows how the calendar ageing capacity loss profile exhibits an exponential decay with an steep capacity loss decrease during the summer months. The elevated temperatures during the summer months increase the Arrhenius reaction rate, accelerating the growth of the SEI layer growth. The SEI layer causes LLI and LAM, resulting in capacity loss. Following the temperature dependence on ageing, the calendar ageing capacity loss curve follows a wavy curve according to the seasonal temperature variations.
- The cycling ageing curve starts with an exponential decay governed by the growth pattern of the SEI layer.
- Like for NMC-AM, the SoC profile exhibits increased SoC variations in November and December due to increased battery cycling for V2G day-ahead electricity trading. The additional Li-ion intercalation due to additional cycling causes, among other things, further growth of the SEI layer as well as lithium plating. Both SEI layer growth and lithium plating cause LLI and LAM, resulting in capacity loss, causing a steeper cycling ageing capacity loss curve towards in November and December.

5.4. Ageing comparison of NMC-AM and LFP-AM

5.4.1. Overview of ageing characteristics

Similarly to Tables 5.1 and 5.3, the table shows the one-year calendar, cycling and total ageing. $Q^{cell}_{throughput}$ is the net energy delivered by a single cell throughout the whole year. $N_{eq.\ full\ cycles}$ is the corresponding full equivalent discharge cycles given that the cell on which the ageing stress factors are based comprises a usable capacity of 4.85 Ah, even though the ageing models are based on a different-sized cells. $N_{partial\ cycles}$ is the number of partial cycles as defined in Subsection 3.2.11. SoC_{avg} is the average SoC. DoD_{avg} is the average cycle depth of the partial cycles. The EoL of each scenario according to the ageing models are found in Tables 5.1 and 5.3 for NMC-AM and LFP-AM, respectively. The temperature profiles are identical in all the scenarios. Moreover, all scenarios model a Lightyear 0 vehicle covering a distance of 19,190 km per year. The share of calendar and cycling ageing at the battery's EoL as determined by LFP-AM are described in the discussion below the table.

Table 5.6: One-year calendar and cycling ageing capacity loss according to NMC-AM and LFP-AM.

Scenario		NMC-AM	LFP-AM
Base	Calendar ageing	1.05%	3.04%
	Cycling ageing	2.80%	2.03%
	Total ageing	3.85%	5.07%
$VIPV_{NL}$	Calendar ageing	0.97%	2.91%
	Cycling ageing	2.81%	2.21%
	Total ageing	3.78%	5.12%
$VIPV_{ESP}$ with T_{ESP}	Calendar ageing	1.26%	3.02%
	Cycling ageing	2.86%	2.07%
	Total ageing	4.12%	5.09%
$VIPV_{NL}$ & $V2G^{50\%\ SoC}_{DA}$	Calendar ageing	1.14%	3.36%
	Cycling ageing	5.46%	2.40%
	Total ageing	6.60%	5.76%
$V2G^{50\%\ SoC}_{DA}$	Calendar ageing	1.14%	3.36%
	Cycling ageing	5.48%	2.40%
	Total ageing	6.62%	5.76%
$V2G^{20\%\ SoC}_{DA}$	Calendar ageing	1.08%	3.19%
	Cycling ageing	8.78%	2.94%
	Total ageing	9.86%	6.13%
$V2G^{50\%\ SoC}_{aFRR}$	Calendar ageing	1.23%	3.64%
	Cycling ageing	4.83%	1.78%
	Total ageing	6.06%	5.42%
$V2G^{20\%\ SoC}_{aFRR}$	Calendar ageing	1.22%	3.63%
	Cycling ageing	4.80%	1.83%
	Total ageing	6.02%	5.46%

5.4.2. Comparative analysis of NMC-AM and LFP-AM

Figure 5.13 shows the one-year SoC, temperature profiles and capacity loss profiles according to NMC-AM and LFP-AM. The profiles batteries for the base scenario in the Netherlands. Table 5.6 provides an overview of the results from both NMC-AM and LFP-AM for each use case scenario with their corresponding one-year use case characteristics.

According to the ageing models, for the base scenario, capacity loss due to calendar ageing is 189% higher in LFP-AM and cycling ageing 28% lower compared to NMC-AM. Thus, the ageing models suggest that additional battery cycling causes less harm for the LFP battery as for the NMC battery.

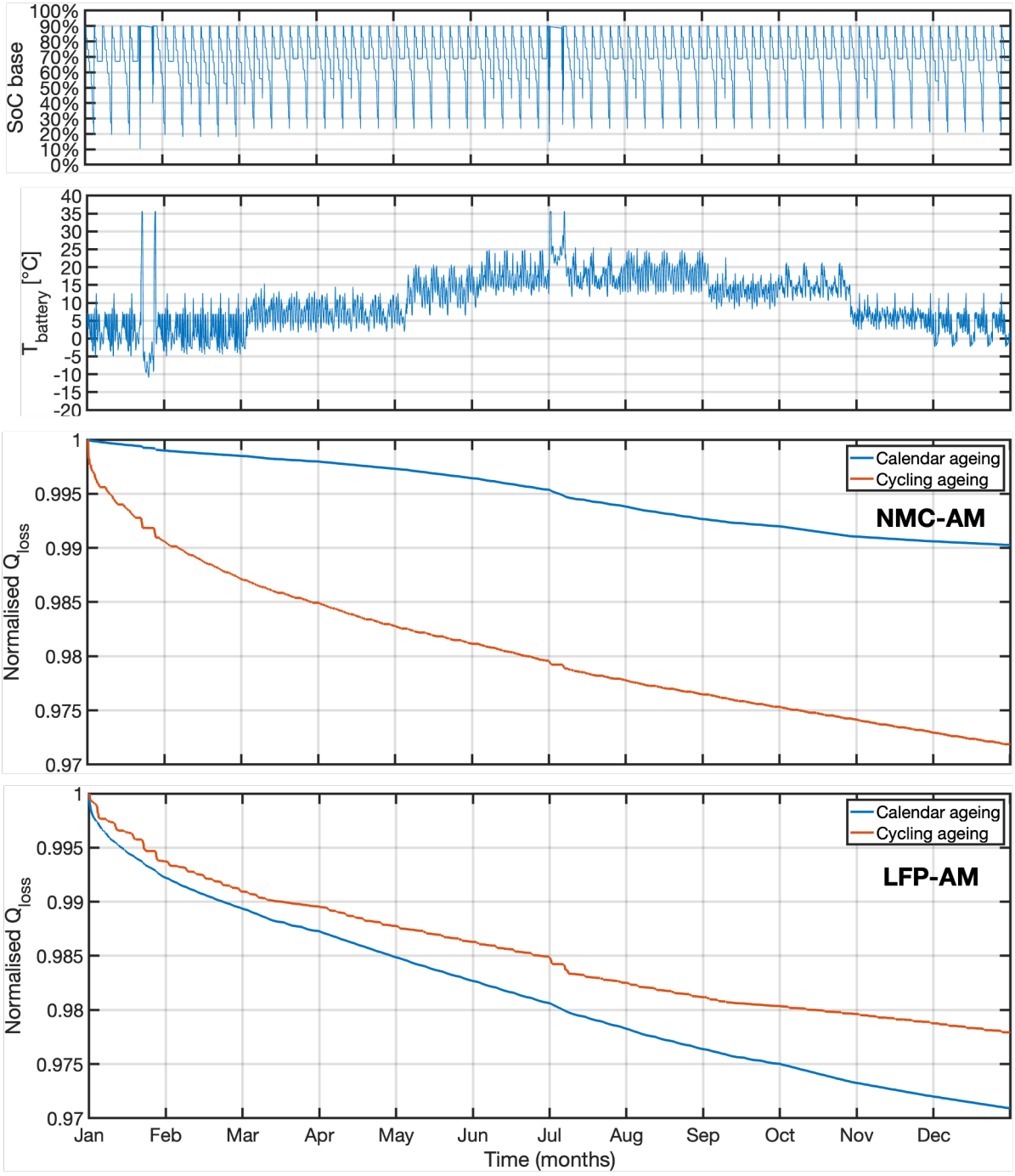

Figure 5.13: NMC and LFP battery ageing comparison: one-year SoC, temperature and Q_{loss} profiles.

- Table 5.6 shows that according to NMC-AM, cycling ageing is dominant in every modelled NMC scenario, while according to LFP-AM, battery calendar ageing is dominant in every modelled LFP scenario.
- In contrast to NMC-AM, the ageing equations of LFP-AMII correlate both calendar and cycling ageing with temperature.
- As shown in the capacity loss profiles of Figure 5.13, according to NMC-AM and LFP-AM, for the NMC battery, calendar ageing at 10 °C is less significant compared to the cycling ageing. In contrast, for the LFP battery, cycling ageing at 10 °C appears to be more significant than calendar ageing.
- Comparing the $V2G_{DA}^{20\%\ SoC}$ scenario with the base scenario for both NMC-AM and LFP-AM, one-year cycling ageing capacity loss increased 214% in the NMC battery and only 44% in the LFP battery. This is in line with the comparative battery analysis of Figure 2.2 which shows that LFP batteries are more resistant to ageing compared to NMC batteries. The authors of the paper specifically mention that LFP have a long cycle life [55].
- Therefore, NMC-AM and LFP-AM suggest that additional battery cycling for V2G services causes less harm for the LFP battery than for the NMC battery. Thus, the results suggest that LFP batteries could be the favoured battery chemistry for EVs participating in V2G services.
- According to NMC-AM, compared to the base scenario, VIPV lowered calendar ageing by 8% in the Netherlands and 9% in Spain. According to LFP-AM, VIPV lowered calendar ageing by 4% in the Netherlands and 10% in Spain for the same relative difference in SoC.
- Figures 8.10 and 8.11 show the V_{OC}(SoC) relations of the NMC and LFP batteries, respectively, that were used in NMC-AM and LFP-AM. The V_{OC}(SoC) curve of the LFP battery appears to be almost between the 10% and 95% SoC, which is typical for LFP batteries.
- It should be noted that the comparison between NMC-AM and LFP-AM is limited for several reasons. First, only one chemical composition of each battery cell is used in the analysis. The characteristics of the battery cells heavily depend on the chemical composition of the metals in the cell. E.g., the ageing results of an 8:1:1 NMC battery cell (80% Ni, 10% Co, 10% Mn) are expected to deviate from the ageing results of an 1:1:1 NMC battery cell. Second, the ageing stress factors used in the calendar ageing equation of LFP-AM is NMC-motivated, and the ageing stress factors used in the cycling ageing equations of LFP-AM are NMC-based.
- It is remarkable that for the NMC battery, the one-year cycling ageing was 94% higher in the $VIPV_{NL}$ & $V2G_{DA}^{50\%\ SoC}$ scenario compared to the $VIPV_{NL}$ scenario, while for the LFP battery, cycling ageing is only 9% higher in the same comparison. Thus, LFP-AM suggests that while additional cycling causes additional cycling ageing for the LFP battery, it causes less additional cycling ageing for the LFP battery than for the NMC battery, which is in line with literature [10].

6

Investigating methods to extend battery calendar life

In this chapter, methods to reduce battery ageing are investigated. While EV batteries are often regulated to reduce ageing during use, they are generally left to degrade during parking periods. Considering that EVs are parked for over 90% of the time [3], battery SoC and temperature regulation during parking periods can potentially reduce calendar ageing. This chapter investigates methods to influence SoC and battery temperatures using VIPV and V2G. Thus, in this chapter, the third sub-objective is further addressed:

iii *Compare the ageing results of the use case scenarios to analyse the impact of VIPV and V2G on battery calendar and cycling ageing.*

Section 6.1 examines the impact of SoC regulation using VIPV and V2G on calendar ageing, after which Section 6.2 investigates the technical feasibility of using VIPV to regulate battery temperature and features a battery temperature sensitivity analysis to determine the potential impact of VIPV-powered temperature regulation on battery life. Considering the limitations of LFP-AM as discussed in Chapter 4, NMC-AM is used for simulating scenarios throughout this chapter.

6.1. Impact of SoC regulation on calendar life

Researchers have found that simply delaying charging to keep the battery's SoC low for an extended period of time, at 25 °C can potentially extend battery life by 1.5 years, while an optimised charging strategy can potentially extend battery life by up 2.6 years [33, 98]. In contrast, Dubarry et al. (2017) found the effect of delayed charging on battery life to be negligible at room temperature, but mention that the effect could be significant at higher temperatures. Considering that the effects of SoC and battery temperature on ageing are intercorrelated, the effect of lower SoC at both low and high temperatures is researched.

To investigate this, scenarios were simulated in which the EV battery was kept constant at 50% SoC and 100% SoC for a whole month per year, both at an average annual battery temperature of 10 °C and 20 °C. These scenarios use the base use case scenario modelled in Chapter 3, in which the EV is parked during a one-month holiday in March. The one-year battery datasets were repeated for multiple years to determine the impact of SoC on the battery's lifetime. Both calendar and cycling ageing are considered to determine the battery's EoL, defined as the year in which the battery reaches a total capacity loss of 20% compared to its initial capacity.

Regulating the SoC could be done by delaying VIPV charging, by charging and discharging the battery using V2G, or by powering electronics in the EV, such as the battery thermal management system.

Figure 6.1 shows the one-year SoC profiles of these scenarios. The battery temperature varies according to the battery temperature profile modelled in Chapter 3.

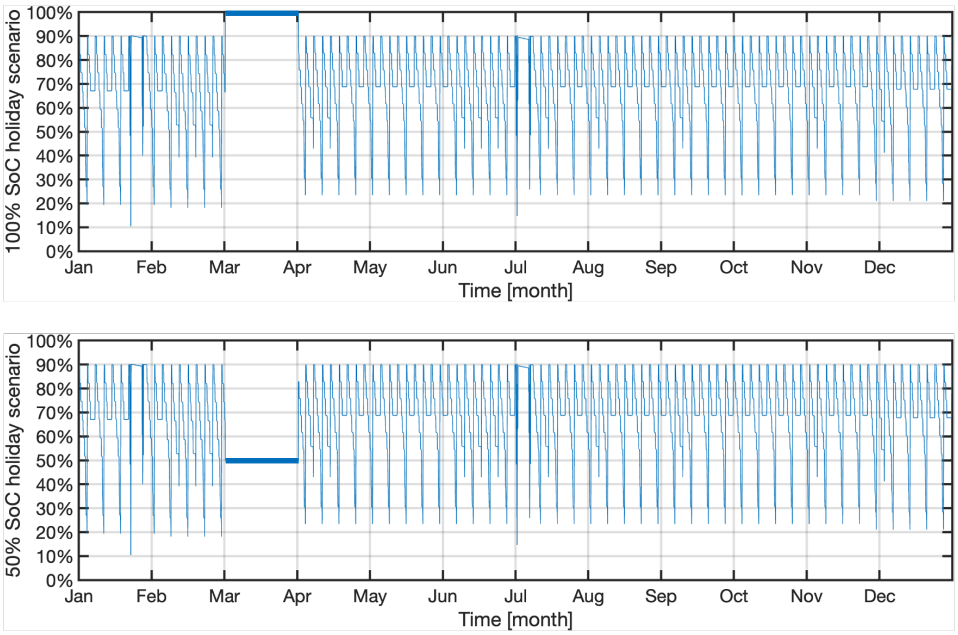

Figure 6.1: One-year SoC profiles for an EV in the base scenario, in which the EV is parked for a whole month. The top graph illustrates the scenario in which the EV is parked with a constant 100% SoC, and the bottom graph illustrates the scenario in which the EV is parked with a constant 50% SoC.

6.1.1. Impact of SoC regulation at low temperatures

In the scenario in which the battery was kept at 100% SoC in March with an average annual battery of 10 °C, according to NMC-AM, the battery reaches its EoL after 14.7 years. In the simulated scenario in which the battery was kept at 50% SoC in March, according to NMC-AM, the battery reaches its EoL after 16.7 years, indicating that 50% SoC regulation for one month per year increased the battery's lifetime by 2 years or 14%.

6.1.2. Impact of SoC regulation at high temperatures

The battery temperature is increased by 10 °C at every time step throughout the year, increasing the annual average battery temperature to 20 °C.

In the scenario in which the battery was kept at 100% SoC in March with an average annual battery of 20 °C, according to NMC-AM, the battery reaches its EoL after 7.7 years. In the scenario in which the battery was kept at 50% SoC in March with an average annual battery of 20 °C, according to NMC-AM, the battery reaches its EoL after 8.6 years, indicating that 50% SoC regulation for one month per year increased the battery's lifetime

by 13 months or 12%. Thus, the analysis shows that according to NMC-AM, lowering the SoC for an extended period of time impacts calendar ageing less at lower ambient temperatures, but could increase battery life at higher ambient temperatures. Further research is required to accurately determine the impact of higher SoC at different ambient temperatures on calendar ageing.

6.2. Impact of temperature regulation on calendar life

In section 5.1, to accurately analyse the impact of VIPV in Spain, a 'Spain' base scenario was modelled in which annual battery temperatures ranged 3.3 °C higher than in the Netherlands. In the analysis, NMC-AM shows that calendar ageing would increase by 32% in the base scenario due to higher temperatures. Thus, according to NMC-AM, higher battery temperatures can heavily impact battery life, indicating that regulating battery temperature may extend battery life.

EVs are expected to be driven in countries with hot and sunny climates in which average annual battery temperatures range significantly higher than the scenarios analysed in Chapter 5. For example, the average annual ambient temperature in the United Arab Emirates (UAE) is found to range about 15 °C higher compared to the Netherlands [110, 111]. In SEVs, power to regulate battery temperature could be sourced from the grid, the battery or from VIPV. Considering that EVs are not always connected to a charging point and considering that sourcing energy from the battery would cause additional cycling ageing, the technical feasibility of sourcing energy from VIPV to regulate battery temperature is investigated.

6.2.1. Technical analysis of VIPV-powered battery temperature regulation

NMC-AM is used to analyse to what extent higher temperatures could accelerate battery ageing compared to the Netherlands. As explained in Section 4.2, NMC-AM includes the temperature factor only in the calendar ageing equation.

Lowering the battery temperature

Equation 6.1 can be used to determine the amount of energy required to power the HVAC system to cool the battery. A scenario is considered in which the EV battery is cooled by 10 °C, e.g. from 35 °C to 25 °C.

$$E_{\text{req}}^{\text{HVAC}} = \frac{c \cdot \Delta T}{3{,}600 \cdot COP} \tag{6.1}$$

with a total heat capacity c of $380 \cdot 10^3$ J/K, a temperature difference ΔT of 10 °C, and a COP of 2.5, the EV's cooling system would require $E_{\text{req}}^{\text{HVAC}}$ = ($c \cdot \Delta\ T$) / 3,600 · COP = (10 K · 380 kJ/K) / (3,600 · 2.5) = 422 Wh of electrical energy. The heat capacity is based on Lightyear's battery pack, as described in Subsection 3.2.7. As COP values generally range between 2 and 4, 2.5 is assumed to be a conservative estimate for the HVAC's COP.

As seen in Section 3.3, during a sunny hour, 5 m^2 of VIPV can generate 400-600 W of power in the Netherlands and between 600-800 W in Spain. This indicates that the solar panels are able to produce enough power to cool the battery temperature by 10 °C in a single sun hour or less. The UAE sees at least 10 hours of sun even in the shortest winter days [112], indicating the high potential of VIPV for regulating battery temperature in sunny climates. Moreover, according to the ageing equations of NMC-AM given in Section 4.2, lowering the battery temperature by a single degree would already be beneficial for calendar life.

Keeping the battery temperature low

Equation 6.2 is used to determine the amount of power required to keep the battery temperature lower than its surrounding ambient temperature. A scenario is considered in which the battery temperature is kept 10 °C lower than the ambient temperature, e.g. to keep the battery temperature constant at 25 °C with a surrounding ambient temperature of 35 °C.

$$P_{\text{req}}^{\text{HVAC}} = \frac{h \cdot A \cdot \Delta T}{COP} \tag{6.2}$$

with a heat transfer coefficient h of 15 W/(m^2 · K), a battery pack area A of 2.88 m^2, a temperature difference ΔT of 10 °C, and COP of 2.5, the EV's cooling system would require $P_{\text{req}}^{\text{HVAC}}$ = *(*$h \cdot A \cdot \Delta T$*)* / COP = (15 W/(m^2 · K) · 2.88 m^2 · 10 K) / 2.5 = 173 W of electrical energy. The heat transfer coefficient and battery pack area are based on Lightyear's battery pack, as described in Subsection 3.2.7.

Considering a conservative VIPV power generation during sun hours of 400 W in the Netherlands and 600 W in Spain, VIPV could cool the battery by ΔT = *(*$P_{\text{potential}} \cdot COP$*)* / *(*$h \cdot A$*)* = 23 °C in the Netherlands and 35 °C in Spain.

6.2.2. Potential impact of VIPV-powered battery temperature regulation

According to NMC-AM in the Netherlands, where the modelled average annual battery temperature is 10 °C, the annual calendar ageing was 1.05%. To determine potential impact of VIPV-powered battery temperature regulation at high temperatures, the UAE was considered. To determine the annual calendar ageing in UAE, 15 °C is added to the battery temperature at every time step throughout the year, increasing the annual average battery temperature to 25 °C. In contrast to the previous chapters, in this analysis, the battery temperature was not capped at 35.4 °C. According to NMC-AM, the increase in battery temperature caused an annual calendar ageing capacity loss of 3.53%, indicating that calendar ageing in the simulated scenario would accelerate by three to four times in UAE compared to the Netherlands. It should be noted that the battery cell used for NMC-AM originates from 2012 and is designed for e-bikes, radios, medical devices and robotics, as shown in Figure 8 of the appendix, which could lead to overestimation errors on the impact of temperature.

To determine the impact of battery temperature on battery calendar life, scenarios with different annual average battery temperatures are modelled. Assuming that solar panels can reduce the annual average battery temperature by an estimated 5 °C, in the scenarios used for the sensitivity analysis, the battery temperatures varied from 25 °C to 10 °C in steps of 5 °C. The SoC and corresponding T_{batt} profiles are shown in Figure 6.2. From top to bottom, these temperature profiles could represent annual battery temperatures in UAE, Isreal, Madrid and the Netherlands. NMC-AM is subsequently used to determine the calendar ageing in each scenario, which is elaborated below.

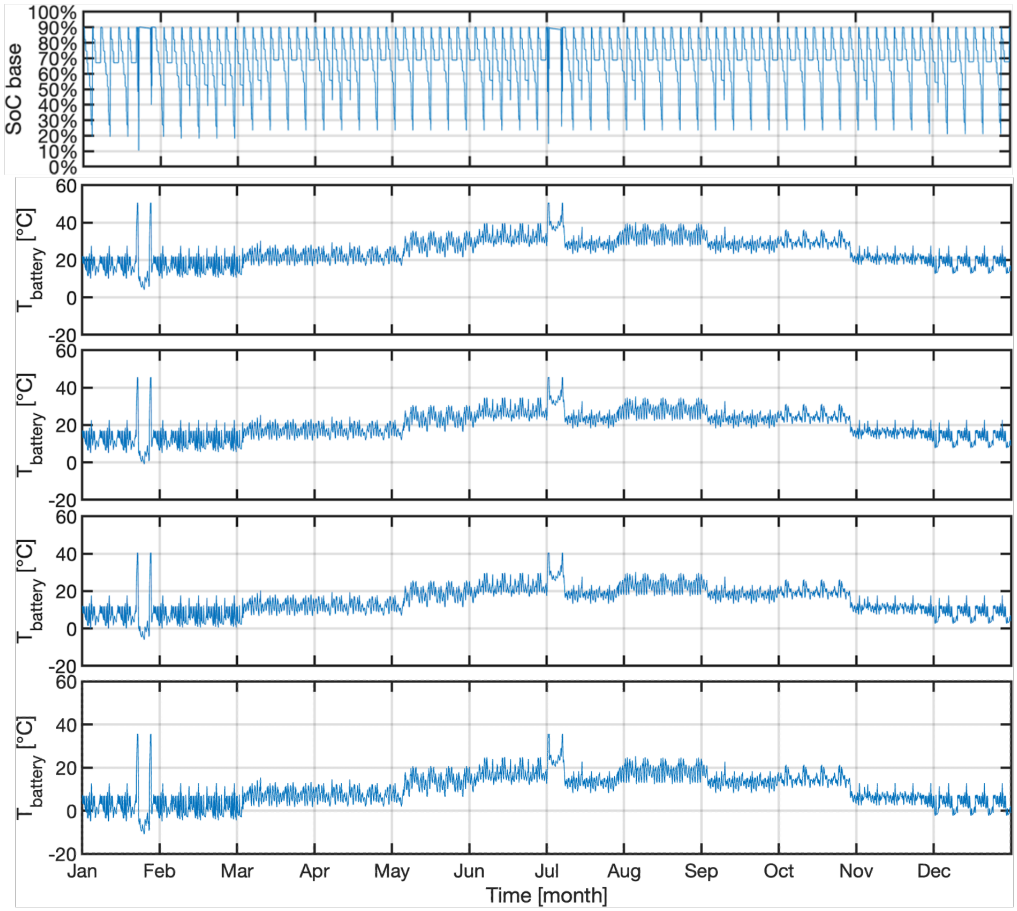

Figure 6.2: From top to bottom: SoC profile used throughout the four scenarios, battery temperature profile with an average battery temperature of 25 °C, 20 °C, 15 °C, and 10 °C.

As mentioned before, EoL is defined as the moment in time at which the battery has retained 80% of its initial capacity. The battery data is developed using the EV battery data generation model described in Chapter 3, in which an annual driving distance of 19,190 km is simulated. The results of the temperature sensitivity analysis according to NMC-AM are summarised in Table 6.1 below.

Table 6.1: Sensitivity analysis results of battery temperature on battery ageing.

Average annual T_{batt}	25 °C	20 °C	15 °C	10 °C
EoL	5.6 years	8.3 years	11.6 years	16.2 years
Distance driven	108,000 km	159,000 km	223,000 km	311,000 km
Increased lifetime & range compared to scenario with 5 °C higher annual average T_{batt}	-	+47%	+40%	+40%

The table shows that according to NMC-AM, if VIPV lowers the average annual battery temperature by 5 °C, total battery life could extend by up to 4.6 years, adding 88,000 km of driving range to its lifetime.

6.3. Conclusions

Simulations using NMC-AM suggest that SoC regulation can extend NMC battery life cell by 2 years, allowing for 38,000 km of additional driving range before the battery reaches its EoL. Additionally, simulations using NMC-AM suggest that VIPV-powered battery temperature regulation can extend NMC battery life by up to 4.6 years, allowing for 88,000 km of additional driving range before the battery reaches its EoL. It should be noted that the cell on which the implemented ageing model is based originates from 2012, which could lead to ageing estimation errors. It is recommended to conduct further research on the impact of SoC and temperature regulation on newer NMC and LFP cells used in EVs. Additionally, further research could determine to what extent VIPV can reduce battery temperature for different geographical locations.

SoC regulation can be performed using delayed VIPV charging, delayed grid charging, or V2G. Battery temperature regulation can be performed using VIPV power or grid power. The required grid connection for V2G simultaneously allows for EVs to use grid power to regulate battery temperature. Taking electricity cost into account, grid-powered battery temperature regulation could be a cost-effective method to extend battery life, especially for EVs experiencing extreme temperatures.

In summary, initial findings suggest that VIPV and V2G can regulate SoC and temperature during parking periods to extend battery life, potentially further improving the economic viability of VIPV and V2G.

7

Conclusions and recommendations

This chapter summarises the contributions of this work and recommends future lines of research emerging from it.

7.1. Conclusions

The EU's plan to electrify its transportation sector can cause power grid congestion and electricity shortage risks for power grid operators. EVs equipped with VIPV and EVs using V2G technology can support grid operators in overcoming these challenges. By charging and discharging the EV battery, the technologies impact the battery's lifespan. As batteries are expected to remain the most expensive subsystem of EVs, the impact of VIPV and V2G on battery life governs their economic viability. Current studies on the impact of VIPV and V2G on battery life are generally simplistic and use unrealistic battery data. Additionally, there is a lack of literature on methods to extend battery life using VIPV and V2G. To fill this research gap, the following research objective was formulated:

Determine the impact of vehicle-integrated photovoltaics and vehicle-to-grid on electric vehicle battery life.

To fulfil this research objective, four sub-objectives were addressed. The methods used to achieve these sub-objectives as well as the drawn conclusions are elaborated upon below.

i *Simulate use case scenarios with and without VIPV and V2G to generate one-year EV battery datasets.*

The first sub-objective was approached by developing an EV battery data generation model to simulate EV use case scenarios with and without VIPV and V2G. A one-year mobility and charging profile was constructed based on EV driving data in the Netherlands and Germany. Using Lightyear's VPM, which has been validated on the sub-system level, five driving cycles were simulated to generate per-second EV battery data, including battery SoC, temperature, voltage, current, C-rate, number of cycles, and throughput. Using Lightyear's SolarSimulator tool, load profiles were modelled for VIPV power generation in Netherlands and Spain. Load profiles were modelled for V2G day-ahead electricity trading and aFRR, both with a battery capacity retention limit during V2G of 50% SoC and 20% SoC. Subsequently, these VIPV and V2G load profiles were merged with EV load profiles to generate eight one-year EV battery datasets. These EV battery datasets represent use case scenarios of an EV with and without VIPV and V2G. Finally, the EV battery data generation model was validated by comparing ageing stress factors derived from the EV battery data generation model with validated data from the VPM.

ii *Implement the EV battery datasets into battery ageing models from literature to quantify battery calendar and cycling ageing for each use case scenario.*

To fulfil the second sub-objective, three ageing models were implemented. The first NMC-based ageing model (NMC-AM) was implemented based on its description from its paper [84]. The second NMC-based ageing model (NMC-AMII) could not be used to compare ageing in the different scenarios due to its limited applicability to battery data. However, NMC-AMII could be used to benchmark results from NMC-AMI.

The LFP-based ageing model (LFP-AM) was also implemented based on its description from its paper [81]. Following this, the eight EV battery datasets were implemented in NMC-AM and LFP-AM to determine the capacity loss due to calendar and cycling ageing in each use case scenario. To more accurately determine the impact of VIPV on battery life in Spain, a sub-scenario of the base scenario was modelled in which the battery temperature was increased to account for higher ambient temperatures in Spain.

iii *Compare the ageing results of the use case scenarios to analyse the impact of VIPV and V2G on battery calendar and cycling ageing.*

The third sub-objective was approached by comparing the one-year capacity loss due to calendar and cycling ageing for the eight use case scenarios according to NMC-AM and LFP-AM. The differences in ageing were explained using the one-year use case characteristics of each scenario, such as annual throughput, number of cycles, average SoC and EoL. Additionally, ageing patterns of calendar and cycling ageing were substantiated by describing the effects of electrochemical ageing mechanisms. Moreover, the ageing characteristics of NMC-AM and LFP-AM were compared. Finally, methods to reduce battery ageing were investigated.

The most significant results of NMC-AM and LFP-AM on the impact of VIPV and V2G on battery calendar and cycling ageing are summarised below. Following this, a concise comparison is given on NMC and LFP battery ageing according to NMC-AM and LFP-AM, after which methods to reduce battery ageing using VIPV and V2G are proposed. Finally, the main limitations of semi-empirical ageing models found in literature are described.

NMC-AM

Impact of VIPV on NMC calendar ageing according to NMC-AM

As VIPV gradually charges the battery, it can reduce the grid charging frequency by 23% in the Netherlands and 44% in Spain, causing the average annual SoC to range 9% lower in the Netherlands and 16% lower in Spain. Lower SoC is beneficial for calendar ageing as higher SoC accelerates the growth of the SEI layer, which causes calendar ageing. NMC-AM suggests that VIPV can reduce one-year calendar ageing capacity loss by 8% in the Netherlands and by 9% in Spain. Simulations show that over a 20-year period, VIPV can reduce NMC calendar ageing by 9% in the Netherlands and by 8% in Spain. The reduction in calendar ageing is due to a decrease in SoC due to gradual VIPV charging. Including the effect of cycling ageing, NMC-AM suggests that VIPV could extend the battery's life by 6 months in both the Netherlands and Spain. The results show that VIPV is beneficial for calendar ageing up to a certain threshold, indicating that when this threshold is met, VIPV power could better be used for other purposes, such as the thermal battery management system or V2G.

Impact of VIPV on NMC cycling ageing according to NMC-AM

Results showed that VIPV can reduce the average cycle depth by 28%, which according to de Hoog et al. (2017) is beneficial for battery cycling life. Moreover, simulations show that VIPV can reduce the battery's annual throughput by 26 kWh, indicating that VIPV can occasionally power the EV drivetrain directly, bypassing the battery, which can reduce cycling ageing. In contrast, results from NMC-AM suggest an increase in cycling ageing in the $VIPV_{NL}$ scenario. Due to limitations of the ageing models, the impact of VIPV on battery cycle life could not be accurately determined.

Impact of V2G on NMC calendar ageing according to NMC-AM

NMC-AM suggests that in the modelled scenario, V2G aFRR can increase one-year calendar ageing capacity loss by up to 17% due to a 22% increase in SoC, as higher SoC causes electrolyte dissolution, which accelerates the growth of the SEI layer. Due to the increased grid connection required for V2G services, uncontrolled V2G can cause the battery's SoC to increase, which increases calendar ageing. NMC-AM suggests that if the EV allows V2G services to discharge the battery to a lower capacity retention limit during V2G, SoC can be reduced, which reduces calendar ageing. In case the capacity retention limit during V2G is 20% SoC, NMC-AM suggests that calendar ageing can be reduced by 5% compared to a 50% SoC retention limit. By implementing a controlled V2G strategy that lowers the average SoC, V2G can reduce calendar ageing.

Impact of V2G on NMC cycling ageing according to NMC-AM

NMC-AM suggests that V2G day-ahead electricity trading with a 20% SoC retention limit during V2G can increase one-year cycling ageing by up to 214% compared to the base scenario, which would shorten battery life by up to 12.5 years. This large increase in cycling ageing is due to a 126% increase in throughput, which

due to additional Li-ion intercalation causes, among other things, further growth of the SEI layer and lithium plating.

LFP-AM

Impact of VIPV on LFP calendar ageing according to LFP-AM

LFP-AM suggests that VIPV can reduce one-year calendar ageing capacity loss by 4% in the Netherlands and by 10% in Spain due to a decrease in SoC. As mentioned before, results show that VIPV can reduce the grid charging frequency by 23% in the Netherlands and by 44% in Spain, causing the average annual SoC to range lower. Lower SoC due to gradual VIPV charging can reduce calendar ageing up to a certain threshold. If this threshold is crossed, additional VIPV charging could increase SoC, which could accelerate calendar ageing. Simulations show that over a 20-year period, VIPV can reduce LFP calendar ageing by 6% in the Netherlands and by 9% in the Spain.

Impact of VIPV on LFP cycling ageing according to LFP-AM

As mentioned before, according to the one-year use case characteristics, VIPV reduces the average cycle depth and the battery's annual throughput by 26 kWh, which are thought to reduce cycling ageing. However, LFP-AM suggests that VIPV can increase one-year cycling ageing capacity loss by 9% in the Netherlands and 24% in Spain. Considering the complexity of the various effects of VIPV on cycling ageing, it is concluded that the impact of VIPV on cycling ageing requires further research.

Impact of V2G on LFP calendar ageing according to LFP-AM

LFP-AM suggests that V2G aFRR can increase one-year calendar ageing capacity loss by up to 16% due to a 22% increase in SoC. Higher SoC causes electrolyte dissolution, which accelerates the growth of the SEI layer. Like for NMC-AM, for uncontrolled V2G, the increased grid connection required for V2G services can increase SoC, which increases calendar ageing. Thus, controlled V2G could lower calendar ageing by regulating SoC. In case the capacity retention limit during V2G is 20% SoC, LFP-AM suggests that calendar ageing can be reduced by 5% compared to a 50% SoC retention limit due to deeper discharge cycles causing a decrease in SoC.

Impact of V2G on LFP cycling ageing according to LFP-AM

LFP-AM suggests that V2G day-ahead electricity trading with a 20% SoC retention limit during V2G can increase one-year cycling ageing capacity loss by 45%, which could shorten battery life by 3.9 years. The increase in cycling ageing is due to a 126% increase in throughput, which due to additional Li-ion intercalation causes, among other things, further growth of the SEI layer and lithium plating. However, V2G caused battery life to shorten significantly less in LFP-AM compared to NMC-AM.

Ageing comparison of NMC-AM and LFP-AM

According to the ageing models, cycling ageing was dominant in every simulated NMC scenario, while calendar ageing was dominant in every simulated LFP scenario. Moreover, according to NMC-AM and LFP-AM, the modelled LFP battery appeared to be more resistant to additional cycling compared to the modelled NMC battery, which is in line with literature. Due to its resistance to additional cycling, simulations indicate that LFP batteries could be favoured over NMC batteries for EVs participating in V2G. Furthermore, according to the ageing models, for NMC, calendar ageing at 10 °C is less significant compared to cycling ageing. In contrast, for LFP, cycling ageing at 10 °C appears to be more significant than calendar ageing.

Investigating methods to reduce battery ageing

As high SoC and battery temperatures accelerate calendar ageing due to SEI layer growth, regulating SoC and battery temperature could extend battery life. Therefore, SoC and battery temperature regulation are investigated as methods to reduce calendar ageing.

Simulations show that if battery charge is kept at 50% SoC instead of 100% SoC for a whole month each year, at an average battery temperature of 10 °C, SoC regulation could extend battery life by 2 years, allowing for 38,000 km of additional driving range before the battery reaches its EoL. Controlled V2G can be used to cycle V2G services at mid-levels SoC, which is beneficial for calendar life. SoC regulation could be performed by delaying charging using VIPV, by delaying grid charging, or by discharging using V2G. V2G can thus best be performed at mid-level SoC, taking the driver's needs into acccount.

Furthermore, based on the battery's thermal properties and the potential VIPV power generation in the Netherlands and Spain, results show that VIPV can cool battery temperature by 10 °C within one hour of

sun, as well as keep the battery 23 °C cooler than the ambient temperature in the Netherlands and 35 °C in Spain. A battery ageing sensitivity analysis was performed using NMC-AM to simulate the impact of battery temperatures ranging from 10 °C to 25 °C in steps of 5 °C. According to NMC-AM, VIPV-powered battery temperature regulation could drastically extend battery life by up to 4.6 years, allowing for 88,000 km of additional driving range before the battery reaches its EoL. Battery temperature regulation can be performed using VIPV or grid power. The required grid connection for V2G simultaneously allows for EVs to use grid power to regulate battery temperature regulation. Taking electricity cost into account, grid-powered battery temperature regulation could prove to be a cost-effective method to extend battery life, especially for EVs experiencing extreme temperatures.

Limitations of semi-empirical ageing models

Semi-empirical ageing models found in literature often lack clarity regarding their implementation, which limits their application on battery data. Specifically, due to a lack of clarity regarding their cycle counting method and definition of a cycle and throughput, applications of these model could lead to ageing estimation errors. Moreover, ageing models are often not based on ageing tests with irregular load profiles. Consequently, when the ageing models are applied on irregular load profiles, they could lead to ageing estimation errors. Furthermore, ageing models are often based on accelerated ageing tests under limited operating conditions, limiting their secondary application to a range of operating conditions. Additionally, ageing models that do not consider path dependency in ageing but rather consider calendar and cycling ageing to be independent and cumulative could underestimate ageing, especially at higher C-rates and during continuous cycling. Lastly, ageing models are usually based on ageing tests of one particular cell chemistry and size. Considering that the characteristics of similar cells may vary in terms of capacity and performance, applying the ageing models to other cells may lead to ageing estimation errors.

iv *Validate the ageing models by simulating ageing tests performed to develop the ageing models.*

The fourth and final sub-objective was approached by reproducing the ageing tests performed to validate NMC-AM and LFP-AM. Moreover, calendar ageing results from NMC-AM and NMC-AMII and from NMC-AM and Lightyear's calendar ageing tests were compared.

First, the implementation of NMC-AM was validated by simulating the validation tests performed by Schmalstieg et al. (2014) to validate their model. Results from NMC-AM simulations were compared with results from the ageing model validation tests performed by the authors, which showed very high accuracy for three different battery temperature scenarios. Second, a comparison of the results from NMC-AM and NMC-AMII showed that calendar ageing in NMC-AMII was less significant at extreme temperatures. Moreover, a simulation of the calendar ageing tests performed by Lightyear show that the cell used in NMC-AM experiences more calendar ageing than Lightyear's battery cell. This is likely because the cell on which NMC-AM is based originates from 2012, indicating that it is of lower quality than Lightyear's cell.

Third, the implementation of LFP-AM was validated by simulating calendar and cycling ageing experiments performed by Schimpe et al. (2018) and comparing modelled ageing results with results from the ageing experiments on which LFP-AM is based. Apart from cycling ageing at T = 0 °C, the simulated results showed high accuracy in following the results of the ageing experiments.

7.2. Recommendations for further research

The higher-level intention of this work was to provide a foundation for future research. Along the way, the assumptions that facilitated this research as well as the findings that emerged from it opened up four directions for future work that can build on the contributions of this thesis.

1. First, it is recommended to integrate the ageing models into the EV battery data generation models, such as Lightyear's VPM. The integration of the ageing models in the EV battery data generation models would allow for capacity and power fade to be looped back into the battery data continuously, as well as increase flexibility in regard to simulation conditions. This would improve ageing estimations and allow for detailed ageing analysis of other cell chemistries. Moreover, as ageing is thought to be cell-dependent, to improve ageing estimations, it is recommended to develop semi-empirical ageing models for the particular cells under question.

2. Second, further research on the impact of VIPV on battery calendar life is recommended to determine methods to reduce battery ageing, which could further improve the business case of VIPV. OEMs could develop strategies that optimally balance VIPV power used for battery charging, battery temperature regulation or V2G. Additionally, it is recommended to investigate how VIPV would impact battery calendar ageing in geographical areas with increased solar irradiance, with different-sized VIPV systems, and with solar conversion efficiencies ranging up to the theoretical c-Si limit of 29%

3. Third, while VIPV was found to extend battery calendar life, gradual VIPV charging has been shown to increase the irregularity of the battery load profile, likely causing semi-empirical ageing models to overestimate cycling ageing. To accurately determine how VIPV impacts battery cycle life, it is recommended to conduct empirical battery ageing tests under identical operating conditions with and without VIPV. Furthermore, it is recommended to research whether cycling ageing estimations could be improved by applying multiple ageing models, models based on irregular load profiles, or machine learning-based ageing models, which have demonstrated high predictive accuracy as well as applicability, as described in Section 2.2.

4. Finally, it is recommended to further investigate methods to reduce battery ageing using VIPV and V2G. As simulations suggest that VIPV and V2G could drastically extend battery life by regulating SoC and temperature, additional research could further improve the business case of VIPV and V2G, accelerating their widespread implementation.

8

Appendix

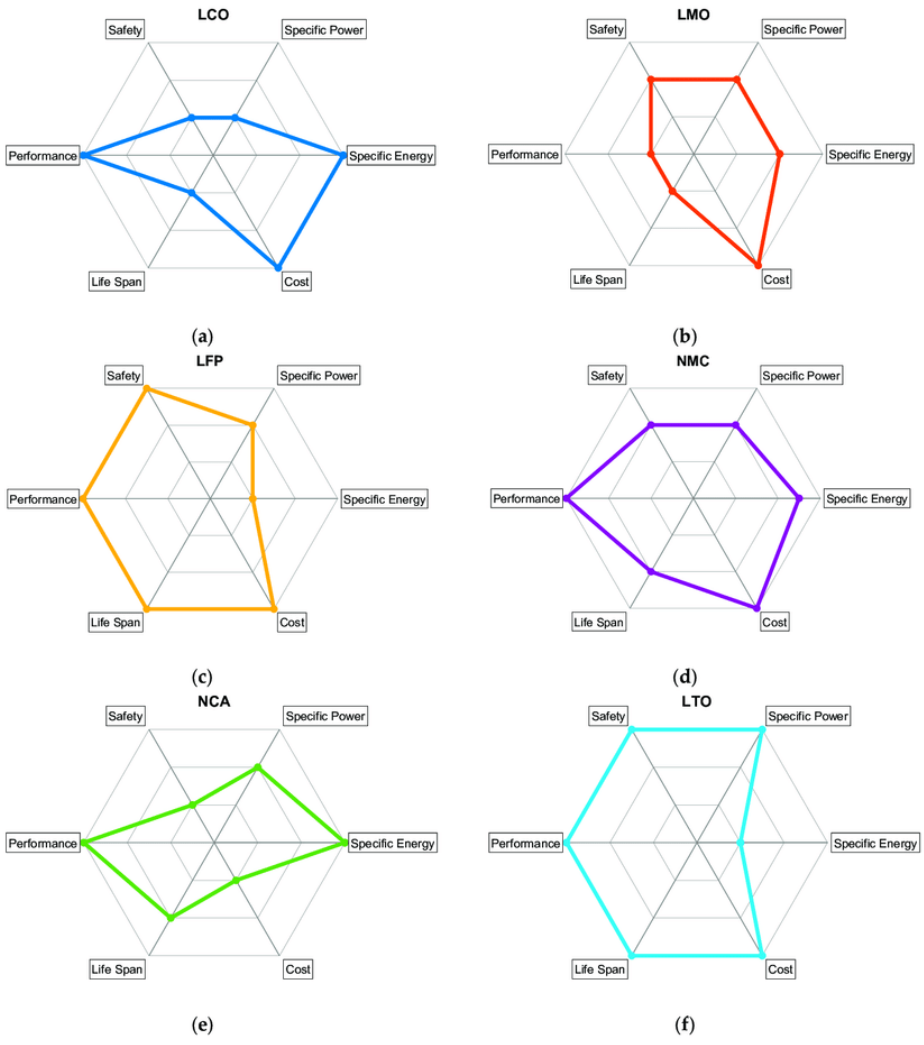

Figure 8.1: Similar overview of Li-ion batteries as Figure 2.2, but with an error in regard to the cost of LTO. (a) LCO; (b) LMO; (c) LFP; (d) NMC; (e) NCA; (f) LTO [78].

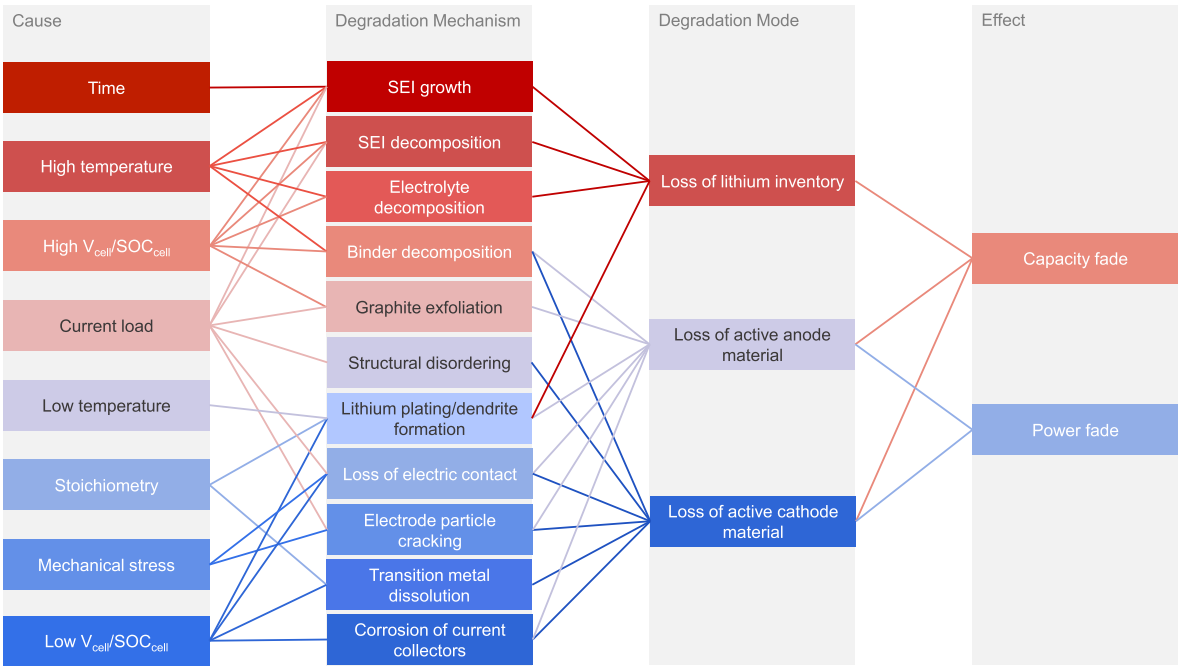

Figure 8.2: Causes of degradation mechanisms, associated degradation modes and subsequent degradation effects on the battery [5].

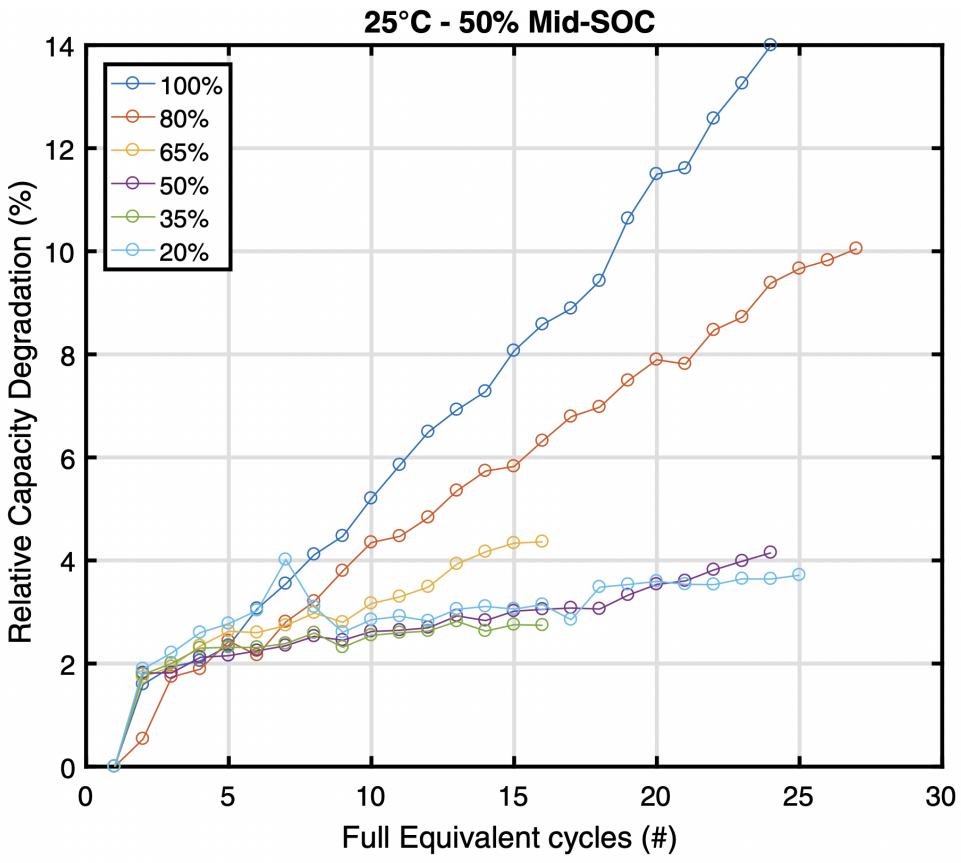

Figure 8.3: Graph illustrating the impact of cycle depth on capacity loss for an NMC battery [14].

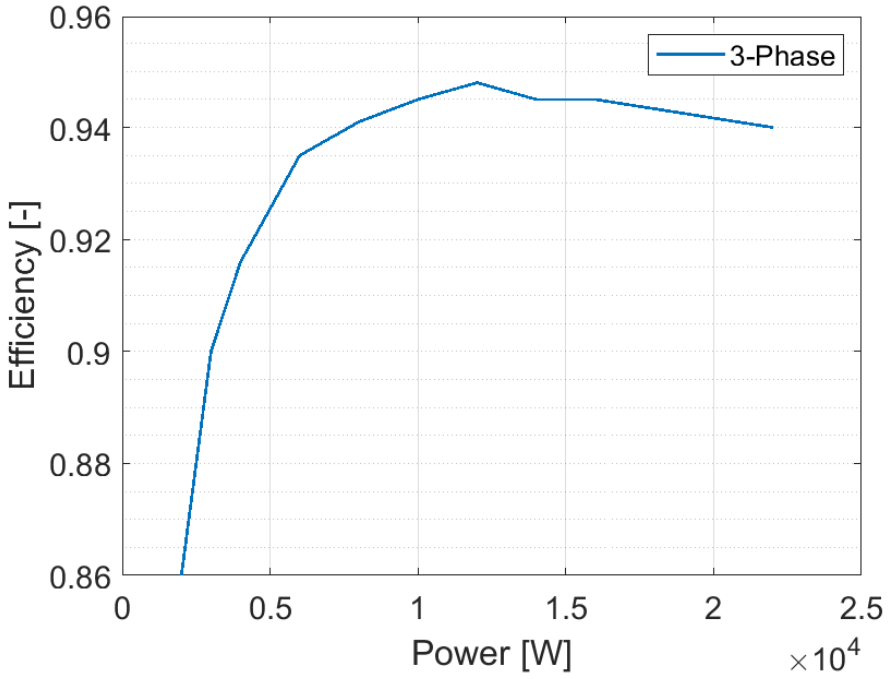

Figure 8.4: Lightyear's OBC efficiency curve.

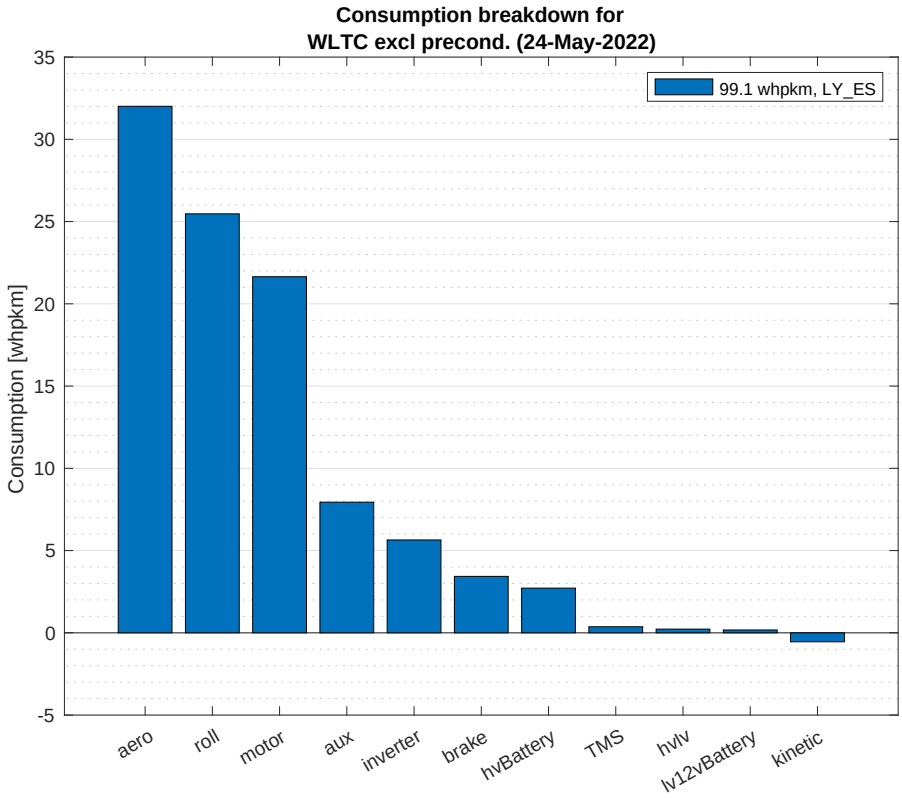

Figure 8.5: Consumption breakdown of the Lightyear vehicle driving one WLTC cycle.

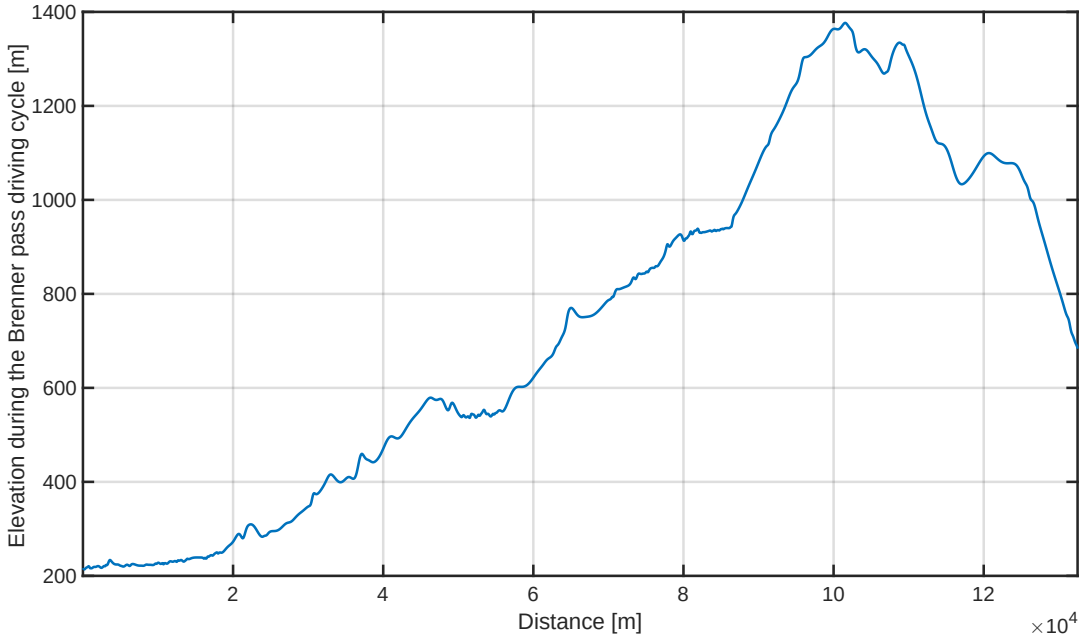

Figure 8.6: Elevation profile for the Brenner pass driving cycle. Data sourced from Lightyear VPM simulations.

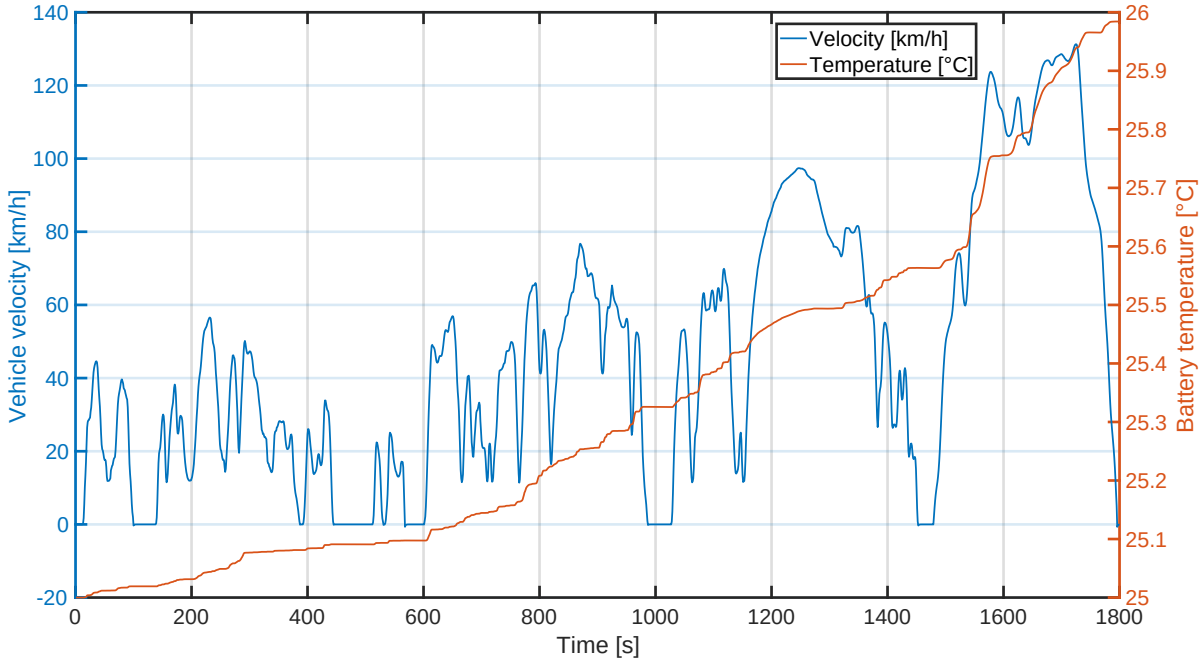

Figure 8.7: Velocity and temperature profiles for a single WLTC cycle with an ambient temperature of 25 °C.

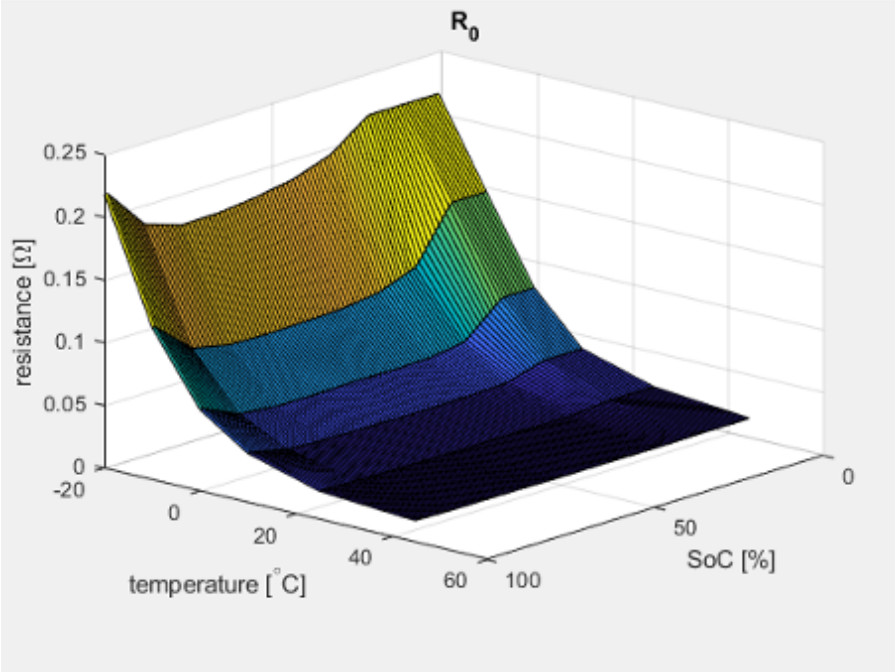

Figure 8.8: 3D graph showing the relation between the internal resistance, the temperature and the SoC of Lightyear's battery pack.

DC I_R discharging:

	-20	-15	-10	-5	0	5	10	15	20	25	30	35	40	45	50
0	131,05	90,32	72,64	60,44	48,24	39,02	33,73	30,77	27,68	25,30	22,97	21,89	20,87	19,96	19,89
5	101,08	69,67	56,03	46,62	37,21	30,10	26,02	23,74	21,35	19,51	17,72	16,88	16,09	15,40	15,34
10	92,09	63,47	51,04	42,47	33,90	27,42	23,71	21,62	19,45	17,78	16,14	15,38	14,66	14,03	13,98
15	84,59	58,31	46,89	39,01	31,14	25,19	21,78	19,86	17,87	16,33	14,83	14,13	13,47	12,88	12,84
20	82,66	56,97	45,82	38,12	30,43	24,61	21,28	19,41	17,46	15,96	14,49	13,81	13,16	12,59	12,55
25	80,96	55,80	44,87	37,34	29,80	24,11	20,84	19,01	17,10	15,63	14,19	13,52	12,89	12,33	12,29
30	80,99	55,82	44,89	37,35	29,81	24,12	20,85	19,02	17,11	15,63	14,20	13,53	12,90	12,34	12,29
35	78,12	53,85	43,30	36,03	28,76	23,26	20,11	18,34	16,50	15,08	13,69	13,05	12,44	11,90	11,86
40	76,72	52,88	42,52	35,38	28,24	22,84	19,75	18,01	16,21	14,81	13,45	12,81	12,22	11,69	11,65
45	78,04	53,79	43,26	35,99	28,73	23,24	20,09	18,33	16,49	15,07	13,68	13,03	12,43	11,89	11,85
50	76,61	52,80	42,46	35,33	28,20	22,81	19,72	17,99	16,18	14,79	13,43	12,79	12,20	11,67	11,63
55	76,58	52,79	42,45	35,32	28,19	22,80	19,71	17,98	16,18	14,78	13,42	12,79	12,19	11,66	11,62
60	75,10	51,76	41,63	34,63	27,65	22,36	19,33	17,63	15,86	14,50	13,16	12,54	11,96	11,44	11,40
65	76,60	52,80	42,46	35,33	28,20	22,81	19,72	17,99	16,18	14,79	13,43	12,79	12,20	11,67	11,63
70	76,61	52,80	42,46	35,33	28,20	22,81	19,72	17,99	16,18	14,79	13,43	12,79	12,20	11,67	11,63
75	76,61	52,80	42,46	35,33	28,20	22,81	19,72	17,99	16,18	14,79	13,43	12,79	12,20	11,67	11,63
80	76,72	52,88	42,52	35,38	28,24	22,84	19,75	18,02	16,21	14,81	13,45	12,81	12,22	11,69	11,65
85	78,12	53,85	43,30	36,03	28,76	23,26	20,11	18,34	16,50	15,08	13,69	13,05	12,44	11,90	11,86
90	76,77	52,92	42,55	35,41	28,26	22,86	19,76	18,03	16,22	14,82	13,46	12,82	12,22	11,69	11,65
95	78,31	53,98	43,41	36,12	28,83	23,32	20,16	18,39	16,54	15,12	13,73	13,08	12,47	11,93	11,89
100	81,15	55,93	44,98	37,42	29,87	24,16	20,89	19,05	17,14	15,67	14,22	13,55	12,92	12,36	12,32

DC I_R charging:

	-20	-15	-10	-5	0	5	10	15	20	25	30	35	40	45	50
0	108,36	74,69	60,06	49,98	39,89	32,27	27,89	25,45	22,89	20,92	18,99	18,10	17,25	16,51	16,45
5	98,26	67,72	54,46	45,31	36,17	29,26	25,29	23,07	20,76	18,97	17,22	16,41	15,65	14,97	14,91
10	90,78	62,57	50,32	41,86	33,42	27,03	23,37	21,32	19,18	17,52	15,91	15,16	14,45	13,83	13,78
15	86,16	59,39	47,76	39,74	31,72	25,66	22,18	20,23	18,20	16,63	15,10	14,39	13,72	13,12	13,08
20	85,83	59,16	47,57	39,58	31,59	25,56	22,09	20,15	18,13	16,57	15,04	14,33	13,67	13,07	13,03
25	82,98	57,20	46,00	38,27	30,55	24,71	21,36	19,49	17,53	16,02	14,55	13,86	13,21	12,64	12,60
30	82,95	57,17	45,98	38,25	30,53	24,70	21,35	19,48	17,52	16,01	14,54	13,85	13,21	12,63	12,59
35	79,64	54,89	44,14	36,73	29,32	23,71	20,50	18,70	16,82	15,37	13,96	13,30	12,68	12,13	12,09
40	78,12	53,85	43,30	36,03	28,76	23,26	20,11	18,34	16,50	15,08	13,69	13,05	12,44	11,90	11,86
45	78,12	53,85	43,30	36,03	28,76	23,26	20,11	18,34	16,50	15,08	13,69	13,05	12,44	11,90	11,86
50	78,12	53,85	43,30	36,03	28,76	23,26	20,11	18,34	16,50	15,08	13,69	13,05	12,44	11,90	11,86
55	78,12	53,85	43,30	36,03	28,76	23,26	20,11	18,34	16,50	15,08	13,69	13,05	12,44	11,90	11,86
60	77,48	53,40	42,94	35,73	28,52	23,07	19,94	18,19	16,37	14,96	13,58	12,94	12,34	11,80	11,76
65	75,45	52,00	41,82	34,80	27,77	22,47	19,42	17,72	15,94	14,57	13,22	12,60	12,01	11,49	11,45
70	76,61	52,80	42,46	35,33	28,20	22,81	19,72	17,99	16,18	14,79	13,43	12,79	12,20	11,67	11,63
75	77,58	53,47	43,00	35,78	28,56	23,10	19,97	18,22	16,39	14,98	13,60	12,96	12,35	11,82	11,78
80	76,61	52,80	42,46	35,33	28,20	22,81	19,72	17,99	16,18	14,79	13,43	12,79	12,20	11,67	11,63
85	78,12	53,85	43,30	36,03	28,76	23,26	20,11	18,34	16,50	15,08	13,69	13,05	12,44	11,90	11,86
90	78,61	54,18	43,57	36,25	28,94	23,41	20,23	18,46	16,61	15,18	13,78	13,13	12,52	11,97	11,93
95	79,64	54,89	44,14	36,73	29,32	23,71	20,50	18,70	16,82	15,37	13,96	13,30	12,68	12,13	12,09
100	85,68	59,06	47,49	39,52	31,54	25,51	22,06	20,12	18,10	16,54	15,02	14,31	13,64	13,05	13,01

Figure 8.9: Overview of the battery cell resistance during discharging (top graph) and charging (bottom graph) for various temperatures (x-axis) and SoC values (y-axis).

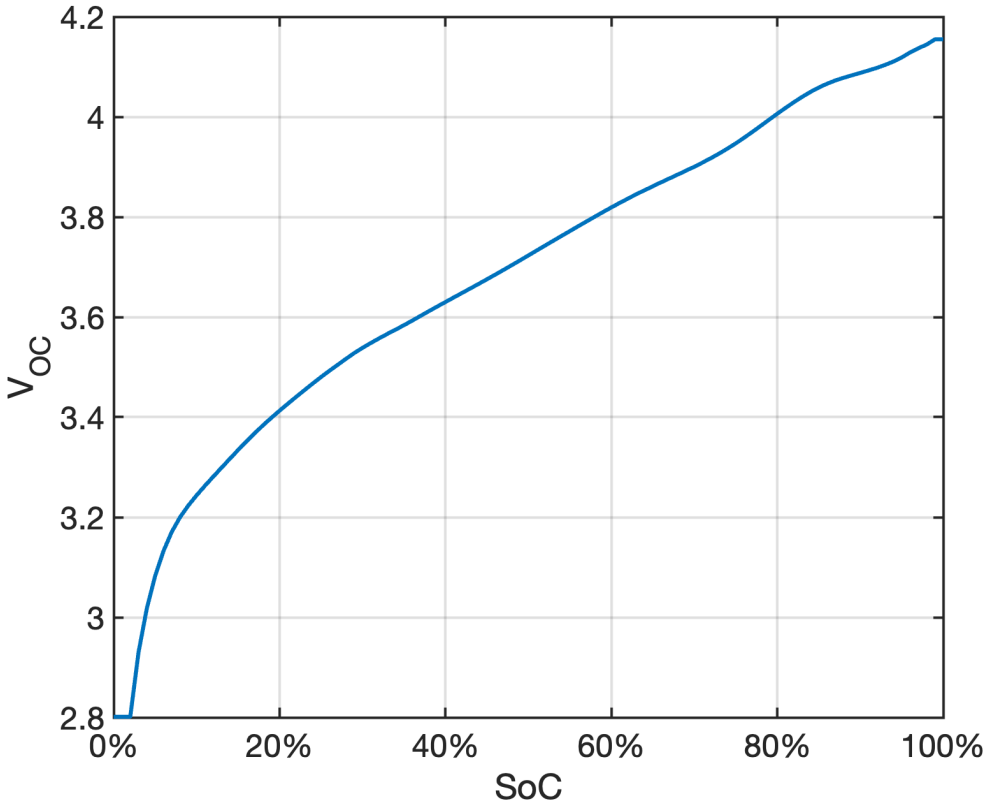

Figure 8.10: V_{OC}(SoC) relation of Lightyear's NMC battery. Source: Lightyear VPM, 2022.

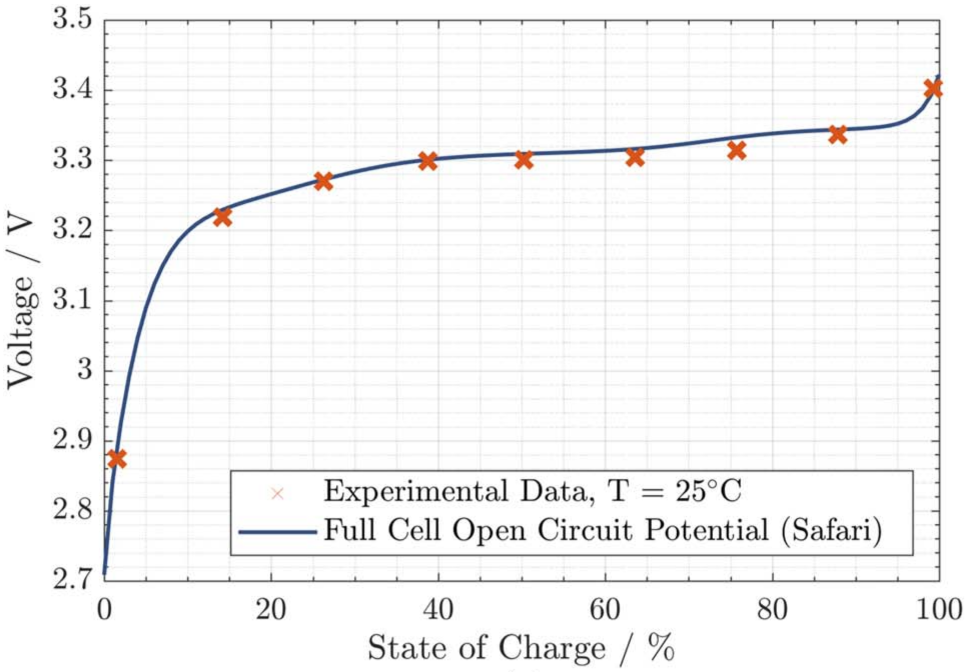

Figure 8.11: The blue line shows the V_{OC}(SoC) relation used in LFP-AM to generate LFP-based ageing stress factors [77].

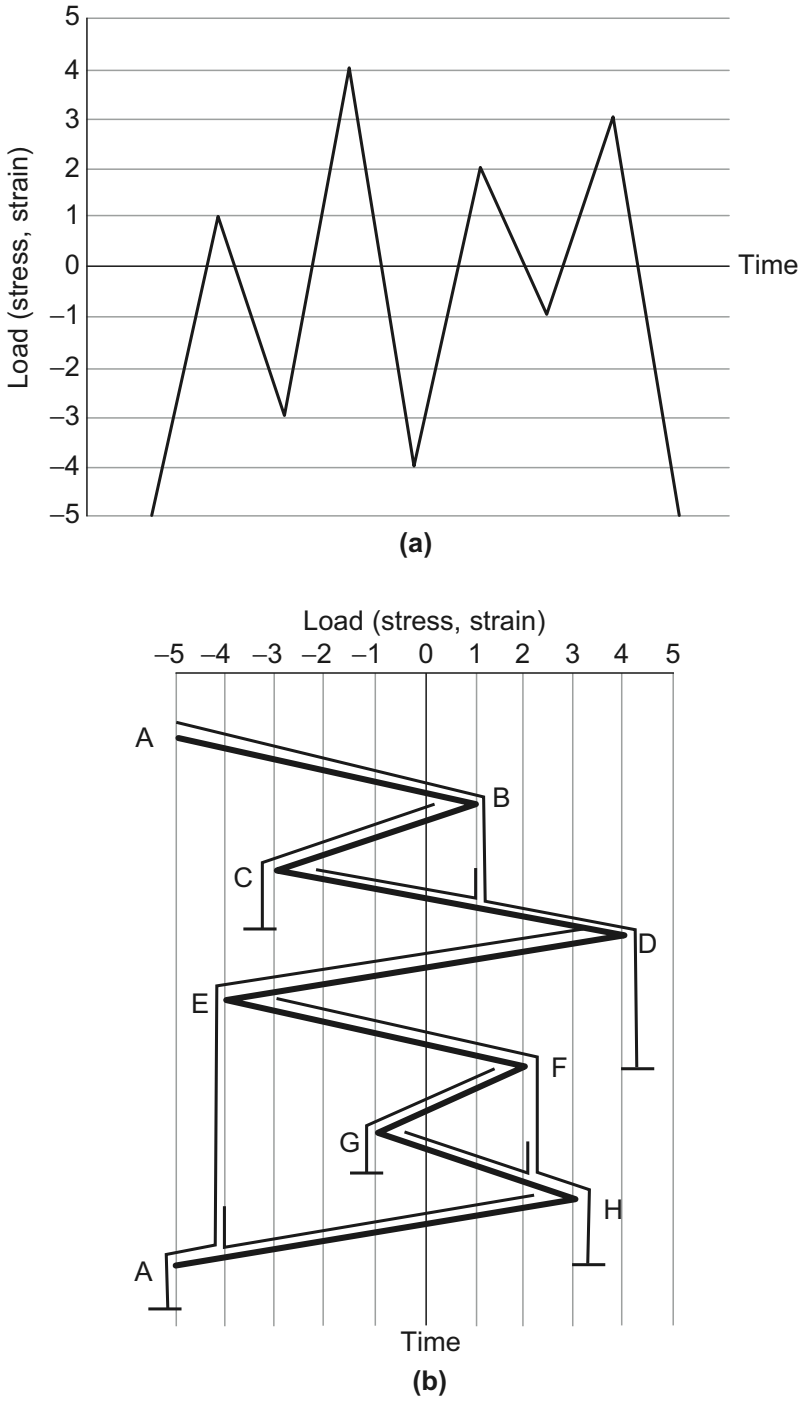

Figure 8.12: Illustration of rainflow counting method where the loading history is rotated clockwise and an imaginary flow of rain starts at each successive extreme point [47].

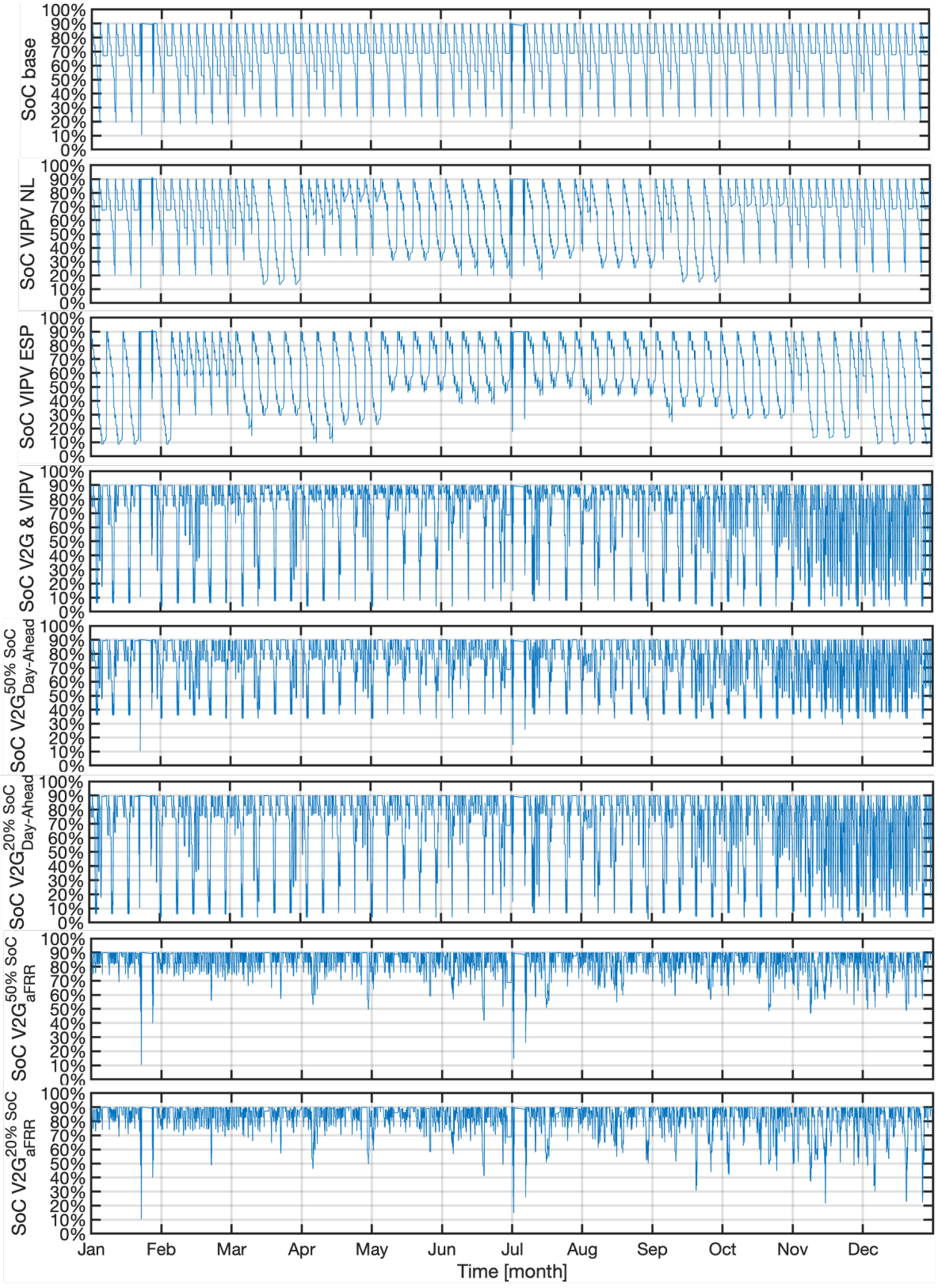

Figure 8.13: SoC profiles, top to bottom order of the scenarios is: Base; $VIPV_{NL}$; $VIPV_{ESP}$; $VIPV_{NL}$ & $V2G_{DA}^{50\%\ SoC}$; $V2G_{DA}^{50\%\ SoC}$; $V2G_{DA}^{20\%\ SoC}$; $V2G_{aFRR}^{50\%\ SoC}$, and $V2G_{aFRR}^{20\%\ SoC}$.

Panasonic
ideas for life

Lithium Ion UR18650E

Features & Benefits

- High energy and power density
- Long, stable, high power
- High safety performance
- Ideal for power assisted bicycles, 2-way radios, medical devices and robotics.

Specifications

Rated capacity(1)	Min. 2000mAh
Capacity(2)	Min. 2050mAh Typ. 2150mAh
Nominal voltage	3.6V
Charging	CC-CV, Std. 1440mA, 4.20V, 3.0 hrs
Weight (max.)	45.5 g
Temperature	Charge: 0 to +45°C Discharge: -20 to +60°C Storage: -20 to +50°C
Energy density(3)	Volumetric: 432 Wh/l Gravimetric: 162 Wh/kg

(1) At 20°C (2) At 25°C (3) Energy density based on bare cell dimensions

Dimensions

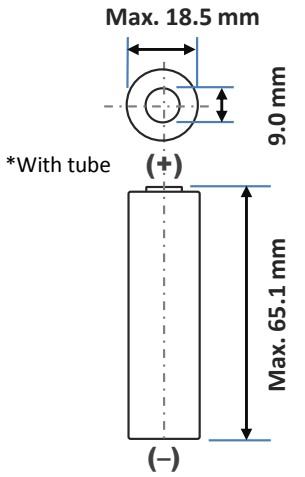

For Reference Only

Charge Characteristics

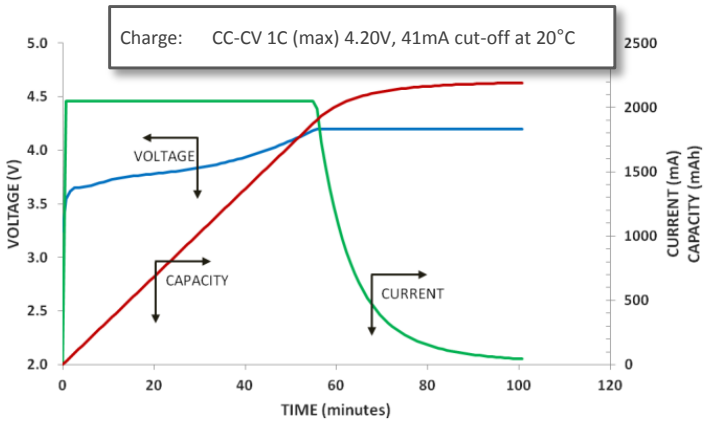

Cycle Life Characteristics

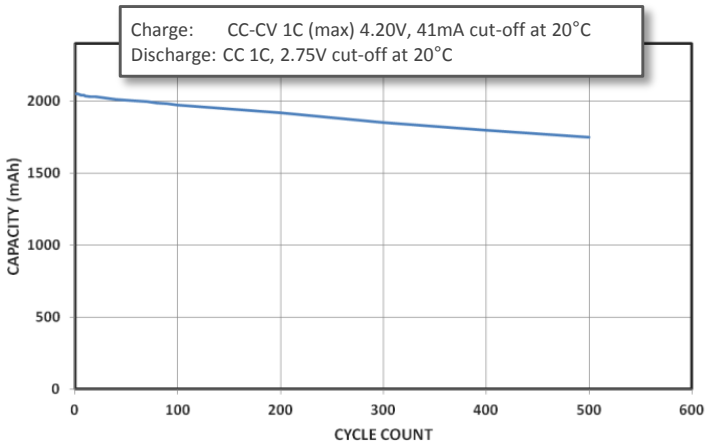

Discharge Characteristics (by temperature)

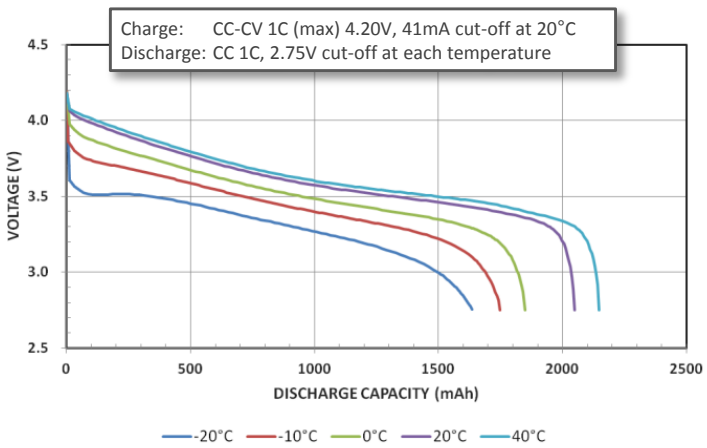

Discharge Characteristics (by rate of discharge)

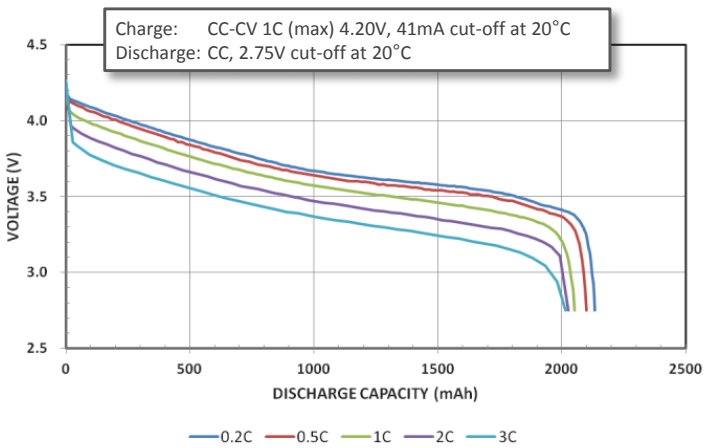

For more information on how Panasonic can assist you with your battery power solution needs, visit us at www.panasonic.com/industrial/batteries-oem or e-mail secsales@us.panasonic.com.

Bibliography

[1] Yvenn Amara-Ouali, Yannig Goude, Pascal Massart, Jean Michel Poggi, and Hui Yan. A review of electric vehicle load open data and models. *Energies*, 14, 4 2021. ISSN 19961073. doi: 10.3390/en14082233.

[2] ASOM. Alliance for Solar Mobility. 2022. https://asom.solar/.

[3] Paul Barter. Reinventing Parking. 2013. https://www.reinventingparking.org/2013/02/cars-are-parked-95-of-time-lets-check.html.

[4] Haodong Chen Qingsong Wang Jinhua Sun Binbin Mao, Peifeng Huang. Self-heating reaction and thermal runaway criticality of the lithium ion battery. *International Journal of Heat and Mass Transfer*, 2020. doi: 10.1016/j.ijheatmasstransfer.2019.119178.

[5] Christoph R. Birkl, Matthew R. Roberts, Euan McTurk, Peter G. Bruce, and David A. Howey. Degradation diagnostics for lithium ion cells. *Journal of Power Sources*, 341:373–386, 2 2017. ISSN 0378-7753. doi: 10.1016/J.JPOWSOUR.2016.12.011.

[6] Isidor Buchmann. BU-205: Types of Lithium-ion. *BatteryUniversity.com*, 2021. https://batteryuniversity.com/article/bu-205-types-of-lithium-ion.

[7] Franziska Bühler, Thomas Franke, Isabel Neumann, Peter Cocron, and Josef F Krems. Experiencing Range in an Electric Vehicle: Understanding Psychological Barriers. 2011. doi: 10.1111/j.1464-0597.2011.00474.x.

[8] CBS. Hoeveel rijden personenauto's? 2021. https://www.cbs.nl/nl-nl/visualisaties/verkeer-en-vervoer/verkeer/verkeersprestaties-personenautos.

[9] P Chatterjee, J Singh, R Singh, Y Avadh, and Sumit Kanchan. Electric Vehicle Modeling in MATLAB and Simulink with SoC SoE Estimation of a Lithium-ion Battery. *IOP Conference Series: Materials Science and Engineering*, 1116:012103, 04 2021. doi: 10.1088/1757-899X/1116/1/012103.

[10] John B. Goodenough* Chunwen Sun, Shreyas Rajasekhara and Feng Zhou. Monodisperse Porous LiFePO4 Microspheres for a High Power Li-Ion Battery Cathode. 2011. doi: https://doi.org/10.1021/ja1110464.

[11] Cobalt Institute. Batteries Electric Vehicles. 2021. https://www.cobaltinstitute.org/essential-cobalt-2/powering-the-green-economy/batteries-electric-vehicles/.

[12] European Commission. Photovoltaic Geographical Information System. 2022. https://re.jrc.ec.europa.eu/pvg_tools/en/.

[13] European Commission. Joint Research Centre European Energy Efficiency Platform (E3P). 2022. https://e3p.jrc.ec.europa.eu/articles/typical-meteorological-year-tmy.

[14] Joris de Hoog, Timmermans Jean-Marc, Daniel Ioan-Stroe, Maciej Swierczynski, Joris Jaguemont, Shovon Goutam, Noshin Omar, Joeri van Mierlo, and Peter Van Den Bossche. Combined cycling and calendar capacity fade modeling of a Nickel-Manganese-Cobalt Oxide Cell with real-life profile validation. *Applied Energy*, Volume 200:47–51, 2017.

[15] DieselNet. Common Artemis Driving Cycles (CADC) - DieselNet. 2018. https://dieselnet.com/standards/cycles/artemis.php.

[16] DieselNet. Emission Test Cycles: WLTC - DieselNet. 2019. https://dieselnet.com/standards/cycles/wltp.php.

[17] Yuanli Ding, Zachary P. Cano, Aiping Yu, Jun Lu, and Zhongwei Chen. Automotive Li-Ion Batteries: Current Status and Future Perspectives. *Electrochemical Energy Reviews*, 2, 3 2019. ISSN 25208136. doi: 10.1007/s41918-018-0022-z.

[18] Matthieu Dubarry, Arnaud Devie, and Katherine Mckenzie. Durability and reliability of electric vehicle batteries under electric utility grid operations: Bidirectional charging impact analysis. *Journal of Power Sources*, 2017. doi: 10.1016/j.jpowsour.2017.05.015. http://dx.doi.org/10.1016/j.jpowsour.2017.05.015.

[19] Madeleine Ecker, Jochen B. Gerschler, Jan Vogel, Stefan Käbitz, Friedrich Hust, Philipp Dechent, and Dirk Uwe Sauer. Development of a lifetime prediction model for lithium-ion batteries based on extended accelerated aging test data. *Journal of Power Sources*, 2012.

[20] EEA. New registrations of electric vehicles in Europe. *European Environment Agency*, 2021. https://www.eea.europa.eu/ims/new-registrations-of-electric-vehicles.

[21] ElaadNL. Open Datasets for Electric Mobility Research. 2020. https://platform.elaad.io/analyses/ElaadNL_opendata.php.

[22] Linda Ager Wick Ellingsen, Bhawna Singh, and Anders Hammer Strømman. The size and range effect: Lifecycle greenhouse gas emissions of electric vehicles. *Environmental Research Letters*, 11, 5 2016. ISSN 17489326. doi: 10.1088/1748-9326/11/5/054010.

[23] EPEX SPOT. Basics of the Power Market. 2022. https://www.epexspot.com/en/basicspowermarket.

[24] European Commission. Zero emission vehicles: first 'Fit for 55' deal will end the sale of new CO2 emitting cars in Europe by 2035. 2022.

[25] Forge Nano. The Effect of an SEI Layer on Anode and Cathode Particles. 2022. https://www.forgenano.com/effect-sei-layer-anode-cathode-particles/.

[26] Thomas Franke, Nadine Rauh, and Josef F. Krems. Individual differences in BEV drivers' range stress during first encounter of a critical range situation. *Applied Ergonomics*, 57:28–35, 11 2016. ISSN 18729126. doi: 10.1016/j.apergo.2015.09.010.

[27] Georg Bieker. A Global Comparison of the Life-Cycle Greenhouse Gas Emissions of Combustion Engine and Electric Passenger Cars. 2021. https://theicct.org/publication/a-global-comparison-of-the-life-cycle-greenhouse-gas-emissions-of-combustion-engine-and-ele

[28] German Federal Ministry for Digital and Transport. Mobility in Germany Study, 2017. https://www.bmvi.de/EN/Services/Statistics/Mobility-in-Germany/mobility-in-germany.html.

[29] John B. Goodenough. How we made the Li-ion rechargeable battery: Progress in portable and ubiquitous electronics would not be possible without rechargeable batteries. John B. Goodenough recounts the history of the lithium-ion rechargeable battery, 3 2018. ISSN 25201131.

[30] John C. Hall, Tony Lin, Glen Brown, Philippe Biensan, and Frederic Bonhomme. Decay processes and life predictions for lithium ion satellite cells. *Collection of Technical Papers - 4th International Energy Conversion Engineering Conference*, 1:632–642, 2006. doi: 10.2514/6.2006-4078.

[31] Xuebing Han, Languang Lu, Yuejiu Zheng, Xuning Feng, Zhe Li, Jianqiu Li, and Minggao Ouyang. A review on the key issues of the lithium ion battery degradation among the whole life cycle. *eTransportation*, 2019.

[32] Mahammad A. Hannan, Md Murshadul Hoque, Aini Hussain, Yushaizad Yusof, and Pin Jern Ker. State-of-the-Art and Energy Management System of Lithium-Ion Batteries in Electric Vehicle Applications: Issues and Recommendations. *IEEE Access*, 6:19362–19378, 3 2018. ISSN 21693536. doi: 10.1109/ACCESS.2018.2817655.

[33] Anderson Hoke, Alexander Brissette, Dragan Maksimović, Annabelle Pratt, and Kandler Smith. Electric vehicle charge optimization including effects of lithium-ion battery degradation. pages 1–8, 2011. doi: 10.1109/VPPC.2011.6043046.

[34] Mohamed S. E. Houache, Chae-Ho Yim, Zouina Karkar, and Yaser Abu-Lebdeh. On the Current and Future Outlook of Battery Chemistries for Electric Vehicles—Mini Review. *MDPI - Batteries*, 2022. https://mdpi-res.com/d_attachment/batteries/batteries-08-00070/article_deploy/batteries-08-00070.pdf?version=1657708793.

[35] Bo Huang, Minghui Hu, Lunguo Chen, Guoqing Jin, Shuiping Liao, Chunyun Fu, Dongyang Wang, and Kaibin Cao. A Novel Electro-Thermal Model of Lithium-Ion Batteries Using Power as the Input. *Electronics*, 10(22), 2021. ISSN 2079-9292. doi: 10.3390/electronics10222753. https://www.mdpi.com/2079-9292/10/22/2753.

[36] Wouter Jansen. Lightyear: Tech progress — The Vehicle Performance Model. 2021. https://lightyear.one/articles/the-vehicle-performance-model-video.

[37] Xing Jin, Ashish P. Vora, Vaidehi Hoshing, Tridib Saha, Gregory M. Shaver, Oleg Wasynczuk, and Subbarao Varigonda. Comparison of Li-ion battery degradation models for system design and control algorithm development. *Proceedings of the American Control Conference*, 0:74–79, 6 2017. ISSN 07431619. doi: 10.23919/ACC.2017.7962933.

[38] Heejung Jung, Rebecca Silva, and Michael Han. Scaling trends of electric vehicle performance: Driving range, fuel economy, peak power output, and temperature effect. *World Electric Vehicle Journal*, 9, 12 2018. ISSN 20326653. doi: 10.3390/wevj9040046.

[39] Jochen Stadler Severin Hahn Gerd Gaiselmann Arnulf Latz Kai Schofer, Florian Laufer and Kai P. Birke. Machine Learning-Based Lifetime Prediction of Lithium-Ion Cells. 2022. https://onlinelibrary-wiley-com.tudelft.idm.oclc.org/doi/full/10.1002/advs.202200630.

[40] Mark Kane. Tesla's 4680-Type Battery Cell Teardown: Specs Revealed. *InsideEVs*, 2022. https://insideevs.com/news/598656/tesla-4680-battery-cell-specs/.

[41] Olga Kanz and Bianca Lim. VIPV Position Paper, 2020. https://www.eera-pv.eu/component/attachments/?task=download&id=378.

[42] Annie Kelly. Apple andGoogle named in US lawsuit over Congolese child cobalt mining deaths. 2019. https://www.responsibleminingfoundation.org/app/uploads/impacts-sources/Glencore_AppleandGooglenamedinUSlawsuitoverCongolesechildcobaltminingdeaths.pdf.

[43] Lingxi Kong and Michael Pecht. Lithium-ion Battery Technology - What is the Energy Density of a Lithium-Ion Battery? *Center for Advanced Life Cycle Engineering (CALCE) Battery Research Group at the University of Maryland*, 2020. https://www.batterypoweronline.com/news/a-look-inside-your-battery-watching-the-dendrites-grow/.

[44] Lingxi Kong and Michael Pecht. Battery Power Online | A Look Inside Your Battery: Watching the Dendrites Grow. 2020. https://www.batterypoweronline.com/news/a-look-inside-your-battery-watching-the-dendrites-grow/.

[45] Stefan Käbitz, Jochen Bernhard Gerschler, Madeleine Ecker, Yusuf Yurdagel, Brita Emmermacher, Dave André, Tim Mitsch, and Dirk Uwe Sauer. Cycle and calendar life study of a graphite|LiNi1/3Mn 1/3Co1/3O2 Li-ion high energy system. Part A: Full cell characterization. *Journal of Power Sources*, 239: 572–583, 2013. ISSN 03787753. doi: 10.1016/j.jpowsour.2013.03.045.

[46] Adrian König, Lorenzo Nicoletti, Daniel Schröder, Sebastian Wolff, Adam Waclaw, and Markus Lienkamp. An overview of parameter and cost for battery electric vehicles. *World Electric Vehicle Journal*, 12(1), 2021. ISSN 2032-6653. https://www.mdpi.com/2032-6653/12/1/21.

[47] Yung-Li Lee and Tana Tjhung. Rainflow Cycle Counting Techniques. *Metal Fatigue Analysis Handbook*, pages 89–114, 2012. doi: 10.1016/B978-0-12-385204-5.00003-3.

[48] Lightyear. Long Range Solar Electric Vehicle - Lightyear One. 2022. https://lightyear.one/lightyear-0.

[49] Mostafa Majidpour, Charlie Qiu, Peter Chu, Hemanshu Pota, and Rajit Gadh. Forecasting the EV charging load based on customer profile or station measurement? *Applied Energy*, 163:134–141, 02 2016. doi: 10.1016/j.apenergy.2015.10.184.

[50] Kevin R. Mallon, Francis Assadian, and Bo Fu. Analysis of on-board photovoltaics for a battery electric bus and their impact on battery lifespan. *Energies*, 10, 2017. ISSN 19961073. doi: 10.3390/en10070943.

[51] Maria Cloud - Flux Power. Lithium-ion Battery Technology - What is the Energy Density of a Lithium-Ion Battery? 2020. https://www.fluxpower.com/blog/what-is-the-energy-density-of-a-lithium-ion-battery?hs_amp=true.

[52] Andrea Marongiu, Marco Roscher, and Dirk Uwe Sauer. Influence of the vehicle-to-grid strategy on the aging behavior of lithium battery electric vehicles. *Applied Energy*, 137:899–912, 1 2015. ISSN 03062619. doi: 10.1016/j.apenergy.2014.06.063.

[53] Francesco Marra, Chresten Træholt, Esben Larsen, and Qiuwei Wu. Average behavior of battery-electric vehicles for distributed energy studies. *IEEE*, 2010. doi: 10.1109/ISGTEUROPE.2010.5638920.

[54] McKinsey & Company. Power spike: How battery makers can respond to surging demand from EVs. 2022. https://www.mckinsey.com/capabilities/operations/our-insights/power-spike-how-battery-makers-can-respond-to-surging-demand-from-evs.

[55] Yu Miao, Patrick Hynan, Annette Von Jouanne, and Alexandre Yokochi. Current li-ion battery technologies in electric vehicles and opportunities for advancements. *Energies*, 12, 3 2019. ISSN 19961073. doi: 10.3390/en12061074.

[56] Nahla Mohamed, Nor Zaihar Yahaya, and Balbir Singh Mahinder Singh. Single-diode model and two-diode model of PV modules: A comparison. *Control System, Computing and Engineering (ICCSCE), 2013 IEEE International Conference*, 2013.

[57] Renaud Revel Serge Pelissier François Duclaud Charles Delacourt Mohammad Kassem, Julien Bernard. Calendar aging of a graphite/LiFePO4 cell. *Journal of Power Sources*, 2014. doi: 10.1016/j.jpowsour.2012.02.068. https://hal.archives-ouvertes.fr/hal-00876555/document.

[58] Morgan Stanley. Global EV Penetration Forecast. 2021. https://www.vaneck.com/nl/nl/blog/emerging-markets/the-electric-vehicle-revolution-charges-ahead/.

[59] Gautham Ram Chandra Mouli, Mahdi Kefayati, Ross Baldick, and Pavol Bauer. Integrated PV charging of EV fleet based on energy prices, V2G, and offer of reserves. *IEEE Transactions on Smart Grid*, 10: 1313–1325, 3 2019. ISSN 19493053. doi: 10.1109/TSG.2017.2763683.

[60] Carrie Siu Natasha A. Chernova, Hui Zhou and M. Stanley Whittingham Fredrick Omenya. Comparative Study Nickel Rich Layered Oxides: NMC 622, NMC 811 and NCA Cathode Materials for Lithium Ion Battery. *The Electrochemical Society*, 2018.

[61] Next Kraftwerke. What is Day-Ahead Trading of Electricity? 2022. https://www.next-kraftwerke.com/knowledge/day-ahead-trading-electricity.

[62] Next Kraftwerke. What is aFRR (automatic frequency restoration reserve) and how does it work? 2022. https://www.next-kraftwerke.com/knowledge/afrr.

[63] Next Kraftwerke. What is a balancing group? 2022. https://www.next-kraftwerke.com/knowledge/balancing-group.

[64] Next Kraftwerke. What is the Electricity Balancing Guideline (EBGL)? 2022. https://www.next-kraftwerke.com/knowledge/electricity-balancing-guideline.

[65] Mengyun Nie, Dinesh Chalasani, Daniel P Abraham, Yanjing Chen, Arijit Bose, and Brett L Lucht. Lithium Ion Battery Graphite Solid Electrolyte Interphase Revealed by Microscopy and Spectroscopy. 2013. doi: 10.1021/jp3118055. https://pubs.acs.org/sharingguidelines.

[66] Naoki Nitta, Feixiang Wu, Jung Tae Lee, and Gleb Yushin. Li-ion battery materials: Present and future. *Materials Today*, 18:252–264, 6 2015. ISSN 18734103. doi: 10.1016/j.mattod.2014.10.040.

[67] Noshin Omar, Mohamed Abdel Monem, Yousef Firouz, Justin Salminen, Jelle Smekens, Omar Hegazy, Hamid Gaulous, Grietus Mulder, Peter Van den Bossche, Thierry Coosemans, and Joeri Van Mierlo. Lithium iron phosphate based battery - Assessment of the aging parameters and development of cycle life model. *Applied Energy*, 113:1575–1585, 2014. ISSN 03062619. doi: 10.1016/j.apenergy.2013.09.003.

[68] Panasonic - SANYO Energy. Panasonic - Lithium Ion Sanyo UR18650E battery cell datasheet. 2012. https://voltaplex.com/media/whitepapers/specification-sheet/Sanyo_E_Specification_Sheet.pdf.

[69] R. Perez, R. Seals, and J. Michalsky. All-weather model for sky luminance distribution-preliminary configuration and validation. *Solar Energy*, 1993.

[70] PV Performance Modelling Collaborative. Single Diode Equivalent Circuit Models. 2018. https://pvpmc.sandia.gov/modeling-steps/2-dc-module-iv/diode-equivalent-circuit-models/.

[71] PwC Strategy&. Hyperefficient EVs can help accelerate and realize the energy transition in the Netherlands. 2022. https://www.strategyand.pwc.com/nl/en/industries/energy-utilities/hyperefficient-evs.html.

[72] Trishna Raj, Andrew A. Wang, Charles W. Monroe, and David A. Howey. Investigation of Path-Dependent Degradation in Lithium-Ion Batteries. 2020. https://chemistry-europe-onlinelibrary-wiley-com.tudelft.idm.oclc.org/doi/full/10.1002/batt.202000160.

[73] Eduardo Redondo-Iglesias, Pascal Venet, and Serge Pélissier. Influence of the non-conservation of SoC value during calendar ageing tests on modelling the capacity loss of batteries. *2015 10th International Conference on Ecological Vehicles and Renewable Energies, EVER 2015*, 6 2015. doi: 10.1109/EVER.2015.7112987.

[74] Eduardo Redondo-Iglesias, Pascal Venet, and Serge Pelissier. Calendar and cycling ageing combination of batteries in electric vehicles. *Microelectronics Reliability*, 88-90:1212–1215, 9 2018. ISSN 0026-2714. doi: 10.1016/J.MICROREL.2018.06.113.

[75] Simone Regondi, Rudi Santbergen, and Olindo Isabella Miro Zeman. Solar-Powered Infotainment Spot 2.0: Design and fabrication of a prototype in collaboration with Kaneka Corporation. 2017.

[76] Marijn Roks, Hielke Schurer, and dr. Ioannis Lampropoulos. Vehicle-to-Everything (V2X) in the Netherlands. *Netherlands Enterprise Agency (RVO)*, 2019. https://english.rvo.nl/sites/default/files/2020/10/V2X%20in%20the%20Netherlands-%20Report.pdf.

[77] Mohammadhosein Safari and Charles Delacourt. Aging of a commercial graphite/LiFePO4 cell. *Journal of The Electrochemical Society*, 158:A1123–A1135, 10 2011. doi: 10.1149/1.3614529.

[78] Gaizka Saldaña, José Ignacio San Martín, Inmaculada Zamora, Francisco Javier Asensio, and Oier Oñederra. Analysis of the current electric battery models for electric vehicle simulation. *Energies*, 12, 2019. ISSN 19961073. doi: 10.3390/en12142750.

[79] Rudi Santbergen, V. A. Muthukumar, , and Arno H. M. Smets. A new method for calculating solar irradiance on PV system facing reflective surfaces. 2016.

[80] Guy Sarre, Philippe Blanchard, and Michel Broussely. Aging of lithium-ion batteries. *Journal of Power Sources*, 127:65–71, 3 2004. ISSN 03787753. doi: 10.1016/j.jpowsour.2003.09.008.

[81] M. Schimpe, M. E. von Kuepach, M. Naumann, H. C. Hesse, K. Smith, and A. Jossen. Comprehensive Modeling of Temperature-Dependent Degradation Mechanisms in Lithium Iron Phosphate Batteries. *Journal of The Electrochemical Society*, 165:A181–A193, 2018. ISSN 0013-4651. doi: 10.1149/2.1181714jes.

[82] Jonas Schlund. *Electric Vehicle Charging Flexibility for Ancillary Services in the German Electrical Power System*. doctoralthesis, Friedrich-Alexander-Universitat Erlangen-Nurnberg (FAU), 2021.

[83] Johannes Schmalstieg, Stefan Käbitz, Madeleine Ecker, and Dirk Uwe Sauer. From Accelerated Aging Tests to a Lifetime Prediction Model: Analyzing Lithium-Ion Batteries. 2013.

[84] Johannes Schmalstieg, Stefan Käbitz, Madeleine Ecker, Dirk Uwe Sauer, Nerea Nieto, Stefan Käbitz, Holger Blanke, and Alexander Warnecke. Calendar and cycle life study of Li(NiMnCo)O2-based 18650 lithium-ion batteries. *Journal of Power Sources*, 248:839–851, 2014. ISSN 03787753. doi: 10.1016/j.jpowsour.2013.09.143.

[85] Dionne Searcey, Michael Forsythe, and Eric Lipton. A Power Struggle Over Cobalt Rattles the Clean Energy Revolution. 2020.
https://www.nytimes.com/2021/11/20/world/china-congo-cobalt.html.

[86] Xavier Seront, Ricardo Fernandez, Nicole Mandl, and Elisabeth Rigler. Annual European Union greenhouse gas inventory 1990–2020 and inventory report 2022. *European Environment Agency (EEA)*, 2022.
https://www.eea.europa.eu/publications/annual-european-union-greenhouse-gas-1.

[87] Kandler Smith, Matthew Earleywine, Eric Wood, Jeremy Neubauer, and Ahmad Pesaran. Comparison of plug-in hybrid electric vehicle battery life across geographies and drive cycles. *SAE Technical Papers*, 2012. ISSN 26883627. doi: 10.4271/2012-01-0666.

[88] SMM - The Leading Metals Information Provider in China. Guoxuan Hi-Tech's LFP battery cells have energy density above 200Wh/kg in test stage. 2020.
https://news.metal.com/newscontent/101032150/
guoxuan-hi-techs-lfp-battery-cells-have-energy-density-above-200whkg-in-test-stage/.

[89] Thomas Steffen, Ashley Fly, and William Mitchell. Optimal electric vehicle charging considering the effects of a financial incentive on battery ageing. *Energies*, 13, 9 2020. ISSN 19961073. doi: 10.3390/EN13184742.
https://www.researchgate.net/publication/344858550_Optimal_Electric_Vehicle_
Charging_Considering_the_Effects_of_a_Financial_Incentive_on_Battery_Ageing.

[90] Maarten Steinbuch. Tesla Model S battery degradation data. 2020.
https://maartensteinbuch.com/2015/01/24/tesla-model-s-battery-degradation-data/.

[91] Darlene Steward. Critical Elements of Vehicle-toGrid (V2G) Economics. 2017.

[92] Laisuo Su, Jianbo Zhang, Caijuan Wang, Yakun Zhang, Zhe Li, Yang Song, Ting Jin, and Zhao Ma. Identifying main factors of capacity fading in lithium ion cells using orthogonal design of experiments. *Applied Energy*, 163:201–210, 2 2016. ISSN 03062619. doi: 10.1016/j.apenergy.2015.11.014.

[93] TenneT. Frequency Containment Reserves (FCR). 2022.
https://www.entsoe.eu/network_codes/eb/fcr/.

[94] TenneT. Dutch Ancillary Services. 2022.
https://www.tennet.eu/markets/dutch-ancillary-services.

[95] Manh Kien Tran, Andre Dacosta, Anosh Mevawalla, Satyam Panchal, and Michael Fowler. Comparative study of equivalent circuit models performance in four common lithium-ion batteries: LFP, NMC, LMO, NCA. *Batteries*, 7, 9 2021. ISSN 23130105. doi: 10.3390/batteries7030051.

[96] Kotub Uddin, Rebecca Gough, Jonathan Radcliffe, James Marco, and Paul Jennings. Techno-economic analysis of the viability of residential photovoltaic systems using lithium-ion batteries for energy storage in the United Kingdom. *Applied Energy*, 206:12–21, 11 2017. ISSN 03062619. doi: 10.1016/j.apenergy.2017.08.170.

[97] Kotub Uddin, Tim Jackson, Widanalage D. Widanage, Gael Chouchelamane, Paul A. Jennings, and James Marco. On the possibility of extending the lifetime of lithium-ion batteries through optimal V2G facilitated by an integrated vehicle and smart-grid system. *Energy*, 133:710–722, 8 2017. ISSN 0360-5442. doi: 10.1016/J.ENERGY.2017.04.116.

[98] Kotub Uddin, Matthieu Dubarry, and Mark B. Glick. The viability of vehicle-to-grid operations from a battery technology and policy perspective. *Elsevier Energy Policy*, 2018. https://doi.org/10.1016/j.enpol.2017.11.015.

[99] Andrew Ulvestad. A Brief Review of Current Lithium Ion Battery Technology and Potential Solid State Battery Technologies. 2018. https://arxiv.org/abs/1803.04317.

[100] United States Environmental Protection Agency. Green Vehicle Guide - Electric Vehicle Myths. 2021. https://www.epa.gov/greenvehicles/electric-vehicle-myths.

[101] Felipe Gonzalez Venegas, Marc Petit, and Yannick Perez. Plug-in behavior of electric vehicles users: Insights from a large-scale trial and impacts for grid integration studies. *eTransportation*, 10, 11 2021. ISSN 25901168. doi: 10.1016/j.etran.2021.100131.

[102] Wiljan Vermeer, Gautham Ram Chandra Mouli, and Pavol Bauer. A Comprehensive Review on the Characteristics and Modelling of Lithium-ion Battery Ageing. *IEEE Transactions on Transportation Electrification*, 6 2022. ISSN 23327782. doi: 10.1109/TTE.2021.3138357.

[103] J. Vetter, P. Novák, M. R. Wagner, C. Veit, K. C. Möller, J. O. Besenhard, M. Winter, M. Wohlfahrt-Mehrens, C. Vogler, and A. Hammouche. Ageing mechanisms in lithium-ion batteries. *Journal of Power Sources*, 147:269–281, 9 2005. ISSN 03787753. doi: 10.1016/j.jpowsour.2005.01.006.

[104] Voltaplex. Sanyo E 18650 Battery, 2000mAh, 6A, 3.6V, Grade A Lithium-ion (UR18650E). 2020. https://voltaplex.com/sanyo-e-18650-battery-ur18650e.

[105] Marnix Wagemaker. Energy Storage in Batteries CH3222SET (2020/21 Q3) TU Delft. 2021.

[106] Dai Wang, Jonathan Coignard, Teng Zeng, Cong Zhang, and Samveg Saxena. Quantifying electric vehicle battery degradation from driving vs. vehicle-to-grid services. *Journal of Power Sources*, 332:193–203, 11 2016. ISSN 0378-7753. doi: 10.1016/J.JPOWSOUR.2016.09.116.

[107] John Wang, Ping Liu, Jocelyn Hicks-Garner, Elena Sherman, Souren Soukiazian, Mark Verbrugge, Harshad Tataria, James Musser, and Peter Finamore. Cycle-life model for graphite-LiFePO4 cells. *Journal of Power Sources*, 196:3942–3948, 4 2011. ISSN 0378-7753. doi: 10.1016/J.JPOWSOUR.2010.11.134.

[108] WebPlotDigitizer. Web based tool to extract data from plots, images, and maps. 2022. https://automeris.io/WebPlotDigitizer/.

[109] Evelina Wikner and Torbjörn Thiringer. Extending Battery Lifetime by Avoiding High SOC. *MDPI Applied Sciences*, 2018. doi: 10.3390/app8101825. www.mdpi.com/journal/applsci.

[110] World Climate Guide. Climate - Dubai (United Arab Emirates). 2020. https://www.climatestotravel.com/climate/netherlands/amsterdam.

[111] World Climate Guide. Climate - Amsterdam (Netherlands). 2020. https://www.climatestotravel.com/climate/united-arab-emirates/dubai.

[112] WorldData.info. Sunrise and sunset in the United Arab Emirates. 2022. https://www.worlddata.info/asia/arab-emirates/sunset.php.

[113] Remus Teodorescu Xin Sui, Maciej Swierczynski and Daniel-Ioan Stroe. The Degradation Behavior of LiFePO4/C Batteries during Long-Term Calendar Aging. *energies*, 2021. doi: 10.3390/en14061732. https://www.researchgate.net/publication/350281395_The_Degradation_Behavior_of_LiFePO4C_Batteries_during_Long-Term_Calendar_Aging.

[114] Chengke Zhou, Kejun Qian, Malcolm Allan, and Wenju Zhou. Modeling of the Cost of EV Battery Wear Due to V2G Application in Power Systems. *IEEE Transactions on Energy Conversion*, 2011. https://ieeexplore-ieee-org.tudelft.idm.oclc.org/stamp/stamp.jsp?tp=&arnumber=5958591.

[115] Albert H. Zimmerman and Michael V. Quinzio. Lithium Plating in Lithium-Ion Cells. 2010. https://www.nasa.gov/sites/default/files/atoms/files/1-lithium_plating_azimmerman.pdf.